

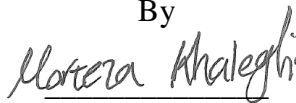
Development of Holographic Interferometric Methodologies for Characterization of Shape and Function of the Human Tympanic Membrane

A Dissertation
submitted to the faculty of the

Worcester Polytechnic Institute

as a partial fulfillment of the requirements for the
Degree of Doctor of Philosophy
in
Mechanical Engineering

By


Morteza Khaleghi

21 April 2015

Approved:



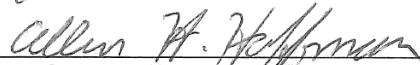
Professor Cosme Furlong, Advisor



Professor John J. Rosowski, Massachusetts Eye & Ear Infirmary,
Harvard Medical School, Committee Member



Professor John M. Sullivan, Committee Member



Professor Allen H. Hoffman, Committee Member



Professor Jamal S. Yagoobi, Graduate Committee Representative

Copyright © 2015

By

CHSLT – Center for Holographic Studies and Laser micro-mechaTronics

Mechanical Engineering Department

Worcester Polytechnic Institute

Worcester, MA 01609-2280

All rights reserved

Abstract

The hearing process involves a series of physical events in which acoustic waves in the outer ear are transduced into acousto-mechanical motions of the middle ear, and then into chemo-electro-mechanical reactions of the inner ear sensors that are interpreted by the brain. Air in the ear canal has low mechanical impedance, whereas the mechanical impedance at the center of the eardrum, the umbo, is high. The eardrum or Tympanic Membrane (TM) must act as a transformer between these two impedances; otherwise, most of the energy will be reflected rather than transmitted. The acousto-mechanical transformer behavior of the TM is determined by its geometry, internal fibrous structure, and mechanical properties. Therefore, full-field-of-view techniques are required to quantify shape, sound-induced displacements, and mechanical properties of the TM. Shapes of the mammalian TMs are in millimeter ranges, whereas their acoustically-induced motions are in nanometer ranges, therefore, a clinically-applicable system with a measuring range spanning six orders of magnitude needs to be realized. In this Dissertation, several full-field measuring modalities are developed, to incrementally address the questions regarding the geometry, kinematics, and dynamics of the sound-induced energy transfer through the mammalian TMs. First, a digital holographic system with a measuring range spanning several orders of magnitude is developed and shape and 1D sound-induced motions of the TM are measured with dual-wavelength holographic contouring and single sensitivity vector holographic interferometry, respectively. The sound-induced motions of the TMs are hypothesized to be similar to those of thin-shells (with negligible tangential motions) and therefore, 3D sound-induced motions of the TM are estimated by combining measurements of shape and 1D motions. In order to test the applicability of the thin-shell hypothesis, and to obtain further details of complex spatio-temporal response of the TMs, holographic systems with

multiple illumination directions are developed and shape and acoustically-induced vibrational patterns of the TMs are quantified in full 3D. Furthermore, to move toward clinical applications and *in-vivo* measurements, high-speed single-shot multiplexing holographic system are developed and 3D sound-induced motions of the TM are measured simultaneously in one single frame of the camera. Finally, MEMS-based high-resolution force sensing capabilities are integrated with holographic measurements to relate the kinematics and dynamics of the acousto-mechanical energy transfer in the hearing processes. The accuracy and repeatability of the measuring systems are tested and verified using artificial samples with geometries similar to those of human TMs.

The systems are then used to measure shape, 3D sound-induced motions, and forces of chinchilla and human cadaveric TM samples at different tonal frequencies (ranging from 400 Hz to 15 kHz) simultaneously at more than 1 million points on its surface. A general conclusion is that the tangential motions are significantly (8-20 dB) smaller than the motions perpendicular to the TM plane, which is consistent with the thin-shell hypothesis of the TM. Force measurements reveal that frequency-dependent forces of the TM, are also spatially dependent so that the maximum magnitudes of the force transfer function of the umbo occurs at frequencies between 1.6 to 2.3 kHz, whereas the maximum values for other points on the TM surface occurs at higher frequency ranges (4.8 to 6.5 kHz).

The Dissertation is divided into two Parts, each contains several Chapters. In the first Part, general overviews of the physiology of the human middle ear, along with brief summaries of previous studies are given, and basics of holographic interferometry are described. In the second Part, developments and implementations achieved in completion of this work are described in the form of a series of manuscripts. Finally, conclusions and recommendations for future work are provided.

Acknowledgements

Foremost, I would like to express my sincere gratitude and appreciations to my advisors Professors Cosme Furlong (at Worcester Polytechnic Institute) and John J. Rosowski (at Harvard Medical School) for giving me the opportunity to do this work and for the valuable guidance and continuous support they have provided along the way.

I would like to also thank my PhD dissertation committee members for their continuous assistance and support during completion of this Dissertation research. Additionally, the project would never have progressed as far as it did without the help of all the members of the Center for Holographic Studies and Laser micro-mechaTronics (CHSLT) at the Mechanical Engineering Department of WPI and Eaton-Peabody Laboratory (EPL) at Massachusetts Eye and ear Infirmary (MEEI). I would like to particularly thank Ivo Dobrev for his constant support, Ellery Harrington for his software developments, Peter Hefti for his assistance with the optical systems, and Jeffrey T. Cheng, Jérémie Guignard, and Mike Ravicz for their constant help and assistance in sample preparations and experimental tests. Special thanks go to Professor Rich Pryputniewicz.

This work has been supported with the funding of the National Institutes of Health (NIH), National Institute of Deafness and other Communication Disorders (NIDCD), Massachusetts Eye and Ear Infirmary (MEEI), the Mittal Fund, and the James Nichols Heald Research Collaboration Award.

Last but not least, I would like to particularly thank my wife Simin for her great patience and encouraging supports and her constant smile throughout all the ups and downs in the past four years. I would like to thank my parents, for their encouraging support and emotional help throughout these years. Without all these wonderful people, I know I couldn't be where I am today.

Table of Contents

Abstract	i
Acknowledgements	iii
Table of Contents	iv
List of Figures	viii
Nomenclature	xv
Objective	xviii
1. Introduction	1
1.1. Problem statement.....	1
1.2. Significance of the problem.....	2
2. Dissertation outline	3
Part 1: Background	6
3. Physiology of the Human Ear	7
3.1. Tympanic Membrane.....	8
3.2. Function of the Middle ear.....	11
3.3. Middle-ear Impedance Matching Mechanisms.....	13
3.3.1. Area Ratio Transformation.....	14
3.3.2. Ossicular Chain Lever Action.....	15
3.3.3. Catenary lever action.....	15
4. Previous Middle ear Studies	17
4.1. Input impedance of the stapes and cochlea.....	17
4.2. Middle ear input-output gains.....	19
4.3. Mechanical model of the middle ear.....	23

4.4.	Lumped parametric model of a human eardrum	25
4.5.	Eardrum modeled as a string with distributed force	27
4.6.	Finite Element Method (FEM).....	28
4.7.	Kinematics of thin shells	31
4.7.1.	Dynamics of Kirchhoff-Love thin shells	34
5.	Existing Methodologies for Otolaryngologist	36
5.1.	Conventional Otoscopy	36
5.2.	Single-point measurements by Laser Doppler Vibrometry (LDV).....	36
5.3.	Full-field motion measurements.....	38
5.3.1.	Time-averaged Holography	39
5.3.2.	Quantitative 1D Holographic Measurements.....	40
5.4.	3D Shape Measurements	41
6.	Digital Holographic Interferometry.....	44
6.1.	Electromagnetic waves.....	45
6.2.	Light Interference.....	47
6.3.	Holographic recording and reconstruction.....	49
6.4.	Fresnel-Kirchhoff Diffraction Theory.....	51
6.5.	Numerical reconstruction By the Fresnel Transform.....	52
6.5.1.	Discrete Fresnel transformation.....	54
6.6.	3D Displacements measurements.....	55
6.7.	3D Shape measurements with Holographic Interferometry.....	57
6.7.1.	Two-refractive Index holographic contouring	58
6.7.2.	Multiple illumination directions holographic contouring	58
6.7.3.	Dual-wavelength holographic contouring.....	59

6.8.	Applications of Holographic Interferometry in Hearing Research	60
PART 2: Developments		62
General Overview		63
7. Paper A: Digital holographic measurements of shape and three-dimensional sound-induced displacements of tympanic membrane		67
7.1.	Shape measuring approach.....	68
7.2.	TM as a thin-shell.....	68
8. Paper B: Measurements of three-dimensional shape and sound-induced motion of the chinchilla tympanic membrane		83
9. Paper C: Three-dimensional vibrometry of the human eardrum with stroboscopic lensless digital holography		93
9.1.	Stroboscopic measurements of motion	94
9.2.	Three-dimensional vibrometry	95
9.3.	General procedures for 3D motion measurements.....	97
10. Paper D: 4D Measurements of the in-Plane and out-of-plane motion of the human tympanic membrane		116
11. Paper E: Simultaneous full-field three-dimensional vibrometry of the human eardrum using spatial-bandwidth multiplexed holography		134
12. Paper F: Characterization of acoustically-induced forces of the human eardrum		146
12.1.	Capacitive force sensing approach	147
12.2.	Compensation for the stress relaxation of TM	149
13. Conclusions and Future Work		158
References		161

List of Figures

- Figure 3.1. Schematic of the auditory system with its primary components including external auditory canal, Tympanic Membrane (TM), Ossicles (including Malleus, Incus, and Stapes), and the Cochlea (adapted from Chittka 2005). ----- 8
- Figure 3.2. Orientation and structure of human Tympanic Membrane (TM): (a) the TM is located at the end of the ear canal with a particular inclination angle, so that the angles formed with the ear canal walls are 140 or 30 degrees; (b) the TM of a human right ear as it is visible from the ear canal (adapted from Ferrazzini, 2003). ----- 9
- Figure 3.3. Human TM and its internal structure: (a) an image of a human TM captured through the ear canal; and (b) the internal structure of the TM tissue showing different categories of fibers and layers (adapted from Lim, 1970). ----- 9
- Figure 3.4. Fibrous structure of a guinea pig TM imaged with scanning electron microscope in: (a) the anterior superior quadrant of the TM ($\times 300$); (b) the posterior superior quadrant of the TM ($\times 300$); (c) the bordering area between the superior and inferior-posterior quadrant ($\times 1000$); and (d) circular fibers cross over the radial fibers and branch and anastomose to each other forming a network ($\times 3400$) PF: Parabolic Fibers, AL: Annular Ligament, RF: Radial Fibers, CF: Circular Fibers (adapted from Kawabata and Ishii, 1971). ----- 11
- Figure 3.5. Human middle ear ossicular chain: (a) schematic of the human external, middle, and inner ears; and (b) human ossicular chain including the malleus (M), incus (I), and stapes (S) (adapted from Rossing 2007).----- 13

Figure 3.6. Middle ear impedance matching mechanisms: (a) area ratio transformation resulting from surface area mismatch between TM and Oval Window; and (b) ossicular chain lever action (adapted from Emanuel and Letowski, 2009). ----- 14

Figure 4.1. A simplified horizontal cross-section of a human temporal bone (right ear) preparation for driving the middle ear in the forward and reverse directions (note the presence of the inner-ear sound source). A small speaker is used as the sound-source in the ear canal to drive the middle ear in the forward direction. The inner-ear sound source coupled to a tube cemented near the round window was used to drive the inner ear in the reverse direction. The ear-canal pressure P_{ec} was measured with an ER-7C probe-tube microphone. To measure the inner-ear pressure P_V , a hydro-pressure transducer was placed in the vestibule. The stapes velocity was measured with a HLV-1000 PolyTec laser vibrometer. An inlet and outlet tube allowed flushing of the inner ear to ensure that it remained fluid filled (Puria 2003). ----- 20

Figure 4.2. Measurements of $M1$, $M2$, $M3$, and ZC from five human temporal bones. The average of the log-magnitude and angle is shown as thick-solid lines in each panel. $M1$ and ZC were measured while the ear was stimulated, with an ear canal sound source, in the forward direction, whereas $M2$ and $M3$ were measured while the ear was stimulated, with the inner ear sound source, in the reverse direction (Puria 2003). ----- 22

Figure 4.3. Mechanical mode of the middle ear: (a) the middle ear is modelled by a series of Masses (M), Stiffnesses (S), and Resistances (R). Subscripts are external auditory canal (E), tympanic membrane (T), middle ear cavity (M), antrum (A), pneumatic mastoid cells (P), handle of malleus (H), incudo-stapedial joint (J), stapes (S), annular ligament (L), basilar membrane (B), and round window (R); and (b) measurements of sound pressure at the tympanic membrane (PT) and in the middle ear (PM) (Onchi, 1961). ----- 23

Figure 4.4. Lumped parametric model of a human ear consisting of six masses ($M1$ to $M6$) suspended by ten dashpots ($C1$ to $C10$) and six springs ($K1, K2, K3, K5, K6, K8$) (Feng and Gan 2004). -----26

Figure 4.5. Comparison between predicted displacements at $M2$ and $M5$ of the lumped model and the experimental single-point LDV measurement (Feng and Gan 2004). -----27

Figure 4.6. Finite element model of the left human middle ear: (a) the model includes the tympanic membrane, three ossicles (malleus, incus, and stapes), two joints, manubrium, ligaments, and muscle tendons ($C1, C2, C3, C4, C5, C7$), tympanic annulus, stapedial annular ligament, external ear canal, middle ear cavity (transparent); and (b) illustration of the connection between malleus and eardrum, incudomalleolar joint, incudostapedial joint, and the eardrum structure (Gan et al., 2004). -----30

Figure 4.7. Comparison of the results of frequency-response predicted by FE method (thick solid line) with single-point experimental measurements at 10 different bones: (a) sound-induced motion at the tip of the manubrium, the umbo; and (b) sound-induced motion at the stapes footplate (Gan et al., 2004). -----30

Figure 4.8. The lack of change in the normal vector during displacement of a thin-shell. In-plane displacement components at a distance z from the mid-plane surface along: (a) x -axis; and (b) y -axis. Mid-plane of the shell is shown with a dashed line. w is the z -axis displacement of the mid-plane surface. -----32

Figure 5.1. Visual inspection of the outer ear (ear canal and eardrum) by qualitative otoscopy (a) schematic of the otoscopy by illuminating the light on the surface of the eardrum; and (b) the physician inspects the ear of a patient qualitatively (adapted from Healthwise Inc.). 36

Figure 5.2. Laser Doppler Vibrometry (LDV) for single-point analyses of middle ear structures: (a) a typical 1D LDV setup for characterization of the umbo transfer function (Rosowski

et al., 2003); (b) 1D LDV used in a hearing research environment for characterization of patient’s hearing loss; (c) retro reflective beads on the surface of the TM in order to enhance the reflection of the laser light source in LDV measurements (Maftoon et al., 2013); and (d) three-dimensional LDV using three different illumination directions (Polytec Inc.,). -----37

Figure 5.3. Single-point 3D sound-induced vibrometry of the umbo of a cat eardrum using 1D LDV that is mounted on a positioning system: (a) definition of the x , y , and z -axes with respect to the estimate of the TM shape; and (b) measured amplitudes of 3D sound-induced motion of the umbo, along the x , y , and z axes (adapted from Decraemer et al., 1994). -----38

Figure 5.4. Time-averaged holograms of the vibrational patterns of a live cat TM at different tonal frequencies: (a) 600 Hz; (b) 950 Hz; (c) 2000 Hz; (d) 2900 Hz; (e) 4000 Hz; and (f) 5000 Hz (adapted from Khanna and Tonndorf 1972). -----39

Figure 5.5. Time-averaged holograms measured in four specimens of cadaveric human, chinchilla, and cat and live chinchilla at three different excitations frequencies (adapted from Rosowski et al., 2009).-----40

Figure 5.6. Magnitudes and phases of sound-induced motion of a human TM at four different tonal frequencies. The data are normalized by the stimulus sound pressure (units of $\mu\text{m}/\text{Pa}$). The size of each image is 800×800 pixels (adapted from Cheng et al., 2013). 41

Figure 5.7. Application of moiré interferometry for characterization of the shape of a gerbil TM: (a) schematic drawing of the projection liquid crystal moiré profilometry setup with LCD projector, lenses (L1,L2,L3) and a CCD camera. The liquid crystal modulator (LCM) grids and polarizers allow phase stepping and grid averaging; and (b) moiré interferogram of a gerbil TM used for characterization of the shape of the TM. To obtain the

interferogram, the difference was taken between the grid line image on a flat plate and the grid line image on the membrane. The fringes represent contours of equal height, and demonstrate the conical shape of the membrane. The fringe plane distance, and hence the height difference per fringe order, is 0.082 mm (adapted from Aernouts and Dirckx 2011; Dirckx and Decraemer 1997).-----42

Figure 6.1. Propagation of electro-magnetic wave in a direction perpendicular to its electric and magnetic fields.-----45

Figure 6.2. Principles of recording and reconstruction of holograms: (a) the hologram is illuminated with both reference and object beams; and (b) the hologram is illuminated with only the reference beam during holographic reconstruction. In the figure, *M* is mirror; *L* is lens; *BS* is beam splitter; and *S* is shutter (Dobrev, 2014). -----49

Figure 6.3. Schematics of the coordinate system nomenclature for lensless digital numerical reconstruction (Kreis, 2005). -----51

Figure 6.4. Geometrical definition of the sensitivity vector that is the vectorial subtraction of the observation vector from the illumination vector (Pryputniewicz et al., 1990).-----56

Figure 6.5. Adjusting the measuring sensitivity range in dual-wavelength holographic contouring by controlling the differences between the first and second wavelengths $\Delta\lambda = \lambda_2 - \lambda_1$: (a) broad changes in the wavelengths (in this case up to 100 nm) leads to fine contour depths $\Lambda_2 \approx 5 \mu m$ and in turn, a better shape measurement resolution; and (b) narrow changes in the wavelength (in this case up to 1 nm) leads to larger contour depths $\Lambda_2 \approx 0.5 mm$ and hence, lower measuring sensitivity. The results are shown for four different central wavelengths 473, 532, 632, and 780 nm. -----60

Figure 7.1. Thin-shell modeling of a TM: (a) measured shape of a chinchilla TM (Khaleghi et al., 2013); and (b) schematic of curvilinear coordinate system (α, β, η) on a TM element with a thickness t . Tangential components of the neutral plane, $d\alpha_0$ and $d\beta_0$, are negligible. 69

Figure 7.2. Application of thin-shell theory to recover three-dimensional motion components from shape and only 1D motion measurements: (a) shape of the TM to determine surface normal vectors; (b) 1D sound-induced motion measurements of the TM through lateral axis (z-axis); (c), (d), and (e) are recovered x - and y -axes, and measured z-axis sound-induced motion, superimposed on the shape of the TM, respectively. The TM was subjected to tonal frequency of 5,730 Hz at the sound pressure level of 101 dB SPL. ---71

Figure 9.1. Signals for stroboscopic measurements of sound-induced displacements of the TM at an example phase of 90 degrees: (a) sinusoidal signal sent to the speaker to stimulate the TM; and (b) pulsed signal sent to the AOM that acts as a high-speed shutter for laser light illumination with a duty cycle of 2-5% of the tonal excitation period. During a full measurement, the phase position of the pulse is varied from 0 to 360 degrees at specified increments to capture the complete cyclic motion.-----94

Figure 9.2. Procedures for stroboscopic measurements of three-dimensional magnitudes and phases of sound-induced motion of the TM. -----97

Figure 9.3. Wrapped optical phases corresponding to stroboscopically-measured motion of a harmonically-driven semi-spherical artificial membrane along four sensitivity vectors at 8 different temporal phases.-----99

Figure 9.4. Unwrapped optical phases corresponding to harmonically-driven motion of a semi-spherical artificial membrane along four sensitivity vectors at 8 different stroboscopic phases. ----- 100

Figure 9.5. The results obtained from FFT algorithm obtained for measurements along four sensitivity vectors $K1$ to $K4$: (a) magnitudes of motions; (b) phases of motion; and (c) the squared of the Pearson Product Correlation Coefficient between the measured phasic variations of the motion and the sinusoidal motion reconstructed from the magnitude and angle of the Fourier determined fundamental component of the phasic motion. ----- 101

Figure 9.6. Three-dimensional vibration measurements at different phases of cyclic vibration of a thin semi-spherical membrane captured by our developed holographic interferometric system. The results have been obtained by solving the system of equations shown in Eq. 6-39 for each phase of stimuli. ----- 103

Figure 9.7. 3D harmonically-driven reconstructed motion along three axes x , y , and z obtained experimentally with the holographic system: (a) motions' magnitudes; (b) motions' phases; and (c) goodness of curve-fitting by estimating the squared of correlation coefficient. The results have been obtained from data shown in Figure 9.6 by fitting a sinusoidal function with a given magnitude (a) and phase (b) at each pixel along each Cartesian axes x , y , and z using developed FFT algorithms. ----- 104

Figure 12.1. MEMS force sensor: (a) a solid model of the sensor; (b) schematic of the internal structure of the sensor; and (c) block diagram of the sensor and its readout circuit (adapted from Sun and Nelson 2007).----- 147

Figure 12.2. Viscoelastic properties of the TM exhibiting stress relaxation: (a) stress relaxation as a function of time under constant strain; and (b) Generalized Maxwell Model (adapted from Zhang et al., 2007).----- 149

Nomenclature

AL	Annular Ligament
<i>B</i>	Magnetic field
BS	Beamsplitter
CCD	Charge-coupled device
CF	Circular Fiber
dB	Decibel
<i>E</i>	Electric field
<i>h</i>	Complex field of a recorded hologram
IFFT2	2D Inverse Fast Fourier Transform
IR	Infrared
LDV	Laser Doppler Vibrometry
MEMS	Micro-Electro-Mechanical Systems
OAE	Oto-acoustic Emission
OW	Oval Window
<i>P</i>	Complex acoustic pressure
<i>Q</i>	Complex acoustic volume flow rate
<i>R</i>	Acoustic resistance
RF	Radial Fiber
SEM	Scanning Electron Microcopy
SPL	Sound Pressure Level
TM	Tympanic Membrane
<i>X</i>	Acoustic reactance

Z	Acoustic impedance
A_{FP}	Area of the stapes footplate
\mathbb{C}	Condition number of the sensitivity matrix
G_{ME}^{RT}	Roundtrip middle-ear pressure gain
\mathbf{k}_s	Sensitivity vector
\mathbf{k}_i	Illumination vector
\mathbf{k}_o	Observation vector
$M1$	Ratio of the vestibule pressure to the ear-canal pressure
$M2$	Ratio of the ear-canal pressure to the inner-ear pressure
$M3$	Ratio of the vestibule pressure to the stapes volume velocity
P_{ec}	Ear canal pressure
P_F	Pressure in the external sound field
P_{OW}	Sound pressure acting on the oval window
P_{RW}	Sound pressure outside the round window
P_S	Sound pressure measured at the stapes head
P_T	Pressure at the lateral side of the TM
P_V	Pressure variation in the fluids of the Scala vestibule
r	impedance ratio of the liquid in the cochlea to the air
\mathbb{S}	Sensitivity matrix
T	Energy transmission coefficient
t_m	Exposure time
U_{ec}	Ear canal volume velocity
U_{ST}	Stapes volume velocity

v_s	Stapes velocity
X_S	Stapes displacement
Z_C	Cochlear input impedance
Z_{SC}	Acoustic input impedance of the stapes and cochlea
ψ	Discrete chirp function
Λ	Synthetic wavelength
Ω	Fringe-locus function
β	Constant related to the light sensitivity of the sensor
φ	Optical phase of the hologram
Ω	Unwrapped optical phase difference
ω	Angular frequency
λ	Laser Wavelength
θ_{ST}	Relative angle between stapes and footplate's normal

Objective

The aim of this work is to develop, implement, and apply three-dimensional full-field holographic systems for measurements and characterizations of the spatio-temporal complexity of the sound-induced motions of the human Tympanic Membrane (TM). This includes developments of novel:

- i. compact biomedical imaging systems with measuring ranges spanning several orders of magnitude, within the same instrument, to characterize shape (i.e., in millimeter scale) and sound-induced motions (i.e., in nanometer scale) for applications in the research clinic,
- ii. stroboscopic system for quantifications of the sound-induced vibrational patterns in full 3D,
- iii. multiplexed single-shot holographic system to minimize the acquisition time required for 3D motion measurements, which eventually may lead to novel full-field quantitative tools to capture 3D vibrational patterns of the TM *in-vivo*,
- iv. methodologies for characterization of micro-scale sound-induced forces in the middle ear to understand the relation between kinematics and dynamics of acoustic energy transfer within the middle ear, and to enable characterization of stress-strain states of the TMs,
- v. numerical methods, software implementation, and algorithms for batch processing of data to efficiently process large amounts of holographic data, and in turn, automatically store the kinematics and dynamics information for future data mining and clustering,

1. Introduction

1.1. Problem statement

It is recognized that sound-induced motions of the eardrum or the Tympanic Membrane (TM) are the first step in the transduction of airborne sound energy to the mechanical energy associated with motions of the middle ear ossicles and the sensory organs within the inner ear. Different multi-physics phenomena involved in the transfer of energy from the outer ear to the middle ear and the inner ear complicate the hearing process. At the very beginning, the travel of airborne acoustic waves down the ear canal and their interaction with the TM forms an acoustic-solid interaction problem. The sound-induced vibrations of the TM set the ossicular chain (smallest bones in the human body) behind the TM into vibration, which in turn, induces chemo-electro-mechanical reactions of the inner ear using the impedance matching mechanisms between the air-filled outer ear and fluid-filled inner ear. These complicated processes and space constraints within the human ear make experimental observation and measurements of these processes challenging, and instead, several numerical and theoretical models have been developed to help further understanding of the hearing processes. However, there are limited experimental descriptions and observations of how the entire surface of the TM moves in response to sound to test these models and hypotheses. Different challenges exist for such measurements and metrology systems with high-resolution (magnitudes of sound-induced motions of the TM can be on the order of a few nanometers or less), high measuring-range (sound-induced motions are in the nanometer range, whereas shape of the TM is in the millimeter range, therefore, a suitable metrology system should have a range spanning nearly six orders of magnitude), and high speed of acquisition (human hearing frequency range is between 20 to 20,000 Hz, and the Nyquist criterion suggests a minimum acquisition rate of 40,000 frames per second) are needed.

1.2. Significance of the problem

Tympanoplasty describes a series of procedures that either repair or reconstruct the TM and the ossicular chain in ears damaged by trauma and/or disease. Otolgic surgeons perform tens of thousands of tympanoplasties each year with mixed results. Simpler TM patching procedures generally produce good hearing results, but about half of the most complicated TM grafts and ossicular reconstructions yield residual conductive hearing losses greater than 30 dB, with some as high as 50-60 dB. However, even simple patching procedures may results in significant residual conductive hearing loss. Our group is developing holographic interferometric tools to investigate and understand the sources of this variability in the efficacy of TM reconstructions. The 3-Dimensional shape and dynamic sound-induced motion measurements of the entire TM surface are coupled with measurements of force at the umbo and other well-defined locations along the surface of the TM. The combination of TM thickness, shape, 3D-motion and force measurements will help us understand the factors that govern signal transmission from the outer ear to the middle ear and finally to the inner ear and will pave the way toward characterization of the TM's mechanical properties.

2. Dissertation outline

This dissertation is organized in two main Parts each containing several Chapters. In the first part, background, a summary of previous works, and principles of holographic interferometry are presented. In the second part, overviews of the developments through this work, in the form of several publications, are presented.

Chapter 3 gives a brief description of the physiology of the human ear, with an emphasis on the function of the middle ear. The main components of the middle ear including the Tympanic Membrane (TM) and the ossicles (malleus, incus, and stapes) and their main task, which is the impedance matching mechanism, are reviewed.

Chapter 4 summarizes previously-developed models for the investigations of middle ear function along with their main assumptions and limitations. The need for experimental measurements of shape, full-field sound-induced motion, and forces in the middle ear are also highlighted.

Chapter 5 reviews the state-of-the-art quantitative and qualitative tools and techniques used by otolaryngologists for diagnosis and research purposes on the human middle ear. Their limitations for full-field quantitative investigations of shape and 3D sound-induced motion of the TM are also explained.

Chapter 6 describes the principles and mathematics of light interference and lensless digital holographic interferometry for quantification of shape and 3D deformation of objects. Constraints and limitations of 3D vibrometry of the objects are given and the needs to overcome those constraints are described.

Chapter 7 describes challenges along the way of measurements of three-dimensional sound-induced motion of the TM. Therefore, to simplify the problem, sound-induced kinematics

of the TM are hypothesized to be similar to those of thin-shells, where motions tangent to the local plane of the membrane are negligible. Development of a holographic system capable of measuring 3D shape and 1D sound-induced motions are described and, using thin-shell hypothesis, 3D sound-induced motions of the TM are estimated.

Chapter 8 provides a comprehensive study of the use of thin-shell hypothesis on chinchilla TM samples at several tonal excitation frequencies.

Chapter 9 describes developments and implementations of a digital holographic interferometry system for measurements of shape and 3D sound-induced motions of the human TMs. A new approach for automatic determination of the sensitivity vectors is introduced, and the accuracy and repeatability of the measurements are verified.

Chapter 10 provides detailed analyses of shape and sound-induced motions of multiple human TM samples. The 3D sound-induced motions are determined at different time intervals realizing four-dimensional measuring capabilities. The shapes of the TM are further analyzed and radii of curvature for the TM shapes are computed.

Chapter 11 describes developments and implementations of a new single-frame multiplexed holographic system for simultaneous measurements of 3D sound-induced motions.

Chapter 12 shows the procedures for integration of a micro-force sensor to 3D holographic systems to enable characterization of sound-induced sub-micro-Newton scale forces. The combination of the two systems (shape, 3D sound-induced motions, and forces) will enable characterization of both kinematics and dynamics of middle ear structures.

Chapter 13 reviews new technological advancements achieved during completion of this Dissertation for the study of shape and function of the middle ear, and in particular the human TM, at a level of details that have not been achieved before. These developments will lead to new discoveries in the mysteries of hearing, and encourage and inspire industrial sectors in

optics, lasers, and imaging systems to package such imaging modalities for clinical applications. Furthermore, this Chapter provides future work including a road map for improving the capabilities of the systems.

Part 1: Background

3. Physiology of the Human Ear

The ear is responsible for translating variations in air pressure, whether from music, speech, or other sources, into the neural activity necessary for our perception and interpretation of sound (Geisler 1998). The auditory periphery can be broken into three functionally and anatomically distinct components: external (acting as a resonator), middle (acting as an impedance matcher), and inner ear (acting as a Fourier analyzer), as shown in Figure 3.1 . The primary role of the external and middle ear is to pass the sound stimulus from the environment to the inner ear. The sound wave is diffracted and scattered by the body, head, and ear, and some fraction of the incident sound energy is gathered at the entrance to the ear canal. The funneled sound is transformed as it travels down the roughly cylindrical ear canal to the Tympanic Membrane (TM). The sound acting on the TM sets the ossicles (malleus, incus, and stapes) into motion. The motion of the ossicular chain conducts acoustic energy into the inner ear through the footplate of the stapes that is supported within the oval window at the entrance to the lymph-filled Scala Vestibuli of the inner ear, or cochlea. The pressure difference between the fluid in the Scala Vestibuli and the Scala Tympani of the inner ear stimulates the cochlear partition, resulting in motion of the partition's basilar membrane, which in turn, is sensed by the hair cells within the partition. Then, hair cells produce graded electrical signals that are sent to the brain for further interpretation and perception (Geisler 1998).

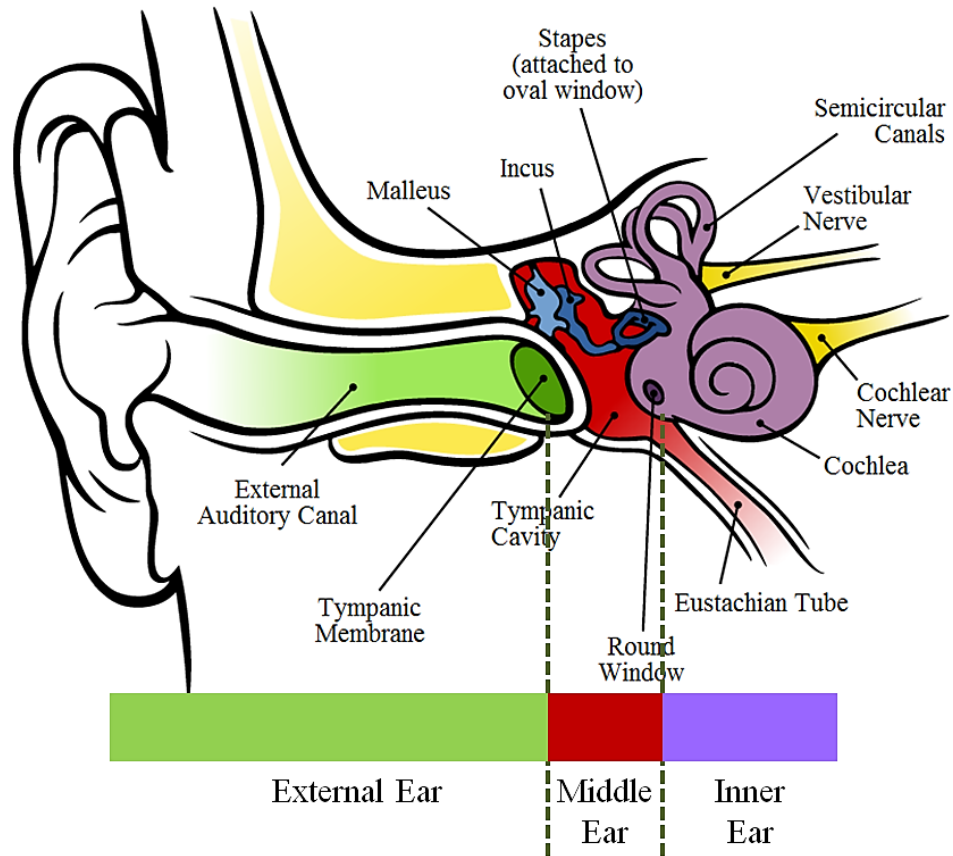


Figure 3.1. Schematic of the auditory system with its primary components including external auditory canal, Tympanic Membrane (TM), Ossicles (including Malleus, Incus, and Stapes), and the Cochlea (adapted from Chittka 2005).

Therefore, acoustically-induced vibrations of the TM play a primary role at the very beginning in the hearing process, in that these motions are the initial mechanical response of the ear to airborne sound (Khanna and Tonndorf 1972; Puria and Steele 2008; Rosowski et al., 2009).

3.1. Tympanic Membrane

The eardrum or Tympanic Membrane (TM) separates the outer ear from the middle ear. As shown in Figure 3.2, the TM is located at the end of the curved ear canal with a particular inclination, which allows it to have a larger surface than the cross-section of the ear canal itself. The angle between the eardrum and the superior and posterior wall of the ear canal is 140 degrees, while the angle between the eardrum and the inferior and anterior wall is 30 degrees.

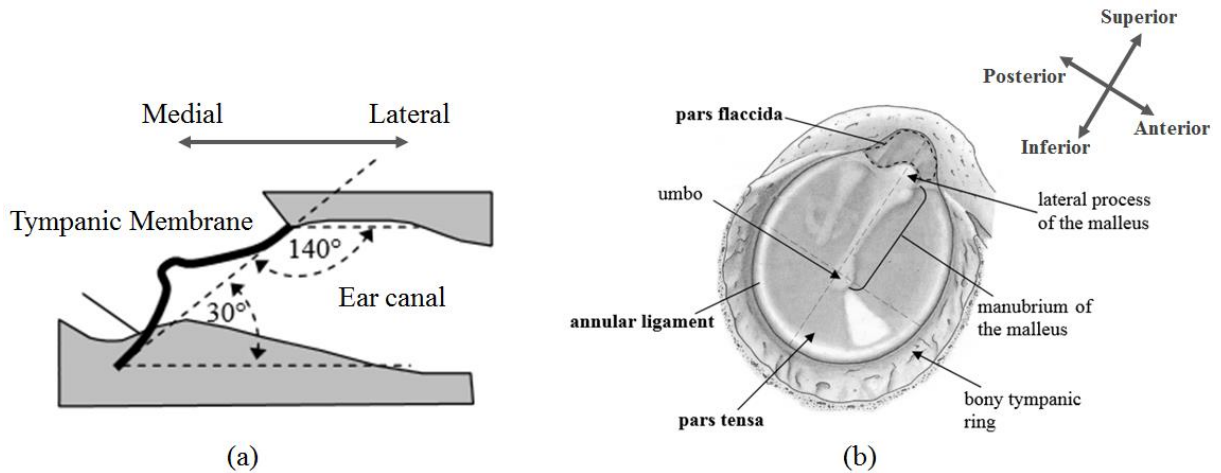


Figure 3.2. Orientation and structure of human Tympanic Membrane (TM): (a) the TM is located at the end of the ear canal with a particular inclination angle, so that the angles formed with the ear canal walls are 140 or 30 degrees; (b) the TM of a human right ear as it is visible from the ear canal (adapted from Ferrazzini, 2003).

Mammalian TMs and in particular, human TMs, are multi-layer fibrous structures consisting of the epidermal (lateral layer), lamina propria (middle layer), and mucosal epithelial (medial layer) layers from the lateral to medial side of the TM (Lim, 1970). Figure 3.3 shows an image of a human TM along with the configuration of the layers and fibers within the tissue of the TM, with collagen fibers oriented along radial and circumferential directions.

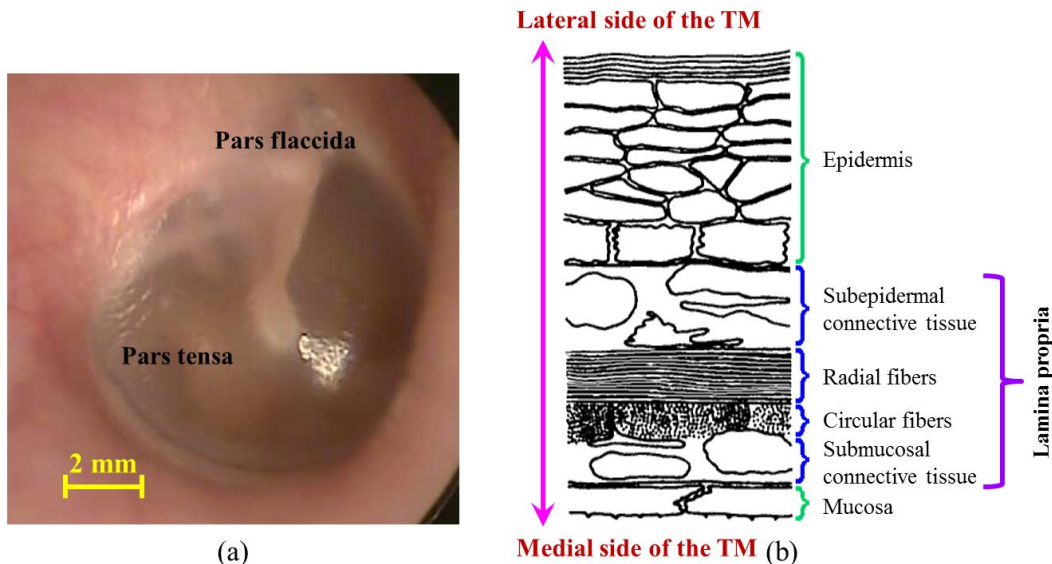


Figure 3.3. Human TM and its internal structure: (a) an image of a human TM captured through the ear canal; and (b) the internal structure of the TM tissue showing different categories of fibers and layers (adapted from Lim, 1970).

The annulus separates the TM into the pars tensa and pars flaccida. As shown in Figure 3.3a, the pars tensa is the major part, which is surrounded by tympanic annulus and is coupled to the manubrium of the malleus, while the pars flaccida is a small portion superior to the manubrium (the handle) of the malleus (Funnell et al., 1982). When the TM vibrates in response to sound pressure in the ear canal, its vibration is confined primarily to the pars tensa, which constitutes approximately 80% of the membrane's surface.

The exterior edge of the TM (annulus or annular ring) consists of a fibrous and cartilaginous tissue that is thicker and stiffer than the rest of the membrane. Figure 3.4 shows the images of the fibrous structure of the TM of a guinea pig captured by scanning electron microscope (Kawabata and Ishii, 1971). As shown in Figure 3.4, four different groups of fiber bundles including parabolic (PF), circular (CF), radial fibers (RF) and the annular ligament (AL), can be observed in different areas on the surface of the membrane.

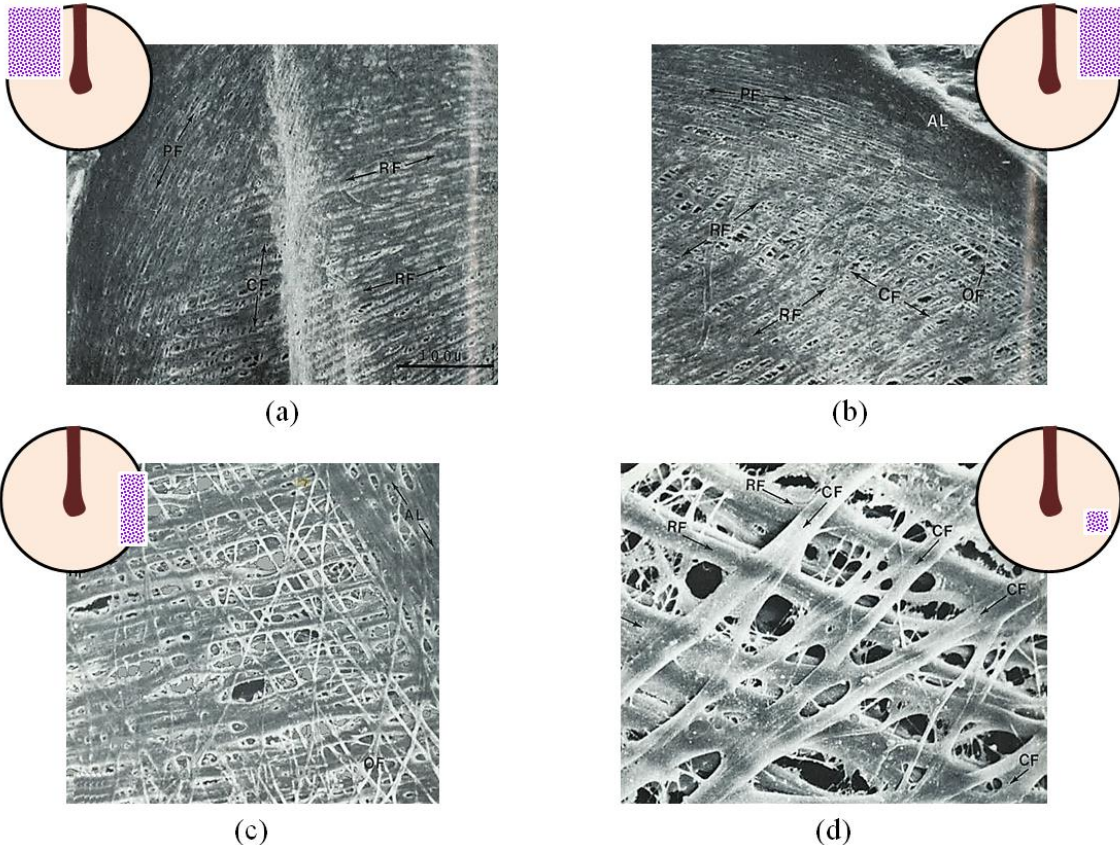


Figure 3.4. Fibrous structure of a guinea pig TM imaged with scanning electron microscope in: (a) the anterior superior quadrant of the TM ($\times 300$); (b) the posterior superior quadrant of the TM ($\times 300$); (c) the bordering area between the superior and inferior-posterior quadrant ($\times 1000$); and (d) circular fibers cross over the radial fibers and branch and anastomose to each other forming a network ($\times 3400$) PF: Parabolic Fibers, AL: Annular Ligament, RF: Radial Fibers, CF: Circular Fibers (adapted from Kawabata and Ishii, 1971).

3.2. Function of the Middle ear

The smallest bones inside the human body are three middle ear ossicular bones (Malleus, Incus, and Stapes) located inside the middle ear space, as shown in Figure 3.5. The middle ear cavity is normally filled with air, and under normal operation conditions, the static air pressure in the middle ear cavity is the same as the atmospheric pressure in the ear canal (Geisler 1998). Equal air pressure on both sides of the TM is needed to maintain the proper shape and tension of the TM. The pressure equalization in the middle ear cavity is maintained by the periodic

opening and closing of the Eustachian tube (auditory tube). This tube connects the middle ear with the nasopharynx (back of the throat) and can be opened or closed by the action of the tensor velipalatine muscles (muscles from the velum and palate). The tube is normally closed, but it pops open during yawning and swallowing. If the air pressure in the middle ear cavity is significantly different from the pressure in the ear canal, this may cause over- or under-stretching of the TM, which leads to inefficient sound transmission, pain and can also produce middle ear diseases. The function of the middle ear is to transfer sound from the air to the fluids of the cochlea (i.e., from P_T to P_V in Figure 3.5a) through the vibration of the TM and three middle ear ossicular bones. The process can be considered as an impedance matcher. The specific acoustic impedance of a medium is the ratio of the sound pressure to the particle velocity of a plane wave propagating through the medium and is a property of the medium itself. When sound impinges on an interface between two media with different impedances, such as an air-water (low pressure, large velocity)-(high pressure, low velocity) interface, energy is reflected from the boundary. The stapes terminates at the entrance of the cochlea, on a flexible membrane called the oval window. The velocity of the stapes v_s is the input signal to the cochlea. It produces a pressure variation P_V in the fluids of the Scala vestibule. The function of the external and middle ears is to capture the energy in the external sound field of sound pressure P_F and transfer it to the stapes motion v_s , and in turn, to the sound pressure P_V in the scala vestibule.

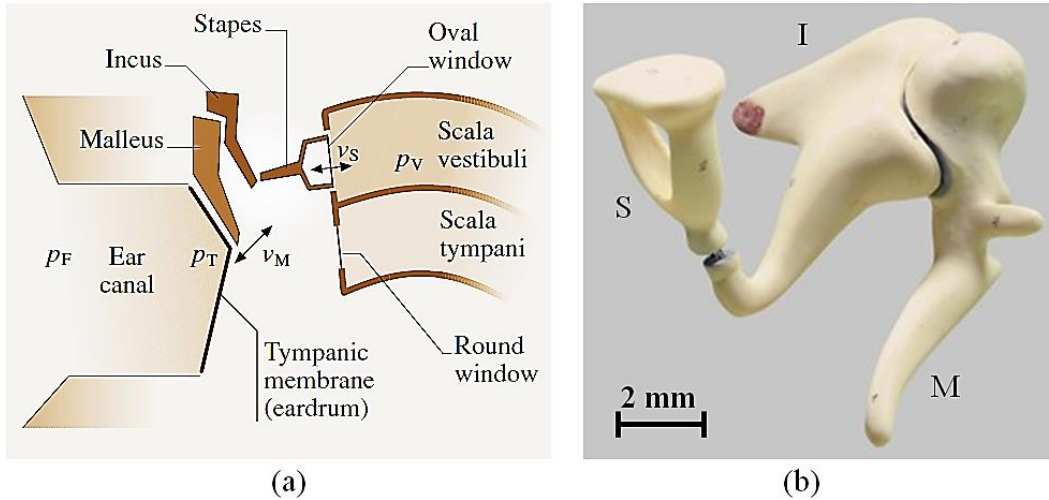


Figure 3.5. Human middle ear ossicular chain: (a) schematic of the human external, middle, and inner ears; and (b) human ossicular chain including the malleus (M), incus (I), and stapes (S) (adapted from Rossing 2007).

3.3. Middle-ear Impedance Matching Mechanisms

The primary function of the middle ear is to act as an impedance matching element between the air-filled outer ear and the fluid-filled inner ear. If we assume that the impedance of cochlear fluids is the same as the specific acoustic impedance of the fluid, the impedance ratio, r , of the liquid in the cochlea to the air is 4000:1, the following equation can be used to determine what the energy transmission coefficient, T , would be without the middle ear function

$$T = \frac{4r}{(r + 1)^2}, \quad (3-1)$$

Equation 3-1 gives a transmission of 0.001 or 0.1%. This transmission value is equivalent to a SPL drop of about 30 dB. To overcome this impedance mismatch, the middle ear employs three mechanical amplification mechanisms

1. Area ratio transformation
2. Ossicular chain lever action

3. Catenary lever action

3.3.1. Area Ratio Transformation

The surface area ratio (pressure) transformer is the first and the most effective impedance matching mechanisms in the middle ear. As shown in Figure 3.6a, it results from the differences in surface areas of the TM and Oval Window (OW: the membrane covering the oval window).

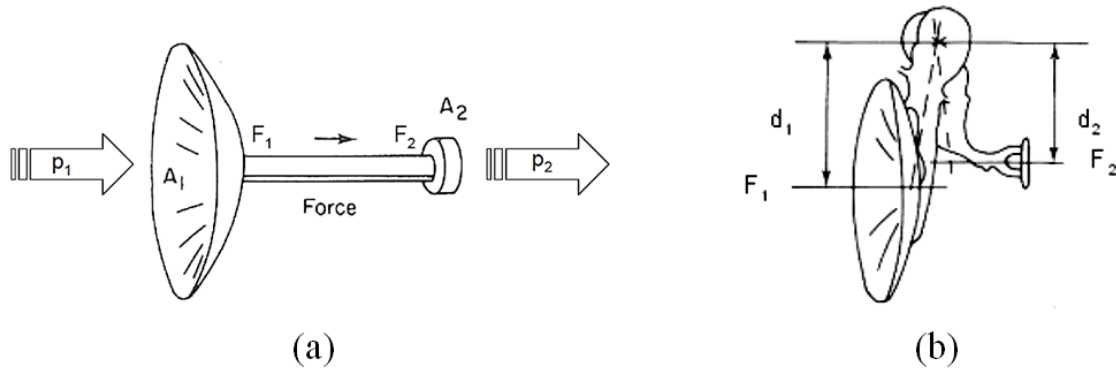


Figure 3.6. Middle ear impedance matching mechanisms: (a) area ratio transformation resulting from surface area mismatch between TM and Oval Window; and (b) ossicular chain lever action (adapted from Emanuel and Letowski, 2009).

A pressure P_1 acts over the surface of the TM and results in a force F_1 . Assuming that the ossicular chain is a lossless system, the force F_2 acting on the oval window is equal to force F_1 , that is, $F_1 = F_2 = F$. Since force (F), surface area (A), and pressure (P) are related by the equation $F = P \times A$, then

$$F = P_1 \times A_1 = P_2 \times A_2 . \quad (3-2)$$

Therefore,

$$P_2 = P_1 \times \frac{A_1}{A_2} . \quad (3-3)$$

Since the vibrating area of the TM ($A_1 = 55 \text{ mm}^2$) is approximately 17.2 times larger than the vibrating area of the oval window membrane ($A_2 = 3.2 \text{ mm}^2$), this results in an increase in SPL at the oval window of approximately 25 dB.

3.3.2. Ossicular Chain Lever Action

The second impedance matching mechanism of the middle ear is shown in Figure 3.6b and is called the ossicular chain lever action, which involves the rotational motion between the malleus and incus. This type of motion is possible because the ossicles are fixed at the junction between the malleus and incus while being suspended in the middle ear cavity by the anterior ligament of the malleus (anteriorly) and the posterior ligament of the incus (posteriorly). This arrangement creates a central pivot point (fulcrum) and allows for the relative rotational motion of the malleus and incus, thereby forming a lever mechanism. In a lever system, an input force F_1 applied at effort arm d_1 results in the output force F_2 acting on load arm d_2 , and their products are equal, which is

$$F_1 \times d_1 = F_2 \times d_2 . \quad (3-4)$$

In the case of the ossicular chain lever, the forces F_1 and F_2 are the forces acting at the malleus and incus and the distances d_1 and d_2 are the lengths of the malleus and incus, respectively. Since the length of the malleus is approximately 1.3 times longer than the length of the incus, this increases the force between the TM and the oval window membrane by approximately 2.3 dB.

3.3.3. Catenary lever action

The third impedance matching mechanism, the catenary lever action (also known as curved membrane effect, or buckling effect of the tympanic membrane) was first explained by Helmholtz (1868). Because of his observation of the membrane's curvature, he hypothesized that the umbo of the TM vibrates less than the remaining surface of the TM, and the magnitude of force and motion vary inversely and regularly along each radius of the curved TM. Since the outside edge of the membrane is firmly attached to the annulus and curves medially to attach to

the umbo, the displacement of the membrane between the annulus and umbo is larger than the umbo motion (Khanna and Tonndorf, 1970). A simple example of this lever action is a tennis net. The tighter the net is stretched, the larger the forces exerted on the two posts holding it. Because the bony annulus is immobile, and due to this catenary action, the sound-induced force at the umbo is amplified relative to the force midway between the umbo and the rim. This creates a lever action which increases the force acting at the umbo by approximately 2 times or 6 dB (Rosowski, 1996).

Therefore the total increase in pressure between the stapes footplate and the TM can be obtained with

$$20 \log(17.2) + 20 \log(1.3) + 20 \log(2) . \quad (3-5)$$

In the literature, 33 dB ratio to compensate for the air-to-cochlea impedance mismatch is called the *ideal transformer prediction* (Rosowski, 1994). Without the impedance matching function of the middle ear, more than 99.9% of the acoustic energy acting on the TM would be reflected back into the ear canal and not used. If the human middle ear matching function is not functioning properly, sound can only be transmitted via a shunt pathway (tympanic membrane to the air in the middle ear to the fluid of the inner ear), which leads to a hearing loss of as much as 60 dB (Peake et al., 1992).

4. Previous Middle ear Studies

There are plenty of publications and reports on developments of different acousto-mechano-electrical models for describing the function of the middle ear. These models have been mainly developed for a better understanding of the sound transmission mechanisms in the human ear. However, all of these models and hypotheses have been established based on several assumptions. The real experimental data about shape and sound-induced motion of the TM and force within the middle ear are indispensable to fully test and verify the accuracy and applicability of these models. In this chapter, an overview of some of the existing models is given to signify the needs for accurate measurements of shape, sound-induced motions and forces within the human auditory systems.

4.1. Input impedance of the stapes and cochlea

As mentioned earlier, acoustic impedance is the ratio of the complex acoustic pressure applied to a system to the resulting complex acoustic volume flow rate through a surface perpendicular to the direction of this acoustic pressure at its point of application such that

$$Z = \frac{P}{Q} = R + iX , \quad (4-1)$$

where P is the complex acoustic pressure in Pa, Q is the complex acoustic volume flow rate in $\text{m}^3 \cdot \text{s}^{-1}$, R and X are the acoustic resistance and reactance measured in $\text{Pa} \cdot \text{m}^{-3} \cdot \text{s}$. Therefore, acoustic impedance Z is a complex quantity that has two parts, resistance (real part) and reactance (imaginary part), that are responsible for the transfer and storage of energy, respectively. The transfer of energy from one system to another is most efficient when both systems have the same impedance (Møller, 1965; Emanuel and Letowski, 2009). In case of

complex impedances, the most efficient transfer occurs when the two impedances are complex conjugates with equal magnitude, but opposite phase.

The acousto-mechanical transformation of the middle ear serves to match the high acoustic impedance of the fluid-filled inner ear with the low acoustic impedance of the air in which sound waves propagate in order to optimize energy transfer between these two systems. The main resistive component is contributed by the input impedance of the cochlea at the oval window that is the entrance to the cochlea. Therefore, in order to calculate the actual impedance mismatch, the input impedance of the oval window and the impedance of the source from which the sound impinges on the window should be determined.

Researchers at Harvard Medical School (Merchant et al., 1996) measured acoustic input impedance of the stapes and cochlea in several human temporal bones. The acoustic input impedance of the stapes and cochlea Z_{SC} in temporal bones have been measured in response to a sound pressure at the stapes head P_S , where the sound pressure stimulus was restricted to the region of the oval window P_{OW} and was much larger than the sound pressure outside the round window P_{RW} (as is the case in normal ears). The load of the stapes and cochlea on the middle ear can be defined as the ratio of the pressure acting on the stapes and the stapes volume velocity with

$$Z_{SC} = \frac{P_{OW}}{U_{ST}} = \frac{P_S}{j\omega X_S A_{FP}} , \quad (4-2)$$

where A_{FP} is the area of the footplate, j is the imaginary constant, ω is the angular frequency that is equal to $2\pi f$, and $j\omega X_S$ is the complex amplitude representing the time derivative of the sinusoidal stapes displacement. Considering a value of 3.2 mm^2 for A_{FP} for human footplate, the frequency-dependent acoustic input impedance of the stapes and cochlea have been calculated to vary between $800,000$ to $10,000,000 \times 10^5 \text{ Pa}\cdot\text{m}^{-3}\cdot\text{s}$ (Merchant et al., 1996).

Zwislocki (1962) also measured this value for cat's ear and he reported values between 350,000 to 1,200,000 dyne. $\frac{s}{cm^5}$ ($\times 10^5$ Pa. m^{-3} .s). All of these impedances are much higher than the characteristic impedance of air, which is approximately 41.5 dyne $\frac{s}{cm^3}$ at 30°C temperature. Therefore, in order to ensure an efficient transfer of energy between the acoustic system of the ear canal and the hydraulic system of the inner ear, the middle ear must compensate for this mismatched impedance by increasing the pressure between the tympanic membrane and oval window by approximately 63 times ($63^2 \sim 4000$).

4.2. Middle ear input-output gains

Generally, our knowledge of middle-ear sound transfer depends on single point measurements of sound-induced umbo and stapes motion, together with a few measurements of TM surface displacement and a few direct measurements of middle-ear pressure gain P_V/P_{TM} . Due to the lack of full-field 3D displacement and shape measurement of the middle ear, theoretical assumptions and modeling have been developed by several researchers all around the world to further characterize the middle-ear input-output transfer function. In its simplest form, the middle ear has been described as a two-port system with one port at the ear canal and the other port at the stapes footplate as follows:

$$\begin{bmatrix} P_{ec} \\ U_{ec} \end{bmatrix} = \begin{bmatrix} \mathbf{A} & \mathbf{B} \\ \mathbf{C} & \mathbf{D} \end{bmatrix} \begin{bmatrix} P_V \\ -U_{ST} \end{bmatrix}, \quad (4-3)$$

where P_{ec} and U_{ec} are the ear canal pressure and volume velocity, P_V and U_{ST} are the vestibule pressure and stapes volume velocity, respectively. Velocities entering the middle ear are defined as positive (U_{ec}) and velocities departing the middle ear are defined as negative ($-U_{ST}$). Equation 4-3 states that the four frequency-dependent input-output variables are related to each other by four matrix elements **A**, **B**, **C**, and **D** that characterize the middle ear function. An

important attribute of the ABCD matrices is that they are independent of the cochlear and ear-canal loads, which allows a better comparison of the properties of the middle ear alone. A schematic of the setup for characterization of input-output parameters of the middle ear is shown Figure 4.1, where the ear-canal pressure P_{ec} , inner-ear pressure P_V , and the stapes volume velocity U_{sT} are directly measured with a microphone probe, hydro-pressure transducer, and a single point LDV, respectively.

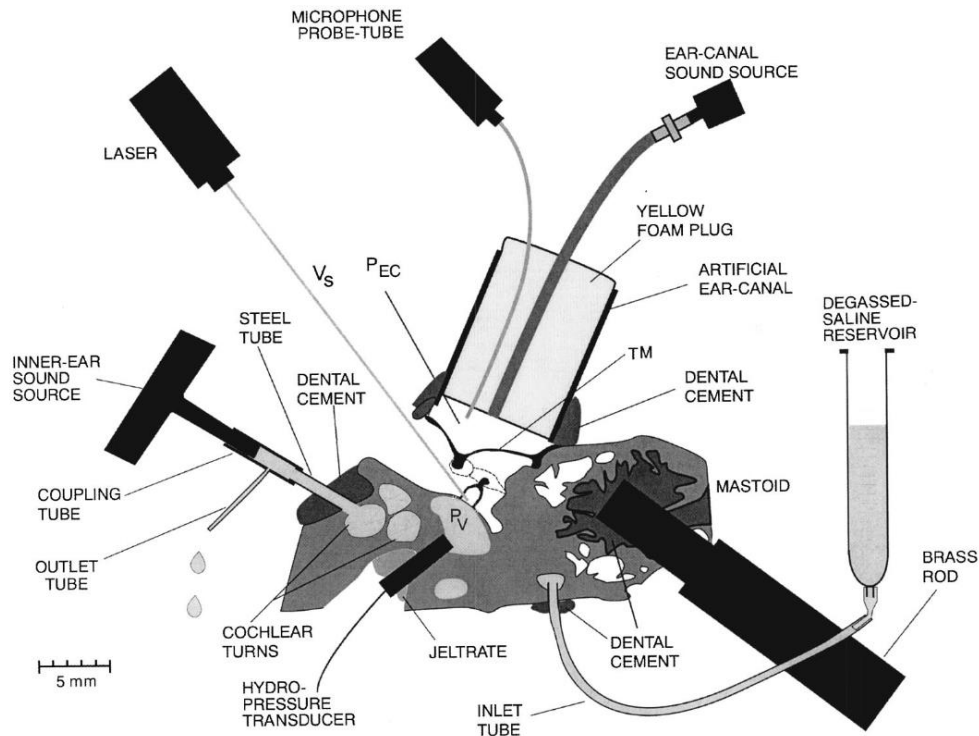


Figure 4.1. A simplified horizontal cross-section of a human temporal bone (right ear) preparation for driving the middle ear in the forward and reverse directions (note the presence of the inner-ear sound source). A small speaker is used as the sound-source in the ear canal to drive the middle ear in the forward direction. The inner-ear sound source coupled to a tube cemented near the round window was used to drive the inner ear in the reverse direction. The ear-canal pressure P_{ec} was measured with an ER-7C probe-tube microphone. To measure the inner-ear pressure P_V , a hydro-pressure transducer was placed in the vestibule. The stapes velocity was measured with a HLV-1000 PolyTec laser vibrometer. An inlet and outlet tube allowed flushing of the inner ear to ensure that it remained fluid filled (Puria 2003).

Four different frequency-dependent complex middle ear parameters M1, M2, M3, and Z_C are defined to determine the transfer function of the middle ear. These variables are defined in the following equations:

$$M1 = \frac{\overrightarrow{P_V}}{\overrightarrow{P_{EC}}} , \quad (4-4)$$

$$M2 = \frac{\overleftarrow{P_{EC}}}{\overleftarrow{P_V}} , \quad (4-5)$$

$$M3 = \frac{\overleftarrow{P_V}}{\overleftarrow{V_{ST}} A_{FP} / \cos(\theta_{ST})} , \quad (4-6)$$

$$Z_C = \frac{\overrightarrow{P_V}}{-\overrightarrow{V_{ST}} A_{FP} / \cos(\theta_{ST})} . \quad (4-7)$$

The right arrow (\rightarrow) indicates forward drive (the sound stimulus delivered to the external ear at the TM), while the left arrow (\leftarrow) indicates the reverse drive (the sound stimulus delivered to the inner ear). Stapes footplate area, A_{FP} is considered to be $\pi \text{ mm}^2$ and stapes angle, θ_{ST} of 55° relative to an axis perpendicular to the footplate and through the stapes head is assumed (Aibara et al., 2001, Puria 2003). This assumption leads to a simple cosine correction between the measured motion of the stapes and its piston-like motion.

The forward middle-ear pressure gain, M1 is the ratio of the vestibule pressure to the ear-canal pressure $M1 = P_V/P_{EC}$. The cochlear input impedance is the ratio of the vestibule pressure, P_V to the stapes volume velocity U_{ST} and is $Z_C = P_V/-U_{ST}$, where U_{ST} is defined as the stapes velocity times the footplate area, A_{FP} . M2 and M3 were measured while the ear was stimulated, with the inner ear sound source, in the reverse direction. The reverse middle-ear pressure gain, M2, is the ratio of the ear-canal pressure to the inner-ear pressure $M2 = P_{EC}/P_V$, and the reverse middle-ear impedance, M3, is the ratio of the vestibule pressure to the stapes volume velocity

and is calculated with $M3 = P_V/U_{ST}$. Figure 4.2 shows the results of obtained for five human temporal bones.

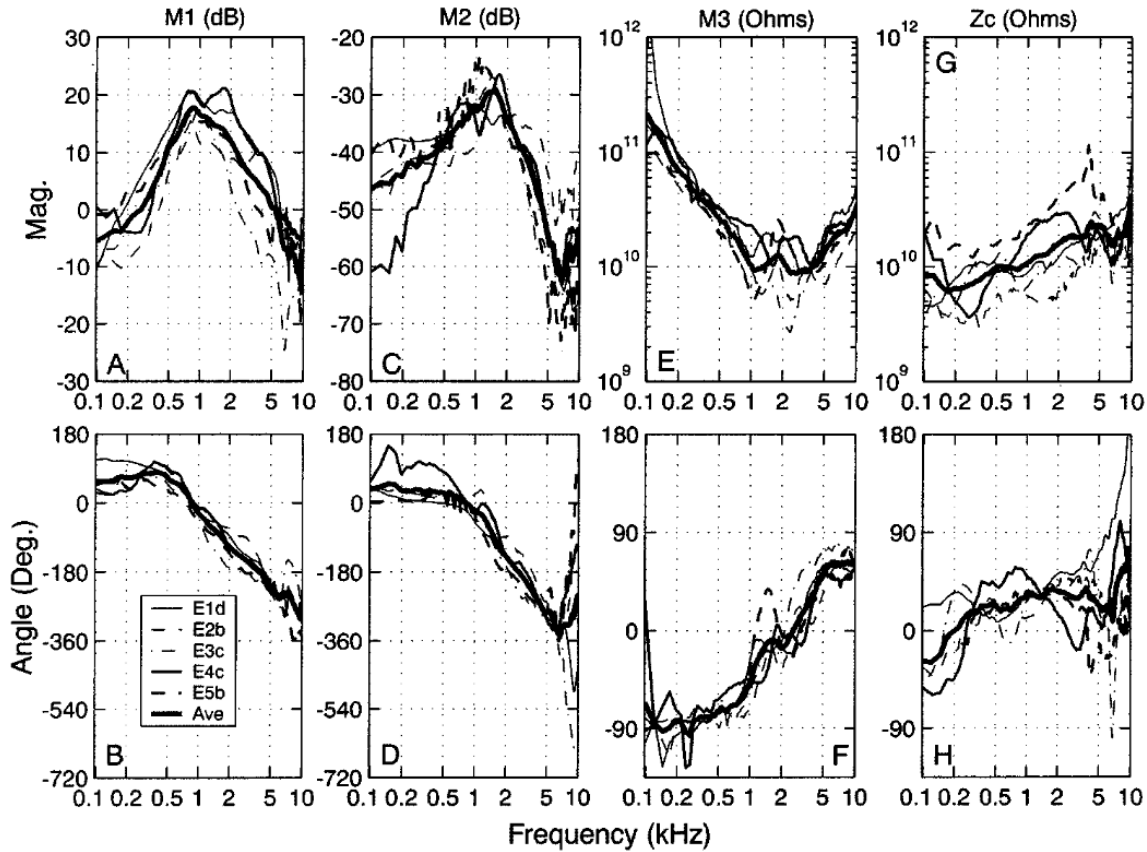


Figure 4.2. Measurements of $M1$, $M2$, $M3$, and Z_C from five human temporal bones. The average of the log-magnitude and angle is shown as thick-solid lines in each panel. $M1$ and Z_C were measured while the ear was stimulated, with an ear canal sound source, in the forward direction, whereas $M2$ and $M3$ were measured while the ear was stimulated, with the inner ear sound source, in the reverse direction (Puria 2003).

Using these variables, the forward middle-ear pressure gain $M1$, the cochlear input impedance (Z_C), the reverse middle-ear pressure gain $M2$, and the reverse middle-ear impedance $M3$ have been obtained in order to characterize the middle ear as a two-port system. Therefore, the effect of the middle ear on OtoAcoustic Emissions (OAE) has been quantified by calculating the roundtrip middle-ear pressure gain G_{ME}^{RT} as the product of $M1$ and $M2$ (Puria 2003) to study how the middle ear modifies the OAE generated by the cochlea and measured in the ear canal.

Based on this mechanical model, the kinetic energy (T), the potential energy (V), and the dissipation (F) of the middle ear can be calculated with

$$T = \frac{1}{2}M_T\dot{x}_T^2 + \frac{1}{2}M_A\dot{x}_A^2 + \frac{1}{2}M_P\dot{x}_P^2 + \frac{1}{2}M_H\dot{x}_H^2 + \frac{1}{2}(M_S + M_C)\dot{x}_S^2, \quad (4-8)$$

$$F = \frac{1}{2}R_T\dot{x}_T^2 + \frac{1}{2}R_A\dot{x}_A^2 + \frac{1}{2}R_P\dot{x}_P^2 + \frac{1}{2}R_H\dot{x}_H^2 + \frac{1}{2}(R_S + R_C)\dot{x}_S^2, \quad (4-9)$$

$$V = \frac{1}{2}S_1x_T^2 + \frac{1}{2}S_2(x_T - x_H)^2 + \frac{1}{2}S_M(x_T - x_A)^2 + \frac{1}{2}S_A(x_A - x_P)^2 + \frac{1}{2}S_Px_P^2 + \frac{1}{2}S_Hx_H^2 + \frac{1}{2}S_J\left(\frac{l_2}{l_1}x_H - x_S\right)^2 + \frac{1}{2}(S_S + S_L + S_C)x_S^2, \quad (4-10)$$

where $\dot{x} = dx/dt$, x is the volume displacement, r is the lever ratio, l_1 is the length of the malleus, l_2 is the length of incus, M_C is the mass of cochlear fluid to be added to the mass of the stapes, M_S , due to incompressibility assumption for the cochlear fluid. Similarly, S_C is the stiffness of the cochlea to be added to the stiffness of the stapes and R_C is the resistance of the cochlear fluid against the displacement of the stapes. In this model M_C , R_C , and S_C have been assumed to be frequency-independent. Equations 4-8, 4-9, and 4-10 are written in Lagrangian equations of motions and the following equations for the motion of the masses of the TM (T), antrum (A), pneumatic mastoid cell (P), and malleus (H) are obtained.

$$M_T\ddot{x}_T + R_T\dot{x}_T + (S_T + S_M)x_T = P_T \exp(j\omega t) + S_2x_H + S_Mx_A, \quad (4-11)$$

$$M_A\ddot{x}_A + R_A\dot{x}_A + (S_M + S_A)x_A = S_Mx_T + S_Ax_P, \quad (4-12)$$

$$M_P\ddot{x}_P + R_P\dot{x}_P + (S_A + S_P)x_P = S_Ax_A, \quad (4-13)$$

$$M_H\ddot{x}_H + R_H\dot{x}_H + (S_2 + S_H + r^2S_J)x_H = S_2x_T + rS_Jx_S, \quad (4-14)$$

where P_T is the sound pressure amplitude of a pure tone, with an angular frequency of ω at the tympanic membrane. They used this model to understand the effects of different vibratory

organs within the human ear and obtained the magnitude and phase of sound-induced motion of the TM at a broad frequency range. However, the main drawback of their model was the fact that the entire TM have been considered as one single mass, with one single displacement value (i.e., x_T), which is not the case in the real world conditions, where sound-induced motion of the TM is different at every single point on its surface. On the other hand, the curved shape of the TM has not been taken into account, therefore, based on their model, a flat latex membrane with similar stiffness and mass should produce similar efficacy as the complex structure of the TM does.

4.4. Lumped parametric model of a human eardrum

Figure 4.4 shows a lumped parametric model consisting of six masses (M) connected by springs (K) and dashpots (C) to simulate the human ear, including the external ear canal, tympanic membrane, middle ear joints and ossicles, and cochlea (Feng and Gan 2004). The air inside the ear canal is modeled by a mass M_1 , which is coupled to the mass M_2 , the TM, through the spring K_2 and dashpot C_2 . Spring K_1 and dashpot C_1 represents the TM annulus. The three ossicular bones (malleus, incus, and stapes) were represented by masses M_3 , M_4 , and M_5 , respectively. The malleus-incus joint and the incus-stapes joint, which connect the three ossicles and form the ossicular chain, have been modeled by two pairs of springs and dashpots: K_5 , C_5 and K_6 , C_6 , respectively. The malleus (M_3) is attached to the TM (M_2) through K_3 , C_3 . The two major ligaments suspending the malleus and incuse were also modeled as dashpots C_4 and C_7 . Cochlear fluid, M_6 , supported by dashpot C_9 and C_{10} . On the other hand, the stapes is coupled with the cochlear fluid through the stapedial annulus (K_8 and C_8).

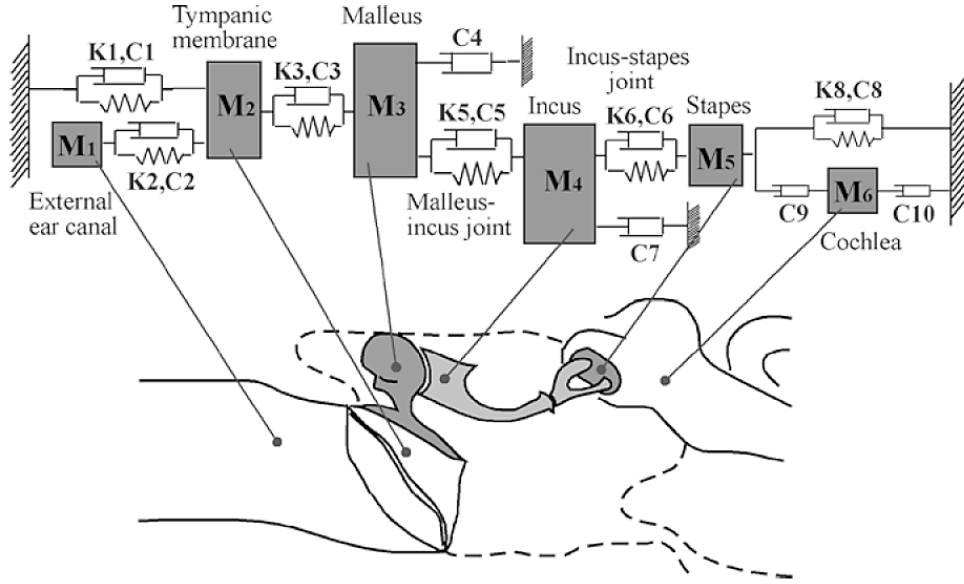


Figure 4.4. Lumped parametric model of a human ear consisting of six masses (M_1 to M_6) suspended by ten dashpots (C_1 to C_{10}) and six springs (K_1 , K_2 , K_3 , K_5 , K_6 , K_8) (Feng and Gan 2004).

The governing equation for the above-mentioned six-mass lumped element model can be written as

$$[\mathbf{M}][\ddot{\mathbf{X}}] + [\mathbf{C}][\dot{\mathbf{X}}] + [\mathbf{K}][\mathbf{X}] = [\mathbf{F}_e], \quad (4-15)$$

where $[\mathbf{M}]$ is the mass matrix, $[\mathbf{C}]$ is the damping matrix, $[\mathbf{K}]$ is the stiffness matrix, $[\mathbf{X}]$ is the displacement matrix (6×1) of the six masses, $[\mathbf{F}_e]$ is the force matrix (6×1) that includes external forces acting on each masses. $[\ddot{\mathbf{X}}]$ and $[\dot{\mathbf{X}}]$ are acceleration and velocity matrices of the system, respectively. Eq. 4-15 can be rewritten for the case of harmonic excitation at the TM, which is

$$[\mathbf{X}] = [\mathbf{A}]e^{i\omega t}, \text{ and} \quad (4-16)$$

$$[\mathbf{F}_e] = [\mathbf{F}]e^{i\omega t}. \quad (4-17)$$

Therefore, Eq. 4-15 can be rewritten as

$$\{-\omega^2[\mathbf{M}] + j\omega[\mathbf{C}] + [\mathbf{K}]\}[\mathbf{A}] = [\mathbf{F}]. \quad (4-18)$$

Figure 4.5 shows the result of this mechanical model calculated for magnitude and phase of sound-induced motion of the umbo and stapes.

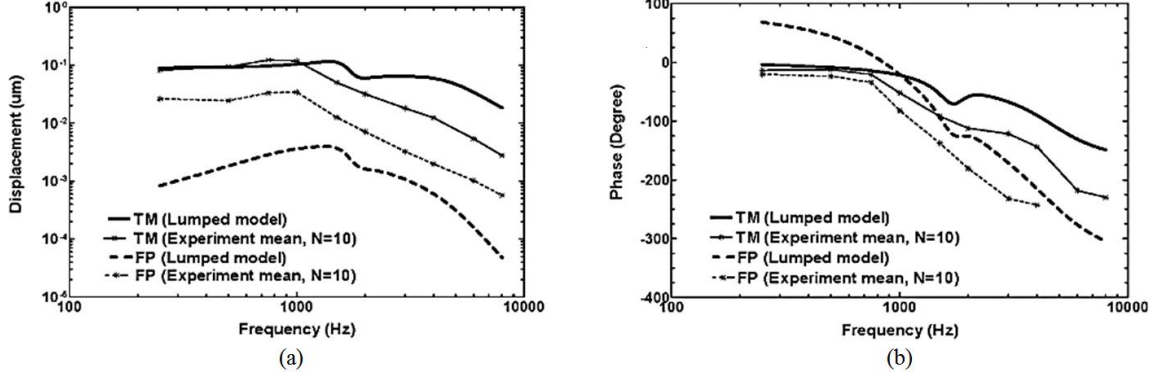


Figure 4.5. Comparison between predicted displacements at M_2 and M_5 of the lumped model and the experimental single-point LDV measurement (Feng and Gan 2004).

4.5. Eardrum modeled as a string with distributed force

The eardrum of a guinea-pig has been modeled with a string with distributed force (Goll and Dalhoff 2011). In contrast to known lumped-element models, the distributed force model of the eardrum takes the distributed effect of the sound field on the tympanic membrane into account. The model was adjusted to forward and reverse transfer functions of the guinea-pig middle ear. They assumed that the TM is a collection of strings that are bounded at the annular ring, and that the umbo is located at the center of the membrane. On the basis of the radial fiber structure of the TM, these assumptions led them to a simple 3-wave model that sums a simple modal pattern of motion with a combination of a backward and forward traveling wave along the string.

The partial differential equation governing the transversal, time- and space-dependent displacement z of a homogenous vibrating string can be expressed as (Rawitscher and Liss, 2011; Goll and Dalhoff 2011)

$$\rho \frac{\partial^2 \tilde{z}(t, x)}{\partial t^2} + \delta \frac{\partial \tilde{z}(t, x)}{\partial t} - \mu \frac{\partial^2 \tilde{z}(t, x)}{\partial x^2} = \tilde{f}(t, x), \quad (4-19)$$

where ρ is the linear mass density, δ is the internal damping factor, μ the tension, and \tilde{f} is the transversal force per unit length. Assuming that the string is driven by a periodic force (e.g., $\tilde{f}(t, x) = e^{i\omega t} f(x)$) with an angular frequency of $\omega = 2\pi f$, so the complex displacement \tilde{z} can be written as the product of a time-dependent and a space-dependent parts

$$\tilde{z}(t, x) = e^{i\omega t} z(x). \quad (4-20)$$

Therefore, by considering Eq. 4-20, the partial differential Eq. 4-19 can be transformed into an ordinary differential equation

$$(-\rho\omega^2 + i\omega\delta)z(x) - \mu \frac{d^2 z(x)}{dx^2} = f(x). \quad (4-21)$$

Eq. 4-21 is a second-order nonhomogeneous linear differential equation with constant coefficients; its solution can be written as the sum of the general solution of the related homogeneous equation and the particular solution. The general solution has been obtained by solving the characteristic equation, whereas the particular solution was calculated by the method of variation of parameters.

4.6. Finite Element Method (FEM)

While previous analytical approaches predicted the general behavior of the middle ear structures for some limited situations, they were not able to model the realistic acousto-mechanical response in the ear involving complex geometry and an array of material compositions. The Finite Element (FE) method has distinct advantages over analytical approaches in modeling complex biological systems. FE models can also predict the detailed vibrational patterns, stress distributions, and dynamic behaviors at any location in a system, which is not possible with analytical and lumped models.

Analysis for sound transmission in the ear involves solid structures (e.g., TM, soft tissues, bones), acoustics (e.g., air in the ear canal and middle ear cavity), and fluid (cochlear fluid), which belong to different engineering disciplines and result in different boundary conditions, element attributes, and model parameters. FE analysis for structure, acoustic, and fluid behavior is usually carried out independently. However, the ear as a complex system, including the external ear canal, eardrum, ossicular bones and joints, suspensory ligaments, and middle ear cavity, requires coupled multi-physics FE analysis.

The first FE model of the ear (for a cat eardrum) was reported in 1978 (Funnell and Laszlo 1978). However, a group of scientists at the University of Oklahoma reported one of the very first complete FE models of the human middle ear (Sun et al., 2002; Gan et al., 2004). They reconstructed a CAD model of a human middle ear based on 780 histological sections of one human temporal bone (left ear of a 61 year-old male). This FE model is shown in Figure 4.6, where major suspensory ligaments (superior malleus and incus C1, lateral malleus C2, posterior incus C3, and anterior malleus C4) and two intra-aural muscle tendons (stapedial muscle C5 and tensor tympani muscle C7) were assumed as elastic constraints with four-noded solid elements. The contribution of cochlear impedance to acousto-mechanical transmission through the middle ear has been modeled as a mass block with 10 dashpots attached between the stapes footplate and fixed bony wall, which represented distributed damping dominant impedance. The value of 20 G Ω cochlear impedance applied on 3.2 mm² of stapes footplate was used to calculate the dashpot damping, which resulted in 10 dashpots with damping coefficient of 0.02 Ns/m each. The TM has been meshed by three-noded shell elements and the ossicular bones were meshed by four-noded tetrahedral solid elements. The incudomalleolar joint, incudostapedial joint, and manubrium that connects the malleus handle to the TM, were meshed by four-noded solid elements.

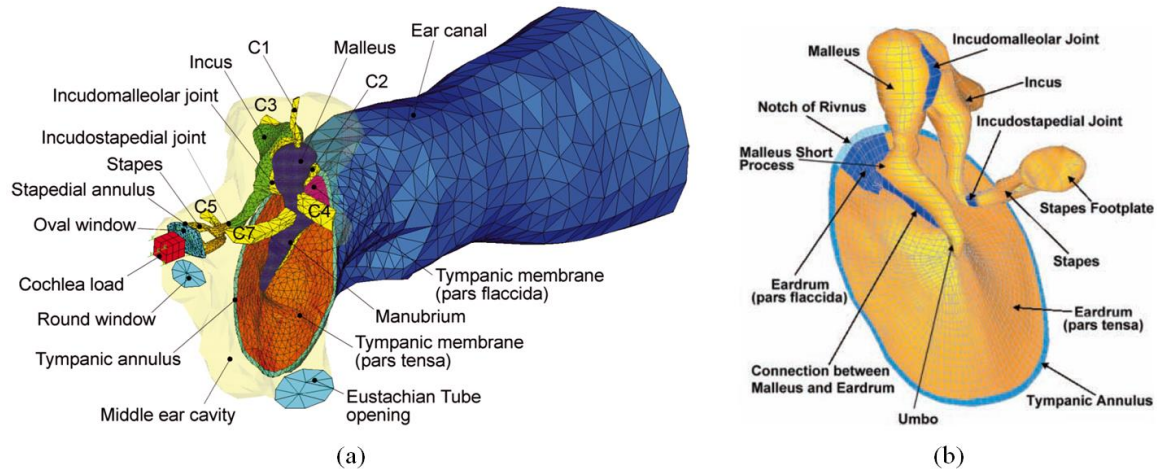


Figure 4.6. Finite element model of the left human middle ear: (a) the model includes the tympanic membrane, three ossicles (malleus, incus, and stapes), two joints, manubrium, ligaments, and muscle tendons (C1, C2, C3, C4, C5, C7), tympanic annulus, stapedial annular ligament, external ear canal, middle ear cavity (transparent); and (b) illustration of the connection between malleus and eardrum, incudomalleolar joint, incudostapedial joint, and the eardrum structure (Gan et al., 2004).

Figure 4.7 shows comparison of the results of the frequency-response motion magnitude of two different points umbo and stapes, obtained with this FE method and the ones obtained experimentally.

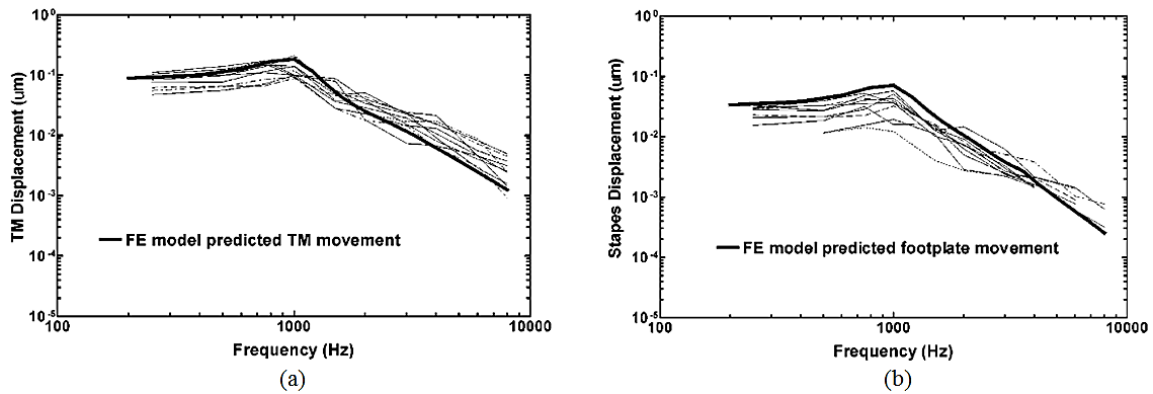


Figure 4.7. Comparison of the results of frequency-response predicted by FE method (thick solid line) with single-point experimental measurements at 10 different bones: (a) sound-induced motion at the tip of the manubrium, the umbo; and (b) sound-induced motion at the stapes footplate (Gan et al., 2004).

Although the model could predict the general sound-induced responses of these two points, due to the lack of full-field experimental sound-induced motion data, the accuracy of the model cannot be further judged.

4.7. Kinematics of thin shells

The term shell is applied to bodies bounded by two curved surfaces, where the distance between the surfaces (thickness) is small compared with other dimensions and its deformations are not large compared to the thickness (Ventsel and Krauthammer, 2001). The locus of points that lie at equal distances from these two curved surfaces defines the middle surface of the shell. A primary difference between a shell structure and a plate structure is that, in the unstressed state, the shell structure has curvature as opposed to the plate's structure that is flat. In other words, a plate may be considered as a special limiting case of a shell that has no curvature, and consequently, shells are sometimes referred to as curved plates. A shell can be classified as thin shell if the following condition is satisfied

$$\max\left(\frac{h}{R}\right) \leq \frac{1}{20}, \quad (4-22)$$

where h and R are the thickness and radius of curvature of the shell, respectively.

Based on the geometrical dimensions of the TM (i.e., approximate thickness of 30-120 μm and radius of 3-5 mm) and small magnitudes of the sound-induced motions relative to its geometrical dimensions (typical amplitudes of vibration of 50-300 nm depending on the excitation frequency and sound pressure level), the TM can be approximated as a thin shell (Rosowski et al., 2013; Khaleghi et al., 2013). The main kinematic assumptions, also known as the Kirchhoff-Love thin-shell hypothesis, are

1. The thickness of the shell, h is small as compared to other dimensions.

2. The middle plane of the shell does not go through any deformation. Thus, the middle plane remains plane after bending deformation. This implies that shear strains ϵ_{xz} and ϵ_{yz} can be neglected, where z is the thickness direction.
3. Straight lines perpendicular to the mid-plane remain perpendicular after deformation.
4. The normal strain across the thickness ϵ_{zz} is ignored. Thus the normal stress component σ_{zz} is neglected as compared to the other stress components.

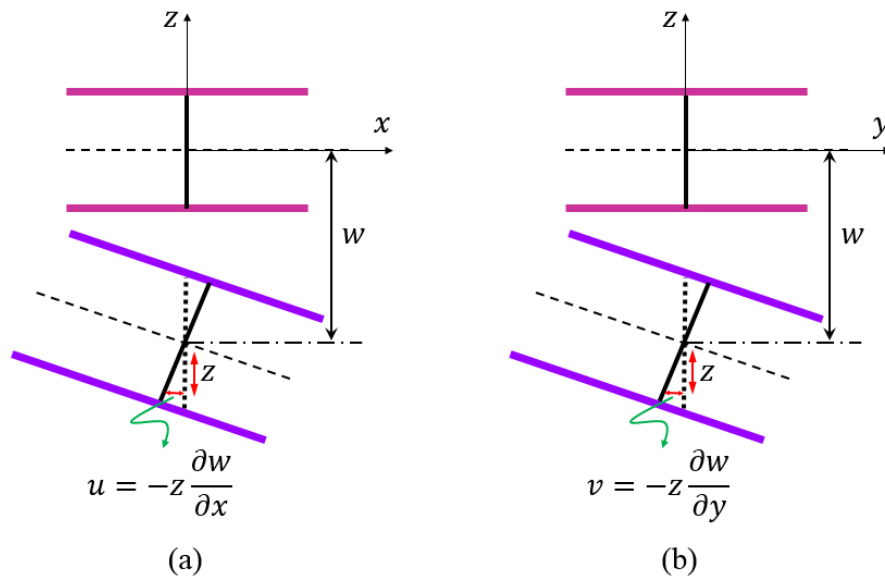


Figure 4.8. The lack of change in the normal vector during displacement of a thin-shell. In-plane displacement components at a distance z from the mid-plane surface along: (a) x -axis; and (b) y -axis. Mid-plane of the shell is shown with a dashed line. w is the z -axis displacement of the mid-plane surface.

As shown in Figure 4.8, as a thin shell undergoes deformation, based on Kirchhoff-Love thin-shell theory, a point at any distance z from the mid-plane will have in-plane deformation components u and v due to the rotation of the normal vector, which can be expressed as

$$u = -z \frac{\partial w}{\partial x}, \quad \text{and} \quad (4-23)$$

$$v = -z \frac{\partial w}{\partial y} . \quad (4-24)$$

The components of the three-dimensional Lagrangian Green strain tensor are defined as

$$\epsilon_{xx} = \frac{1}{2} \left[\frac{\partial u_i}{\partial x_j} + \frac{\partial u_j}{\partial x_i} + \frac{\partial u_k}{\partial x_i} \frac{\partial u_k}{\partial x_j} \right] . \quad (4-25)$$

Enforcing the requirement that the plate does not change its thickness during deformation and assuming negligible higher order terms in Eq. 4-25, the strain tensor components are reduced to the von Kármán strains and can be shown with

$$\epsilon_{xx} = -z \frac{\partial^2 w}{\partial x^2} + \frac{1}{2} \left(\frac{\partial w}{\partial x} \right)^2 , \quad (4-26)$$

$$\epsilon_{yy} = -z \frac{\partial^2 w}{\partial y^2} + \frac{1}{2} \left(\frac{\partial w}{\partial y} \right)^2 , \quad (4-27)$$

$$\epsilon_{xy} = -z \frac{\partial^2 w}{\partial x \partial y} + \frac{1}{2} \frac{\partial w}{\partial x} \frac{\partial w}{\partial y} . \quad (4-28)$$

Consequently the stress-strain relationships for the plate under static and plane stress conditions are,

$$\begin{bmatrix} \sigma_{xx} \\ \sigma_{yy} \\ \sigma_{xy} \end{bmatrix} = \frac{E}{1 - \nu^2} \begin{bmatrix} 1 & \nu & 0 \\ \nu & 1 & 0 \\ 0 & 0 & 1 - \nu \end{bmatrix} \begin{bmatrix} \epsilon_{xx} \\ \epsilon_{yy} \\ \epsilon_{xy} \end{bmatrix} , \quad (4-29)$$

where E is the elastic modulus of the shell, and ν is the poisson's ratio. Therefore, considering the strain terms shown in Eqs. 4-26, 4-28, 4-27, the stress terms shown in the left-hand side of Eq. 4-29 can be expanded to

$$\sigma_{xx} = \frac{E}{1 - \nu^2} \left[\left(-z \frac{\partial^2 w}{\partial x^2} + \frac{1}{2} \left(\frac{\partial w}{\partial x} \right)^2 \right) + \nu \left(-z \frac{\partial^2 w}{\partial y^2} + \frac{1}{2} \left(\frac{\partial w}{\partial y} \right)^2 \right) \right] , \quad (4-30)$$

$$\sigma_{yy} = \frac{E}{1 - \nu^2} \left[\nu \left(-z \frac{\partial^2 w}{\partial x^2} + \frac{1}{2} \left(\frac{\partial w}{\partial x} \right)^2 \right) + \left(-z \frac{\partial^2 w}{\partial y^2} + \frac{1}{2} \left(\frac{\partial w}{\partial y} \right)^2 \right) \right] , \quad (4-31)$$

$$\sigma_{xy} = \frac{E}{1 + \nu} \left[-z \frac{\partial^2 w}{\partial x \partial y} + \frac{1}{2} \frac{\partial w}{\partial x} \frac{\partial w}{\partial y} \right]. \quad (4-32)$$

4.7.1. Dynamics of Kirchhoff-Love thin shells

In the previous Section, it was assumed that all the external forces are applied slowly, so that the resulting stresses and deformations are independent of time. In the case of dynamic loading (i.e., time-dependent external forces or displacements), the governing equations for dynamics of shells can be obtained by partial differential equations based on Newton's laws or by integral equations based on the considerations of virtual work. For an isotropic and homogeneous shell, the in-plane deformations can be neglected and the dynamic equation of motion can be reduced to a biharmonic equation with

$$\begin{aligned} -D \left[\frac{\partial^4 w(x, y, t)}{\partial x^4} + 2 \frac{\partial^4 w(x, y, t)}{\partial x^2 \partial y^2} + \frac{\partial^4 w(x, y, t)}{\partial y^4} \right] \\ = q(x, y, t) + \rho h \frac{\partial^2 w(x, y, t)}{\partial t^2}, \end{aligned} \quad (4-33)$$

Where ρ is the mass density of the shell and D is the bending stiffness (also known as flexural rigidity) of the plate and for a plate with a thickness h

$$D = \frac{h^3 E}{12(1 - \nu^2)}. \quad (4-34)$$

For free vibration $q(x, y, t)$ is set to zero and Eq. 4-33 becomes

$$D \nabla^2 \nabla^2 w + \rho h \ddot{w} = 0. \quad (4-35)$$

Therefore, for comprehensive dynamic analyses of thin-shell structures, similar to analyses of sound-induced motions of mammalian TMs, shape (providing x , y , z , and radii of curvature) and displacement field of such a shell should be accurately measured. On the other hand, and by having a closer look at the previously-developed middle ear models and studies, including those

briefly described in this Chapter, the main assumption that most of them have used (FEM is an exception) is that the TM has been considered as a lumped (single) element, and therefore, the spatio-temporal complexity of sound-induced motion, as well as its complex shape have not been taken into account. Therefore, full-field quantitative measurements of shape and motion of the TM are required in order to test the accuracy and applicability of these models and shed the light on the details of the function of the TM.

5. Existing Methodologies for Otolaryngologist

5.1. Conventional Otoscopy

Otoscopy is an examination that involves looking into the ear with an instrument called an otoscope. This is performed in order to examine the external auditory canal and the eardrum.

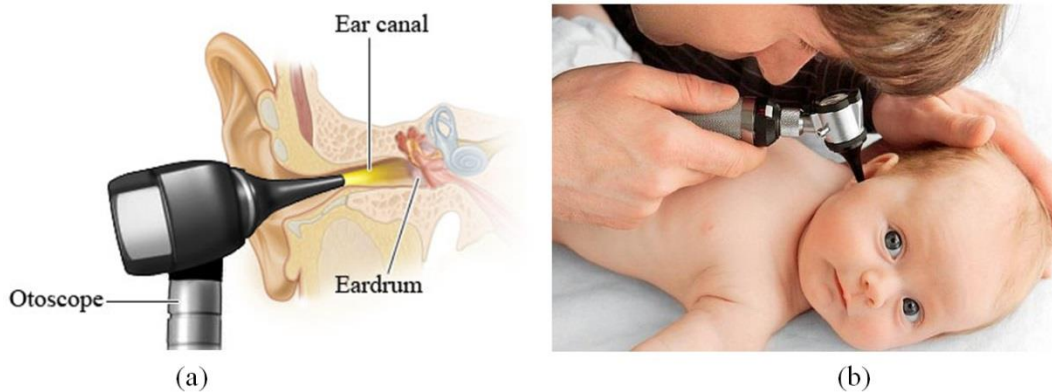


Figure 5.1. Visual inspection of the outer ear (ear canal and eardrum) by qualitative otoscopy (a) schematic of the otoscopy by illuminating the light on the surface of the eardrum; and (b) the physician inspects the ear of a patient qualitatively (adapted from Healthwise Inc.).

Typical otoscopes can be used to visually and qualitatively examine the outer and middle ear to assess healthiness of the eardrum and make sure that, for instance, the ear canal is clean or the TM is not perforated. However, they are unable to quantitatively investigate the shape and sound-induced motions of the TM.

5.2. Single-point measurements by Laser Doppler Vibrometry (LDV)

The use of Laser Doppler Vibrometry (LDV) for various hearing research applications has been reported. The applications include, but not limited to, characterizations of the transfer function of the manubrium and its tip, the umbo (Foth et al., 1996; de La Rochefoucauld and Olson 2010; Rosowski et al., 2003), vibrations and rotational axis characterization of the

mammalian ossicles (Decraemer et al., 2014), and the use of a scanning LDV for the investigations of the human TM motion in the presence of middle ear liquid (Zhang et al., 2014). Figure 5.2 shows single-point 1D and 3D LDV measurements that have been used for different medical and research applications.

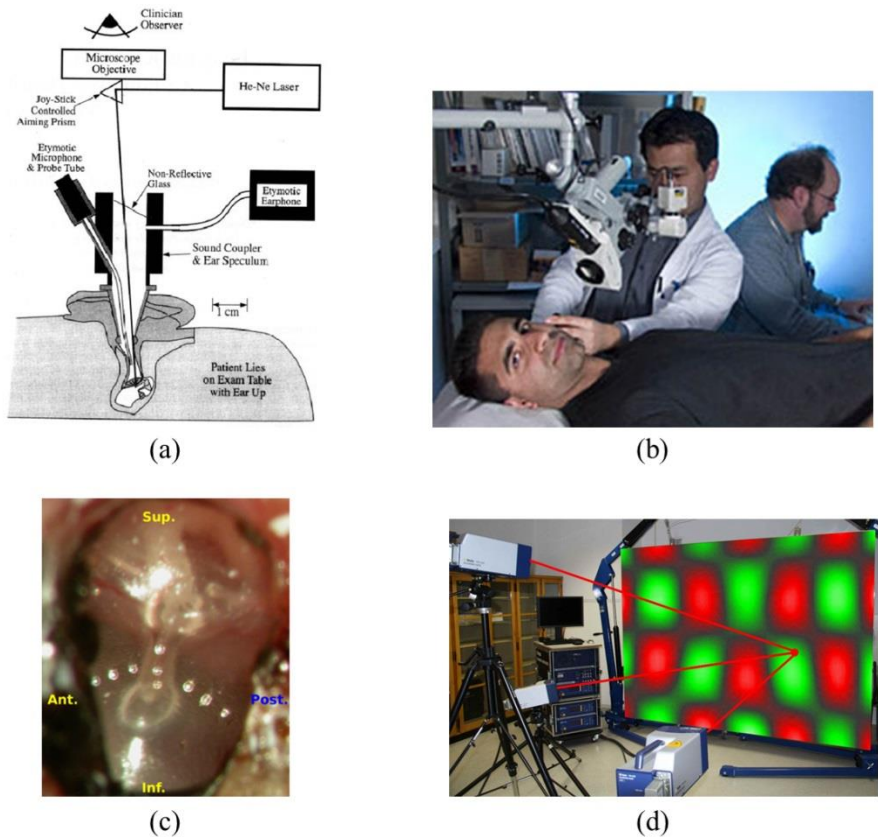


Figure 5.2. Laser Doppler Vibrometry (LDV) for single-point analyses of middle ear structures: (a) a typical 1D LDV setup for characterization of the umbo transfer function (Rosowski et al., 2003); (b) 1D LDV used in a hearing research environment for characterization of patient’s hearing loss; (c) retro reflective beads on the surface of the TM in order to enhance the reflection of the laser light source in LDV measurements (Maftoon et al., 2013); and (d) three-dimensional LDV using three different illumination directions (Polytec Inc.,).

One of the very first 3D sound-induced motion measurements of the middle ear have been reported in 1994 (Decraemer et al., 1994). The LDV head was positioned on a 2D goniometer system enabling variation of the sensitivity vector of the measurements in repetitive measurements. Figure 5.3a shows the definition of the 3D Cartesian axes x , y , z and the way the

TM is located in this coordinate system, where the z -axis is along the axis of the ear canal. The measured components of motions are shown in Figure 5.3b, where generally speaking, the x - and y -axes motions are smaller than the z -axis motion, but, due to lack of the shape knowledge, it is hard to judge relative sizes of motion components tangent and normal to the plane of the TM.

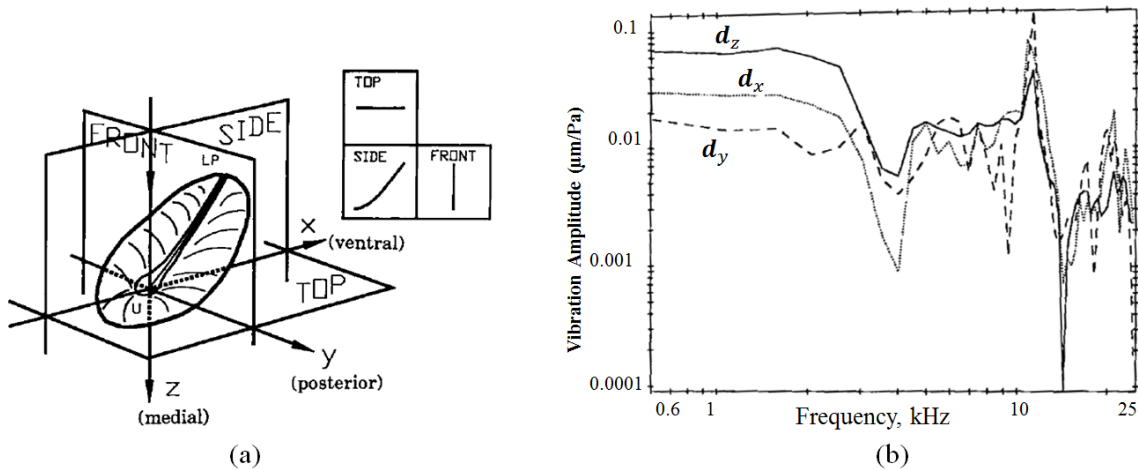


Figure 5.3. Single-point 3D sound-induced vibrometry of the umbo of a cat eardrum using 1D LDV that is mounted on a positioning system: (a) definition of the x , y , and z -axes with respect to the estimate of the TM shape; and (b) measured amplitudes of 3D sound-induced motion of the umbo, along the x , y , and z axes (adapted from Decraemer et al., 1994).

5.3. Full-field motion measurements

LDV is a great technique, but, can only quantify sound-induced motion of the TM at one single point. Recently, scanning LDV has been developed (Polytec) to overcome this limitation by allowing the laser beam to be moved across the surface of interest and scan a series of points in order to provide a 2D map of the vibration of the membrane. However, for biological samples with time-varying nature, repeating the experiments for several times at different points is not an ideal methodology. Therefore, holographic interferometry is preferred, because it has the sensitivity similar to LDV, yet can simultaneously measure full-field vibrational patterns at millions of points on the surface of the object (depending on the resolution of the camera).

5.3.1. Time-averaged Holography

In 1972, Khanna and Tonndorf showed the very first application of time-averaged holographic interferometry on the study of the vibrational patterns of the cat TMs (Khanna and Tonndorf 1972). An electromagnetic shutter was used to momentarily expose the plate and the time-averaged hologram of the vibration of the TM have been produced by illuminating on a high-resolution photographic plate (Agfa-Gervaert 10E70) with both reference and object beams, when the object was set in vibrations at the desired frequency and amplitude. Figure 5.4 shows six time-averaged holograms corresponding to vibrational patterns of a live cat TM stimulated with six different frequencies.

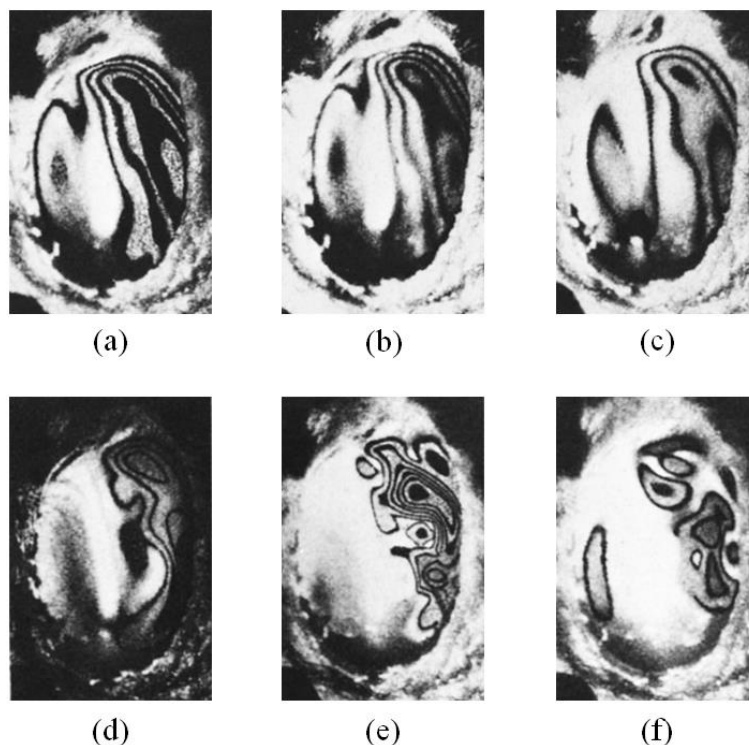


Figure 5.4. Time-averaged holograms of the vibrational patterns of a live cat TM at different tonal frequencies: (a) 600 Hz; (b) 950 Hz; (c) 2000 Hz; (d) 2900 Hz; (e) 4000 Hz; and (f) 5000 Hz (adapted from Khanna and Tonndorf 1972).

In 2009, John J. Rosowski and his colleagues at Harvard Medical School and Worcester Polytechnic Institute developed a computer-assisted time-averaged holographic system for the

investigations of the sound-induced motion of the surface of the mammalian TMs (Rosowski et al., 2009). They managed to capture and show time-averaged holograms corresponding to sound-induced motion of the TMs of different species (human, cat, and chinchilla) at different tonal frequencies from 400 Hz up to 25 kHz.

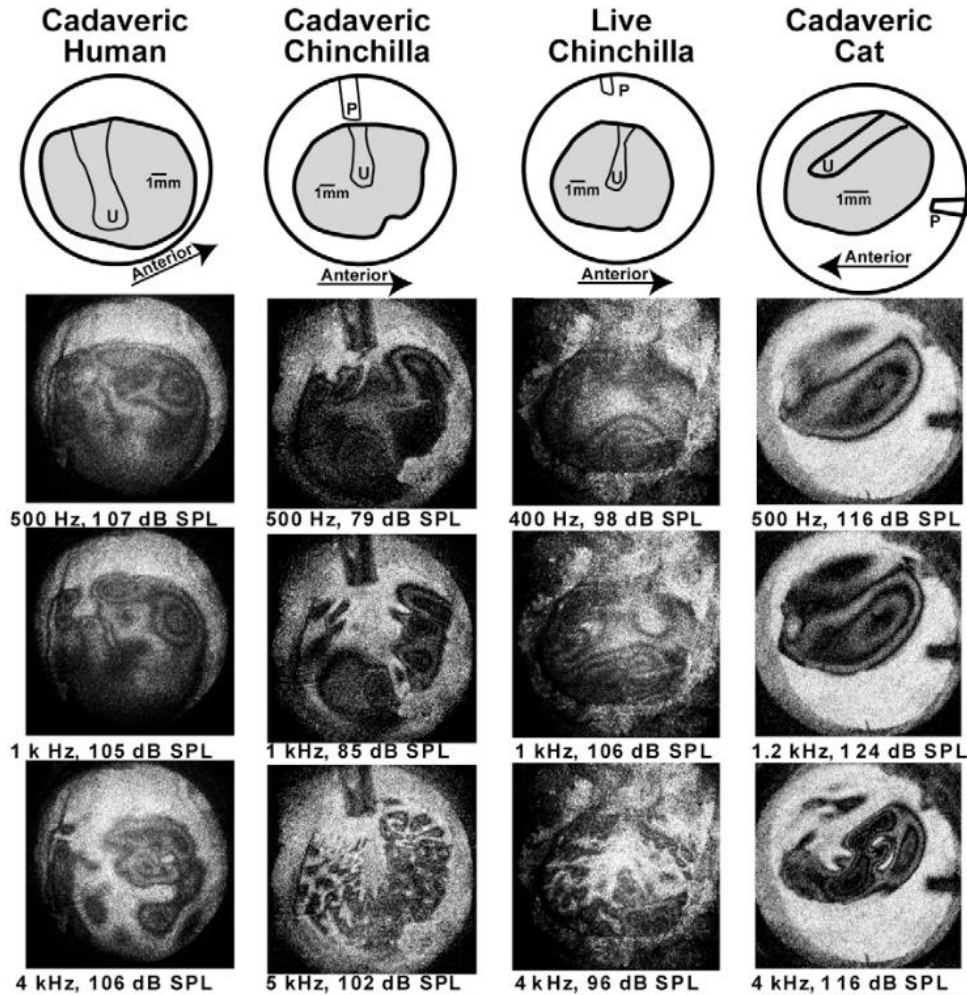


Figure 5.5. Time-averaged holograms measured in four specimens of cadaveric human, chinchilla, and cat and live chinchilla at three different excitation frequencies (adapted from Rosowski et al., 2009).

5.3.2. Quantitative 1D Holographic Measurements

Although time-averaged holographic measurements of the TM motions revealed complexity of TM motion at different tonal frequencies, quantification of these vibrational

patterns was still challenging. Stroboscopic holographic interferometry was introduced and applied to quantify sound-induced motion of the TM (Hernández-Montes et al., 2009; Furlong et al., 2009; Cheng et al., 2010 and 2013). The optical path length between the TM and the recording camera is affected by the sound-driven vibrations of the TM, producing time-related variations in the intensity of the interference pattern at each camera pixel. In stroboscopic measurements, the camera records holographic images while the object is illuminated by a train of brief laser pulses that are locked to one of nine phases of the acoustic stimulus. Two holograms illuminated at different stimulus phases are used to compute the deformation of the TM between the two phases. Figure 5.6 shows magnitudes and phases of sound-induced motion of a human TM at four different tonal frequencies, obtained with stroboscopic holographic interferometry (Cheng et al., 2013).

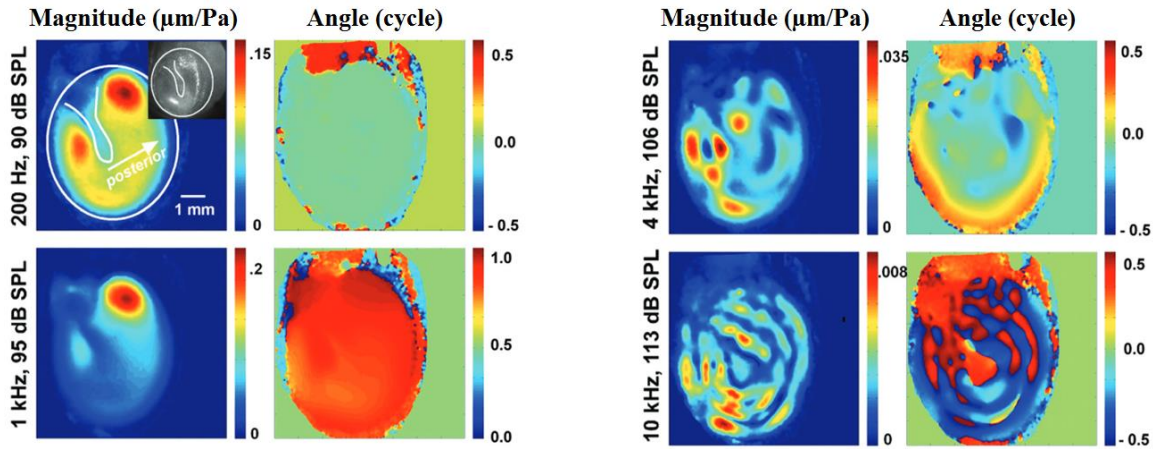


Figure 5.6. Magnitudes and phases of sound-induced motion of a human TM at four different tonal frequencies. The data are normalized by the stimulus sound pressure (units of $\mu\text{m}/\text{Pa}$). The size of each image is 800×800 pixels (adapted from Cheng et al., 2013).

5.4. 3D Shape Measurements

There are different contact and noncontact techniques that can be used to quantify 3D shape of the objects. In the case of the middle ear, and in particular, for quantifying the 3D shape of the TM, due to its delicate structure and the space constraints in the ear canal, the most

ideal technique must be first, noncontact and second, small enough to fit within the ear canal for in-vivo measurements. Researchers in the field of middle ear have been mainly using moiré interferometry to measure the shape of the TM (Dirckx and Decraemer 1997, Aernouts and Dirckx 2011). As shown in Figure 5.7, a grid is projected onto the surface of interest and a camera, placed at an angle with the projection direction, records the sum of the demodulated grid and the original one. In this way, a fringe pattern is observed. After averaging out the grid noise and recording multiple phase-shifted fringe maps, a topographic map is calculated, as shown in Figure 5.7b.

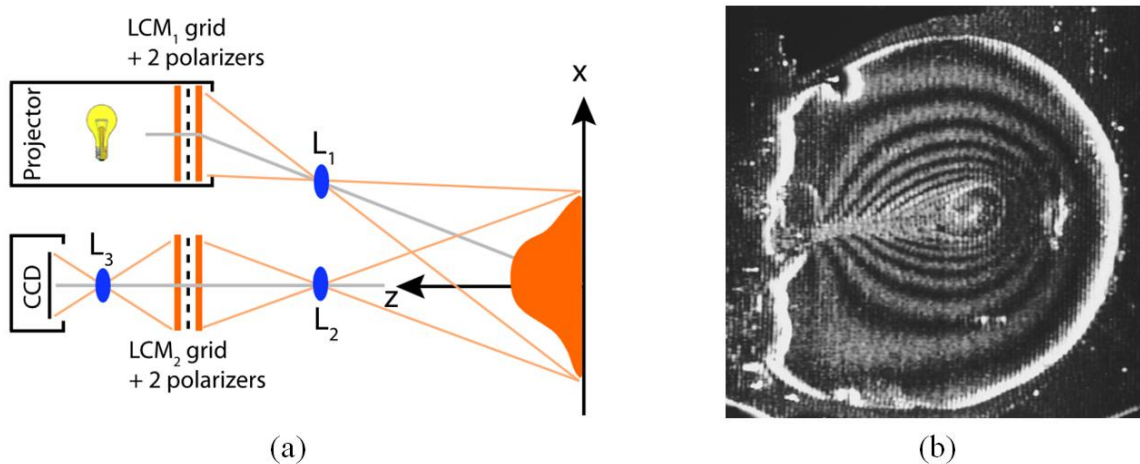


Figure 5.7. Application of moiré interferometry for characterization of the shape of a gerbil TM: (a) schematic drawing of the projection liquid crystal moiré profilometry setup with LCD projector, lenses (L_1, L_2, L_3) and a CCD camera. The liquid crystal modulator (LCM) grids and polarizers allow phase stepping and grid averaging; and (b) moiré interferogram of a gerbil TM used for characterization of the shape of the TM. To obtain the interferogram, the difference was taken between the grid line image on a flat plate and the grid line image on the membrane. The fringes represent contours of equal height, and demonstrate the conical shape of the membrane. The fringe plane distance, and hence the height difference per fringe order, is 0.082 mm (adapted from Aernouts and Dirckx 2011; Dirckx and Decraemer 1997).

However, for in-vivo applications, where the shape of the patient's TM needs to be measured through the ear canal, having a moiré interferometric system similar to the one shown in Figure 5.7 is challenging, because of the necessity of triangulation angle in moiré interferometry, and in general, in structured light profilometry techniques. On the other hand, a

system with minimum opto-electronic components should be realized in order to avoid any potential misalignment when approaching to the TM through the ear canal. Therefore, as will be described in the next Chapter, lensless holographic interferometry is considered as an alternative methodology for measurements of shape and sound-induced motion of the TM and further developments are implemented based on these techniques.

6. Digital Holographic Interferometry

Based on the problem statement given in Chapter 1, Digital Holographic Interferometry (DHI) is chosen as an appropriate technique to achieve all the aims, which are full-field measurements of shape and 3D sound-induced motions of the TM, because

- DHI provides measurements of shape and motion by capturing the entire surface of the objects using a digital CCD camera
- DHI provides wavelength-dependent measuring resolution ($\lambda/60$, Vest 1979; Hernández-Montes et al., 2009), therefore, nanometer-scale sound-induced motions of the TM can be captured using appropriate wavelengths (i.e., Ultraviolet and visible light sources) and CCD detectors
- DHI delivers the temporal resolution required for characterization of acoustically-induced motion of the TM (i.e., in microsecond regimes), since, the temporal resolution of the DHI is defined with frame rate and exposure time of the CCD camera, which can go down to femtoseconds

The holographic process consists of two steps: recording and reconstruction. In the past, silver halide holographic plates used to be utilized for recording of the holograms (Smith, 1977). As digital technologies progressed, the conventional silver halide holographic plates have been replaced with digital cameras in order to avoid the wet chemical processing involved in the reconstruction of the conventional holography and also to increase the speed and efficiency of the recording and the reconstruction of the holograms. In this Chapter, principles of electromagnetic waves, light interference, recording and reconstruction of digital holograms are described. Furthermore, the use of holographic interferometry for measurements of shape and deformations of objects are also described.

6.1. Electromagnetic waves

The primary phenomena in holography are interference and diffraction, which take place because of the wave nature of light (Kreis 2006). Light can be described as a transverse electromagnetic wave with time varying electric, \mathbf{E} , and magnetic, \mathbf{B} , fields. These two fields are perpendicular to each other and the composed wave of \mathbf{E} and \mathbf{B} travels in the direction of $\mathbf{E} \times \mathbf{B}$ as shown in Figure 6.1.

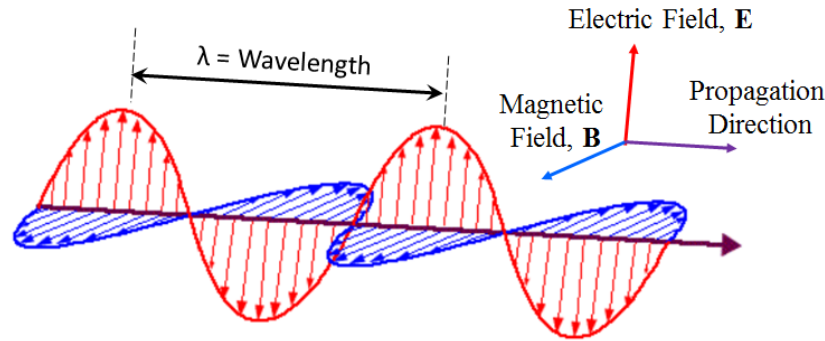


Figure 6.1. Propagation of electro-magnetic wave in a direction perpendicular to its electric and magnetic fields.

The propagation of light is described by the wave equation, which is derived from the Maxwell equations. The wave equation for propagation of light in vacuum is

$$\nabla^2 \mathbf{E} - \frac{1}{c^2} \frac{\partial^2 \mathbf{E}}{\partial t^2} = 0, \quad (6-1)$$

where \mathbf{E} is the electrical field strength vector, ∇ is the Laplace operator

$$\nabla^2 = \frac{\partial^2}{\partial x^2} + \frac{\partial^2}{\partial y^2} + \frac{\partial^2}{\partial z^2}, \quad (6-2)$$

where (x, y, z) are the Cartesian spatial coordinates, t denotes the temporal coordinate, time, and c is the propagation speed of the wave that depends on the refractive index of the propagation medium and the speed of light, c_0 , in vacuum (i.e. $\sim 3 \times 10^8$ m/s).

The direction of vibration of the light is described by its polarization and it is transverse to the direction of propagation (Hecht, 1998). The polarization direction could be horizontal, vertical or in any combination of these. Light waves vibrating in a single plane are called plane polarized light. For a plane polarized light propagating in the z -direction, Eq. 6-1 could be converted to a scalar wave equation

$$\frac{\partial^2 E}{\partial z^2} - \frac{1}{c^2} \frac{\partial^2 E}{\partial t^2} = 0 . \quad (6-3)$$

The wave field described by the scalar wave equation, Eq. 6-3, retains its form during propagation (Hecht 1998). The scalar wave equation is a linear differential equation, thus the superposition principle is valid. Most practical applications of holography rely on a solution of the wave equation called the harmonic wave

$$E(z, t) = E_0 \cos(kz - \omega t + \phi) , \quad (6-4)$$

where E_0 is the real amplitude of the wave, the $kz - \omega t + \phi$ term is the phase of the wave, ϕ is the initial phase offset, k is the wave number and ω is the angular frequency of the light wave

$$\omega = 2\pi f = \frac{2\pi c}{\lambda} \quad \text{and} \quad k = \frac{2\pi}{\lambda} , \quad (6-5)$$

where f and λ are the frequency and corresponding wavelength of the light wave. The wave number, k , quantifies the fundamental relationship between phase of the harmonic wave and its spatial and temporal distribution. Using Euler's formula, the trigonometric functions in Eq. 6-4 can be represented as complex exponentials

$$E(z, t) = \frac{1}{2} E_0 e^{i(kz - \omega t + \phi)} + \frac{1}{2} E_0 e^{-i(kz - \omega t + \phi)} = \frac{1}{2} E_0 e^{i(kz - \omega t + \phi)} , \quad (6-6)$$

where the second term of Eq. 6-6 represents the complex conjugate of the first term and it can be omitted since only the real part of Eq. 6-6 represents the physical light wave. The spatial distribution of the harmonic wave forms surfaces of constant phase, called wavefronts, which are

normal to the direction of propagation of the harmonic wave. A wavefront that has constant phase in all planes orthogonal to the propagation direction for a given time t is called a planar wave. Analogously, a spherical wavefront is called spherical wave and an arbitrary coordinate system, the position vector $\mathbf{r} = (x, y, z)$ and the wave (propagation) vector \mathbf{k} , $\mathbf{k} = (k_x, k_y, k_z)$, can be used to define the harmonic wave by substituting them into Eq. 6-6 to yield (within a constant)

$$E(\mathbf{r}, t) = E_0 e^{i(\mathbf{k}\cdot\mathbf{r} - \omega t + \phi)} . \quad (6-7)$$

6.2. Light Interference

The basic principle of holographic interferometry is the interference between two or more coherent light waves when they are superimposed. In order to mathematically describe the coherent superposition, two linearly polarized waves of the same frequency, emitted by the same source, with wave vector directions \mathbf{k}_1 and \mathbf{k}_2 , phases ϕ_1 and ϕ_2 , and amplitudes E_{01} and E_{02} are considered:

$$\mathbf{E}_1(\mathbf{r}, t) = E_{01} e^{i(\omega t - \mathbf{k}_1 \cdot \mathbf{r} + \phi_1)}, \text{ and} \quad (6-8)$$

$$\mathbf{E}_2(\mathbf{r}, t) = E_{02} e^{i(\omega t - \mathbf{k}_2 \cdot \mathbf{r} + \phi_2)} . \quad (6-9)$$

The superposition of the two waves shown in Eqs. 6-8 and 6-9 can be obtained with

$$\mathbf{E}(\mathbf{r}, t) = \sum \mathbf{E}_i(\mathbf{r}, t) = \mathbf{E}_1(\mathbf{r}, t) + \mathbf{E}_2(\mathbf{r}, t) . \quad (6-10)$$

The vacuum wavelengths of visible light are in the range of 400 nm (violet) to 800 nm (near IR). The corresponding frequency range is 750 THz to 380 THz. Therefore, common light sensors, such as photographic film, photodiodes, and CCDs, are not able to detect such high frequencies due to the technical and physical reasons (Kreis, 2005; Schnars et al., 2015). The only directly

measurable quantity is the intensity that is proportional to the average of the square of the electrical field and can be obtained with

$$I = \frac{1}{2} \varepsilon_0 n c |E|^2 = \frac{1}{2} \varepsilon_0 n c E E^* , \quad (6-11)$$

where ε_0 is the vacuum permittivity, c is the light speed, and n is the refractive index of the medium. In practice, only the proportionality of the intensity, I , to the electric field strength, $|E|^2$, is considered, i.e., $I \sim |E|^2$, which can be written as

$$I(\mathbf{r}, t) = |E|^2 = E E^* = (E_1 + E_2)(E_1 + E_2)^* , \quad (6-12)$$

where $*$ denotes the complex conjugate. Substituting Eq. 6-10 into 6-12 results in

$$I(\mathbf{r}, t) = [E_{01} e^{i(\omega t - \mathbf{k}_1 \cdot \mathbf{r} + \phi_1)} + E_{02} e^{i(\omega t - \mathbf{k}_2 \cdot \mathbf{r} + \phi_2)}] \\ \times [E_{01} e^{-i(\omega t - \mathbf{k}_1 \cdot \mathbf{r} + \phi_1)} + E_{02} e^{-i(\omega t - \mathbf{k}_2 \cdot \mathbf{r} + \phi_2)}] . \quad (6-13)$$

The exponential terms with temporal variables cancel out each other and Eq. 6-13 can be simplified to

$$I(\mathbf{r}, t) = E_{01}^2 + E_{02}^2 + E_{01} E_{02} [e^{i(\mathbf{k}_1 \cdot \mathbf{r} - \mathbf{k}_2 \cdot \mathbf{r} + \phi_1 - \phi_2)} + e^{-i(\mathbf{k}_1 \cdot \mathbf{r} - \mathbf{k}_2 \cdot \mathbf{r} + \phi_1 - \phi_2)}] , \quad (6-14)$$

which can be further simplified to

$$I(\mathbf{r}, t) = E_{01}^2 + E_{02}^2 + E_{01} E_{02} \cos(\mathbf{K} \cdot \mathbf{r} + \phi) , \quad (6-15)$$

where $\mathbf{K} = \mathbf{k}_1 - \mathbf{k}_2$ and $\phi = \phi_1 - \phi_2$. Equation 6-15 can be written in terms of intensities of the two waves

$$I(\mathbf{r}) = I_1 + I_2 + 2\sqrt{I_1 I_2} \cos(\mathbf{K} \cdot \mathbf{r} + \phi) . \quad (6-16)$$

Therefore, the resulting interference pattern between two waves of equal frequency does not depend on the temporal variation of their electromagnetic field (Kreis, 2005).

6.3. Holographic recording and reconstruction

Holograms are usually recorded with an optical set-up consisting of a light source (e.g. a laser), beam guiding components (e.g., mirrors and lenses) and a recording device (e.g. a hologram plate). Figure 6.2 shows the two main steps of holographic process, which are *Recording* and *Reconstruction*. In the recording step, principles of interferometry can be used to record the wavefronts scattered off the surface of an object at a specified time. In the recording step, as shown in Figure 6.2a, light with sufficient coherence length (Kreis, 2005) is split into two waves *Reference* and *Object* by a beamsplitter (BS). One wave, called the object wave, illuminates the object and is then scattered and reflected to the recording medium, e.g., a photographic plate or a camera sensor. The second wave, called the reference wave, illuminates the sensor directly.

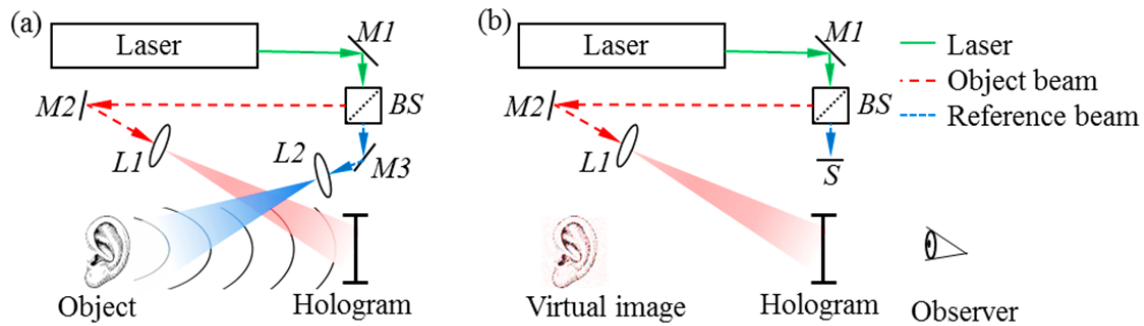


Figure 6.2. Principles of recording and reconstruction of holograms: (a) the hologram is illuminated with both reference and object beams; and (b) the hologram is illuminated with only the reference beam during holographic reconstruction. In the figure, M is mirror; L is lens; BS is beam splitter; and S is shutter (Dobrev, 2014).

In this case, the reference and object waves can be described with

$$O(x, y) = o(x, y)e^{i[\phi_o(x, y)]}, \text{ and} \quad (6-17)$$

$$R(x, y) = r(x, y)e^{i[\phi_r(x, y)]}. \quad (6-18)$$

where o and ϕ_o are the amplitude and phase of the complex object wave and r and ϕ_r are the amplitude and phase of the complex reference wave. The interference between the two waves at

the plane of the sensor (hologram plate) is recorded by the holographic plate. Similar to Eq. 6-12, the intensity, $I(x, y)$, of the complex field of the hologram can be expressed as

$$I(x, y) = |O(x, y) + R(x, y)|^2 = I_o(x, y) + I_r(x, y) + 2\sqrt{I_o(x, y)I_r(x, y)} \cos[\Delta\phi(x, y)] , \quad (6-19)$$

where $I_o(x, y)$ and $I_r(x, y)$ are the intensities of the two waves at the hologram plane, and $\Delta\phi$ is the phase difference between the two waves. The recorded holographic wavefront, $h(x, y)$, at the sensor is proportional to $I(x, y)$

$$h(x, y) = h_0(x, y) + \beta t_m I(x, y) \cong \beta t_m I(x, y) , \quad (6-20)$$

where β is a constant related to the light sensitivity of the sensor (holographic plate or camera sensor), t_m is the exposure time (measurement time), and h_0 represents the read-out noise (or amplitude transmission of the unexposed plate) of the sensor and it will be neglected in further descriptions of the holographic recording process.

During the reconstruction step, as shown in Figure 6.2b, the object beam is typically turned off (by a shutter) and the hologram is illuminated with the reference beam only. This produces a virtual image of the original object that can be observed by a viewer through the holographic plate. The reconstruction process can be mathematically described as a multiplication between the hologram and the reconstruction (reference) wave. Based on Eqs. 6-19 and 6-20, the reconstructed hologram, U , at the recording plane can be expressed as

$$U = h * R = \beta t_m [(r^2 + o^2)R + r^2O + R^2O^*] , \quad (6-21)$$

where the spatial dependence, (x, y) , of all variables has been omitted for brevity. The first term represents undiffracted wave, also called zero diffraction order, which does not have any information about the phase of the object wave. The second term is the reconstructed object wave that forms an image at the object plane that can be observed through the recording media,

as shown in Figure 6.2b, assuming a holographic plate was used. The third term produces an out-of-focus real image of the object.

6.4. Fresnel-Kirchhoff Diffraction Theory

During the process of holographic reconstruction, the reconstruction (reference) wave is diffracted by the aperture of the hologram and it produces a diffraction pattern at the image plane. Figure 6.3 illustrates the coordinate systems where (x, y) are Cartesian coordinates in the hologram plane, (ξ, η) are Cartesian coordinates in the image plane, z is the Cartesian coordinate along the surface normal of the hologram plane in the direction of the image plane.

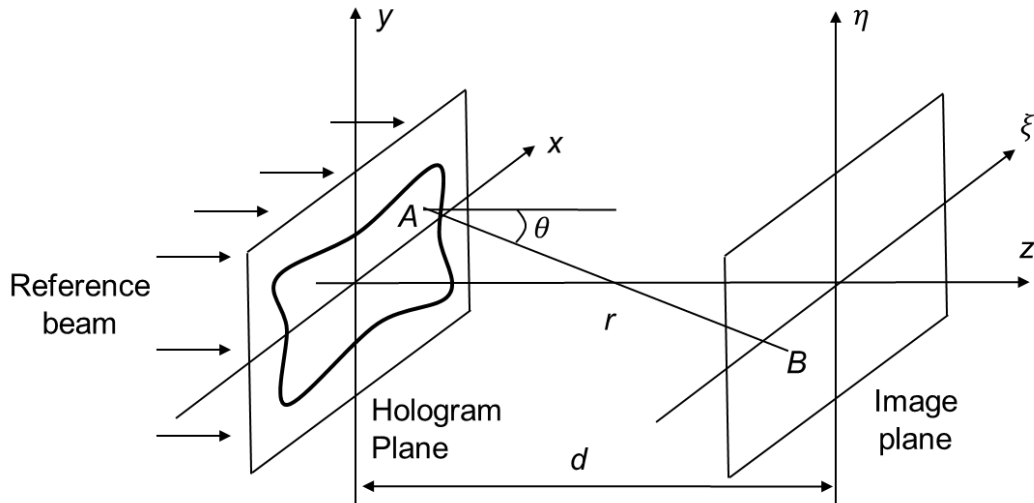


Figure 6.3. Schematics of the coordinate system nomenclature for lensless digital numerical reconstruction (Kreis, 2005).

During numerical reconstruction, the propagating wavefronts can be modeled by the Fresnel-Kirchhoff diffraction formula (Schnars et al., 2015) that is

$$\Gamma(\xi, \eta, z) = \frac{i}{\lambda} \iint_{-\infty}^{\infty} h(x, y) R(x, y) \frac{e^{-i\frac{2\pi}{\lambda}r}}{r} \cos \theta \, dx dy, \quad (6-22)$$

where $\cos \theta = z/r$, $\Gamma(\xi, \eta, z)$ is the reconstructed hologram, and r is the distance between any two points on the hologram and image planes, as shown in Figure 6.3, and is defined as

$$r = \sqrt{(x - \xi)^2 + (y - \eta)^2 + z^2} . \quad (6-23)$$

6.5. Numerical reconstruction By the Fresnel Transform

Fresnel-Kirchhoff diffraction formula shown in Eq. 6-22 is computationally expensive and for practical applications of the Fresnel transformation, several assumptions should be made in order to simplify and optimize this equation. It can be assumed that the distance between the hologram and the image plane is large compared to the lateral size of the hologram and the image (Kolenovic, et al., 2004; Kreis et al., 2005; Schnar et al., 2015). This means that r in the denominator of the integral shown given in Eq. 6-22 can be replaced by z . However, since r is typically in the centimeter to meter range and λ is in the sub-micron range, slight variations of r in the exponential term may lead to significant phase errors. Thus, an approximation of r is required in order to simplify the exponential term. This leads to the Fresnel approximation that relies on the binomial expansion of Eq. 6-23 using a Taylor series to approximate r with

$$r = d + \frac{(x - \xi)^2}{2d} + \frac{(y - \eta)^2}{2d} - \frac{1}{8} \frac{[(x - \xi)^2 + (y - \eta)^2]^2}{d^3} + \dots . \quad (6-24)$$

The Fresnel approximation is valid as long as the quadratic term in the binomial expansion series (i.e., the forth term in Eq. 6-24) leads to a phase changes $\ll 1$ radian, which means

$$d \gg \sqrt[3]{\frac{\pi}{4\lambda} [(x - \xi)^2 + (y - \eta)^2]^2} . \quad (6-25)$$

Equation 6-25 defines the near field region, where the Fresnel approximation can be applied.

Therefore, Eq. 6-24 can be simplified to

$$r = d + \frac{(x - \xi)^2}{2d} + \frac{(y - \eta)^2}{2d} . \quad (6-26)$$

Assuming that the requirements stated by Eqs. 6-25 and 6-26 are met, the Fresnel approximation, Eq. 6-26, can be applied to the exponential term of Eq. 6-22 as follows

$$\begin{aligned} \Gamma(\xi, \eta, z) &= \frac{i}{\lambda d} \exp \left[-i \frac{2\pi}{\lambda} d \right] \\ &\times \iint_{-\infty}^{\infty} h(x, y) \exp \left[-i \frac{\pi}{\lambda d} ((x - \xi)^2 + (y - \eta)^2) \right] dx dy . \end{aligned} \quad (6-27)$$

If the multiplication term in the argument of the exponential under the integral is carried out, then Eq. 6-27 can be written as

$$\begin{aligned} \Gamma(\xi, \eta, z) &= \frac{i}{\lambda d} \exp \left[-i \frac{2\pi}{\lambda} d \right] \exp \left[-i \frac{\pi}{\lambda d} (\xi^2 + \eta^2) \right] \times \iint_{-\infty}^{\infty} h(x, y) \exp \left[-i \frac{\pi}{\lambda d} (x^2 + \right. \\ &\left. y^2) \right] \exp \left[i \frac{2\pi}{\lambda d} (x\xi + y\eta) \right] dx dy . \end{aligned} \quad (6-28)$$

This equation is known as Fresnel Transformation, which enables reconstruction of the wavefield in a plane (plane of the real image) behind the hologram.

To digitize the Fresnel Transform shown in Eq. 6-28, the substitutions $u = \xi/\lambda d$ and $v = \eta/\lambda d$ are introduced and Eq. 6-28 can be modified to

$$\begin{aligned} \Gamma(u, v) &= \frac{i}{\lambda d} \exp \left[-i \frac{2\pi}{\lambda} d \right] \exp[-i\pi\lambda d(u^2 + v^2)] \\ &\times \iint_{-\infty}^{\infty} h(x, y) \exp \left[-i \frac{\pi}{\lambda d} (x^2 + y^2) \right] \exp[i2\pi(xu + yv)] dx dy . \end{aligned} \quad (6-29)$$

Aside from a constant intensity and quadratic phase factors preceding the integral, Eq. 6-29 is the two-dimensional inverse Fourier Transform of the product of the hologram function, $h(x, y)$, with a 2D chirp function $\exp \left[-i \frac{\pi}{\lambda d} (x^2 + y^2) \right]$. In practical applications with recordings of diffuse (optically rough) objects, the constant intensity and phase factors preceding the double-

integrals of Eq. 6-29 can be omitted since only the phase change and not the absolute phase of the object field is of importance, therefore Eq. 6-29 can be expressed as (Kreis, 2005)

$$\Gamma(u, v) = \text{IFFT2} \left[h(x, y) e^{-i\frac{\pi}{\lambda d}[x^2+y^2]} \right]. \quad (6-30)$$

6.5.1. Discrete Fresnel transformation

The function $\Gamma(u, v)$ shown in Eq. 6-30 can be digitized if the hologram function, $h(x, y)$, is sampled on a rectangular sensor array with $M \times N$ pixels and a pixel pitch of Δx and Δy . According to Fourier Transform procedures, Δu and Δv can be written in terms of the pixel sizes $\Delta x, \Delta y$ with

$$\Delta u = \frac{1}{M\Delta x} \quad , \quad \Delta v = \frac{1}{N\Delta y} . \quad (6-31)$$

Therefore, the horizontal and vertical resolution of the reconstructed hologram, $\Delta\xi$ and $\Delta\eta$ (i.e., the pixel size in the image plane) can be obtained with

$$\Delta\xi = \frac{1}{M\Delta u} = \frac{d\lambda}{M\Delta x} , \quad (6-32)$$

$$\Delta\eta = \frac{1}{N\Delta v} = \frac{d\lambda}{N\Delta y} . \quad (6-33)$$

Therefore, the discrete form of Eq. 6-29 can be mathematically expressed as the Fast Fourier Transformation (FFT) of

$$\Gamma(m, n, d) = \text{IFFT2}[h(k, l)R(k, l)\psi(k, l, d)] , \quad (6-34)$$

where IFFT2 is the discrete 2D Inverse Fast Fourier Transform (FFT), $h(k, l)$ is the discretized hologram recorded by the sensor, $R(k, l)$ is discrete numerical model of the reconstruction (reference) wave, and $\psi(k, l, d)$ is the discrete chirp function used for reconstruction at a position z away (behind the sensor) from the hologram plane

$$\psi(k, l, d) = \exp \left[\frac{-i\pi}{\lambda d} [k^2 \Delta x^2 + l^2 \Delta y^2] \right]. \quad (6-35)$$

Equation 6-34 allows for numerical reconstruction of a digitally recorded hologram. Adjustment of the reconstruction distance, d , during the numerical reconstruction process, allows focusing at a user defined imaging plane, thus allowing free-focusing capabilities after the recording of the hologram (Schnars and Jüptner 2002; Kreis 2005). The intensity and optical phase of the numerically-reconstructed hologram can be respectively obtained with

$$I(m, n) = |\Gamma(m, n)|^2, \text{ and} \quad (6-36)$$

$$\varphi(m, n) = \text{atan2} \frac{\Im[\Gamma(m, n, d)]}{\Re[\Gamma(m, n, d)]}, \quad (6-37)$$

where \Im and \Re denotes the imaginary and real parts. In order to avoid the $[-\pi/2, \pi/2]$ ambiguity of the \tan^{-1} function, the computationally efficient atan2 function is utilized, allowing for quantification of the phase within the full $[-\pi, \pi]$ range. Furthermore, the mathematical nature of atan2 function leads to sudden jumps in the optical phase data from $-\pi$ to π and vice versa and these discontinuities should be removed in the *phase unwrapping* post-processing step (Herráez et al., 2002; Karasev et al., 2007; Pham et al., 2010).

6.6. 3D Displacements measurements

Digital holography allows for quantification of the deformation of an object, by comparing holograms of the object before and after deformation. The holograms are individually reconstructed using Eq. 6-34 and the Fringe-locus function of a double-exposure (DE) hologram, i.e., the unwrapped optical phase difference of two reconstructed holograms corresponding to deformed and reference states of the object, is used to obtain the 3D displacement with

$$\Omega(m, n) = \text{unwrap}(\varphi_{def} - \varphi_{ref}) = \frac{2\pi}{\lambda} \mathbf{k}_s \cdot \mathbf{d}(m, n), \quad (6-38)$$

where $\Omega(m, n)$ is the fringe-locus function at coordinates m and n in the reconstruction plane, φ_{def} and φ_{ref} are optical phases of the reconstructed holograms recorded at deformed and reference states of the object, respectively, $\mathbf{k}_s(\mathbf{K}_x, \mathbf{K}_y, \mathbf{K}_z)$ is the sensitivity vector, defined by vectorial subtraction of the observation vector from the illumination vectors, and $\mathbf{d}(m, n)$ is the displacement vector with three components of \mathbf{d}_x , \mathbf{d}_y , and \mathbf{d}_z . Assuming a coordinate system as given in Figure 6.4, the directions of observation and illumination vectors are described by unit vectors \mathbf{k}_o and \mathbf{k}_i . Based on this geometrical setup, the resulting sensitivity vector is defined as $\mathbf{k}_s = \mathbf{k}_o - \mathbf{k}_i$ (Vest, 1979). The sensitivity vector, \mathbf{k}_s , indicates the direction of the component of the displacement field vector, $\mathbf{d}(x, y, z)$, of the object's surface, which the holographic system is sensitive to. In other words, at each object point the holographic system measures the projection of the displacement vector, \mathbf{d} , onto the sensitivity vector, \mathbf{k}_s .

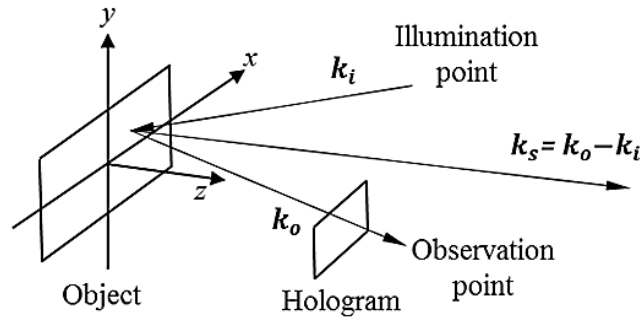


Figure 6.4. Geometrical definition of the sensitivity vector that is the vectorial subtraction of the observation vector from the illumination vector (Pryputniewicz et al., 1990).

In order to measure all three components of the displacement vector, \mathbf{d} , shown in Eq. 6-38, at least three independent measurements with different sensitivity vectors are required. In our approach, and to minimize experimental errors, optical phase maps are obtained with four sensitivity vectors to form an over determined system of equations that is solved with the least-squares error minimization method with

$$\{\mathbf{d}\} = [[\mathbb{S}]^T[\mathbb{S}]]^{-1}\{[\mathbb{S}]^T\{\Omega\}\}, \quad (6-39)$$

where $[\mathbb{S}]$ is the sensitivity matrix containing all the sensitivity vectors \mathbf{K}_i , and $\{\Omega\}$ is the fringe-locus function vector. In this method, all the sensitivity vectors need to be as linearly independent as possible for the system to provide accurate results. Therefore, the condition number, \mathbb{C} , of the square matrix, $[F] = [\mathbb{S}]^T[\mathbb{S}]$, characterizing the geometry of a holographic setup is calculated with (Osten, 1985)

$$\mathbb{C}(\mathbb{S}) = \sqrt{\frac{\lambda_{max}(F)}{\lambda_{min}(F)}}, \quad (6-40)$$

where λ_{max} , and λ_{min} are the maximum and the minimum eigenvalues of $[F]$. A condition number close to one indicates a well-conditioned matrix, but this represents a holographic setup with large angles of illumination (Vest, 1979; Osten, 1985; Furlong, 1999). However, in our application and because of the particular cone-like geometry of the TM and the presence of the bony structures around it, the maximum possible angles of illumination are limited. Therefore, a holographic setup has to be arranged to achieve the largest angles of illumination within the constraints imposed by the geometry of the TM.

6.7. 3D Shape measurements with Holographic Interferometry

Contouring in general means the modulation of the image of a 3D object by fringes corresponding to contours of constant phases (Kreis 2005). In holographic contouring, the shape-related fringe pattern arises from the superposition of two holograms recorded and reconstructed at two states with different sensitivity vectors, which relates the geometric shape of an object to the measured optical phases. The sensitivity vector in holographic interferometry contains three variables, wavelength, refractive index, and illumination and observation directions (Vest 1985, Li 2009). Therefore, the differences in the two states are either due to

change in the refractive indexes (Zelenka and Varner 1969; Hung et al., 1978; Chen et al., 2000), the change in the positions of the illumination directions (Joenathan et al., 1990; Zou et al., 1992; Pedrini et al., 1999; Furlong 1999), or the changes in the applied wavelengths (Polhemus 1973; Furlong 2000; Wagner et al., 2000; Yamaguchi et al., 2006). The other technique for shape measurements is time-of-flight method, which is based on the direct measurement of the time of flight of a laser pulse (Makynen et al., 1994; Cui et al., 2010). During measurements, an object pulse is reflected back to the receiving sensor and a reference pulse is passed through an optical fiber and received by the sensor. The time difference between the two pulses is converted to distance. The main three approaches for holographic contouring are described below.

6.7.1. Two-refractive Index holographic contouring

In this technique, the object is located in an immersion cell containing a specific liquid. By changing the refractive index of the fluid around the object between the two exposures of the hologram, interference fringes are produced (Zelenka and Varner 1969; Hung et al., 1978). Two holograms are captured at two different refractive indices and the phase difference between the two states is related to the shape of the object, $Z(x, y)$, with

$$Z(x, y) = \frac{\lambda (\phi_1 - \phi_2)}{2\pi(n_1 - n_2)} = \Delta\phi(x, y) \frac{\lambda}{2\pi(n_1 - n_2)}, \quad (6-41)$$

where n_1 and n_2 are the two refractive indices of the fluid surrounding the object during each of the two exposures, and $\Delta\phi$ is the phase difference.

6.7.2. Multiple illumination directions holographic contouring

The second shape measurement techniques can be achieved by changing the illumination direction between the two exposures of the hologram. A change in the illumination beam produces a change in the phase of the wavefront which depends on the object shape (Pedrini et

al., 1999; Furlong 1999). The change in the illumination direction can be achieved by translating the illumination point from one to another. The phase difference between the two states can be obtained with

$$\Delta\phi(x, y) = 2k \sin \frac{\Delta\theta}{2} x \cos \left[\theta + \frac{\Delta\theta}{2} \right] - 2k \sin \frac{\Delta\theta}{2} h(x, y) \sin \left[\theta + \frac{\Delta\theta}{2} \right], \quad (6-42)$$

where $h(x, y)$ is the object height, and $\Delta\theta$ is the angle change between the two illuminations.

6.7.3. Dual-wavelength holographic contouring

Fringe pattern corresponding to the shape of an object can be generated by phase measurements of the object using an interferometer with a wavelength λ . However, these shape measurements are limited to geometries with heights of less than a few wavelengths, e.g., for geometries with heights less than 20 μm for a wavelength of 780 nm. In order to extend the shape measuring range, a dual-wavelength holographic contouring technique is developed and implemented, in which the height measurements are performed based on a beating frequency between the two wavelengths (Seebacher et al., 1998; Furlong and Pryputniewicz 2000). In this case, first, the complex amplitude of the object of interest is recorded and reconstructed with wavelength of λ_1 . Then, the wavelength is tuned to a new value of λ_2 and the complex amplitude of the object is recorded and reconstructed with wavelength of λ_2 . The optical phases obtained with the two wavelengths are subtracted from one another in order to obtain a fringe pattern corresponding to the shape of the object with

$$\Omega = \phi_1 - \phi_2 = 2\pi \frac{x}{\lambda_1} - 2\pi \frac{x}{\lambda_2} = 2\pi \left(\frac{\lambda_2 - \lambda_1}{\lambda_1 \lambda_2} \right) \text{OPL} = 2\pi \frac{\text{OPL}}{\Lambda}, \quad (6-43)$$

where OPL is the optical pathlength of the laser light. It has been mathematically shown (Polhemus 1973) that the dual-wavelength contouring technique generates the same fringe

pattern as if the shape measurements would have been interferometrically performed with a synthetic wavelength of Λ that is equal to $\Lambda = \frac{\lambda_1 \lambda_2}{|\lambda_1 - \lambda_2|}$. In parallel illumination-observation configurations, the contour depth is equal to half the synthetic wavelength ($\Delta z = \Lambda/2$) and therefore, the height at each point on the surface of the object can be calculated with

$$z(x, y) = \frac{\Lambda}{4\pi} \Omega(x, y), \quad (6-44)$$

One of the prominent advantages of this holographic contouring technique is that the measuring sensitivity can be adjusted by controlling the differences between the first and second wavelengths. As shown in Figure 6.5, larger wavelength differences, $\Delta\lambda = \lambda_2 - \lambda_1$, provide smaller contour depth, which in turn, enables better shape measuring resolutions.

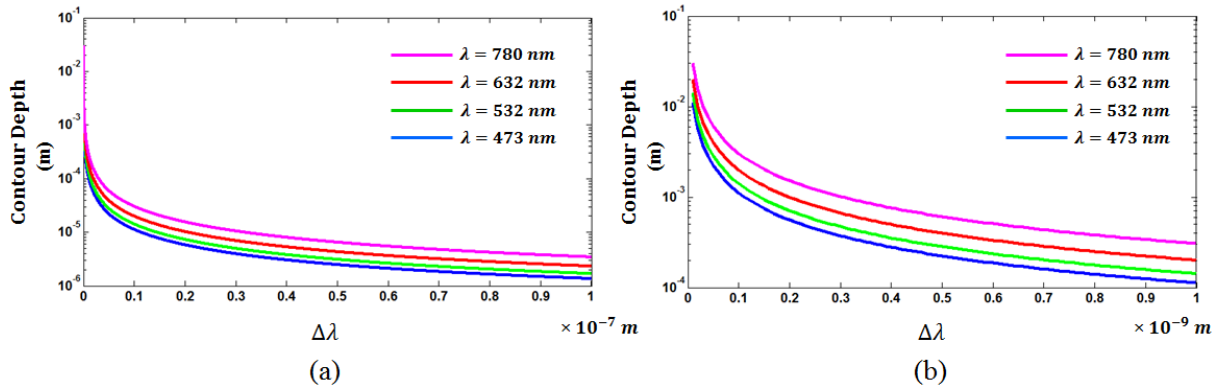


Figure 6.5. Adjusting the measuring sensitivity range in dual-wavelength holographic contouring by controlling the differences between the first and second wavelengths $\Delta\lambda = \lambda_2 - \lambda_1$: (a) broad changes in the wavelengths (in this case up to 100 nm) leads to fine contour depths $\Lambda/2 \approx 5 \mu m$ and in turn, a better shape measurement resolution; and (b) narrow changes in the wavelength (in this case up to 1 nm) leads to larger contour depths $\Lambda/2 \approx 0.5 mm$ and hence, lower measuring sensitivity. The results are shown for four different central wavelengths 473, 532, 632, and 780 nm.

6.8. Applications of Holographic Interferometry in Hearing Research

Study of the sound-induced vibrational patterns of different mammalian TMs has been an ongoing area of interest for many researchers. Previous studies on the applications of holographic interferometry for the study of the middle ear can be divided into three main

categories: qualitative investigations of the sound-induced vibrational patterns of the TM using conventional time-averaged and double exposure holography (Khanna and Tonndorf 1972; von Bally 1978; Uyemura et al., 1979; von Bally and Greguss 1982; Ogura et al., 1979 and 1983); quantitative one-dimensional measurements of sound-induced motions of the TMs (Wada et al., 2002; Rosowski et al., 2009; Cheng et al., 2010; Chang et al., 2013; Cheng et al., 2013; Dobrev et al., 2014); and measurements of 3D shapes of the TMs (Decraemer et al., 1991; Solís et al., 2012).

One of the main goals of this Dissertation is to realize a clinically-applicable integrated holographic system capable of full-field qualitative and quantitative measurements of shape, and 3D sound-induced motions of the TMs. The main challenge along the way is that a broad measuring range is indispensable for such a holographic system to cover both shape (i.e., in the millimeter range) and 3D sound-induced motions (i.e., in the nanometer range). Therefore, a clinically-applicable holographic system with a measuring range spanning nearly six orders of magnitude needs to be realized. Furthermore, the system should be capable of being miniaturized and packaged to be used in the clinics and for *in-vivo* applications.

PART 2: Developments

General Overview

In this Part, developments and contributions towards expanding the capabilities of the previous state-of-the-art technologies are described by realizing metrological imaging modalities to improve the knowledge and understanding about shape and function of the mammalian TMs. The developments have been organized in several consecutive publications that incrementally describe advancements leading to innovative tools for the study of the middle ear mechanics.

Chapter 7 describes developments and applications of a holographic system that is used to estimate 3D sound-induced displacements of TM by combining shape information and 1D components of displacement. Shape and displacement measurements are carried out with a lensless dual-wavelength digital holographic system with shape measured in two-wavelength mode and 1D displacements measured in single wavelength mode. The assumptions we used in the computation of the 3-Dimensional sound-induced motions from measured shape and 1D-displacements are based on considering the TM as a thin-shell, where sound-induced displacement vectors at each point on the surface of the TM are hypothesized to be along the normal vectors of its shape. This approach is tested and verified using FEM models and then, the system is used to measure shape and 1D motion, and in turn, to estimate all 3D sound-induced motions of the TM at several tonal excitation frequencies.

Chapter 8 describes the use of thin-shell hypothesis on a chinchilla TM sample at several tonal frequencies. The measurement of shape and its application to realize thin-shell hypothesis enable to separate the measured motions into those components orthogonal to the plane of the tympanic ring, and those components within the plane of the tympanic ring. The predicted

in-plane motion components (x - and y -axis motions) are generally smaller than the motions normal to the plane of the tympanic ring (z -axis motion), and the tangential motions are assumed to be negligible. The needs for true measurements of 3D sound-induced motions of the TMs are also highlighted.

Chapter 9 describes developments of a three-dimensional holographic system capable to near-simultaneously measure shape and three-dimensional sound-induced motion of the TM. 3D components of sound-induced displacements of the TM are measured with the method of multiple illumination directions in holographic interferometry using a series of repetitive stroboscopic measurements for each sensitivity vectors. To accurately obtain sensitivity vectors, a new technique is developed and used in which the sensitivity vectors are obtained from the images of a specular sphere that is being illuminated from different directions. Shape and 3D acoustically-induced displacement components of cadaveric human TMs at several excitation frequencies are measured at more than one million points on its surface.

The physiological applications of the developed holographic system are described in Chapter 10, where, the system is used to quantify shapes and 4-Dimensional sound-induced motions (in space (x, y, z) and time (t)) of multiple TM samples at several tonal frequencies. The results obtained from the shape measurements are combined with 3D components of displacements in order to obtain motion components tangent (in-plane) and normal (out-of-plane) to the local plane of the TM. The results support thin-shell hypothesis of the TMs, in which the tangential motion components are negligible and the motion vectors are hypothesized to be mainly along the normal vector of the surface of the membrane.

Due to the time-varying nature of biological tissues like the TM, a novel method for 3D deformation measurements based on multiplexed holography is described in Chapter 11, which allows for simultaneous holographic measurements along multiple sensitivity vectors. The developed methodology is a critical step forward towards *in-vivo* measurements of 3D TM motions. The holograms of the objects of interest are recorded with three simultaneous incoherently-superimposed pairs of reference and object beams, such that the modulation image corresponding to each illumination direction is reconstructed at a different position of the image. An image registration algorithm based on the shift theorem of the Fourier Transform is implemented to register the images. The time needed for a given 3D motion measurement is decreased at least threefold. We demonstrate that the present method is a valid alternative to repetitive holographic methods and offers promising perspectives towards accurate 3D deformation measurements of biological specimens for *in-vivo* applications.

To further expand our knowledge on the dynamics of sound-induced energy transfer through the middle ear, measurements of sound-induced forces are also required. Force sensing techniques are usually invasive and due to the viscoelastic properties of the TM, any interaction between the probe and the TM may result in modification of its mechanics. In chapter 12, efforts to measure sound-induced forces of the TM using minimally-invasive sensing methodologies are described. The methodologies consist of integrating MEMS-based sensors with the developed holographic systems for simultaneous characterizations of kinematics and dynamics of the TM. The MEMS-based force sensors have sub-micro-Newton resolution and are capable of measurements along a single axis on a localized area of the sample on the order of $50 \times 50 \mu\text{m}^2$. A computer-controlled 3D nano-positioner automatically places and scans the force sensor at several locations on the TM that are critical for the transfer of energy from the outer ear to the

inner ear. These developments are enabling new approaches for quantitative investigations of middle ear mechanics.

7. Paper A: Digital holographic measurements of shape and three-dimensional sound-induced displacements of tympanic membrane

Overview

This paper, published in *Optical Engineering* in 2013, describes the development of a single holographic system capable of measurements of shape and sound-induced motions of the mammalian tympanic membranes. The Shapes of the mammalian TMs are in millimeters range, whereas sound-induced motions of such membranes are in nanometers range. It is truly challenging to find one single imaging system with resolutions spanning six orders of magnitude from millimeter (for shape measurements) to nanometer (for sound-induced motion measurements), but we have developed a holographic system capable of near-simultaneous measurements of shape and acoustically-induced motion of the TMs. Conventional methods for 3D motion measurements require data from at least three different sensitivity vectors, which, due to space constraints, is challenging for measurements of the sound-induced motions of mammalian ear drums. Based on geometrical similarities of mammalian TMs with those of thin-shells, Kirchhoff-Love's thin-shell theory is applied to the case of mammalian TMs in order to *estimate* three-dimensional sound-induced motions from shape and motion measurements obtained along only one single sensitivity vector. Therefore, the sound-induced kinematics of mammalian TMs are hypothesized to be similar to those of thin-shells, where the sound-induced motion vector is along the vector normal to the local surface and motion components tangent to the surface of the TM are negligible. The applicability of this thin-shell hypothesis is tested and verified using Finite Element Methods and an implementation of the method using real chinchilla's TM samples is presented.

7.1. Shape measuring approach

There are several techniques for holographic measurements of 3D shape of the objects. However, delicate structure and space constraints within the human ear restrict the use of some of those techniques. For instance, the shape measuring technique based on inducing a change in the refractive index of the medium is not applicable for measurements of mammalian TMs, since the object needs to be located within a medium with a refractive index that can be tuned, e.g., the TM would be submerged in water, which is an undesirable method. Another shape measuring technique, holographic contouring by changing the illumination direction, is also challenging for measurements of TMs' shapes, because, for instance in humans, the TM is located at the end of a curved canal with a length of 3 centimeter and a diameter of 8 millimeter, and changing the illumination direction in such a restricted area is difficult. Therefore, for TM shape measurements, and considering the metrological challenges, dual-wavelength holographic contouring technique are developed. The dual-wavelength capability can be embedded into an optical fiber-based configuration capable of measurements of both, shape and motions. Furthermore, the system can be miniaturized and packaged for clinical and *in-vivo* applications.

7.2. TM as a thin-shell

Figure 7.1 shows an example of the shape of a mammalian TM modeled as a thin-shell (Rosowski et al., 2013; Khaleghi et al., 2013). For each differential TM element, shown in Figure 7.1b, a curvilinear coordinate system (α, β, η) can be defined and corresponding components of displacement, d_α , d_β , and d_η , are expressed as

$$\begin{cases} d_\alpha(\alpha, \beta, \eta) = d_\alpha^0(\alpha, \beta) + \eta \frac{\partial d_\eta^0(\alpha, \beta)}{\partial \alpha} \\ d_\beta(\alpha, \beta, \eta) = d_\beta^0(\alpha, \beta) + \eta \frac{\partial d_\eta^0(\alpha, \beta)}{\partial \beta} \\ d_\eta(\alpha, \beta, \eta) = d_\eta^0(\alpha, \beta) \end{cases}, \quad (7-1)$$

where d_α^0 , d_β^0 , and d_η^0 are tangential and normal components of displacements of the neutral plane.

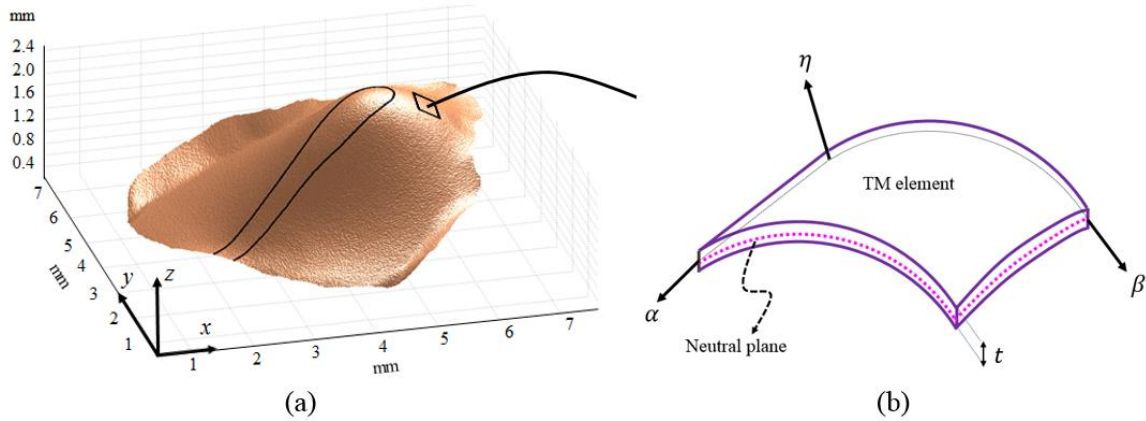


Figure 7.1. Thin-shell modeling of a TM: (a) measured shape of a chinchilla TM (Khaleghi et al., 2013); and (b) schematic of curvilinear coordinate system (α, β, η) on a TM element with a thickness t . Tangential components of the neutral plane, d_α^0 and d_β^0 , are negligible.

Based on thin-shell assumptions (Chen et al., 1987; Love, 1888), straight lines, initially normal to the neutral plane, remain straight and normal to it after deformation and the length of such element is not altered. The lack of change in the direction of the normals to the neutral plane during deformation leads to negligible out-of-plane shear strains $\gamma_{\alpha\eta}$ and $\gamma_{\beta\eta}$. Furthermore, considering the relatively small magnitudes of sound-induced motion of the TM (100-300 nm) compared to its thickness (50-150 μm), the gradient terms, shown in the tangential components of Eq. 7-1, are assumed to be negligible and in turn, the neutral plane is assumed to remain unstrained after deformation, resulting in d_α^0 , and d_β^0 being zero. The second assumption, that is the constant thickness of the shell during the deformation process, results in negligible

normal strain, $\epsilon_{\eta\eta}$. Therefore, based on Eq. 7-1, the displacement vector on the TM element remains, mainly, out-of-plane, which is along the normal vector of the surface. This displacement vector, then, can be decomposed along three axes x, y, z , providing 3D components of displacement. Using these thin-shell assumptions, it is possible to obtain 3D components of displacement of the TM by having displacement's component along only a single axis (e.g. ear canal axis), and combining it with components of the normal vectors of the shape. Therefore, principal components of displacement \mathbf{d}_x , \mathbf{d}_y , and \mathbf{d}_z at every point on the surface of the membrane along Cartesian axes x, y , and z , can be obtained by decomposition of the displacement vector along the normal vector's components \mathbf{n} ($\mathbf{n}_x, \mathbf{n}_y, \mathbf{n}_z$) with

$$\mathbf{d}_x = \mathbf{n}_x \frac{|\mathbf{d}_z|}{|\mathbf{n}_z|}, \text{ and} \tag{7-2}$$

$$\mathbf{d}_y = \mathbf{n}_y \frac{|\mathbf{d}_z|}{|\mathbf{n}_z|}. \tag{7-3}$$

By using this approach, complexity in the 3D displacement measurements, that requires acquiring displacements data from at least three independent directions, will be bypassed by measuring the shape and 1D displacement, both measured from a single axis.

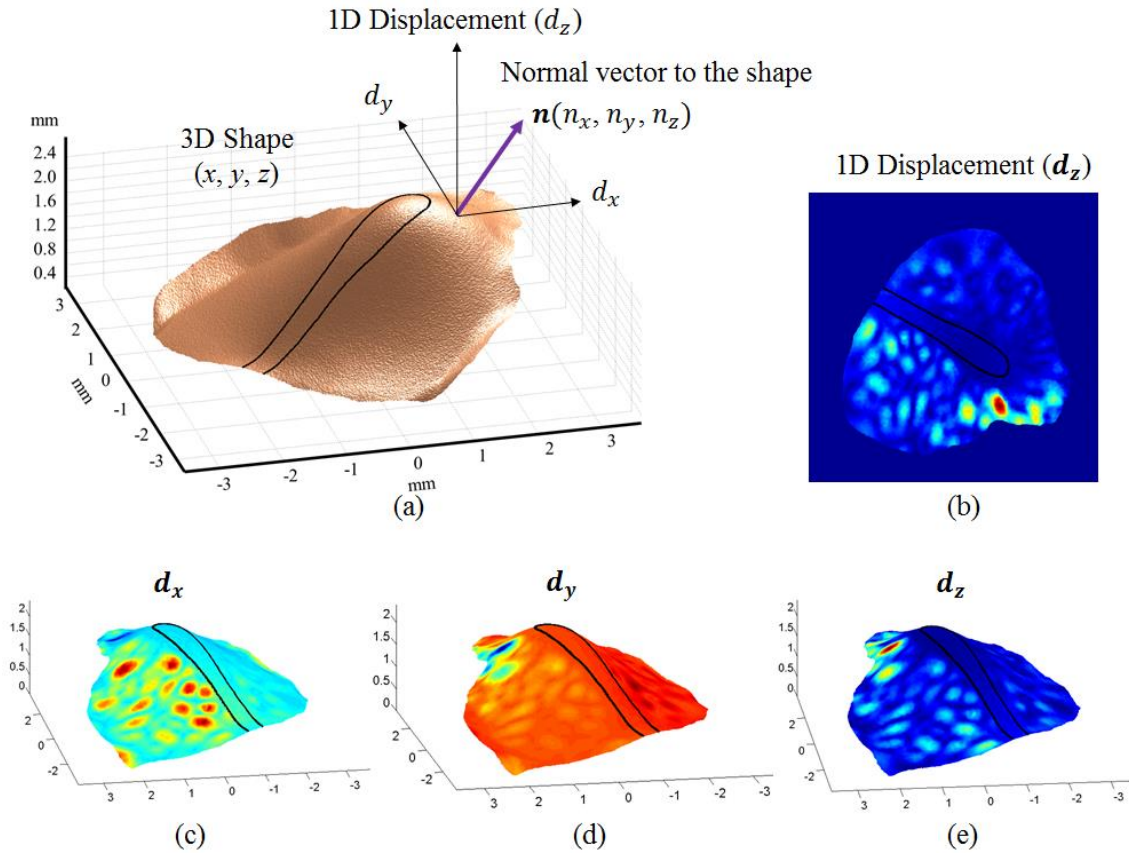


Figure 7.2. Application of thin-shell theory to recover three-dimensional motion components from shape and only 1D motion measurements: (a) shape of the TM to determine surface normal vectors; (b) 1D sound-induced motion measurements of the TM through lateral axis (z-axis); (c), (d), and (e) are recovered x - and y -axes, and measured z -axis sound-induced motion, superimposed on the shape of the TM, respectively. The TM was subjected to tonal frequency of 5,730 Hz at the sound pressure level of 101 dB SPL.

Digital holographic measurements of shape and three-dimensional sound-induced displacements of tympanic membrane

Morteza Khaleghi

Weina Lu

Ivo Dobrev

Worcester Polytechnic Institute
Center for Holographic Studies and Laser
micro-mechaTronics
Worcester, Massachusetts 01609
and
Worcester Polytechnic Institute
Mechanical Engineering Department
Worcester, Massachusetts 01609
E-mail: mkm@wpi.edu

Jeffrey Tao Cheng

Massachusetts Eye and Ear Infirmary
Eaton-Peabody Laboratory
Boston, Massachusetts 02114
and
Harvard Medical School
Department of Otolaryngology
Boston, Massachusetts 02114

Cosme Furlong

Worcester Polytechnic Institute
Center for Holographic Studies and Laser
micro-mechaTronics
Worcester, Massachusetts 01609
and
Worcester Polytechnic Institute
Mechanical Engineering Department
Worcester, Massachusetts 01609
and
Massachusetts Eye and Ear Infirmary
Eaton-Peabody Laboratory
Boston, Massachusetts 02114
and
Harvard Medical School
Department of Otolaryngology
Boston, Massachusetts 02114

John J. Rosowski

Massachusetts Eye and Ear Infirmary
Eaton-Peabody Laboratory
Boston, Massachusetts 02114
and
Harvard Medical School
Department of Otolaryngology
Boston, Massachusetts 02114

Abstract. Acoustically induced vibrations of the tympanic membrane (TM) play a primary role in the hearing process, in that these motions are the initial mechanical response of the ear to airborne sound. Characterization of the shape and three-dimensional (3-D) displacement patterns of the TM is a crucial step to a better understanding of the complicated mechanics of sound reception by the ear. Sound-induced 3-D displacements of the TM are estimated from shape and one-dimensional displacements measured in cadaveric chinchillas using a lensless dual-wavelength digital holography system (DWDHS). The DWDHS consists of laser delivery, optical head, and computing platform subsystems. Shape measurements are performed in double-exposure mode with the use of two wavelengths of a tunable laser, while nanometer-scale displacements are measured along a single sensitivity direction with a constant wavelength. Taking into consideration the geometrical and dimensional constraints imposed by the anatomy of the TM, we combine principles of thin-shell theory together with displacement measurements along a single sensitivity vector and TM surface shape to extract the three principal components of displacement in the full-field-of-view. We test, validate, and identify limitations of this approach via the application of finite element method to artificial geometries. © The Authors. Published by SPIE under a Creative Commons Attribution 3.0 Unported License. Distribution or reproduction of this work in whole or in part requires full attribution of the original publication, including its DOI. [DOI: [10.1117/1.OE.52.10.101916](https://doi.org/10.1117/1.OE.52.10.101916)]

Subject terms: digital holography; middle-ear mechanics; shape and three-dimensional displacement measurements; sound-induced response; thin-shell theory; tympanic membrane.

Paper 130200SS received Feb. 5, 2013; revised manuscript received Jun. 24, 2013; accepted for publication Jun. 26, 2013; published online Jul. 17, 2013.

1 Introduction

The tympanic membrane (TM) is an essential part of the terrestrial vertebrate middle ear. Its function as an acousto-mechanical transformer greatly increases the sensitivity of the ear to sound.¹ Despite the importance of the TM, the relationship between its structure and its sound-reception

function is not fully understood. Current methodologies for characterization of TM function in the laboratory and clinic have limitations: time-averaged holography is qualitative rather than quantitative, laser-Doppler vibrometry is usually limited to single-point (or a series of single-point) measurements of mobility, and most measurement techniques

only measure displacements along a single direction. Furthermore, none of the current clinical tools for diagnosis of hearing losses measure the shape of the TM and the question of how shape affects function is an open question.²

The shape of the TM has been measured by different optical techniques (e.g., Moiré interferometry^{3,4,5} and fringe projection⁶). However, the temporal resolution and sensitivity of such three-dimensional (3-D) shape measurements are usually not sufficient to accurately measure the sound-induced motions of the TM. The lack of an accurate tool for simultaneous measurements of shape and 3-D vibrations of the TM is problematic. Conventional methods to measure the full-field 3-D displacements of the TM need at least three illumination or observation directions to realize three sensitivity vectors.^{7,8} In this paper, a new technique is proposed to determine the full-field 3-D displacement components of the TM based on its shape and one-dimensional (1-D) displacement measurements.^{2,9} The shape of the TM is measured by a lensless dual-wavelength digital holography system (DWDHS) that uses a tunable near-infrared laser. Concurrently, 1-D displacement measurements of acoustically induced motion of the TM are obtained by stroboscopic holography with a single laser wavelength and parallel illumination-observation recording geometry. Decomposing the shape's normal vector at each point on the surface of the TM into three orthogonal axes, combining the shape information with the 1-D displacement at each point on the surface of the TM, and taking advantage of thin-shell theory principles allow estimation of the full 3-D displacement at each point on the surface of the TM. Therefore, a single, compact otoscope system could determine both the shape and 3-D acoustically induced displacement components of the TM.

2 Theoretical Considerations

2.1 TM as a Thin-Shell

The shape, planar dimensions, and thickness of the TM vary among various vertebrate species.¹⁰ For human TM, Uebo et al.¹¹ measured mean thickness values between 50 and 150 μm in several TMs of humans of different ages. Ruah et al.¹² measured thicknesses at different regions of several TMs of humans aged between two days and 91 years. In adults the thickness varied between individuals and within regions: the pars flaccida varied from 80 to 600 μm , the posterosuperior pars tensa from 100 to 500 μm , posteroinferior tensa from 20 to 200 μm , anterosuperior tensa from 50 to 340 μm , anteroinferior tensa from 30 to 430 μm , and the umbo from 820 to 1700 μm . Decraemer and Funnell¹⁰ measured the thickness of the TM of three different species, including cats, gerbils, and humans, by confocal microscopy. For cats, the measured thickness was 12.5 to 60 μm ; for gerbils, 7 to 70 μm ; and for humans, 115 to 145 μm . Aernouts et al.¹³ measured the thickness of the human TM by confocal microscopy and found variations between 97 and 110 μm .

Can we think of the TM as a thin-shell? Novozhilov¹⁴ developed an engineering criterion that classifies a shell as thin if the following condition is satisfied:

$$\max\left(\frac{h}{R}\right) \leq 0.05, \quad (1)$$

where h is the thickness of the shell and R its radius of curvature. For chinchilla TM, a radius of curvature of 3.95 mm

is obtained by the method proposed by Funnell.¹⁵ In all of the references cited in this paper this ratio is much smaller than 0.05, except around the manubrium, where the membrane is thicker; therefore, we modeled as a thin-shell.

According to plate and shell theory, and specifically considering Kirchhoff's assumptions,¹⁶ in an elastic, homogenous, and isotropic thin-shell, where the displacement at any point of the shell is small compared with the thickness of the shell, (1) the displacement at any point on the surface of the membrane is perpendicular to the middle surface of the membrane and remains normal to it during and after deformation and (2) there is no displacement tangent to the surface of the membrane.

Although the TM is not strictly homogenous and isotropic, it is often approximated as such.¹⁰

2.2 Lensless Digital Holography

Digital holography enables quantitative measurements of shape and displacements of objects by recording holograms with digital cameras and reconstructing them numerically. This allows imaging and focusing capabilities at arbitrary locations without the need of optical lenses and corresponding mechanisms. The Fresnel-Kirchhoff integral, Eq. (2), is used for holographic numerical reconstruction.^{17,18}

$$\Gamma(\xi, \eta) = \frac{i}{\lambda} \iint_{-\infty}^{+\infty} h(x, y) R(x, y) \frac{\exp\left(-i \frac{2\pi}{\lambda} \rho\right)}{\rho} \times \left(\frac{1}{2} + \frac{1}{2} \cos \theta\right) dx dy, \quad (2)$$

$$\rho = \sqrt{(x - \xi)^2 + (y - \eta)^2 + d^2}, \quad (3)$$

where λ is the wavelength of the laser, $h(x, y)$ is the complex hologram function, $R(x, y)$ is the complex amplitude distribution of the reference wave used for the reconstruction, ρ , which is expanded in Eq. (3), is the distance between a point on the hologram plane (x, y) and a point in the reconstruction plane (ξ, η) , and d is the reconstruction distance. The DWDHS discretizes and digitizes the function $\Gamma(\xi, \eta)$ in Eq. (2) to the form of Eq. (4), by sampling the hologram function $h(x, y)$ on a CCD sensor of $M \times N$ pixels.

$$\Gamma(m, n) = \frac{i}{\lambda d} \exp\left[-i\pi\lambda d \left(\frac{m^2}{M^2\Delta x^2} + \frac{n^2}{N^2\Delta y^2}\right)\right] \times \sum_{k=0}^{M-1} \sum_{l=0}^{N-1} h(k, l) R(k, l) \times \exp\left[-i \frac{\pi}{\lambda d} (k^2\Delta x^2 + l^2\Delta y^2)\right] \times \exp\left[i2\pi\left(\frac{km}{M} + \frac{ln}{N}\right)\right], \quad (4)$$

where m and n are coordinates in the reconstruction plane, k and l are coordinates in the CCD plane, M and N are number of pixels of the CCD sensor, and Δx and Δy are the pixel dimensions. Figure 1 illustrates numerical reconstructions at specific distances from the CCD sensor of a digitally

recorded hologram corresponding to a chinchilla TM stimulated with a tone of 7 kHz at 91 dB sound pressure level (SPL).

2.2.1 Shape measurements by dual-wavelength digital holography

A two-wavelength holographic contouring technique is applied to generate depth contours related to the geometry of the TM. The technique is based on the utilization of a coherent polarized light source with wavelength tuning capabilities.²⁰ The technique requires acquisition of a set of optical amplitude and phase information at wavelength λ_1 , the reference state, as well as acquisition of a second set of amplitude and phase information at wavelength λ_2 , the deformed state. Interferometric depth contours, related to the geometry of the TM under investigation, are generated by speckle phase correlation of two sets of phase-stepped speckle intensity patterns.

The phase difference of the two corresponding sets of data $\Delta\phi$ is given by

$$\Delta\phi = \phi_2 - \phi_1 = \frac{2\pi}{\Lambda} \text{OPL}, \quad (5)$$

where ϕ_1 is the phase of the optical path length recorded at the first wavelength λ_1 , ϕ_2 is the phase of the optical path length recorded at the second wavelength λ_2 , OPL is the optical path length defined as the distance from the illumination point to an object point and to an observation point, and Λ is the synthetic wavelength given by

$$\Lambda = \frac{\lambda_1 \lambda_2}{|\lambda_1 - \lambda_2|}. \quad (6)$$

From Eq. (6), it is clear that the smaller the difference between the two wavelengths used, the larger the synthetic wavelength and, consequently, the smaller the optical phase difference.

In two-wavelength contouring, the phase difference, $\Delta\phi$, is a discontinuous wrapped function varying in the interval $[-\pi, \pi]$; thus phase unwrapping algorithms are applied to obtain a continuous phase distribution called the fringe-focus function, $\Omega(x, y)$, for calculation of the relative height of each point on the surface of the object $Z(x, y)$ with

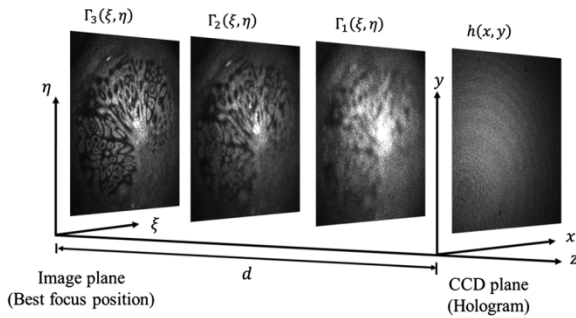


Fig. 1 Recording and numerical reconstruction of a digital hologram at specific distances from the CCD detector. Numerical reconstruction, performed at video rates, enables imaging and focusing capabilities without the need of optical elements. The object of interest is a chinchilla TM stimulated with a tone of 7 kHz at 91 dB SPL.¹⁹

$$Z(x, y) = \frac{\Omega(x, y) * \Lambda}{4\pi}. \quad (7)$$

If the angle between illumination and the observation directions, θ , is zero, the distance between two consecutive contours is

$$\Delta z = \frac{\Lambda}{1 + \cos(\theta)} = \frac{\Lambda}{2}. \quad (8)$$

2.2.2 Full-field three-dimensional displacement measurements

Conventional methods for measurement of 3-D displacements of objects by holographic interferometry use at least three illumination points or three observation points to define three sensitivity vectors. We describe a new method that utilizes measurements of the 1-D sound-induced displacements along the optical (z) axis together with the 3-D decompositions of shape information into surface normal vectors to calculate the displacements in the other two orthogonal directions (x and y). Figure 2 illustrates the algorithm we applied to compute the 3-D displacement maps.

A double-exposure stroboscopic mode is used for quantitative measurements of displacements between two loading states. In stroboscopic holography mode, the computed optical phase change, which is related to displacement, is based on the difference between measurements corresponding to

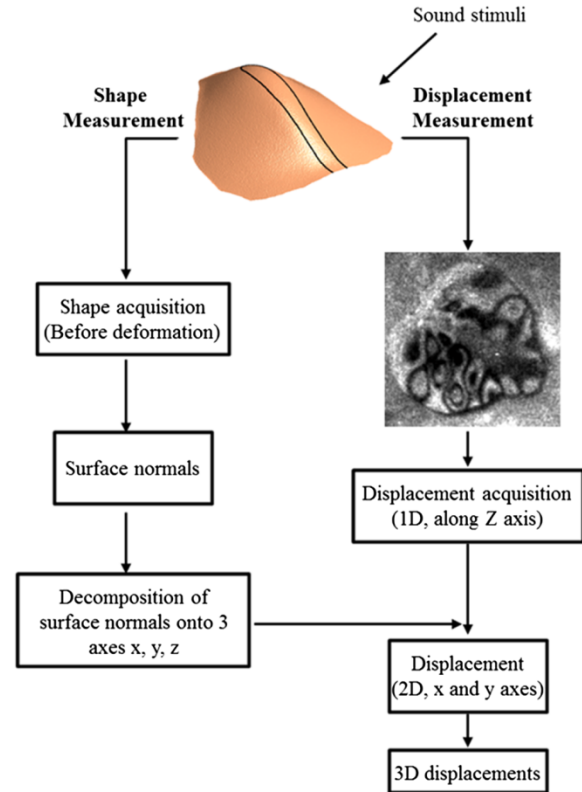


Fig. 2 Algorithm used to extract 3-D components of displacement by measurements of shape and one component of displacement.

two different stimulus phases, where the phases are defined by the pulsing of the “strobe switch” (an acousto-optic modulator capable of high-frequency switching) that is phase-locked to the acoustic stimulus. In our measurements, the sinusoidal motion of the TM driven by a tone was determined from holograms of the TM that were gathered during strobed laser pulse illumination at each of eight evenly spaced stimulus phases ($\varnothing = 0, \frac{\pi}{4}, \frac{\pi}{2}, \dots, \frac{7\pi}{4}$). Each laser pulse has a duration of 5 to 10% of the period of the tonal stimulus. The result gives a difference between the two states in the form of a wrapped phase map. By considering our parallel illumination-observation experimental setup, only out-of-plane displacements along the optical axis can be measured. DWDHS records four images containing holographic patterns that result from the phase-shifting of the reference beam in steps of multiples of $\pi/2$, at both reference and deformed states. The intensities at each pixel measured by the camera at each of the four reference phase steps are I_1, \dots, I_4 in the reference state and I'_1, \dots, I'_4 in the deformed state. The optical phase difference between these two states is

$$\Omega(x, y) = \tan^{-1} \left[\frac{(I_1 - I_3)(I'_4 - I'_2) - (I_4 - I_2)(I'_1 - I'_3)}{(I_1 - I_3)(I'_1 - I'_3) + (I_4 - I_2)(I'_4 - I'_2)} \right], \quad (9)$$

which enables the measurements of out-of-plane displacement by

$$U_z(x, y) = \frac{\Omega(x, y) * \lambda}{4\pi}. \quad (10)$$

The hypothesis that the major components of acoustically induced displacements occur along the local surface normal of the TM makes it possible to recover the two principal components of TM motion in the plane of the tympanic ring, \vec{U}_x and \vec{U}_y , in a Cartesian coordinate system defined by the corresponding sensitivity vector, as shown in Fig. 3. Specifically, single-axis measurements, \vec{U}_z , together with the knowledge of shape normal vectors, $\vec{n}(\vec{n}_x, \vec{n}_y, \vec{n}_z)$, enable estimation of the two additional corresponding orthogonal components of displacement, \vec{U}_x and \vec{U}_y , with

$$\vec{U}_x = \vec{n}_x \frac{|\vec{U}_z|}{|\vec{n}_z|}, \quad (11)$$

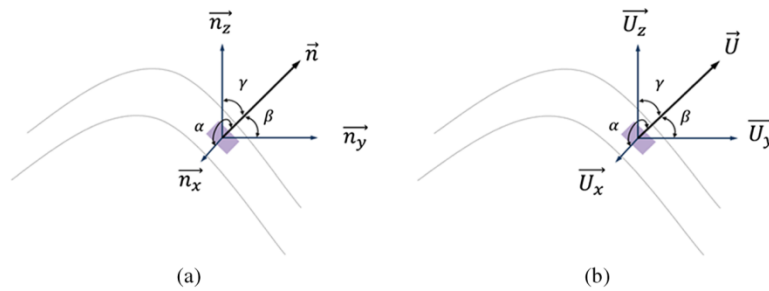


Fig. 3 Decomposition of the surface normal vector and resultant displacement at one point: (a) \vec{n} is the surface normal vector and \vec{n}_x, \vec{n}_y , and \vec{n}_z are decomposed components of \vec{n} along x, y and z axes. (b) \vec{U} is the resultant displacement and \vec{U}_x, \vec{U}_y , and \vec{U}_z are decomposed components of \vec{U} along x, y and z axes. α, β , and γ are the angles between the direction of \vec{U} or \vec{n} and the x, y, z axes.

$$\vec{U}_y = \vec{n}_y \frac{|\vec{U}_z|}{|\vec{n}_z|}. \quad (12)$$

As illustrated in Fig. 3, angles between displacement in x, y, z directions and the resultant displacement are the same as angles between the normal vectors in x, y, z directions and the normal vector.

2.3 Test of the Proposed Approach

In order to test our approach, a finite element method (FEM) modal analysis of an ideal semi-spherical membrane with physical properties similar to those of a TM is implemented and the results imported and processed in MATLAB. Figure 4 shows the test procedures, while the geometry, mechanical properties, and modeling parameters incorporated into the finite element analysis (FEA) model analyses are listed in Table 1.

Outputs of the FEM modal analysis are the resultant displacement, \vec{U}_{res} , as well as displacement along the x, y and z axes. By taking the fourth mode of vibration, for example, and by applying Eqs. (11) and (12), the two additional displacements \vec{U}_x and \vec{U}_y are calculated and plotted in Fig. 5.

A significant criterion used in the testing of our approach is the computation of the differences between the displacements obtained from the FEM analysis and the predicted components based on the thin-shell hypothesis. These differences are shown in Fig. 6. Because of the nature of the eigenvectors obtained by FEM, data from each FEM solution and prediction are normalized by the maximal displacement value on the TM surface.

Table 2 shows the root mean square (RMS) and standard deviation of the differences between FEM and predicted displacements averaged over the surface for different modes of vibration after data normalization. The results show that the RMS difference and the standard deviation around the mean is less than 5%, which indicates that the predicted x and y displacement components obtained by our approach are well matched by the displacements obtained by FEM analysis.

3 Experimental Procedures

3.1 Digital Optoelectronic Holography System

The lensless DWDHS consists of laser delivery (LD), optical head (OH), and computing platform (CP) subsystems. The LD subsystem contains a tunable near-infrared diode laser

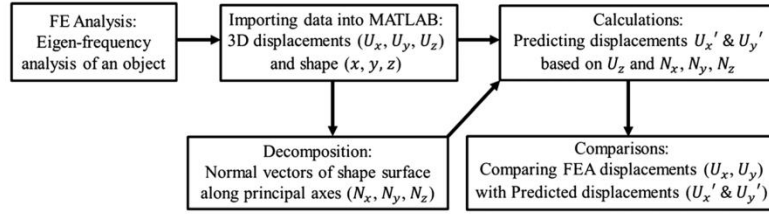


Fig. 4 Procedure for testing our approach by FEM simulations.

Table 1 Geometry, mechanical properties, and FEM parameters of the semi-spherical test object.

Geometry		Mechanical properties		FEA parameters	
Spherical radius	2.5 mm	Young's modulus	60 MPa	No. of nodes	15,697
Thickness	30 μ m	Poisson's ratio	0.33	No. of elements	7747
		Mass density	1100 kg/m ³		

Note: Boundary conditions: fully constrained along entire perimeter.

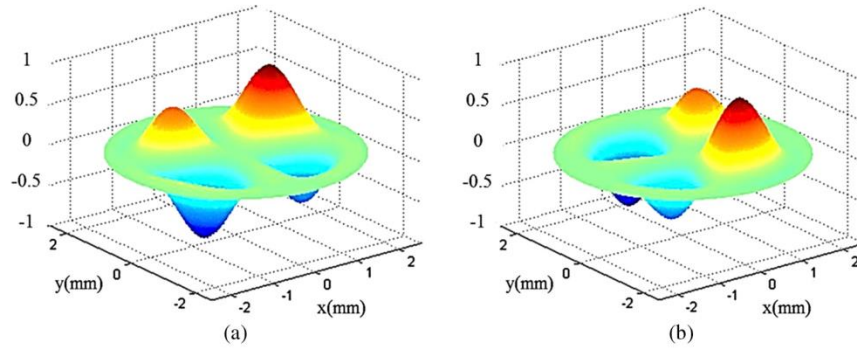


Fig. 5 Computed x and y components of displacements obtained by applying our approach: (a) Predicted displacement along x -axis (\bar{U}_x). (b) Predicted displacement along y -axis (\bar{U}_y).

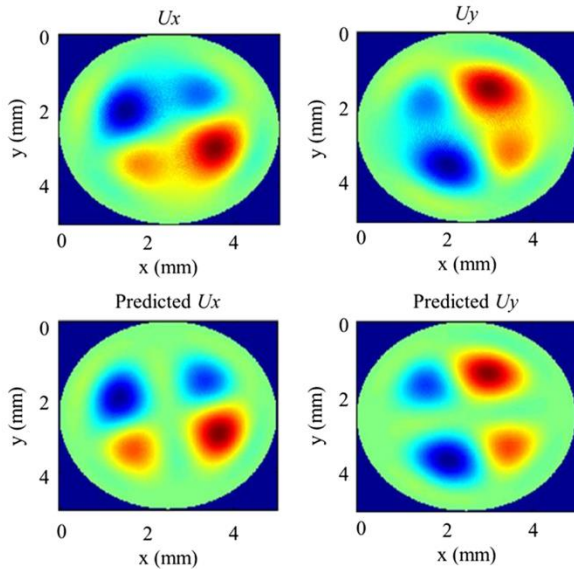


Fig. 6 Comparisons of x and y components of displacements between FEM solutions (U_x and U_y) and predictions obtained by our approach after data normalization.

in the range from 770 to 789 nm with a central wavelength of 779 nm, an anamorphic prism pair, an acousto-optic modulator, a half-wave plate, and a fiber coupler assembly. The output of LD is delivered to the OH directly. The OH was designed using 3-D optical ray tracing simulations, in which selected components are rotated in specific angles to overcome reflection issues.²¹ A 5 megapixel (2452×2054 pixels) digital camera with pixel size of 3.45 by 3.45 μ m² in OH is used for image recording at high rates, while the CP acquires and processes images in either

Table 2 Root mean square (RMS) and standard deviation (SD) of the difference between FEM solutions and predictions for different modes of vibration for the ideal semi-spherical test object.

Difference		Mode 1	Mode 2	Mode 3	Mode 4
x	RMS (%)	3.08	3.52	3.18	0.71
	STD (%)	3.10	4.18	2.91	0.90
y	RMS (%)	3.11	3.38	3.52	0.71
	STD (%)	3.12	3.07	4.30	0.91

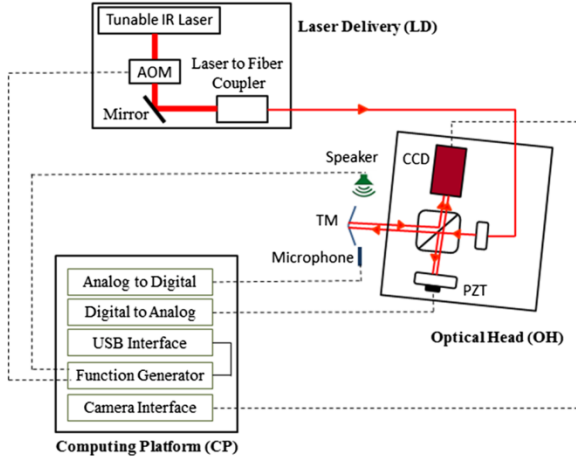


Fig. 7 Schematic views of different subsystems of our DWDHS. Laser delivery consists of an infrared tunable laser, acousto-optic modulator, mirror, and laser to fiber coupler; optical head contains a modulator, Michelson interferometer; and computing platform controls the recording parameter such as sound-excitation level and frequency, phase-shifting, synchronizations for stroboscopic measurements and all the acquisition parameters. The dashed lines are analog signal lines and digital control and sense lines.

time-averaged or double-exposure modes.²² Figure 7 shows the major components of the DWDHS.

3.2 Design of Optical Head Subsystem

The OH subsystem is based on a Michelson optical configuration, shown in Fig. 8. The input to the interferometer is a single-mode polarization-maintaining fiber terminated with an fiber-optic connector/angled physical contact connector that attaches to a collimator (C) producing a circular beam of 7.1 mm diameter. The collimated beam is directed to a nonpolarizing broadband (700 to 1100 nm) beam splitter cube (BC) that splits the light into reference and object

beams. A neutral density filter (NDF) and a linear polarizer (P) are embedded on the optical path of the reference beam to control the beam ratio; the ratio has an optimal value between 2 and 5 and depends on the reflectivity of the tested sample. NDF provides coarse adjustment and the P fine adjustment. There are no components in the optical path of the object beam since we utilize lensless digital holographic methods. The reflected reference and object wavefronts are combined at the CCD sensor and a piezoelectric transducer is used for temporal phase-shifting.

In our initial OH configurations, we observed that the BC can introduce significant internal reflections that affect the quality of the reconstructed digital holograms. Therefore, the geometry of the interferometer was modified by applying rotations to some of the components within the optical path of the reference beam in order to identify a suitable optical configuration. In Fig. 8, the original axis describing the location of all parts is shown by the vertical dotted line. The BC was rotated by an angle of α with respect to the vertical axis, and the mirror, M , and CCD camera were rotated by 2α in order to maintain the mirror and the camera parallel to each other. The angle α was changed from -18 to $+18$ deg in 2-deg increments. The resultant numerically reconstructed^{23,24} digital holograms obtained after applying these rotations are shown in Fig. 9. Selected images with interference fringes generated on a conical metal object for shape measurements are shown. Marks on the object were introduced to help numerical focusing of the object. While significant reflections degraded the holograms measured at α between $+18$ and -18 deg, good quality, low-reflection holograms were obtained at larger angles. By quantifying image intensity and contrast, it was determined that 14 deg was a suitable choice.

3.3 Sound Generation and Measurement

In displacement measurement experiments, the TM is excited by a sound source. The sinusoidal output of the function generator was amplified by a unity gain power amplifier and used to drive a dynamic speaker coupled to an inverted

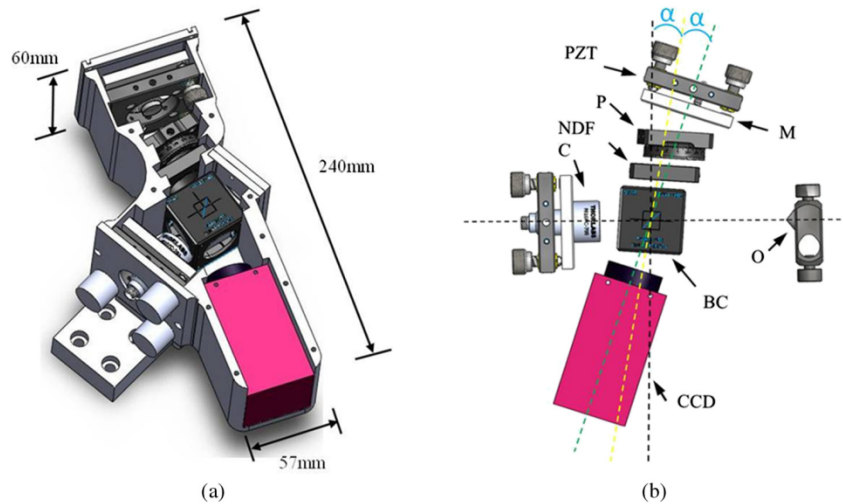


Fig. 8 Computer aided design (CAD) models of the designed and implemented optical head: (a) Assembled package showing characteristic dimensions. (b) View showing its principal components. PZT, piezoelectric transducer; M , mirror; p , linear polarizer; NDF , neutral density filter; BC , beam splitter cube; CCD , digital camera; C , collimating lens with fiber-optic (FC) connector for optical fiber input; and O , object.

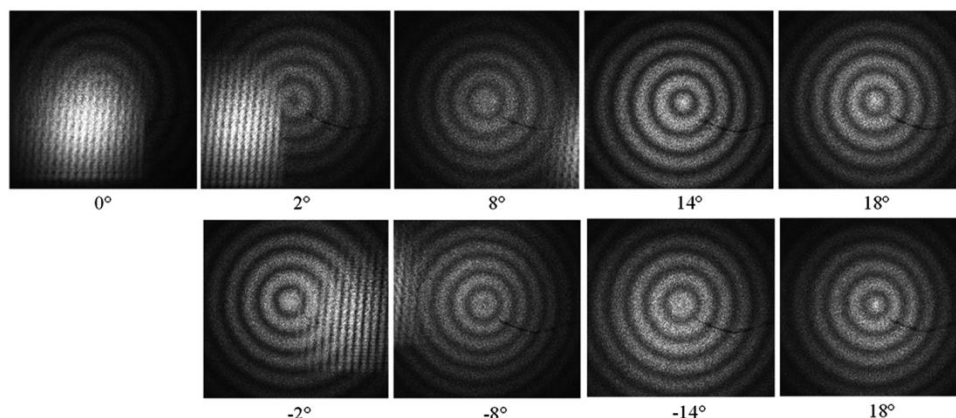


Fig. 9 Comparison of interferogram quality corresponding to different optomechanical configurations used during optimization of the OH by changing the incident angle of the BC. The configuration corresponding to 14 deg rotation was chosen in the final configuration.

horn. The narrow mouth of the horn was positioned about 8 cm away from the TM. A PCB Piezotronics (Depew, New York) prepolarized 1/4-inch microphone with a calibrated probe tube was positioned just at the edge of the TM to measure the SPL. In the experiments, sinusoidal sound stimuli varied in frequency from 414 to 10,000 Hz with levels between 70 and 120 dB SPL.

3.4 Sample Preparation

The heads of chinchillas used in other physiological experiments were harvested from dead animals. The bilateral bullae were exposed and the bullar walls partially removed to expose the tympanic cavity. The cartilaginous ear canals were resected, and the bony external auditory canals were drilled away until 80 to 90% of the TM surface was visible.^{9,25} When using laser imaging, it is essential that the surface upon which the beams are emitted is reflective enough to produce a good clean image. Due to the translucent nature of the TM, the surface of the membrane needs to be coated with a suitable material to increase the light reflection from

the surface. While there are many chemical compounds that could be used to paint the TM, most are unsuitable due to concerns and limitations regarding what is permissible for future use in the human TM.²⁶

First, the coating must not be toxic or cause any inflammation or irritation to the skin. Second, there must be a safe method for applying and removing the coating. Beyond health concerns, there are also concerns about what impact the coating will have on the results of the experiments. If the coating is too thick or too rigid, it may affect how the membrane vibrates, leading to incorrect measurements.²⁷ Third, the coating needs to be highly reflective, specifically within the wavelength region of the laser that is used during the experiments (780 nm). Last, the coating needs to be evenly distributed on the membrane, as any large-scale unevenness could alter the vibration patterns or the quality of the reflected light.²⁶ Based on literature²⁸ and the experience from physicians and researchers at the Massachusetts Eye and Ear Infirmary, zinc oxide (ZnO) was used as paint. ZnO is commonly used in cosmetics, is highly reflective, and is soluble in weak acetic acid for easy removal from

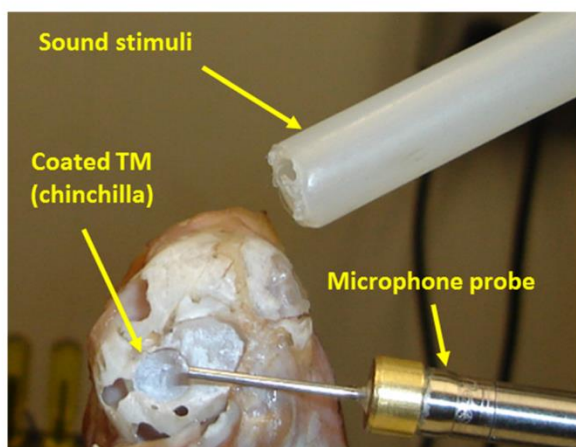


Fig. 10 Chinchilla's TM is coated with zinc oxide to increase light reflection. The TM is shown surrounded by the bone of the middle-ear wall. The placement of the tube conducting sound to the ear and the probe microphone are also illustrated.

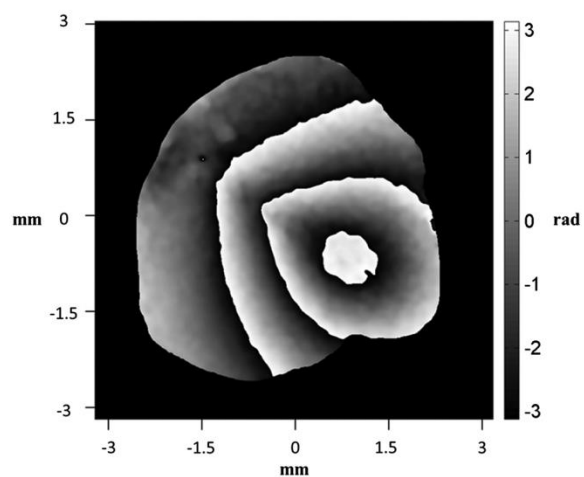


Fig. 11 Masked and filtered wrapped optical phase of the shape of the TM, computed by lensless DWDHS.⁹

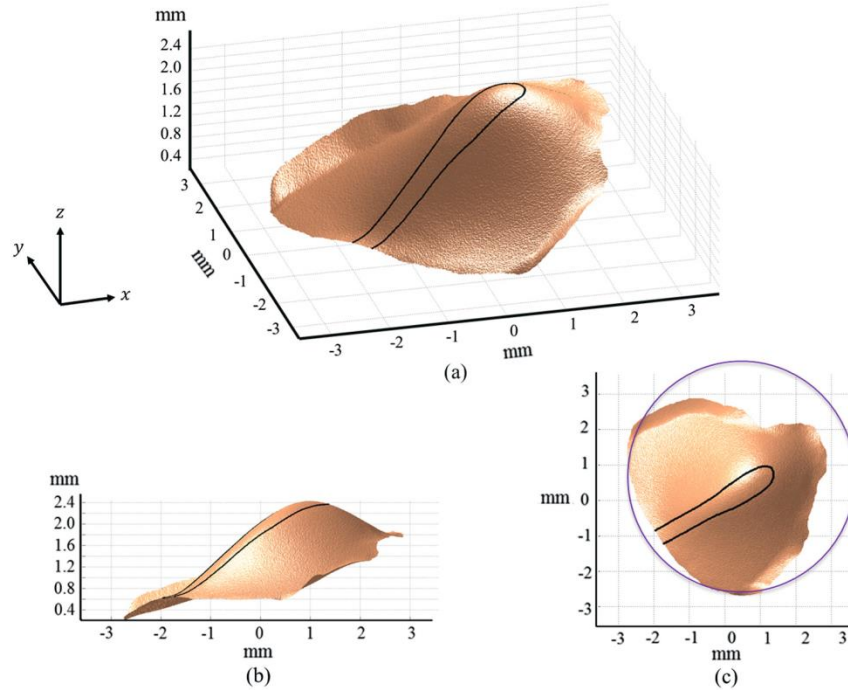


Fig. 12 Measured shape of the TM of a chinchilla: (a) Three-dimensional shape. (b) Two-dimensional side view of the shape. (c) Two-dimensional top view of the shape; the outline of the entire tympanic ring is highlighted by a circle. The outline shows the handle of the malleus (the manubrium). The umbo of the manubrium is at the apex of the TM cone.

the membrane. Figure 10 shows a coated TM of a chinchilla subjected to the sound stimuli in a displacement measurement test.

4 Results

4.1 Shape and Surface Normal Vectors

The shape of a chinchilla’s TM measured by DWDHS is shown in Figs. 11 and 12. Figure 11 shows the masked and filtered wrapped optical phase of the shape of the TM obtained by dual-wavelength double exposure. In these measurements, the first exposure (reference state) was captured at the wavelength of 779.8 nm and the second exposure (deformed state) at 780.2 nm, leading to a synthetic wavelength of 1.52 mm, a little smaller than the depth of the TM cone.

Figure 12 shows the unwrapped scaled image of the optical phase that quantifies the shape of the lateral surface of the TM, where a z value of 0 corresponds to the location of the bony rim that supports the TM and larger z values code a deeper location within the ear. The outline of the handle of the malleus (the manubrium) embedded in the medial surface of the TM is also illustrated. The depth of the membrane (from the umbo to the rim) is about 2.4 mm and the diameter of the membrane is about 7 mm. Because it is not possible to completely remove the bony canal that surrounds the TM, the image does not reconstruct the entire surface; this limitation is most severe at values of $x \in (1:3)$ and $y \in (1:3)$, which correspond to more ventral (inferior) portions of the TM.

The principal components of the surface normal vector along the three orthogonal x , y , and z observation axes

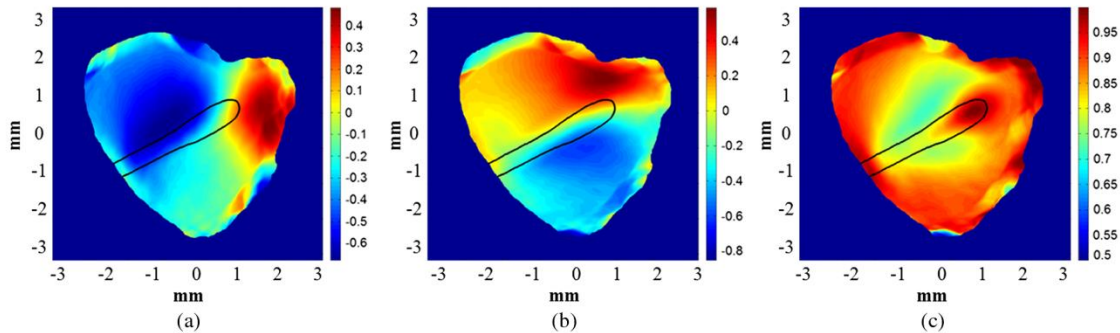


Fig. 13 Principal components of surface normals along x -axis (a), y -axis (b), and z -axis (c).⁹ The outline shows the handle of the malleus (the manubrium).

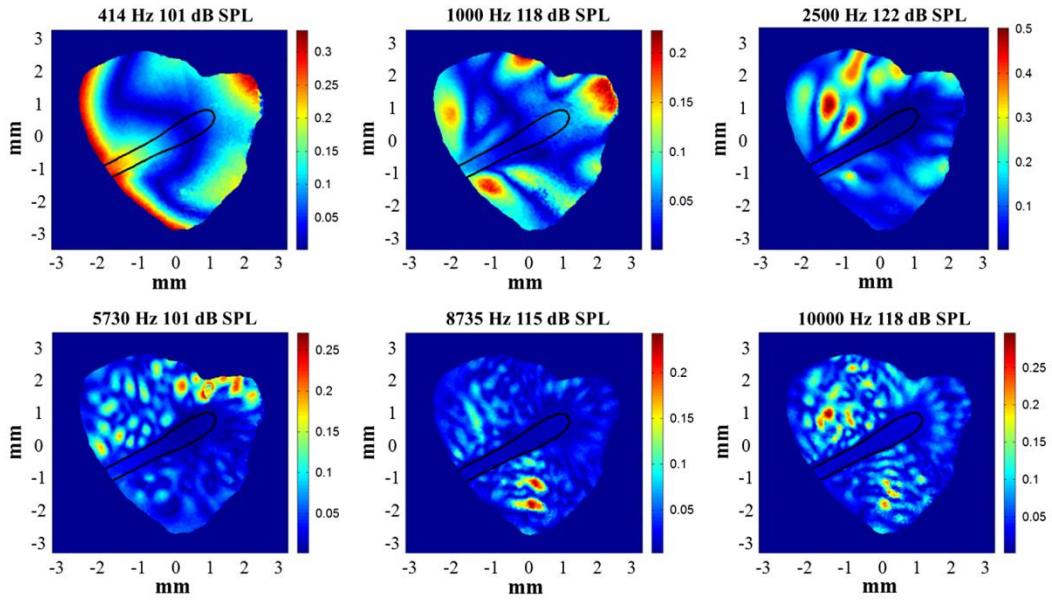


Fig. 14 Out-of-plane or z-axis peak displacements measured at six different frequencies by DWDHS. Displacements are in the unit of μm .⁹

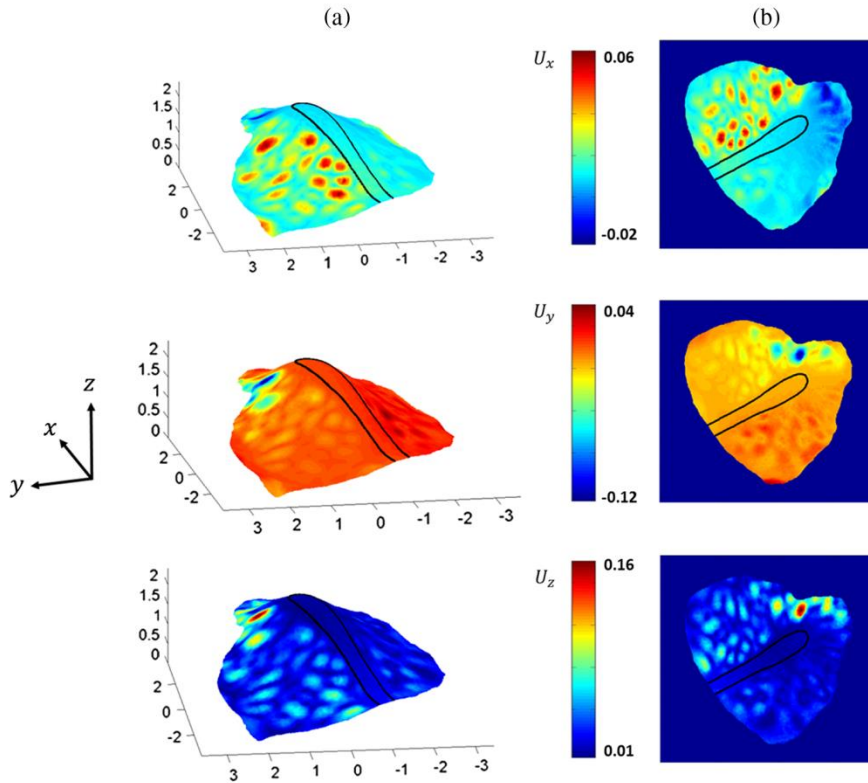


Fig. 15 Principal components of displacement along three orthogonal axes of the TM as obtained by application of our approach. TM was subjected to sound stimuli of 5730 Hz and sound pressure level of 101 dB: (a) 3-D view. (b) 2-D top view. The z axis corresponds to the lateral-medial direction with medial as positive, which was defined by the longitudinal axis of the illuminating and reflected laser beam. The x direction is approximate to the rostral (anterior)-caudal (posterior) axis with rostral positive. The y direction is approximate to the dorsal (superior)-ventral (inferior) direction with ventral positive. Displacements are in the unit of μm .

are obtained by vector decomposition of the surface normal vector as shown in Fig. 3(a). The results of this decomposition are shown in Fig. 13. Since the umbo is located at the apex of the TM cone, the surface at the umbo is nearly parallel to the TM ring and orthogonal to the observation direction that defines the z axis. Therefore, the normal vector at the umbo is dominated by its z -component (z -component near 1, and significantly small x and y components). Also note that the cone-like shape of the TM and the near match between the z -projection and the axis of the cone yields z -components that are all positive, while the x - and y - components may be negative or positive depending on the spatial gradient of the membrane surface in x and y .⁹

4.2 One-Dimensional Displacement Measurements Along One Optical Axis

Sinusoidal continuous sound stimuli were applied to the membrane and the displacements of the surface were recorded and computed at six frequencies of interest: 414, 1000, 2500, 5730, 8735, and 10,000 Hz with SPLs between 100 and 122 dB. The levels were selected to produce measurable sound-induced TM displacements.

Stroboscopic holography was used to measure TM motions. In stroboscopic holography, the acousto-optic modulator contained within the DWDHS strobes the laser, so that the object and the CCD are illuminated by a series of brief pulses. Each pulse is 5 to 10% of the period of each cycle of the acoustic stimulus, and within each camera frame the pulses are locked to a single phase of the stimulus cycle. Each camera image then represents the summed response to a large number of strobe impulses that are all locked to the same stimulus phase. To describe the variations in TM displacement with the phase of the stimulus, a holographic image (each calculated from four images with stepped optical phase of the reference beam) was gathered at each of the eight stimulus phases of either 0, 45, 90...315 deg relative to the zero-crossing of the sinusoidal voltage that drives the earphone.^{29,30}

Figure 14 shows out-of-plane (z -axis) displacements of the TM at different stimulus frequencies. The vibration patterns are categorized based on the sound excitation frequency. The vibrational pattern of 414 Hz is simple, which is characterized by one or two spatial maxima. The vibrational patterns of 1000 and 2500 Hz are complex,²⁵ which are characterized by multiple spatial maxima and minima separated by areas of small displacement. Above 4 kHz, the displacement patterns of chinchilla TM are ordered, which are characterized by many small areas of maximal displacement around the manubrium, with some order to the location of the maxima.

4.3 Recovering the Three Components of Displacement

By applying Eqs. (11) and (12), and the measured z -axis component of displacement (U_z), and taking advantage of the corresponding normal vectors extracted from the measured shape, the x -axis (U_x), y -axis (U_y), and resultant (U_{res}) components of displacement are calculated. To help identify the computed 3-D components of displacement on the TM surface, these displacements are overlaid on the measured 3-D shape of the TM for one of the experiments in which a sound stimulus of 5730 Hz and 101 dB

SPL sound level stimulates the TM, as shown in Fig. 15, which demonstrates that the x and y components of displacement (U_x and U_y) are smaller than the out-of-plane component (U_z). The resultant displacement has a maximum value within the posterior-inferior quadrant of the TM.

5 Conclusions

We presented a new approach to measure 3-D displacements of TM by combining shape information and 1-D components of displacement. Shape and displacement measurements are carried out with a lensless DWDHS, with shape measured in two-wavelengths mode and 1-D displacements measured in single-wavelength mode. The assumptions we used in our computation of the 3-D components of displacement from measured shape and 1-D displacements are based on considering the TM as a thin-shell, so that the principal components of TM vibration are hypothesized to be parallel to the principal components of the normal vectors of the surface of the TM. This approach was tested using FEM models. However, further testing of our approach will be performed in the next steps of this research, including the development of improved FEM models as well as direct measurements of x , y components of displacement by other digital holographic methods that involve speckle correlation and multiple sensitivity vectors. We expect that our efforts toward the development of methodologies for the concurrent measurement of shape and the three components of displacement vectors will lead to realizable full-field-of-view tools for the study of the normal and pathologic middle-ears.

Acknowledgments

This work was supported by the National Institute on Deafness and Other Communication Disorders, the Mass Eye & Ear Infirmary, and the Worcester Polytechnic Institute, Mechanical Engineering Department. We would also like to acknowledge the support of all of the members of the Center for Holographic Studies and Laser micro-mechanics laboratories and particularly of Peter Hefti and Ellery Harrington.

References

1. J. Tonndorf and S. M. Khanna, "The tympanic membrane as a part of the middle ear transformer," *Acta Oto-laryngologica* **71**(1-6), 177-180 (1971).
2. W. Lu, "Development of a multi-wavelength lensless digital holography system for 3D deformations and shape measurements of tympanic membranes," MS Thesis, Mechanical Engineering Department, Worcester Polytechnic Institute (2012).
3. W. F. Decraemer, J. J. J. Dirckx, and W. R. J. Funnell, "Shape and derived geometrical parameters of the adult, human tympanic membrane measured with a phase-shift Moiré interferometer," *Hear. Res.* **51**(1), 107-122 (1991).
4. J. J. J. Dirckx and W. F. Decraemer, "Phase shift Moiré apparatus for automatic 3-D surface measurement," *Rev. Sci. Inst.* **60**(12), 3698-3701 (1989).
5. J. J. J. Dirckx and W. F. Decraemer, "Moiré topography for basic and clinical hearing research," *Rec. Devel. Opt.* **3**, 271-296 (2003).
6. J. Liang, "Determination of the mechanical properties of guinea pig tympanic membrane using combined fringe projection and simulation," MS Thesis, Mechanical Engineering Department, Oklahoma State University (2009).
7. R. J. Pryputniewicz and W. W. Bowley, "Techniques of holographic displacement measurement: an experimental comparison," *App. Opt.* **17**(11), 1748-1756 (1978).
8. M. Khaleghi et al., "3-Dimensional quantification of surface shape and acoustically-induced vibrations of TM by digital holography," in *Proc. FRINGE 2013*, Springer (2013).
9. J. J. Rosowski et al., "Measurements of three-dimensional shape and sound-induced motion of the chinchilla tympanic membrane," *Hear. Res.* **301**, 44-52 (2013).

10. W. F. Decraemer and W. R. J. Funnell, "Anatomical and mechanical properties of the tympanic membrane," in *Chronic Otitis Media. Pathogenesis-Oriented Therapeutic Management*, B. Ars, Ed., pp. 51–84, Kugler Publications, The Netherlands (2008).
11. K. Uebo et al., "Thickness of normal human tympanic membrane," *Ear. Res. Jpn.* **19**, 70–73 (1988).
12. C. B. Ruah et al., "Age-related morphologic changes in the human tympanic membrane," *Arch. Otolaryngol. Head and Neck Surg.* **117**(6), 627–634 (1991).
13. J. Aermouts, J. R. M. Aerts, and J. J. J. Dirckx, "Mechanical properties of human tympanic membrane in the quasi-static regime from in situ point indentation measurements," *Hear. Res.* **290**(1–2), 45–54 (2012).
14. V. V. Novozhilov, *Theory of Thin Elastic Shells*, 2nd ed., P. Noordhoff, Groningen, The Netherlands (1964).
15. W. R. J. Funnell, "A theoretical study of eardrum vibrations using the finite-element method," PhD Thesis, Department of Electrical Engineering, McGill University (1975).
16. A. E. H. Love, "On the small free vibrations and deformations of elastic shells," *Philos. Trans. R. Soc. A* **179**, 491–549 (1888).
17. U. Schnars and W. Jüptner, "Digital recording and numerical reconstruction of holograms," *Meas. Sci. Technol.* **13**(9), 85–101 (2002).
18. E. Kolenovic, C. Furlong, and W. Jüptner, "Inspection of micro-optical components by novel digital holographic techniques," in *Proc. SEM*, pp. 470–475 (2004).
19. I. Dobrev et al., "Digital holographic otoscope for measurements of the human tympanic membrane in-vivo," *Proc. SPIE* **8494**, 849409 (2012).
20. C. Furlong and R. J. Pryputniwicz, "Absolute shape measurements using high-resolution optoelectronic holography methods," *Opt. Eng.* **39**(1), 216–223 (2000).
21. Lambda Research Corporation, *TracePro*, Littleton, MA (2012).
22. E. Harrington et al., "Automatic acquisition and processing of large sets of holographic measurements in medical research," *Proc. SEM* **5**, 219–228 (2011).
23. J. M. Flores-Moreno et al., "Holographic otoscope for nano-displacement measurements of surfaces under dynamic excitation," *Scanning* **33**(5), 342–352 (2011).
24. C. Furlong et al., "Assessing eardrum deformation by digital holography," *J. Biomed. Opt. Med. Imag.* (2013).
25. J. J. Rosowski et al., "Computer-assisted time-averaged holography of the motion of the surface of the tympanic membrane with sound stimuli of 0.4 to 25 kHz," *Hear. Res.* **253**(1–2), 83–96 (2009).
26. S. Goldish et al., "Packaging and optimization of a digital holographic otoscope for clinical use," Major Qualifying Project, Mechanical Engineering Department, Worcester Polytechnic Institute (2010).
27. J. T. Cheng et al., "Wave motion on the surface of the human tympanic membrane: holographic measurement and modeling analysis," *JASA* **133**(2), 918–937 (2013).
28. J. J. J. Dirckx and W. F. Decraemer, "Optoelectronic Moiré projector for real-time shape and deformation studies of the tympanic membrane," *J. Biomed. Opt.* **2**(2), 176–185 (1997).
29. J. T. Cheng et al., "Motion of the surface of the human tympanic membrane measured with stroboscopic holography," *Hear. Res.* **263**(1–2), 66–77 (2010).
30. C. Furlong et al., "Miniaturization as a key factor to the development and application of advanced metrology systems," *Proc. SPIE* **8413**, 84130T (2012).



digital image processing.

Morteza Khaleghi received his MSc degree in mechanical and manufacturing engineering from Iran University of Science and Technology. Currently, he is pursuing his PhD degree at Worcester Polytechnic Institute (WPI), Worcester, Massachusetts. He is a research assistant at the Center for Holographic Studies and Laser micro-mechanics (CHSLT) of WPI. His research interests include developments of 3-D optical metrology systems, medical imaging, and



Weina Lu received her BS degree in environmental engineering from University of Science and Technology Beijing, Beijing, China, in 2009, and her MSc degree in mechanical engineering from WPI, Massachusetts, in 2012. Since then, she has been working at the Wellman Center for Photomedicine at Massachusetts General Hospital in the field of biomedical optics.



Ivo Dobrev received his BS degrees in mechanical engineering and robotics engineering from WPI in Worcester, Massachusetts, in 2009. He is currently a PhD candidate in the mechanical engineering department of WPI. He is a graduate research assistant at the CHSLT of WPI. His research interests include high-speed optical metrology in field environment and *in vivo*, lensless digital holography, shearography, structured light measurements, transient measurements, digital image processing, mechatronics, system design and integration.



Jeffrey Tao Cheng is an instructor in otology and laryngology at Harvard Medical School, working on middle-ear mechanics and tissue biomechanics through measurements and modeling.



Cosme Furlong is an associate professor of mechanical engineering, working in mechanics, optical metrology, and nanoengineering, science and technology.



John J. Rosowski is a professor of otology and laryngology, and also of health sciences and technology, working in acoustics and mechanics of the external, middle, and inner ear, as well as the comparative middle and external ear structure and function.

8. Paper B: Measurements of three-dimensional shape and sound-induced motion of the chinchilla tympanic membrane

Overview

The precise mechanism by which the TM gathers and couples sound-energy to the ossicular system is a continuous point of investigations. In the previous Paper, we hypothesized that the kinematics of the mammalian TMs resemble thin-shells. One incentive for establishing this hypothesis is that the intact human eardrum is located at the end of the ear canal (3 centimeter long and 8 mm in diameter) and application of typical 3D motion measurements techniques (which require at least three different illumination or observation directions) is limited. In this paper, published in *Hearing Research* in 2013, the thin-shell hypothesis is applied to chinchilla TM and the results at multiple tonal excitation frequencies are shown with emphasis on the medical side and importance of the technique. The importance of accurate shape measurements and in turn, the effects of shape local normal vectors on final 3D sound-induced motions are highlighted. One of the limitations of the thin-shell hypothesis is that the relative sizes of the predicted motion components along the x - and y -axes are fixed by anatomy and don't vary with frequency. Furthermore, the thin-shell assumption predicts that motions that occur in the plane of the tympanic ring are either in-phase or half a cycle out of phase with the motions normal to the tympanic ring. Therefore, the need for real 3D sound-induced motion measurements are also highlighted to test and potentially verify the applicability of this hypothesis.



ELSEVIER

Contents lists available at SciVerse ScienceDirect

Hearing Research

journal homepage: www.elsevier.com/locate/heares

Research paper

Measurements of three-dimensional shape and sound-induced motion of the chinchilla tympanic membrane



John J. Rosowski^{a,b,*}, Ivo Dobrev^{c,d}, Morteza Khaleghi^{c,d}, Weina Lu^{c,d},
Jeffrey Tao Cheng^{a,b}, Ellery Harrington^d, Cosme Furlong^{a,b,c,d}

^a Eaton-Peabody Laboratory, Massachusetts Eye and Ear Infirmary, 243 Charles Street, Boston, MA 02114, USA

^b Department of Otology and Laryngology, Harvard Medical School, Boston, MA, USA

^c Department of Mechanical Engineering, Worcester Polytechnic Institute, Worcester, MA, USA

^d Center for Holographic Studies and Laser micro-mechanics, Worcester Polytechnic Institute, Worcester, MA, USA

ARTICLE INFO

Article history:

Received 13 August 2012

Received in revised form

24 November 2012

Accepted 27 November 2012

Available online 13 December 2012

ABSTRACT

Opto-electronic computer holographic measurements were made of the tympanic membrane (TM) in cadaveric chinchillas. Measurements with two laser wavelengths were used to compute the 3D-shape of the TM. Single laser wavelength measurements locked to eight distinct phases of a tonal stimulus were used to determine the magnitude and the relative phase of the surface displacements. These measurements were made at over 250,000 points on the TM surface. The measured motions contained spatial phase variations consistent with relatively low-order (large spatial frequency) modal motions and smaller magnitude higher-order (smaller spatial frequency) motions that appear to travel, but may also be explained by losses within the membrane. The measurement of shape and thin shell theory allowed us to separate the measured motions into those components orthogonal to the plane of the tympanic ring, and those components within the plane of the tympanic ring based on the 3D-shape. The predicted in-plane motion components are generally smaller than the out-of-plane perpendicular component of motion. Since the derivation of in-plane and out-of plane depended primarily on the membrane shape, the relative sizes of the predicted motion components did not vary with frequency.

Summary: A new method for simultaneously measuring the shape and sound-induced motion of the tympanic membrane is utilized to estimate the 3D motion on the membrane surface.

This article is part of a Special Issue entitled "MEMRO 2012".

© 2012 Elsevier B.V. All rights reserved.

1. Introduction

The precise mechanism by which the tympanic membrane (TM) gathers and couples sound energy to the ossicular system is a continuing point of investigation by measurements (e.g. Cheng et al., in press; de La Rochefoucauld and Olson, 2010; Rosowski et al., 2011) and models (Funnell and Laszlo, 1977; Rabbitt and Holmes, 1986; Funnell et al., 1987; Blayney et al., 1997; Gan et al., 2002; Koike et al., 2002; Fay et al., 2005; Parent and Allen, 2007, 2010; Goll and Dalhoff, 2011). Our understanding of this issue is clouded by several significant complications including: (1) the complex nature of the sound-induced TM displacements, (2) many

of the measurements of TM motion are based on optical techniques which are only sensitive to one direction of TM motion, and (3) the conical structure of the TM complicates the relationship between unidirectional measurements of surface motion and the actual three-dimensional motions of the surface of the TM and also suggests complexities in the relationship between TM surface motions and the forces produced along the manubrium at the input to the middle-ear ossicular system.

Several optical techniques have been used to estimate the shape of the TM, as well as changes in TM shape introduced by static pressure (e.g. Moire interferometry: Decraemer et al., 1991; Dirckx and Decraemer 1992, 2001; optical coherence tomography (OCT): Chang et al. in preparation; Ilgner et al. MEMRO 2012). However, the temporal resolution and sensitivity of such three-dimensional measurements are usually not sufficient to measure accurately the sound-induced motions of the TM (an exception is high-speed OCT, e.g. Chang et al. in preparation). In this paper we describe a new technique for near simultaneous measurements of the shape

* Corresponding author. Eaton-Peabody Laboratory, Massachusetts Eye and Ear Infirmary, 243 Charles Street, Boston, MA 02114, USA. Tel.: +1 617 573 4237; fax: +1 617 720 4408.

E-mail address: John_Rosowski@meei.harvard.edu (J.J. Rosowski).

and sound-induced motions of the TM in cadaveric chinchillas. The combination of measurements allows us to estimate the components of the TM that are in-the-plane and out-of-the-plane of the tympanic ring.

2. Methods

2.1. Computer controlled opto-electronic holography

Our basic technique is to capture two-dimensional holographic interference patterns in order to reconstruct holographic images of shape or motion (Hernández-Montes et al., 2009; Flores-Moreno et al., 2011). The measurement methods are based on a tunable near infrared laser beam (adjustable wavelength of 770–789 nm), that is split into reference and object beams within an optical head (Fig. 1). One of the split beams illuminates the measurement object, and the other is a reference beam for which the light path can be shifted by 0, 1/4, 1/2 or 3/4 of a wavelength by a mirrored piezoelectric transducer (the optical path-length shifter). The reference beam and the reflected object beam are recombined to produce an interference pattern that is imaged by a high-speed CCD camera. The camera, laser wavelength and the phase shifting of the reference beam path length are under computer control. The computer uses a 2-D FFT of the images captured at each of the four reference beam path lengths with a numerical holographic reconstruction algorithm to compute the interference pattern at the level of the object (Kolenovic et al., 2004; Flores-Moreno et al., 2011). These interference patterns are gathered with two-different wavelengths to measure shape, or with a single wavelength at different stimulus phases to determine sound-induced motions in the direction of the object illumination beam.

2.2. Measurements of membrane shape: two wavelength mode

Measurements of shape were made by illuminating the TM within a cadaveric chinchilla head with the tympanic ring placed roughly orthogonal to the object beam. With the laser wavelength (λ_1) set at 779.8 nm, the camera gathered two-dimensional images

of the light intensity of the interference patterns at the baseline optical path length (I_0) and with the reference path lengthened by 1/4, 1/2 and 3/4 (I_1, I_2 , and I_3 respectively) by the path-length shifter. The laser wavelength was adjusted to 780.2 nm (λ_2) and images were taken at the four different reference path lengths: I'_0, \dots, I'_3 . The optical phase difference, $\varphi(x,y)$, between the two sets of images was computed:

$$\varphi(x,y) = \tan^{-1} \left[\frac{(I_1 - I_3)(I'_2 - I'_4) - (I_2 - I_4)(I'_1 - I'_3)}{(I_1 - I_3)(I'_1 - I'_3) - (I_2 - I_4)(I'_2 - I'_4)} \right]. \quad (1)$$

This two-dimensional phase image was filtered and masked (Fig. 2), then unwrapped and converted to variations in the depth from the tympanic ring using a synthetic wavelength of

$$\Lambda = \frac{\lambda_1 \lambda_2}{|\lambda_2 - \lambda_1|} = \frac{779.8 \times 780.2}{780.2 - 779.8} = 1.521 \text{ mm}. \quad (2)$$

Because differences in the distance between the object and the optical head affect the path lengths of both the incident and reflected object beams, a 2π change in the wrapped phase is related to a difference in position of $\Lambda/2$, i.e.,

$$z(x,y) = \Lambda \frac{\varphi'(x,y)}{4\pi}, \quad (3)$$

where $\varphi'(x,y)$ is the unwrapped masked and filtered phase.

2.3. Measurements of sound-induced motion: stroboscopic holography

Our techniques for describing the sinusoidal motion of the TM surface at frequencies as high as 20 kHz (Cheng et al., 2010) are summarized here. The laser wavelength was fixed, and a high-speed opto-acoustic modulator (Hernández-Montes et al., 2009) placed in the output beam of the laser to strobe the laser on and off (Fig. 1). The strobe was locked to selected phases of the sound stimulus cycle period with a duty cycle of 5–10% of a period. Strobe measurements were made at eight separate stimulus phases ($0, \pi/$

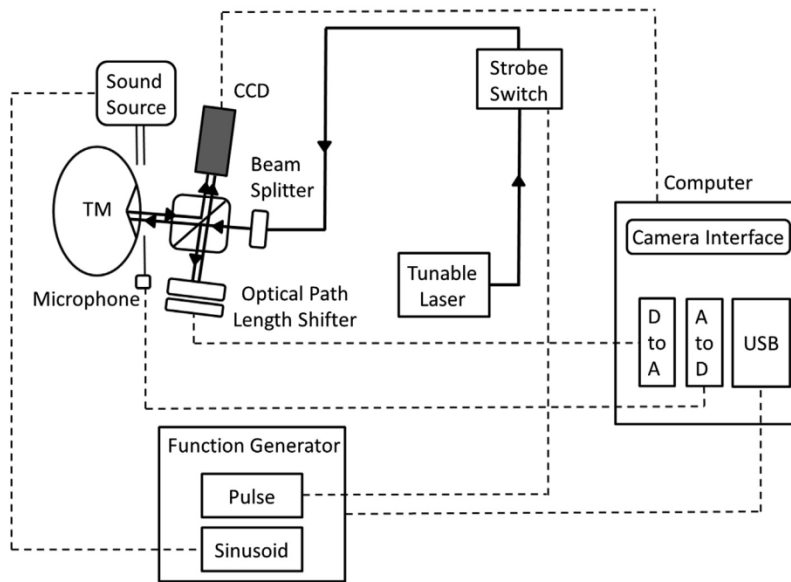


Fig. 1. The tunable laser, strobe switch, optical path length shifter, CCD camera, stimulus and timing generator, earphone, microphone and the measurement control computer. The dashed lines are analog and digital stimulus and sensing lines.

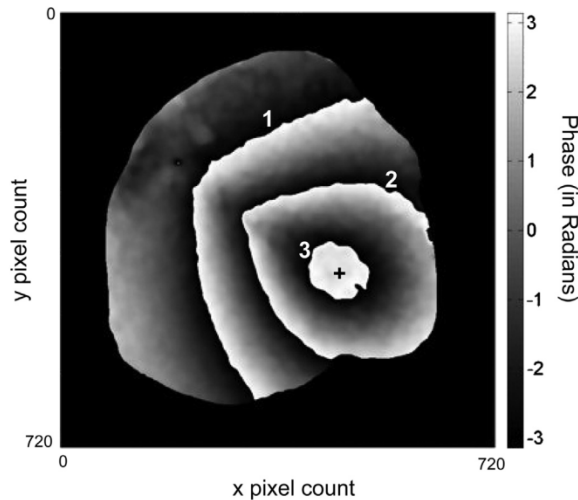


Fig. 2. Masked and filtered wrapped phase image, $\phi(x,y)$, computed from a two-laser shape measurement. The gray scale of each pixel is coded with a value between $+\pi$ and $-\pi$. The three fringe lines (the transitions between black and white that are labeled with white numbers) suggest the total phase change between the outer rim and the apex of the cone (marked by a '+') is just over 6π , and equivalent to a rim to a cone height of $(6\pi/4\pi) \times 1.521$ or 2.28 mm (Equation (3)).

$4, \pi/2, \dots, 7\pi/4$). The changes in optical phase related to the different stimulus phases at each of the 720×720 pixels were calculated using Equation (1), the phases patterns in each image were unwrapped and normalized, and the resultant phases converted to displacement using the appropriate laser wavelength (780.2 nm). The position versus stimulus phase functions gathered at each of the camera pixels were Fourier transformed and the magnitude and phase of the fundamental and second harmonic components computed. The magnitude of the second harmonic was always at least 30 dB below the fundamental, except in regions where the motion magnitude was less than the effective 5–10 nm resolution of our measurement system. In order to judge the quality of the Fourier description of the magnitude and angle of the motion at each pixel, we computed the Pearson Product Correlation Coefficient between the measured phasic variations of the motion and the sinusoidal motion reconstructed from the magnitude and angle of the Fourier determined fundamental component of the phasic motion. The square of this correlation R^2 was generally greater than 0.8 except at locations where the magnitude of the measured motions was less than 10 nm.

2.4. Specimen preparation

Measurements were made on thawed chinchilla heads that had been frozen and stored. The time after collection varied between days and months. The ears investigated were the ears contralateral to the experimental ear in single-sided physiological experiments (e.g. Chhan et al., 2013). The cartilaginous external ear canal was removed and the posterior and inferior middle ear cavities were widely opened. The peripheral portions of the bony external canal were drilled away, and much, but not all, of the medial portion of the bony canal were removed. The curved pocket shape of the medial bony ear canal and its complex support within the bones surrounding the middle ear, made it impossible to expose more than 80% of the TM to direct view (with the tympanic ring orthogonal to the illuminating light beam) without damaging the support of the tympanic membrane. An acute view angle gave

access to much of the TM surface, but compromised the sensitivity of our measurements, which are only sensitive to motions in the direction of the illuminating laser beam. In removing the bony ear canal it was usually not possible to maintain the thin dermal layer of the TM that also covered the inside of the bony canal. Finally the TM was painted with a thin layer of a 60 mg/ml of zinc oxide (ZnO) in saline solution.

2.5. Sound generation and measurement

The sinusoidal output of the stimulus generator was amplified by a unity gain power amplifier and used to drive to a dynamic speaker coupled to a reverse elliptical horn based on a Tucker-Davis Technologies (Alachua, FL) CF1 speaker. The sound stimulus left the narrow mouth of the horn, which was positioned about 8 cm away from the TM. A PCB Piezotronics (Depew, New York) pre-polarized $\frac{1}{4}$ inch microphone with a calibrated probe tube was positioned just at the edge of the TM to make measurements of sound pressure magnitude. Our techniques did not enable accurate measurement of the absolute phases of TM motion and sound pressure at the TM. However, our estimates of the relative phase of motion of different locations on the TM surface to the same stimulus are quite accurate (within 0.01 radians) as long as the motion at the TM location is larger than 10 nm.

3. Results

3.1. Shape of the TM

Fig. 3 shows the shape of the TM of a chinchilla taken from a viewing angle that exposed all of the dorsal TM to view and about 1/3 of the ventral half. The z axis of the plots correspond to the lateral medial axis, with medial as positive, and the peak is the location of the spatulated umbo of the chinchilla. The outline of the umbo and the rest of the manubrium are shown in the figure. The depth of the membrane (from the umbo to the rim) is about 2.2 mm. The diameter of the membrane is about 5 mm.

An alternative method for describing the TM shape is to define its surface in terms of the magnitudes of the three Cartesian components that describe the vector normal to the TM surface at each point on the surface (Fig. 4). The shape data were processed by Matlab scripts that identified the plane that was tangent to the surface and the unit vector normal to the surface at each point on the TM $\mathbf{n}(x,y)$. This normal vector could then be broken into three orthogonal Cartesian components n_x , n_y , and n_z (which define the signed magnitudes of the component vectors), with the direction of the z component defined by the optical axis of the measurement system. The roughly conical shape of the TM and the similarity of the normal vector and its z component leads $n_z(x,y)$ to vary only between 0 and +1. However, $n_x(x,y)$, and $n_y(x,y)$ can be either positive or negative depending on the gradient of the surface in either x or y .

3.2. Sound-induced motion of the TM

Examples of the sound induced motion of the TM surface, measured along the optical axis of the laser (which corresponds to the direction of the z component of the normal vector) are illustrated in Fig. 5. The motion response at all frequencies shows significant variations in the motion at different locations, and the spatial complexity of the motion response increases with increasing frequency. While the use of our techniques with human cadaveric material has yielded good matches with umbo displacement measurements made with different techniques (e.g. Rosowski et al., 2011), the absolute value of the umbo

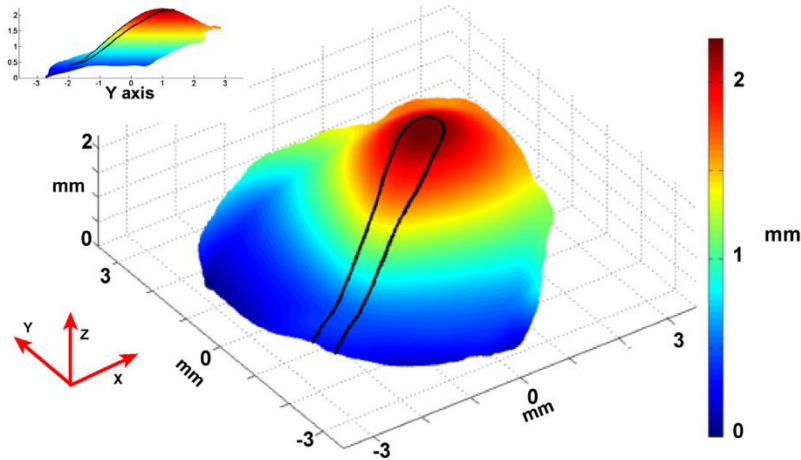


Fig. 3. A reconstruction of the shape of a chinchilla TM. The z axis corresponds to the lateral–medial direction with medial as positive that was defined by the longitudinal axis of the illuminating and reflected laser beam. The x direction corresponds roughly to the rostral (anterior)–caudal (posterior) axis with rostral positive. The y direction corresponds roughly to the dorsal (superior)–ventral (inferior) direction with ventral positive. The black outline shows the connection of the TM to the manubrium of the malleus. The umbo of the manubrium is at the apex of the TM cone, which is colored deep red. The ventral (inferior) edge of the TM is hidden from view by a significant remnant of the bony ear canal. The inset in the upper left corner shows a 2-dimensional view of the TM looking along the x-axis.

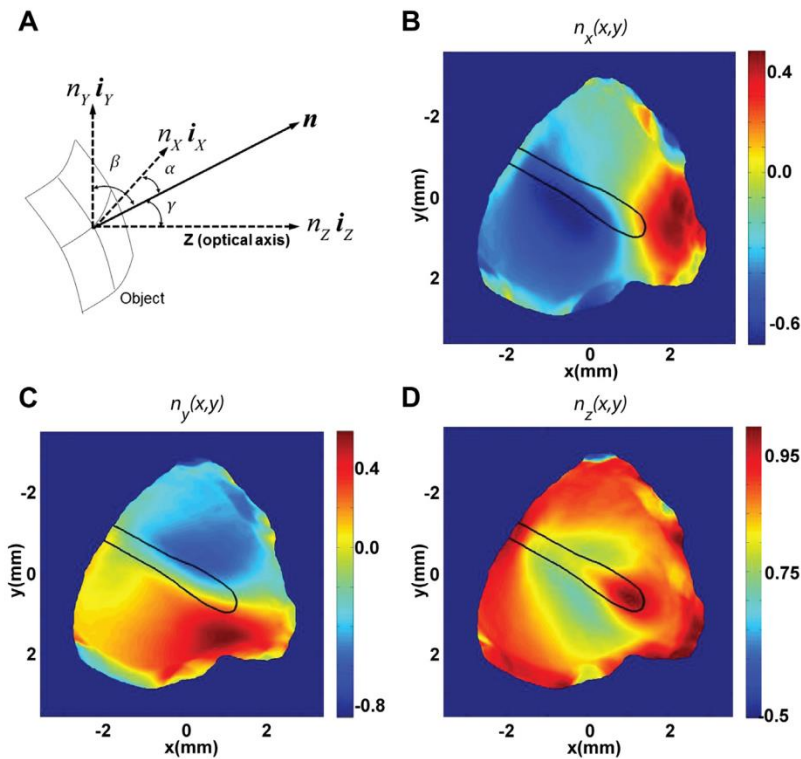


Fig. 4. A lateral surface view of the three Cartesian components of the unit vector normal to the TM surface. A) A schematic illustrating the normal vector \mathbf{n} at a point on the TM surface, and its decomposition into three Cartesian vectors with signed magnitudes of n_x , n_y , and n_z and corresponding unit vectors based on a z axis defined by the direction of the illuminating and reflected laser light. The α , β and γ describe the angles between the normal vector and the Cartesian vectors. B & C). Color rendering of $n_x(x,y)$ and $n_y(x,y)$. Note that x and y components of the normal vector are negative for positions where the gradient of the TM surface in x and y is negative. The outline of the manubrium is included in the figure for orientation. D). A color rendering of $n_z(x,y)$. Due to the conical shape of the TM and the similarity of $n_z(x,y)$ to the normal vector, $n_z(x,y)$ is always positive. The components of the normal unit vector are unitless.

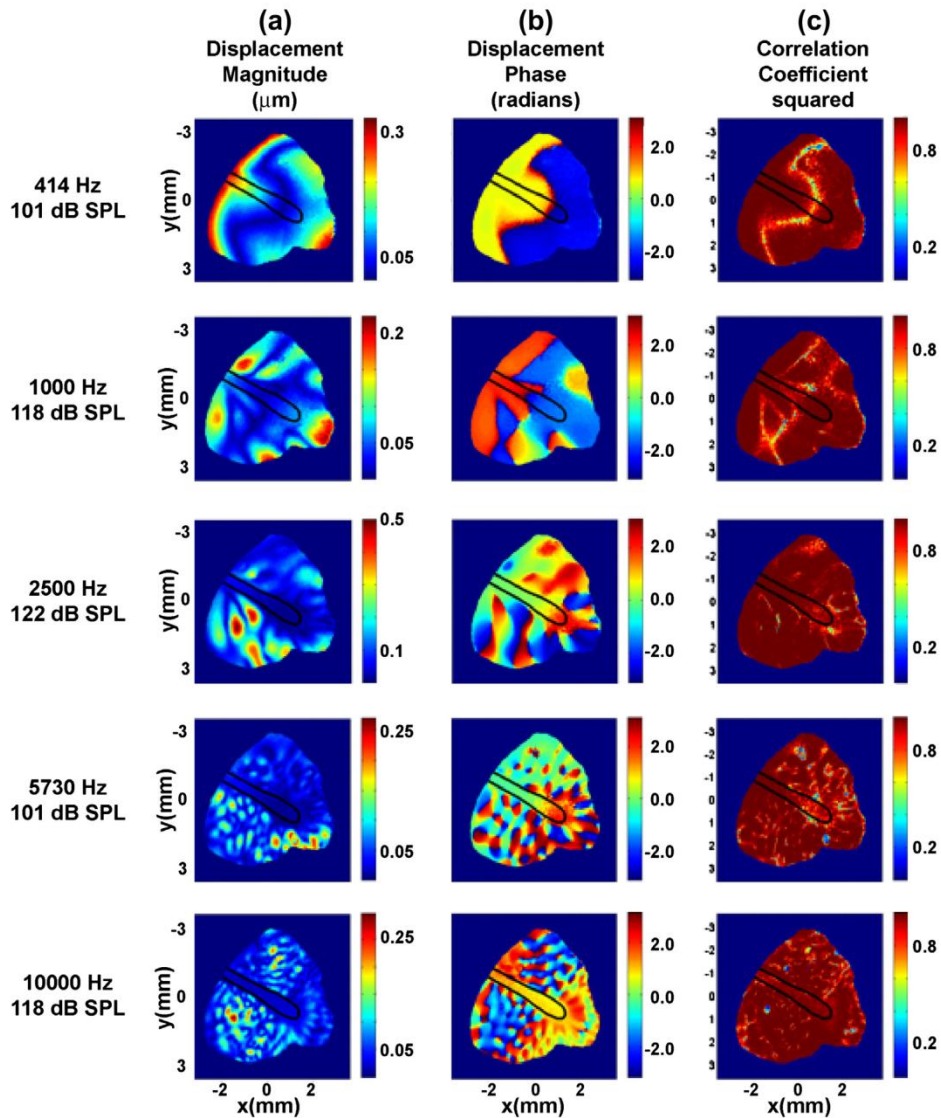


Fig. 5. Color renderings of the fundamental Fourier magnitude and angle of the sound-induced motion of the TM surface along the z axis made at 5 combinations of stimulus frequency and level. The leftmost data column contains the computed magnitudes of motion. The center column contains the computed angles. The rightmost column shows the square of the correlation coefficient between the measured time waveform at each point and the waveform predicted by the Fourier magnitude and angle. Each figure in the data table shows the location of the manubrium, with the umbo at its central tip. The magnitude color bars are coded in micrometers. The phase color bars are in radians. The correlation color bar show variations in R^2 between 0 and 1.

displacements we measured in this specimen were at least a factor of three smaller than the mean chinchilla umbo displacements reported by Ruggero et al. (1990). Similar results were observed in one other chinchilla TM.

At the lowest frequency measured (414 Hz) the largest motions on the TM surface are at the dorsal (superior) edge of the TM and in the ventral (inferior) regions. There is a putative nodal line of near zero motion between these two regions. (The umbo actually straddles this zero motion line.) The phase measurements suggest the two regions are moving half a cycle out of phase with each other, where the phase changes abruptly at the location of near zero motion. The co-localization of near zero motion and a rapid phase half-cycle change is consistent with the presence of a nodal line. The

correlation plot shows that the measured sinusoidal motions are well fit by the estimates of the magnitude and angle of the motion ($R^2 > 0.9$) at all locations except the nodal line, where the magnitudes of motion are too small (< 10 nm) to be determined accurately.

With 1000 and 2500 Hz stimuli the patterns of motion become more complicated: the number of local magnitude peaks on the surface increases to at least 8, and the area of each magnitude peak is decreased in size. There is also an increase in the complexity of the phase maps with smaller areas of contiguous phase about one for each local magnitude maximum. At 1000 Hz there are multiple nodal lines of near zero magnitude associated with half-cycle phase changes. At 2500 Hz, most of the spatial variations tend to be more graded or of step sizes smaller than half-cycle.

As frequency increases there is a continued increase in the number of local spatial maxima and regions of spatially distinct phase, with an order to the arrangement of the maxima. We no longer see clear nodal lines; however, the entire manubrium (which is firmly attached to the chinchilla TM all along its length) and the umbo generally show very small motion response. While we see an increase in regions of spatially distinct phase of motion, contiguous regions often have phase values that cluster around some mean value. For example, with 10,000 Hz stimulation, the regions of the membrane in the lower-left hand quadrant of the figure tend to phase values that vary between -1 and -2 radians, while the lower right hand quadrant has regions with phases close to 1 radian. At frequencies below 10,000 Hz, the phase of the umbo (the tip of the manubrium) differs from the phase of the rest of the manubrium, but these phases are similar to the phases of the adjacent TM locations. At 10,000 Hz the entire manubrium (including the umbo) moves with similar phase, though this phase differs from the phase of the membrane adjacent to much of the manubrium.

4. Discussion

4.1. Comparison with other estimates of sound-induced motion

The spatial and frequency dependence of the magnitude of displacements in Fig. 5 are consistent with time-average-holography measurements of the TM motion in chinchillas that were reported by Rosowski et al. (2009), the only other report of the motion of the entire surface of the chinchilla TM. The progression of an increasing number of spatial maxima and a decreased size of the area of each maxima as stimulus frequency increases is observed in measurements made in both live and cadaveric chinchillas reported in that study. Time-average holography cannot address the relative phases of the measured displacements without extended techniques.

There are significant similarities and differences between stroboscopic holography measurements of the motion of the TM surface in chinchilla and cadaveric human TMs (Cheng et al., 2010; Rosowski et al., 2011; Cheng et al. in press). In both preparations, we see a progression in the patterns of motion from simple to complex to ordered patterns of motion as frequency increases, as noted by Rosowski et al. (2009). However, the frequencies where the transitions between these behaviors occur are lower in chinchillas than in humans. Related to this issue, Cheng et al. (in press) demonstrate that the entire human TM moves in phase at frequencies lower than 1 kHz, while at the lowest frequency we measure in the chinchilla (414 Hz), we see half-cycle phase differences between different halves of the TM, with a nodal line nearly perpendicular to the manubrium running through the umbo (Fig. 5). Similar patterns in which one half of the TM moves a half-cycle out-of-phase from the other half are not observed in humans with acoustic stimulation. It is possible that the inter-species differences in displacement pattern are a result of the difference between the circularly symmetric chinchilla TM and the relatively asymmetric human TM (Puria and Steele, 2010).

If we scale stimulus frequency by a factor of about 2.5 and compare the 1–2.5 kHz range in chinchilla to ~ 2.5 to 6.25 kHz in human, we can discern similar behaviors. At 4, 5 and 6 kHz in humans, Cheng et al. (in press) describe two kinds of phase variations across the TM surface: gradual phase changes that are suggestive of either traveling surface waves or significant damping within the TM surface (Aernouts et al. MEMRO, submitted for publication), and relatively sudden half-cycle phase changes associated with local magnitude minima suggestive of nodes on the TM surface. The small number of these nodes in both humans and

chinchillas is consistent with low-order modal patterns of motion (Cheng et al., in press).

At 8–16 kHz in humans, and 3.5 kHz and higher in chinchilla there are numerous (>15) regions defined by oval local magnitude peaks with associated oval regions of similar phase values. There is little evidence of rapid half cycle phase shifts. Instead the phase patterns of adjacent regions generally show cyclic variations in phase of less than 0.25 cycles. This pattern has been interpreted by us (Cheng et al., 2010; Rosowski et al., 2011) to result from the combination of a large-spatial wavelength mode-like displacement, and a smaller spatial wavelength traveling-wave like component of smaller magnitude. As Aernouts et al. (submitted for publication MEMRO) point out, such patterns are also consistent with the summing of a large magnitude low-order modal motion of the membrane and a smaller magnitude higher-order modal in a membrane with losses.

4.2. A simple model relating shape and motion

Three dimensional motions can be recovered by measurements of optical phase with displacements, \mathbf{U} , and optical phase, ϕ , related by the fringe-locus function

$$\phi = \mathbf{K} \cdot \mathbf{U}, \tag{4}$$

where $\mathbf{K} = \mathbf{K}_2 - \mathbf{K}_1$ is the sensitivity vector characterizing the illumination-observation geometry of the optical setup and $\mathbf{U} = \mathbf{P}' - \mathbf{P}$ are vectors representing induced motions, as shown in Fig. 6. The expanded form of Equation (4)

$$\phi = (K_x, K_y, K_z) \cdot (U_x, U_y, U_z) \tag{5}$$

indicates that in order to recover the three components of motion, (U_x, U_y, U_z) that introduce measurable optical phase changes at point (x, y, z) on an object, it is necessary to (1) determine the object's shape, which together with the knowledge of the points of illumination and observation, $\mathbf{P}_1, \mathbf{P}_2$, respectively, define the sensitivity vector (K_x, K_y, K_z) and (2) recover corresponding optical

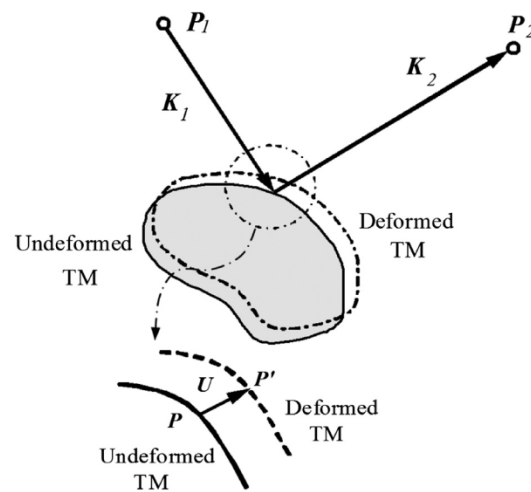


Fig. 6. Illumination-observation geometry of an interferometric optical setup: (a) overall geometry; and (b) detail showing motions, \mathbf{U} , at a single point on the object. Points of illumination and observation are $\mathbf{P}_1, \mathbf{P}_2$ and vectors of illumination and observation are $\mathbf{K}_1, \mathbf{K}_2$. Geometry relates motions with sample shape as well as with optical phase measurements via Equation (4).

phase, ϕ , by multiple measurements requiring at least three independent sensitivity vectors (Stetson, 1975; Vest, 1979; Pryputniewicz, 1986).

Our optical configurations (Hernández -Montes et al., 2009; Flores-Moreno et al., 2011; Lu, 2012) have been designed to define parallel illumination-observation conditions that lead to a simplified fringe-locus function

$$\phi = \frac{2\pi}{\lambda} (0, 0, K_z) \cdot (U_x, U_y, U_z), \quad (6)$$

where λ is the laser wavelength and $(0, 0, K_z) = (0, 0, 2)$ is the sensitivity vector defining parallel illumination-observation conditions. Similar to Equation (3), Equation (6) describes measurements along a single axis with the recovered motions of the TM corresponding to the components of the deformation vectors that are parallel to the measuring optical axis. A method that we are investigating to recover the three components of the deformation vector in an absolute coordinate system consists of using multiple sensitivity vectors with Equation (5). The method requires making measurements along multiple directions of observation. Though promising for shape measurements, further investigations are underway in order to minimize temporal decorrelation of displacements that occur when sensitivity vectors are changed.

Our recently developed approach to recover three dimensional motions of acoustically excited TM by the use of a single optical instrument and a single sensitivity vector consists of simultaneously applying Equations (3) and (6) together with well-accepted structural mechanics theories and assumptions. From the structural point of view, the TM can be considered as a thin shell because the maximum value of the ratio of its thickness and any other of its dimensions is <0.05 (Timoshenko, 1959; Saada, 1974). In addition, the acoustically induced deformations of interest with magnitudes $<1 \mu\text{m}$ are substantially smaller than the 10–30 μm of the thickness of the chinchilla TM (Decraemer and Funnell, 2008), as has been demonstrated in other species by earlier work (Khanna and Tonndorf, 1972; Rosowski et al., 2009; Cheng et al., in press). Therefore, by considering thin shell theory (Fig. 6), and assuming negligible TM thickness changes introduced by acoustic excitation, we have developed and computationally validated, with $<3\%$ uncertainty, the hypothesis that the major components of acoustically induced deformations occur parallel to the local surface normals of the middle thickness layer of the TM (Lu, 2012). Such a judgment is consistent with Kirchhoff's thin shell theory with small displacements (Love, 1888), and with estimates of the very small sound-induced TM thickness change (Chang et al. in preparation).

4.3. Estimation of the normal component of TM motion

With our hypothesis that the major components of acoustically induced deformations occur parallel to the local surface normals of the TM and measurements with an optical setup characterized by Equation (6), it is possible to recover the normal components of TM motion, \mathbf{U} , in a Cartesian coordinate system defined by the corresponding sensitivity vector, Fig. 7. Specifically, single axis measurements, U_z , together with the knowledge of surface normals, $\mathbf{n} = (n_x, n_y, n_z)$, enable estimation of the two additional corresponding orthogonal components of motion, U_x and U_y with

$$U_x = n_x \frac{U_z}{n_z}, \quad U_y = n_y \frac{U_z}{n_z}, \quad (7)$$

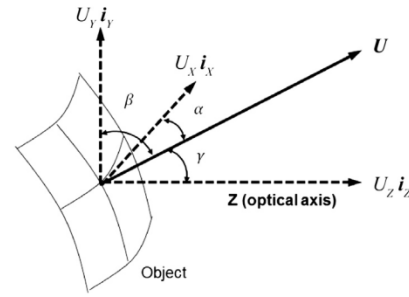


Fig. 7. The relationship between the displacement normal to the TM surface \mathbf{U} and the signed magnitudes of the three Cartesian components that describe the normal displacement U_x , U_y , and U_z .

and the resultant normal TM motion, \mathbf{U} , with

$$\mathbf{U} = |\mathbf{U}| \cdot (n_x, n_y, n_z), \quad \text{and} \quad |\mathbf{U}| = \sqrt{U_x^2 + U_y^2 + U_z^2} \quad (8)$$

4.4. Estimation of the x and y components of TM motion

We have used Equation (7) to estimate the x and y components of the TM motion (U_x and U_y) from measurements of the motion in z (U_z) and the shape in the same chinchilla TM (Fig. 8). The right-hand pair of columns (C & D) in Fig. 8 illustrate great similarity between the magnitudes of the measured U_z and the computed motion normal to the surface (the resultant, \mathbf{U}). Such similarity is expected in these measurements because of the near alignment of the direction normal to the TM surface and the z-axis that is demonstrated by the z-component of the normal vector, n_z , having a value of 0.75–1 over most of the TM surface (Fig. 4D). Furthermore, since n_z is always positive (Fig. 4), the temporal phase of the motion measured along the z-axis is the same as the phase of motion in the direction normal to the TM surface.

Columns A, B and D of Fig. 8, on the other hand, suggest large differences between the magnitude and phase of the resultant normal displacement (\mathbf{U}) and its x- and y-components (U_x and U_y): The x and y displacement components are of significantly smaller magnitude and there are regions of the TM surface where the predicted U_x and U_y are negative relative to \mathbf{U} . (This negativity implies \mathbf{U} and the component with a negative value are a half-cycle out of phase.) U_x and U_y are negative at locations where the x- or y-component of the unit normal vector are negative, while the differences in magnitude occur because the magnitudes of the x- or y-component of the unit normal vector generally fall between 0 and 0.5.

Because the z measurement axis is roughly orthogonal to the tympanic ring, the x- and y-components computed in Equation (7) describe motions in the plane of the tympanic ring, where the magnitude and phase of such 'in-plane' motions is directly related to that of the measured z-component and the components of the normal unit vector computed from the shape of the TM (Fig. 3). The significance of the in-plane motion components is unknown. It is worthwhile noting that, according to our thin-shell assumption and the small size of the measured displacements relative to membrane dimensions, the motion of the TM is well approximated by motion along the direction normal to the TM surface, and we assume no additional motion components in the plane tangential to each TM location.

The predicted motions in the plane of the tympanic ring (columns A & B of Fig. 8) are computed by the product of the

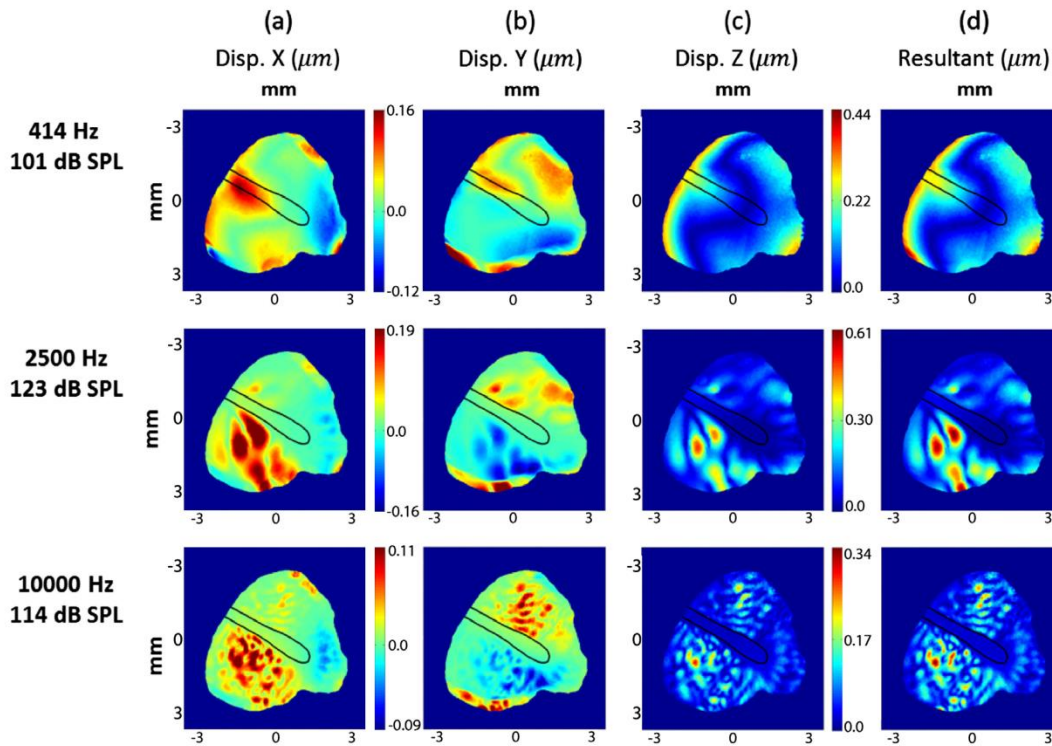


Fig. 8. The components of the normal displacement U (A & B). The x and y components of the normal displacement calculated as describe above. The color bar in between (which scale both positive and negative values in μm) applies to both columns. Because U_x and U_y are the product of the normal displacement magnitude and the x and y components of the normal unit vector, the scales include both negative and positive values (C & D). The magnitude of the z component of the normal displacement U_z and the computed normal displacement U . The color bars in between these two columns only scale positive values.

measured z -component of the displacement, U_z , and the ratio of the positive or negative real number defined by the x - or y -component of the normal unit vector to the positive real number defined by the z -component of the normal unit vector (Equation (7)). Therefore, the thin-shell assumption predicts the motions that occur in the plane of the tympanic ring are either in-phase or half a cycle out of phase with the motions of the normal vector. This contrasts with oral reports (Jackson et al., presented at MEMRO 2012 and ARO 2012) that 3-D laser Doppler measurements of TM motion in humans show in-plane motion components with phases different from that of the out-of-plane motions and magnitudes comparable to the out-of-plane motions. The cause of these discrepancy is unknown, but could be related to limitations of the thin shell assumptions we apply in this report, or to difficulties in the 3-D laser determination of motions within the plane of a surface whose orientation to the laser varies in space.

5. Summary

We describe a new optical method for near simultaneous measurements of the 3D-shape and 1D motion measurements of the tympanic membrane based on opto-electronic computer assisted holography. These methods have been applied to the study of the sound-induced motions of the chinchilla TM. The coupling of these two methodologies with the hypothesis that the TM acts primarily as a thin shell in which the primary motion component is normal to the surface of the membrane allows us to estimate the three-dimensional motion of over 250,000 points

on the TM surface. By this theory, the relative phases of the in-plane and out-of-plane motion depend on the gradient of the TM surface, and the in-plane motions can never be larger in magnitude than the motion normal to the TM surface. However, the computed in-plane motions can be larger than the motion estimated from a single measurement direction in which the measurement vector is not normal to the TM surface. The sound-induced motion of the chinchilla TM has several features in common with those observed in humans (Cheng et al., in press); however, these features occur in lower frequency ranges in chinchilla.

Acknowledgments

We thank Mike Ravicz, Jef Aernouts, and Saumil Merchant for significant contributions to this work. This work has been funded by NIDCD grants to JJR, and the Mittal Foundation.

References

Aernouts, J., Cheng, J.T., Horwitz, R., Rosowski, J.J., Aerts, J.R.M., Dirckx, J.J.J., Mechanics of human tympanic membrane at acoustic frequencies: holographic measurement and finite element modeling analysis. *Hear. Res.*, (MEMRO 2012), submitted for publication.
 Blayney, A.W., Williams, K.R., Rice, H.J., 1997. A dynamic and harmonic damped finite element analysis model of stapedotomy. *Acta Otolaryngol.* 117, 269–273.
 Chang, E.W., Cheng, J.T., Rösli, C., Rosowski, J.J., Yun, S.H. Functional virtual endoscopy of chinchilla middle ear. *Nature*, in preparation.
 Cheng, J.T., Aarnisalo, A.A., Harrington, E., Hernandez-Montes, M.d.S., Furlong, C., Merchant, S.N., Rosowski, J.J., 2010. Motion of the surface of the human tympanic membrane measured with stroboscopic holography. *Hear. Res.* 263, 66–77.

- Cheng, J.T., Hamade, M., Harrington, E., Furlong, C., Merchant, S.N., Rosowski, J.J., Wave motion on the surface of the human tympanic membrane: holographic measurement and modeling analysis. *J. Acoust. Soc. Am.*, in press.
- Chhan, D., Rössli, C., McKinnon, M.L., Rosowski, J.J., 2013. Evidence of inner ear contribution in bone conduction in chinchilla. *Hear. Res.* 301, 66–71.
- de La Rochefoucauld, O., Olson, E.S., 2010. A sum of simple and complex motions on the eardrum and manubrium in gerbil. *Hear. Res.* 263, 9–15.
- Decraemer, W.F., Funnell, W.R.J., 2008. Anatomical and mechanical properties of the tympanic membrane. In: Ars, B. (Ed.), *Chronic Otitis Media. Pathogenesis-oriented Therapeutic Management*. Kugler Publications, The Hague, The Netherlands, pp. 51–84.
- Decraemer, W.F., Dirckx, J.J.J., Funnell, W.R.J., 1991. Shape and derived geometrical parameters of the adult, human tympanic membrane measured with a phase-shift moiré interferometer. *Hear. Res.* 51, 107–122.
- Dirckx, J.J.J., Decraemer, W.F.S., 1992. Area change and volume displacement of the human tympanic membrane under static pressure. *Hear. Res.* 62, 99–104.
- Dirckx, J.J.J., Decraemer, W.F., 2001. Effect of middle ear components on eardrum quasi-static deformation. *Hear. Res.* 157, 124–137.
- Fay, J., Puria, S., Decraemer, W.F., et al., 2005. Three approaches for estimating the elastic modulus of the tympanic membrane. *J. Biomech.* 38, 1807–1815.
- Flores-Moreno, J.M., Furlong, C., Rosowski, J.J., Harrington, E., Cheng, J.T., Scarpino, C., Mendoza, S.F., 2011. Holographic otoscope for nano-displacement measurements of surfaces under dynamic excitation. *Scanning* 33, 342–352.
- Funnell, W.R., Laszlo, C.A., 1977. Modeling of the cat eardrum as a thin shell using the finite-element method. *J. Acoust. Soc. Am.* 63, 1461–1467.
- Funnell, W.R., Decraemer, W.F., Khanna, S.M., 1987. On the damped frequency response of a finite-element model of the cat eardrum. *J. Acoust. Soc. Am.* 81, 1851–1859.
- Gan, R.Z., Sun, Q., Dyer Jr., R.K., et al., 2002. Three-dimensional modeling of middle-ear biomechanics and its applications. *Otol. Neurotol.* 23, 271–280.
- Goll, E., Dalhoff, E., 2011. Modeling the eardrum as a string with distributed force. *J. Acoust. Soc. Am.* 103, 1452–1462.
- Hernández-Montes, M.d.S., Furlong, C., Rosowski, J.J., Hulli, N., Harrington, E., Cheng, J.T., Ravicz, M.E., Santoyo, F.M., 2009. Optoelectronic holographic otoscope for measurement of nano-displacements in tympanic membrane. *J. Biomed. Opt.* 14, 034023.
- Ilgner, J., Farkas, C., Lenenbach, A., Westhofen, M., 2012. Optical Coherence Tomography for In-vivo Middle Ear Imaging, MEMRO 2012 Program and Abstracts, pg 39.
- Jackson, R., Cai, H., Puria, S., 2012. In Search of In-surface Modes of Sound Transmission on the Eardrum Using Three-dimensional Laser Doppler Vibrometry, MEMRO 2012 Program and Abstracts, pg 24.
- Khanna, S.M., Tonndorf, J., 1972. Tympanic membrane vibrations in cats studied by time-averaged holography. *J. Acoust. Soc. Am.* 51, 1904–1920.
- Koike, T., Wada, H., Kobayashi, T., 2002. Modeling of the human middle ear using the finite-element method. *J. Acoust. Soc. Am.* 111, 1306–1317.
- Kolenovic, E., Furlong, C., Jüptner, W., 2004. Inspection of Micro-optical Components by Novel Digital Holographic Techniques. Proceedings SEM, Costa Mesa CA, pp. 470–475.
- Love, A.E.H., 1888. On the small free vibrations and deformations of elastic shells. *Phil. Trans. Roy. Soc.* 17, 491–549.
- Lu, W., 2012. Development of a multi-wavelength lensless Digital Holography System for 3D Deformations and Shape Measurements of Tympanic Membranes, MS thesis. Mechanical Engineering Department, Worcester Polytechnic Institute.
- Parent, P., Allen, J.B., 2007. Wave model of the cat tympanic membrane. *J. Acoust. Soc. Am.* 122, 918–931.
- Parent, P., Allen, J.B., 2010. Time-domain “wave” model of the human tympanic membrane. *Hear. Res.* 263, 152–167.
- Pryputniewicz, R.J., 1986. Computer-aided fringe analysis. *Proc. SPIE* 673, 250–257.
- Puria, S., Steele, C., 2010. Tympanic-membrane and malleus-incus-complex co-adaptations for high-frequency hearing in mammals. *Hear. Res.* 263, 183–190.
- Rabbitt, R.D., Holmes, M.H., 1986. A fibrous dynamic continuum model of the tympanic membrane. *J. Acoust. Soc. Am.* 80, 1716–1728.
- Rosowski, J.J., Cheng, J.T., Ravicz, M.E., Hulli, N., Harrington, E.J., Hernandez-Montes, M.d.S., Furlong, C., 2009. Computer-assisted time-averaged holography of the motion of the surface of the tympanic membrane with sound stimuli of 0.4 to 25 kHz. *Hear. Res.* 253, 83–96.
- Rosowski, J.J., Cheng, J.T., Merchant, S.N., Harrington, E., Furlong, C., 2011. New data on the motion of the normal and reconstructed tympanic membrane. *Otol. Neurotol.* 32, 1559–1567.
- Ruggero, M.A., Rich, N.C., Robles, L., et al., 1990. Middle ear response in the chinchilla and its relationship to mechanics at the base of the cochlea. *J. Acoust. Soc. Am.* 87, 1612–1629.
- Saada, A.S., 1974. *Elasticity Theory and Applications*. Pergamon Press, Inc.
- Stetson, K.A., 1975. Homogenous deformations: determination by fringe vectors in hologram interferometry. *App. Opt.* 14, 2256–2259.
- Timoshenko, S., 1959. *Theory of Plates and Shells*, second ed. McGraw-Hill.
- Vest, C., 1979. *Holographic Interferometry*. Wiley, NY.

9. Paper C: Three-dimensional vibrometry of the human eardrum with stroboscopic lensless digital holography

Overview

In this paper, published in Journal of Biomedical Optics in 2015, the development of a unique holographic system capable of near-simultaneous measurements of shape and three-dimensional sound-induced motion of the human TM is described. The sound-induced motions of the TM are measured stroboscopically along four different sensitivity vectors to realize a system of equations that in turn, enables computation of 3D motions. A new technique is proposed for accurate estimation of the sensitivity vectors to decrease the experimental errors induced by manual calculation of the sensitivity vectors. Artificial samples with repetitive motions are used to characterize repeatability and accuracy of the measurements. The system is then used to quantify, three-dimensional sound-induced motion of human TMs at different tonal frequencies. Furthermore, these 3D data are used in combination with the shape of the TMs to enable characterization of motion components tangent and normal to the TM surface. These results also enable experimental evaluation of the validity and applicability of the thin-shell hypothesis. A general conclusion is that the motion components tangent to the local plane of the TM are smaller than the ones perpendicular to the plane. The system, opto-electro-mechanical components, and its working principles are described in the following paper, however, some general procedures are discussed in the following Sections.

9.1. Stroboscopic measurements of motion

Sound-induced vibrations of mammalian TMs are fast phenomena whose capture requires high-speed acquisition methods. In our system, we use stroboscopic measurements (Furlong et al., 2009; Cheng et al., 2010; Rosowski et al., 2013; Khaleghi et al., 2013) with a conventional speed camera to capture the repetitive fast motions produced by sinusoidal stimuli. Acoustically-induced motions of the TM are frozen at different stimulus phases using pulses of laser light to illuminate the sample at particular points during the sinusoidal excitation signal. As shown in Figure 9.1, a dual-channel function generator is used with one of the channels set to a sine wave for stimulating the TM through a speaker. The second channel is set to the same frequency, but with a pulse wave to drive an Acousto-Optic Modulator (AOM) to enable and disable the laser beam illumination. Typically, each laser pulse has a duration of 2-5% of the period of the tonal stimulus (Rosowski et al., 2013). This generates the same effect as a strobe light by only capturing the motion of the TM at desired phases of the stimulus wave.

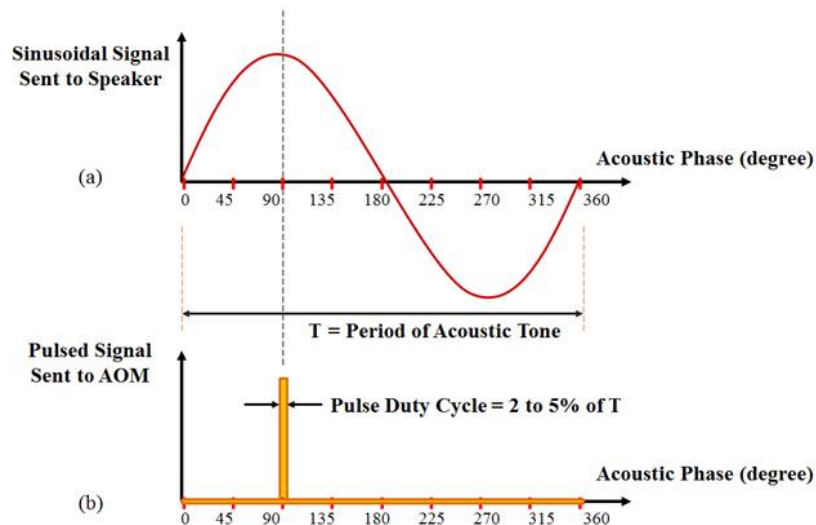


Figure 9.1. Signals for stroboscopic measurements of sound-induced displacements of the TM at an example phase of 90 degrees: (a) sinusoidal signal sent to the speaker to stimulate the TM; and (b) pulsed signal sent to the AOM that acts as a high-speed shutter for laser light illumination with a duty cycle of 2-5% of the tonal excitation period. During a full measurement, the phase position of the pulse is varied from 0 to 360 degrees at specified increments to capture the complete cyclic motion.

A double-exposure technique that compares the deformed state strobe hologram gathered at one phase and a hologram gathered at a reference phase (usually 0) is used to compute the displacement of a series of strobe holograms to describe the phase-locked sound-induced variation in the optical phase. The result is a wrapped phase map that describes the differences in optical phase between the deformed and reference states. At every double-exposure strobe hologram, including reference and deformed states, the system records four images containing holographic patterns that result from the phase stepping of the reference beam (RB) in steps of multiples of $\frac{\pi}{2}$, equivalent to adding steps of 1/4 of a wavelength. Considering the intensities at each pixel measured by the camera at each of the four phase steps to be I_1, \dots, I_4 in the reference state, and I'_1, \dots, I'_4 in the deformed state, the wrapped optical phase difference between any two states is related to displacements of the sample and obtained with

$$\Delta\varphi(m, n) = \text{atan2} \left[-\frac{(I_1 - I_3)(I'_4 - I'_2) - (I_4 - I_2)(I'_1 - I'_3)}{(I_1 - I_3)(I'_1 - I'_3) + (I_4 - I_2)(I'_4 - I'_2)} \right]. \quad (9-1)$$

9.2. Three-dimensional vibrometry

Principal components of displacements, \mathbf{d}_x , \mathbf{d}_y , \mathbf{d}_z of a given point of a sinusoidally-driven object are all harmonic functions of time, i.e.,

$$\mathbf{d}_x(x, y) = |\mathbf{d}_x(x, y)| \cdot \sin[2\pi f_0 + \varphi_x(x, y)], \quad (9-2)$$

$$\mathbf{d}_y(x, y) = |\mathbf{d}_y(x, y)| \cdot \sin[2\pi f_0 + \varphi_y(x, y)], \quad (9-3)$$

$$\mathbf{d}_z(x, y) = |\mathbf{d}_z(x, y)| \cdot \sin[2\pi f_0 + \varphi_z(x, y)], \quad (9-4)$$

with appropriate amplitudes and phases relative to the sound pressure. In order to quantify all three components of displacement vector, \mathbf{d}_x , \mathbf{d}_y , and \mathbf{d}_z , the harmonically-induced motion of the objects should be stroboscopically recorded at least three times from three linearly-independent sensitivity vectors. In our experimental system and to minimize the experimental errors, sinusoidal motion of the objects are repetitively captured along four different sensitivity vectors, realizing an over-determined system of equations (i.e., four knowns and three unknowns) and then, the 3D data are quantified.

In repetitive measurements of vibrations, the phase of the harmonic load and in turn, the vibrational phase of the sample cannot be granted to be similar when repeating the measurements from different sensitivity vectors. This issue was one of the most troublesome challenges through measurements of 3D motion of vibratory objects with the method of multiple illumination directions, and instead, researchers have suggested the use of multiple observation directions for such measurements (Pryputniewicz and Bowley 1978; Vest, 1979). However, for our application (i.e., 3D sound-induced motion measurements of human TM) the method of multiple observation directions is not preferred, because first, it requires complicated image processing algorithms to register data from different cameras coordinate systems to one common coordinated system for all of the observers; and second, having three different cameras requires larger space, which is not applicable for the study of the space-limited middle ear. Therefore, the method of multiple illumination directions is preferred and the phase issue is solved as follows. Figure 9.2 shows the overall procedures for quantification of 3D sound-induced motion of the TM. Sinusoidal motions of the TM are frozen at nine equally-spaced stimuli phases and the digital holograms corresponding to sound-induced motion of the TM at each stroboscopic phase are recorded. This step (step 1 in Figure 9.2) is repeated four times along four different

sensitivity vectors \mathbf{K}_1 to \mathbf{K}_4 . Therefore, temporal variations of sound-induced motion of the TM at each point on its surface are obtained along all the sensitivity vectors (step 2 and 3 in Figure 9.2). Due to the potential phase lags between the measurements, the system of equations shown in Eq. 6-39 is solved at every single stroboscopic phase $0, 45, 90, \dots, 360^\circ$, individually (step 4 in Figure 9.2).

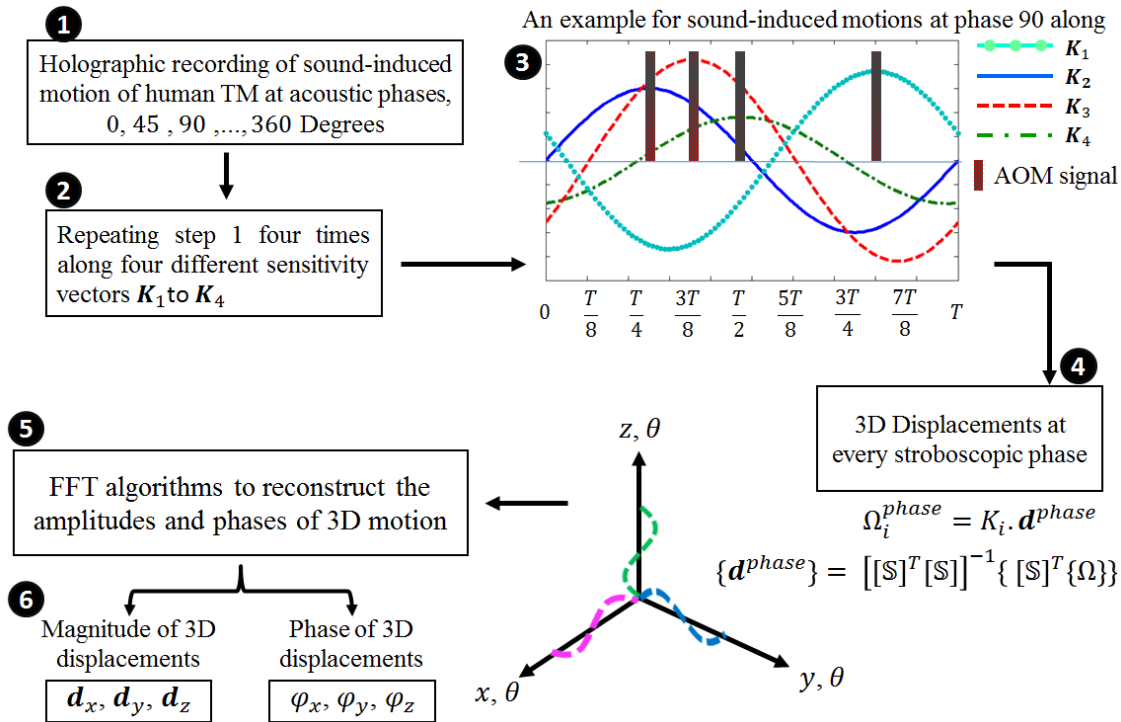


Figure 9.2. Procedures for stroboscopic measurements of three-dimensional magnitudes and phases of sound-induced motion of the TM.

FFT algorithms are then used along each Cartesian axes x, y, z with 8 discrete temporal points (motion measurements at each 8 stroboscopic phases) in order to obtain magnitudes and phases of motion at every single pixel on the surface of the TM (step 5, 6 in Figure 9.2).

9.3. General procedures for 3D motion measurements

In this Section, an example is given to further describe the procedures for quantification of magnitudes and phases of three-dimensional motions of a harmonically-driven membrane. The

stroboscopic measurements of motion are repeated four times along four different sensitivity vectors by varying the illumination direction. For each sensitivity vector, sinusoidally-driven motion of the membrane is frozen at 9 distinct instances corresponding to 9 equally-spaced vibrational phases 0, 45, 90, ..., 360. Figure 9.3 shows wrapped optical phases obtained with Eq. 9-1 corresponding to stroboscopic measurements of motions at each stimuli phase along four sensitivity vectors. 2D phase unwrapping algorithms (Herráez et al., 2002) are then used to unwrap the discontinuous phase maps (data shown in Figure 9.3) and the results are shown in Figure 9.4.

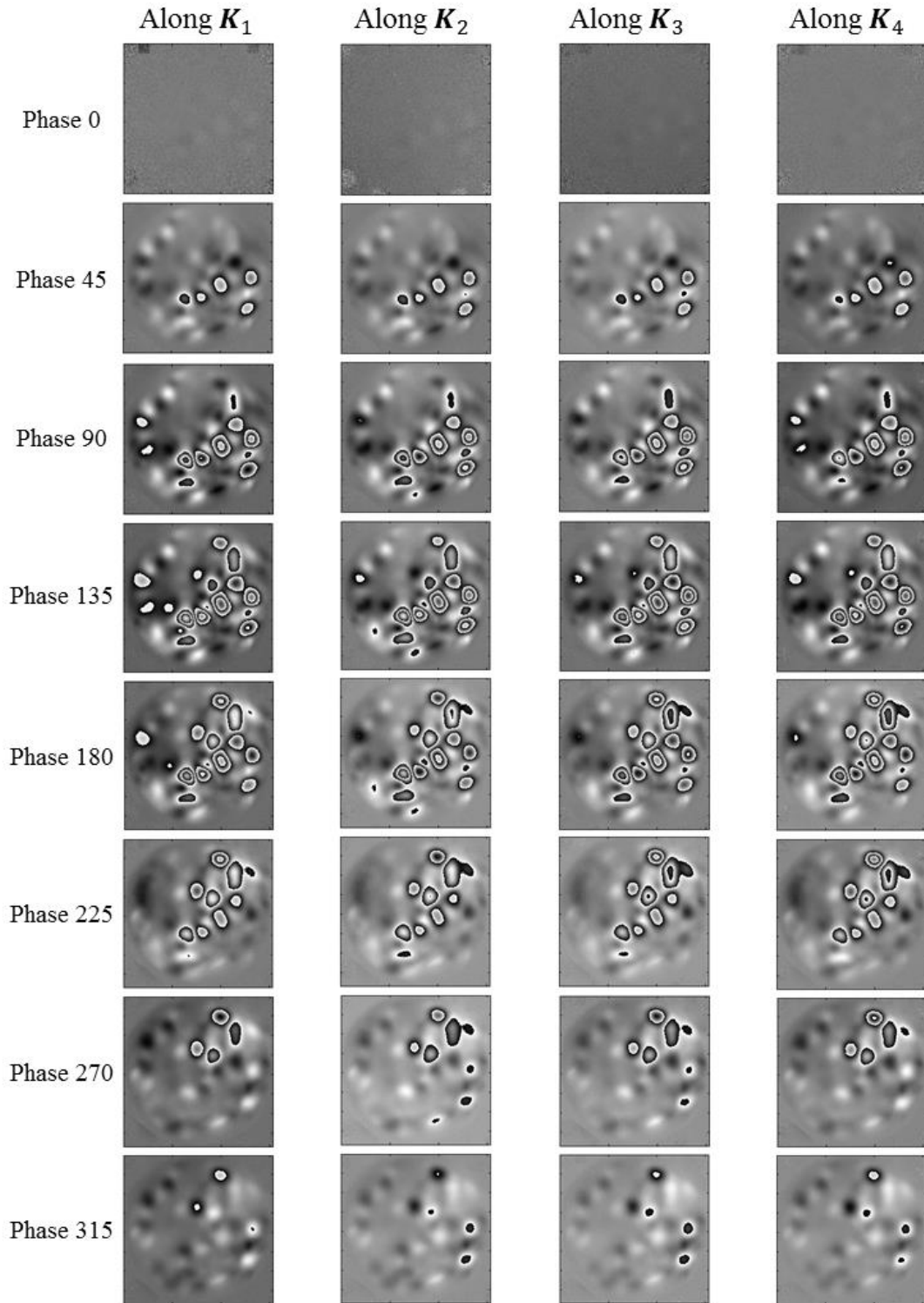


Figure 9.3. Wrapped optical phases corresponding to stroboscopically-measured motion of a harmonically-driven semi-spherical artificial membrane along four sensitivity vectors at 8 different temporal phases.

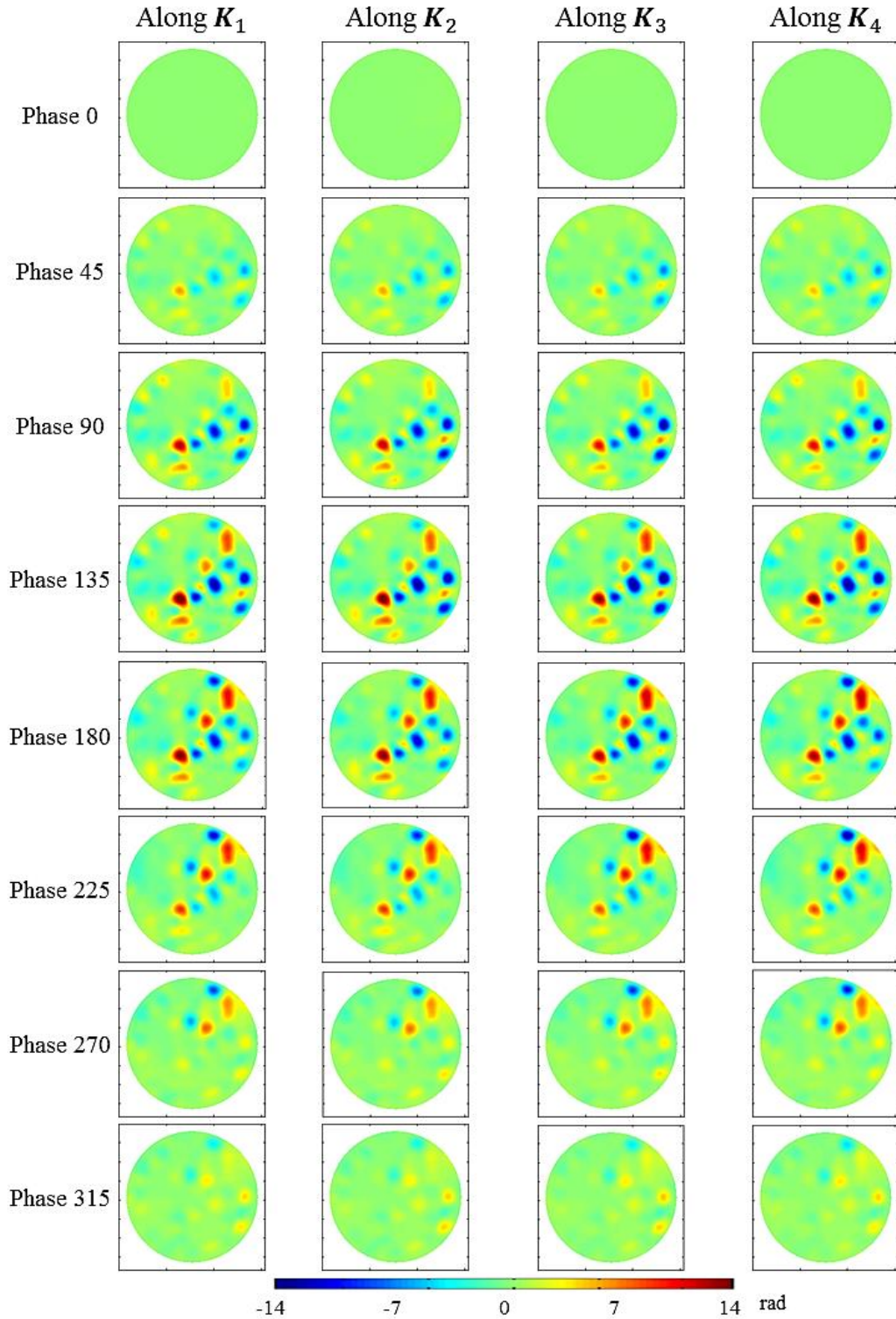


Figure 9.4. Unwrapped optical phases corresponding to harmonically-driven motion of a semi-spherical artificial membrane along four sensitivity vectors at 8 different stroboscopic phases.

The position versus stimulus phase functions gathered at each of the camera pixels were Fourier transformed and the magnitudes and phases of the fundamental and second harmonic components are computed for data of all four sensitivity vectors (Cheng et al., 2010; Khaleghi et al., 2015). The magnitude of the second harmonic was always at least 30 dB below the fundamental, except in regions where the motion magnitude was less than the effective 10 nm resolution of our measurement system. Figure 9.5 shows representative examples for magnitudes (top) and phases (middle) of the reconstructed motions along four sensitivity vectors K_1 to K_4 .

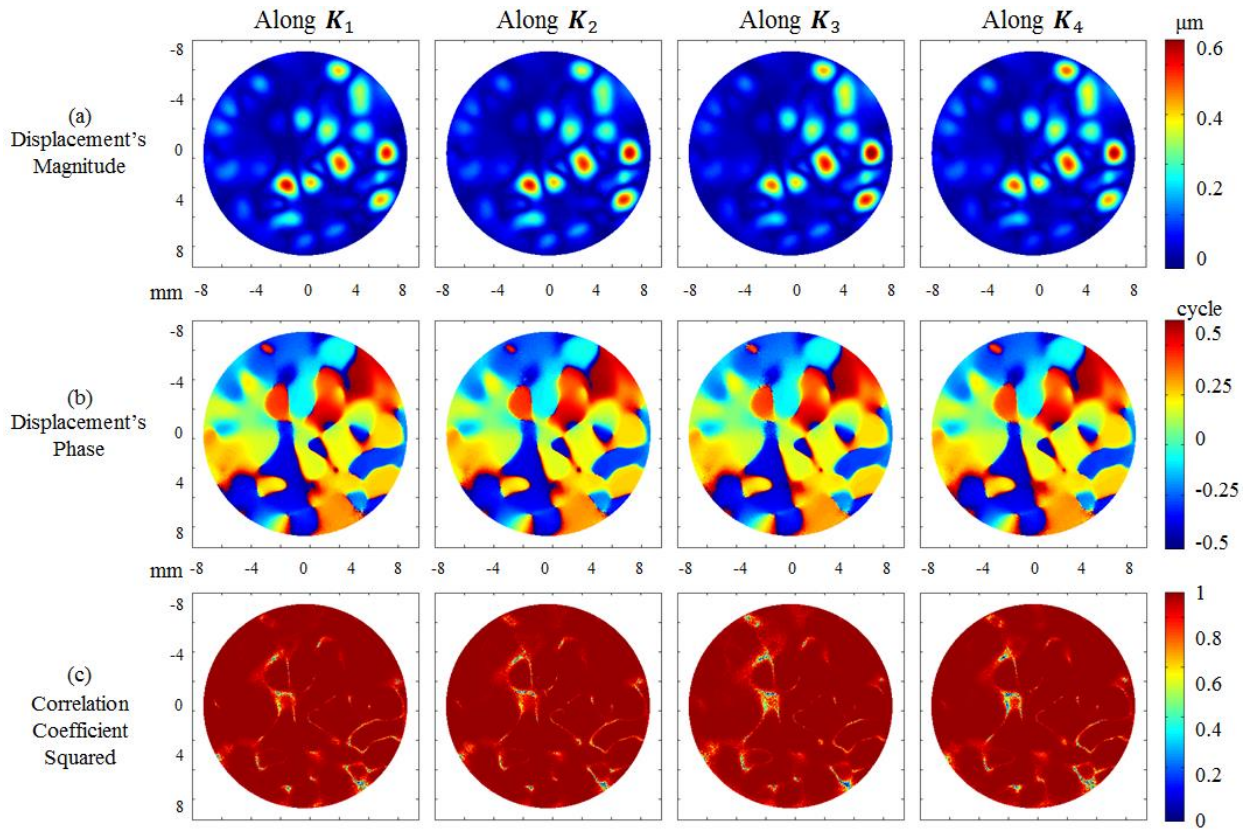


Figure 9.5. The results obtained from FFT algorithm obtained for measurements along four sensitivity vectors K_1 to K_4 : (a) magnitudes of motions; (b) phases of motion; and (c) the squared of the Pearson Product Correlation Coefficient between the measured phasic variations of the motion and the sinusoidal motion reconstructed from the magnitude and angle of the Fourier determined fundamental component of the phasic motion.

In order to evaluate the quality of the Fourier description of the magnitude and angle of the motion at each pixel, we computed the Pearson Product Correlation Coefficient between the measured phasic variations of the motion and the sinusoidal motion reconstructed from the magnitude and angle of the Fourier determined fundamental component of the phasic motion. As shown in Figure 9.5c, the square of this correlation R^2 is generally greater than 0.9 except at locations where the magnitude of the measured motions was less than 10 nm.

In order to measure magnitudes and phases of three-dimensional motion of the membrane, Eq. 6-39 is solved at every single stroboscopic phases 0, 45, 90, ..., 360, individually to realize 3D motion of the membrane at every single phases of the vibration cycle. Figure 9.6 shows representative examples of the 3D motion of the membrane at stroboscopic phases of 45, 90, 135, 180, 225, 270 degrees. Motions along each Cartesian axes x , y , and z , are then Fourier transformed to enable characterization of magnitudes and phases of motion along all three axes. The results of this FT are shown in Figure 9.7 illustrating magnitudes and phases of three-dimensional motion of the sample.

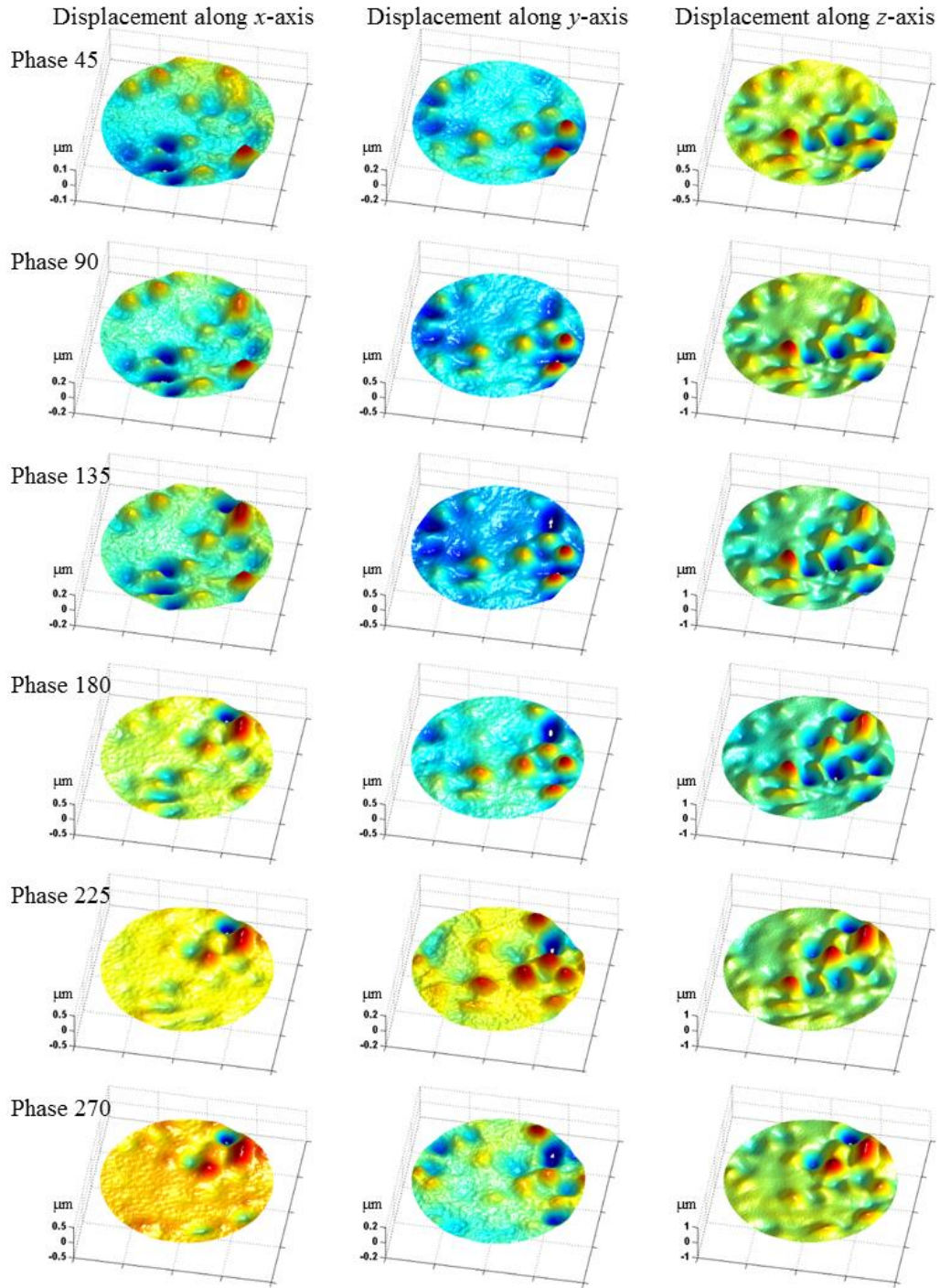


Figure 9.6. Three-dimensional vibration measurements at different phases of cyclic vibration of a thin semi-spherical membrane captured by our developed holographic interferometric system. The results have been obtained by solving the system of equations shown in Eq. 6-39 for each phase of stimuli.

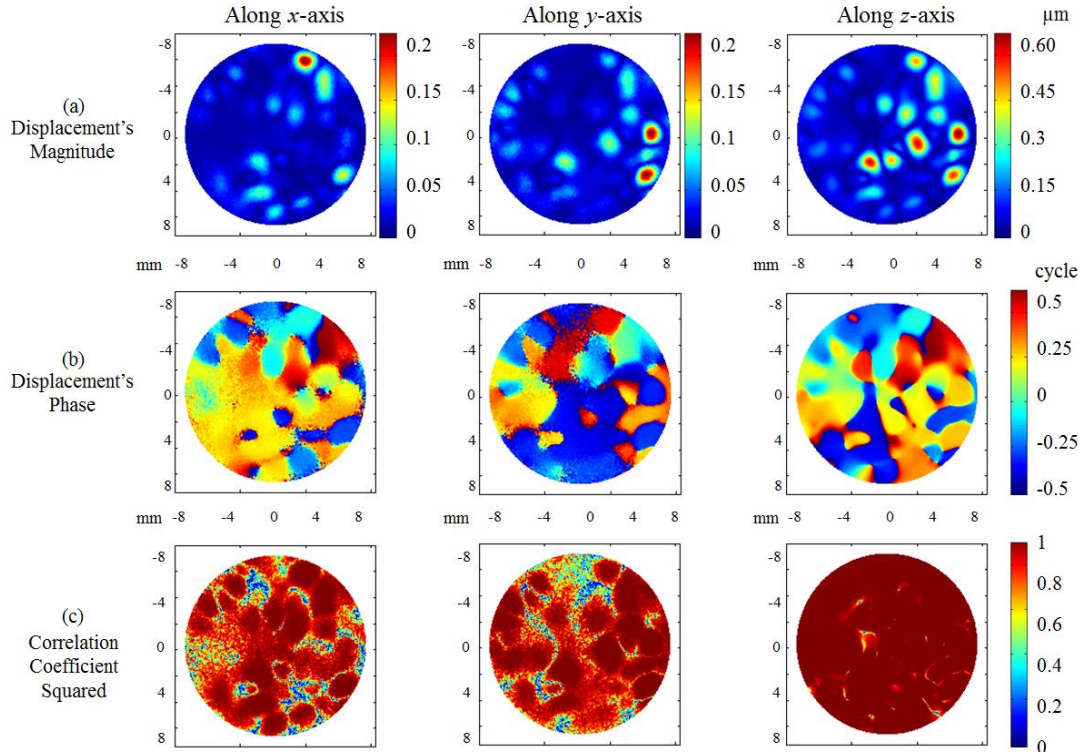


Figure 9.7. 3D harmonically-driven reconstructed motion along three axes x , y , and z obtained experimentally with the holographic system: (a) motions' magnitudes; (b) motions' phases; and (c) goodness of curve-fitting by estimating the squared of correlation coefficient. The results have been obtained from data shown in Figure 9.6 by fitting a sinusoidal function with a given magnitude (a) and phase (b) at each pixel along each Cartesian axes x , y , and z using developed FFT algorithms.

Three-dimensional vibrometry of the human eardrum with stroboscopic lensless digital holography

Morteza Khaleghi,^{a,*} Cosme Furlong,^{a,b,c} Mike Ravicz,^{b,c} Jeffrey Tao Cheng,^{b,c} and John J. Rosowski^{b,c}

^aWorcester Polytechnic Institute, Department of Mechanical Engineering, Center for Holographic Studies and Laser Micro-mechanics, Worcester, Massachusetts 01609, United States

^bEaton-Peabody Laboratory, Massachusetts Eye and Ear Infirmary, Boston, Massachusetts 02114, United States

^cHarvard Medical School, Department of Otolaryngology, Boston, Massachusetts 02114, United States

Abstract. The eardrum or tympanic membrane (TM) transforms acoustic energy at the ear canal into mechanical motions of the ossicles. The acousto-mechanical transformer behavior of the TM is determined by its shape, three-dimensional (3-D) motion, and mechanical properties. We have developed an optoelectronic holographic system to measure the shape and 3-D sound-induced displacements of the TM. The shape of the TM is measured with dual-wavelength holographic contouring using a tunable near IR laser source with a central wavelength of 780 nm. 3-D components of sound-induced displacements of the TM are measured with the method of multiple sensitivity vectors using stroboscopic holographic interferometry. To accurately obtain sensitivity vectors, a new technique is developed and used in which the sensitivity vectors are obtained from the images of a specular sphere that is being illuminated from different directions. Shape and 3-D acoustically induced displacement components of cadaveric human TMs at several excitation frequencies are measured at more than one million points on its surface. A numerical rotation matrix is used to rotate the original Euclidean coordinate of the measuring system in order to obtain in-plane and out-of-plane motion components. Results show that in-plane components of motion are much smaller (<20%) than the out-of-plane motions' components. © The Authors. Published by SPIE under a Creative Commons Attribution 3.0 Unported License. Distribution or reproduction of this work in whole or in part requires full attribution of the original publication, including its DOI. [DOI: [10.1117/1.JBO.20.5.051028](https://doi.org/10.1117/1.JBO.20.5.051028)]

Keywords: 3-D displacement measurements; digital holography; holographic contouring; stroboscopic measurements; tympanic membrane.

Paper 140728SSR received Nov. 3, 2014; accepted for publication Dec. 31, 2014; published online Feb. 4, 2015.

1 Introduction

The hearing process involves a series of physical events in which acoustic waves in the outer ear are transduced into mechanical motions of the middle ear, acoustic and mechanical motions in the inner ear, and then into chemo-electro-mechanical reactions of the inner ear sensors that are interpreted by the brain.¹ Air in the ear canal has low mechanical impedance, whereas the mechanical impedance at the center of the eardrum, the umbo, is high. The eardrum or tympanic membrane (TM) must act as a transformer between these two impedances; otherwise, most of the energy will be reflected rather than transmitted.^{2,3} The acousto-mechanical transformer behavior of the TM is determined by its shape, internal fibrous structure, and mechanical properties.⁴⁻⁶ Therefore, full-field-of-view techniques are required to quantify shape, sound-induced displacements, and mechanical properties of the TM.⁷⁻⁹ In our previous works,¹⁰⁻¹² we have reported holographic interferometric measurements of sound-induced displacements over a majority of the surface of mammalian TMs. A potential criticism of these measurements is that the displacements were measured only along one direction that was along the normal vector to the tympanic ring. Therefore, it was not possible to characterize all three-dimensional (3-D) motion components including those tangent (in-plane) and normal (out-of-plane) to the local plane of the TM. In this paper, developments of a single holographic system capable of measuring both shape with sub-millimeter

resolution, and 3-D sound-induced motion of the TM with sub-micrometer resolution, are described. The accuracy and repeatability of the measuring system is tested and verified using artificial samples with geometries similar to those of human TMs. Then the system is used to measure the shape and 3-D sound-induced motions of human cadaveric TM samples at different tonal frequencies. Data obtained from the shape of the membrane are combined with the measured 3-D sound-induced motion components along three axes, x , y , and z , in order to obtain the motion's components tangent and normal to the local plane of the TM, enabling a more comprehensive view of TM mechanics.

2 Methods

2.1 Lensless Digital Holography

In conventional holography, an optical lens is used to focus on an object of interest; however, our techniques are based on lensless digital holography in which reconstructions and focusing of the holograms are numerically obtained by Fresnel-Kirchhoff integrals.¹³ Using temporal phase-stepping algorithms,^{14,15} the complex amplitude of the hologram, $h(k, l)$, is obtained with

$$h(k, l) = [I_3(k, l) - I_1(k, l)] + i[I_4(k, l) - I_2(k, l)], \quad (1)$$

where I_1 to I_4 are intensity patterns of four consecutive phase-stepped frames of the camera with an induced phase step of $\pi/2$ between them, and k and l are the coordinates of the pixel in the CCD (hologram plane). As shown in Fig. 1, numerical reconstruction algorithms are based on two-dimensional (2-D)

*Address all correspondence to: Morteza Khaleghi, E-mail: mkm@wpi.edu

Fast Fourier Transform (FFT) of the product of a reconstruction reference wave, $R(k, l)$, complex amplitude of the hologram, $h(k, l)$, and a chirp function, $\psi(k, l)$, that can be obtained with

$$\Gamma(m, n) = Q(m, n) \times \text{FFT2}[R(k, l)h(k, l)\psi(k, l)], \quad (2)$$

where $\Gamma(m, n)$ is the complex reconstructed hologram at coordinates m and n in the reconstruction plane, $R(k, l)$ is the complex amplitude of the reference wave, $Q(m, n)$ and $\psi(k, l)$ are the quadratic phase factor and 2-D chirp function, respectively, and are defined by

$$Q(m, n) = \exp\left[-i\pi\lambda d\left(\frac{m^2}{N^2\Delta x^2} + \frac{n^2}{N^2\Delta y^2}\right)\right], \quad (3)$$

and

$$\psi(k, l) = \exp\left[\frac{-i\pi}{\lambda d}(k^2\Delta x^2 + l^2\Delta y^2)\right], \quad (4)$$

where Δx and Δy are the pixel size of the CCD sensor, N^2 is the number of pixels, λ is the laser wavelength, and d is the reconstruction distance. As shown in Fig. 1, the chirp function is a complex 2-D oscillatory signal, where the frequency of oscillation linearly varies with the spatial coordinate and is used for numerical reconstruction of the hologram at different distances of d . The reconstructed hologram, $\Gamma(m, n)$, is a complex function that contains both the amplitude and optical phase, $\varphi(m, n)$, that is defined by

$$\varphi(m, n) = \arg[\Gamma(m, n)]. \quad (5)$$

The fringe-locus function of a double-exposure (DE) hologram, i.e., the unwrapped optical phase difference of two reconstructed holograms corresponding to deformed and reference states of the object, is related to displacement with^{15,16}

$$\Omega(m, n) = \text{unwrap}(\varphi_{\text{def}} - \varphi_{\text{ref}}) = \frac{2\pi}{\lambda} \mathbf{K} \cdot \mathbf{d}(m, n), \quad (6)$$

where $\Omega(m, n)$ is the fringe-locus function at coordinates m and n in the reconstruction plane, φ_{def} and φ_{ref} are the optical phases of the reconstructed holograms recorded at deformed and reference states of the object, respectively, $\mathbf{K}(K_x, K_y, K_z)$ is the sensitivity vector, defined by vectorial subtraction of the observation vector from the illumination vectors, and $\mathbf{d}(m, n)$ is the displacement vector with three components of d_x , d_y , and d_z .

2.2 Stroboscopic Measurements of Displacement

Sound-induced vibrations of the TM are fast phenomena that require high-speed acquisition methods to be captured. In our system, we use stroboscopic measurements^{17–21} with a conventional speed camera to capture the repetitive fast motions produced by sinusoidal stimuli. Acoustically induced motions of the TM are frozen at different stimulus phases using pulses of laser light to illuminate the sample at particular points during the sinusoidal excitation signal. As shown in Fig. 2, a dual-channel function generator is used with one of the channels set

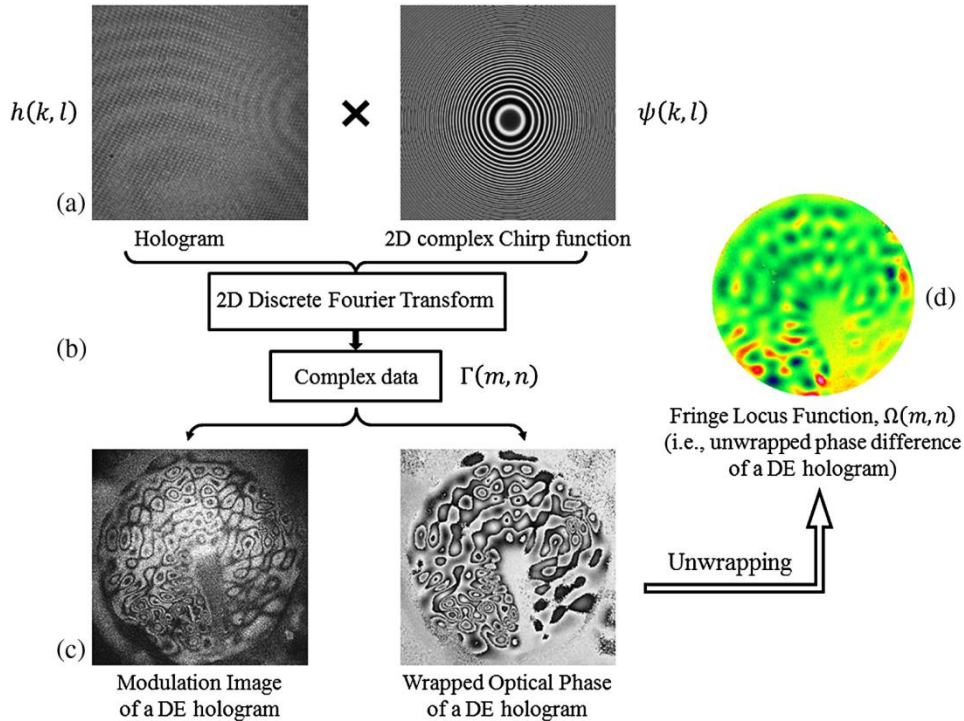


Fig. 1 Numerical algorithms used for reconstruction of digitally recorded holograms: (a) multiplication of complex amplitude of hologram, $h(k, l)$, with 2-D complex chirp function, $\psi(k, l)$, (b) numerical reconstruction of the hologram, $\Gamma(m, n)$, by 2-D FFT, (c) typical examples of modulation and wrapped optical phase of a reconstructed double-exposure (DE) hologram corresponding to sound-induced displacements of a TM sample, and (d) unwrapping the optical phase difference to obtain the fringe locus function, $\Omega(m, n)$.

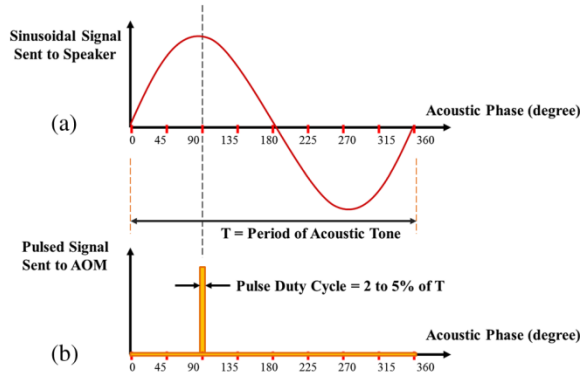


Fig. 2 Signals for stroboscopic measurements of sound-induced displacements of the TM at an example phase of 90 deg: (a) sinusoidal signal sent to the speaker to stimulate the TM and (b) pulsed signal sent to the acousto-optic modulator (AOM) that acts as a high-speed shutter for laser light illumination with a duty cycle of 2% to 5% of the tonal excitation period. During a full measurement, the phase position of the pulse is varied from 0 to 360 deg at specified increments to enable capturing of the entire cyclic motion.

to a sine wave for stimulating the TM through a speaker. The second channel is set to the same frequency but with a pulse wave to drive an acousto-optic modulator (AOM) to enable and disable the laser beam illumination. Typically, each laser pulse has a duration of 2% to 5% of the period of the tonal stimulus.^{11,18} This generates the same effect as a strobe light by only capturing the motion of the TM at desired phases of the stimulus wave.

A DE technique that compares the deformed state strobe hologram gathered at one phase and a hologram gathered at a reference phase (usually 0) is used to compute the displacement of a series of strobe holograms to describe the phase-locked sound-induced variation in the optical phase. The result is a wrapped phase map that describes the differences in optical phase between the deformed and reference states. At every DE strobe hologram, including reference and deformed states, the system records four images containing holographic patterns that result from the phase stepping of the reference beam (RB) in steps of multiples of $\pi/2$. Considering the intensities at each pixel measured by the camera at each of the four phase steps to be I_1, \dots, I_4 in the reference state, and I'_1, \dots, I'_4 in the deformed state, the wrapped optical phase difference between any two states is related to displacements of the sample and is obtained with

$$\Delta\phi(m, n) = \text{atan2} \left[\frac{(I_1 - I_3)(I'_4 - I'_2) - (I_4 - I_2)(I'_1 - I'_3)}{(I_1 - I_3)(I'_1 - I'_3) + (I_4 - I_2)(I'_4 - I'_2)} \right]. \quad (7)$$

2.3 Dual-Wavelengths Shape Measurement

The shape of the TM is measured with the method of dual-wavelength holographic contouring.^{22,23} The technique requires acquisitions of a set of optical amplitude and phase information at wavelength λ_1 , as well as a second set of amplitude and phase information at wavelength λ_2 . As shown in Fig. 3, depth contours related to the shape of the object under investigation are defined by

$$\Delta\phi(m, n) = \phi_2 - \phi_1 = \frac{2\pi}{\Lambda} \text{OPL}, \quad (8)$$

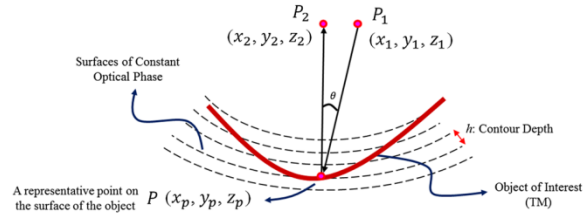


Fig. 3 Optical path length (OPL) of the laser light in dual-wavelength holographic contouring. P_1 is the point of illumination, P_2 is the point of observation, and P is a point on the surface of the object of interest. Surfaces of constant optical phase intersect the object of interest generating contours of depth h .

where ϕ_1 is the phase of the optical path length (OPL) recorded at the first wavelength λ_1 , ϕ_2 is the phase of the OPL recorded at the second wavelength λ_2 , and OPL is the OPL of the laser light from the point of illumination, (x_1, y_1, z_1) , to a point on the surface of the object, (x_p, y_p, z_p) , and to the point of observation, (x_2, y_2, z_2) , and is defined with

$$\text{OPL} = \sqrt{[(x_p - x_1)^2 + (y_p - y_1)^2 + (z_p - z_1)^2]} + \sqrt{[(x_2 - x_p)^2 + (y_2 - y_p)^2 + (z_2 - z_p)^2]}. \quad (9)$$

The phase difference obtained with Eq. (8) is equivalent to performing measurements with a synthetic wavelength of Λ given by

$$\Lambda = \frac{\lambda_1 \lambda_2}{|\lambda_1 - \lambda_2|}, \quad (10)$$

which defines the contour depth, $h \approx (\Lambda/2)$.

In dual-wavelength contouring using phase-stepping algorithms, the phase difference, $\Delta\phi$, is a discontinuous wrapped function varying in the interval $[-\pi, \pi]$, thus phase unwrapping algorithms are applied to obtain a continuous phase distribution, $\Omega(m, n)$, for calculation of the relative height of each point on the surface of the object $Z(m, n)$ by

$$Z(m, n) = \frac{\Lambda}{2\pi[1 + \cos(\theta)]} \Omega(m, n). \quad (11)$$

2.4 3-D Displacement Measurements

To ensure that measurements are reliable and independent of the measuring method, the holographic system is configured so that principal components of displacements, d_x , d_y , d_z , can be measured with two different holographic interferometric approaches. The first one is based on the method of multiple illumination directions, whereas the second one uses a hybrid in-plane and out-of-plane displacement measurement method to obtain 3-D displacement data. In the hybrid method, in-plane measurements provide displacements' components along the x - and y -axes (perpendicular to the observation direction) and out-of-plane measurements provide displacements' components along the z -axis (along the observation direction).

2.4.1 Method of multiple illumination directions

Full field-of-view, 3-D, sound-induced displacements of the TM are measured with the method of multiple illumination

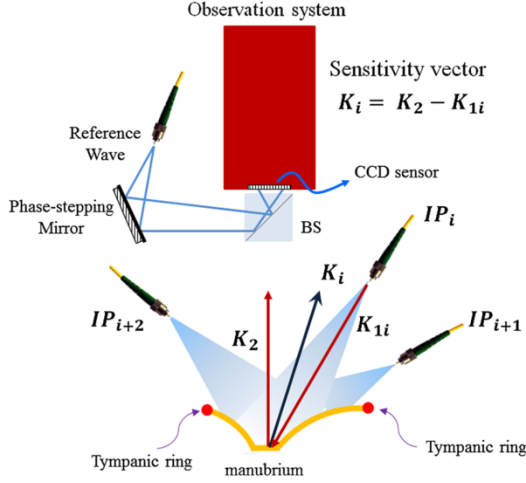


Fig. 4 3-D displacement measurements of the TM surface by the method of multiple illumination directions. Sensitivity vectors for each illumination direction, \mathbf{K}_i , are obtained by vectorial subtraction of the corresponding unit observation vector, \mathbf{K}_2 , from the unit illumination vector, \mathbf{K}_{1i} . The geometry of the TM limits the maximum angle of illumination that can be implemented to achieve a well-conditioned sensitivity matrix.

directions in holographic interferometry.^{24,25} In order to measure the three components of the displacement vector, \mathbf{d} , shown in Eq. (6), at least three independent measurements with different sensitivity vectors are required. In our approach, and to minimize experimental errors,^{24,26} optical phase maps are obtained with four sensitivity vectors to form an over determined system of equations that is solved in Matlab with the least-squares error minimization method with

$$\{\mathbf{d}\} = [\mathbf{S}]^T [\mathbf{S}]^{-1} \times \{\mathbf{S}\}^T \{\Omega\}, \quad (12)$$

where $[\mathbf{S}]$ is the sensitivity matrix containing all the sensitivity vectors \mathbf{K}_i , shown in Fig. 4, and $\{\Omega\}$ is the fringe-locus function vector. In this method, all the sensitivity vectors need to be as linearly independent as possible for the system to provide accurate results. Therefore, the condition number, C , of the square matrix, $[\mathbf{F}] = [\mathbf{S}]^T [\mathbf{S}]$, characterizing the geometry of a holographic setup is calculated with²⁷

$$C(\mathbf{S}) = \sqrt{\frac{\lambda_{\max}(\mathbf{F})}{\lambda_{\min}(\mathbf{F})}}, \quad (13)$$

where λ_{\max} , and λ_{\min} are the maximum and the minimum eigenvalues of $[\mathbf{F}]$. A condition number close to one indicates a well-conditioned matrix, but this represents a holographic setup with large angles of illumination.^{15,28} However, because of the particular cone-like geometry of the TM and the presence of the bony structures around it, as illustrated in Fig. 4, the maximum possible angles of illumination are limited. Therefore, a holographic setup has to be arranged to achieve the largest angles of illumination within the constraints imposed by the geometry of the TM. In this case, the condition number is greater than one, therefore, the accuracy of the measurements obtained with such a holographic setup has to be verified.

2.4.2 Hybrid in-plane and out-of-plane method

A hybrid method that utilizes independent and direct measurements of “out-of-plane” and “in-plane” displacements is used to test and verify the measurements obtained with the method of multiple sensitivity vectors. In this hybrid method, in-plane measurements provide displacement components along the x - and y -axes (perpendicular to the observation direction), and out-of-plane measurements provide displacements along the z -axis (along the observation direction), so that all three displacement components can be obtained independently.

Figure 5 shows optical configurations of the two measuring schemes. As shown in Fig. 5(a), an out-of-plane displacement d_{out} induces a change in the OPL of the laser light (OPD). Based on the geometry of the system, OPD is related to the out-of-plane displacement d_{out} with

$$\text{OPD} = d_{\text{out}} \cos(\theta_1), \quad (14)$$

where θ_1 is the angle between the illumination and observation directions. Using the wavenumber equation, $k = 2\pi/\lambda$, OPD is converted to the out-of-plane fringe-locus function, Ω_{out} , with $\Omega_{\text{out}} = (2\pi/\lambda)\text{OPD}$, and consequently, the out-of-plane displacement d_{out} is calculated with

$$d_{\text{out}} = \frac{\lambda \Omega_{\text{out}}}{2\pi[1 + \cos(\theta_1)]}. \quad (15)$$

In the case of in-plane measurements, the object is illuminated with two symmetrical beams that interfere with each

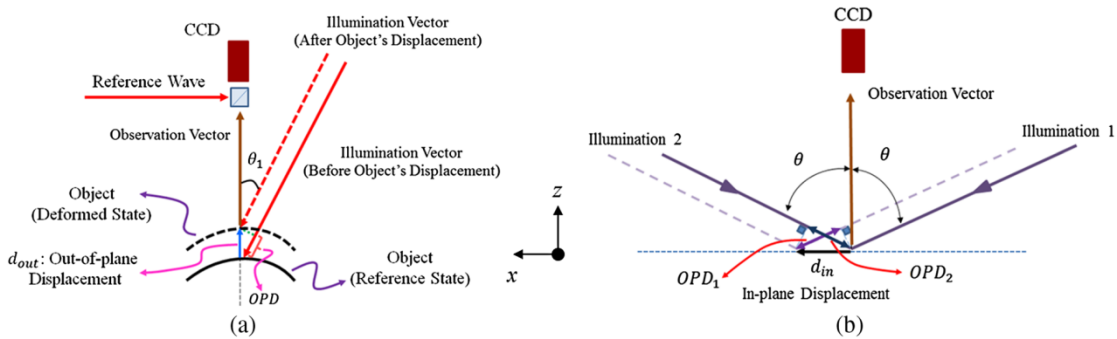


Fig. 5 Two displacement measurement schemes that are combined to achieve 3-D displacement measurements in the hybrid method: (a) configuration for out-of-plane (along z -axis) displacement measurements and (b) configuration for in-plane (along x - or y -axes) displacement measurements. The dashed lines represent illuminations after displacement occurs. OPD is OPL difference.

other and realize a self-reference configuration.²⁹ As shown in Fig. 5(b), once in-plane displacement, d_{in} , occurs, the OPL of each interfering beam changes, which causes a relative phase change between the two interfering beams. Figure 5(b) shows only one of the in-plane components of displacement, however, displacement components along both the x - and y -axes are independently measured with this method.

Equations (16) and (17) show the relation between OPD and the in-plane fringe-locus function corresponding to the in-plane displacement d_{in}

$$OPD_1 = OPD_2 = d_{in} \cos\left(\frac{\pi}{2} - \theta\right) = d_{in} \sin(\theta), \quad (16)$$

$$\Omega_{in} = \frac{2\pi}{\lambda} (OPD_{total}), \quad (17)$$

where $OPD_{total} = OPD_1 + OPD_2$. Using Eqs. (16) and (17), in-plane displacement, d_{in} , is calculated with

$$d_{in} = \frac{\lambda \Omega_{in}}{4\pi \sin(\theta)}, \quad (18)$$

where Ω_{in} is the in-plane fringe-locus Function, λ is the wavelength of the laser, and θ is the angle between the illumination and observation directions.

2.5 Experimental Setup

The schematic of the developed Digital Opto-Electronic Holographic System (DOEHS) is shown in Fig. 6. The DOEHS can measure microscale variations in shape as well as nanoscale displacements of the TM using both 3-D displacement measurement methods described in Sec. 2.4. The DOEHS consists of three main subsystems including laser delivery (LD), computing platform (CP), and optical head (OH). An external-cavity tunable diode laser capable of continuous tuning with minimal

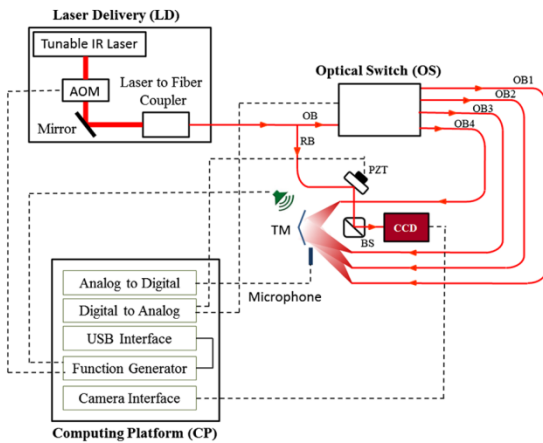


Fig. 6 Schematic of the developed holographic system for shape and 3-D displacement measurements. The laser delivery (LD) subsystem consists of a near-infrared tunable laser (with central wavelength of 780 nm), acousto-optic modulator (AOM), mirror, and laser to fiber coupler; the computing platform (CP) controls the recording parameter such as sound-excitation frequency and sound pressure level, phase-stepping, synchronizations for stroboscopic measurements, and controlling the optical switch (OS) for high-speed multiplexing between any of the object beams (OB1-OB4). The dashed lines are analog and digital signal lines.

mode hopping (New Focus, Velocity) is placed in the LD, which provides a near IR laser light with a central wavelength of 780 nm. A polarization maintaining fiber coupler (Thorlabs PM-780-HP) splits the light into two beams to be used as reference (10%) and object (90%) beams. A MEMS optical switch, with a response time of less than 0.5 ms (Thorlabs OSW 8104), is used to multiplex between the object beams (OB) of each illumination direction once triggered by a Digital to Analog signal. The CCD is illuminated with the RB through a beam splitter and through a piezo-mounted mirror that is used for phase stepping. A 5 Megapixel (2452×2054 pixels) digital camera with a pixel pitch of $3.45 \mu\text{m}$ in the OH is used for image recording and the CP acquires and processes images in either time-averaged or DE stroboscopic modes.³⁰ The sinusoidal output of the function generator is amplified by a unity gain power amplifier and is used to drive the speaker. A microphone with a calibrated probe tube was positioned just at the edge of the TM to make measurements of sound pressure. In stroboscopic measurements, the light illumination is synchronized with the sound-waveform by means of a digital pulse signal from the function generator to the AOM.

2.6 Determination of the Sensitivity Vectors

In the method of multiple illumination directions, accurate determination of the position of each illumination source is required to define the corresponding sensitivity vectors. A new technique is developed in which all the sensitivity vectors are obtained by automatic analyses of the images of a specular sphere illuminated from different directions in order to avoid the uncertainties introduced by manual measurements. As shown in Fig. (7), a specular sphere is placed in front of the imaging system to acquire images from all four directions of illumination. The center of the image is marked in the acquisition software LaserView³⁰ and the sphere is accurately located in this position and within a circular mask provided by the software to ensure that the sphere is placed along the optical axis of the holographic system. As shown in Fig. 7(a), the mirror-like reflection creates a specular highlighted area on the sphere.³¹ Each image is cropped and enhanced by image processing techniques that include histogram equalization, threshold definition, and edge detection. Then, a sphere is numerically fitted on the detected circular edge which represents the outline of the sphere. The normal vector of the fitted sphere at the centroid of the specular highlighted area, for each direction of illumination, defines the sensitivity vector, \mathbf{K}_i , which can be expressed as

$$\mathbf{K}_i = N_x(x_{0i}, y_{0i}), N_y(x_{0i}, y_{0i}), N_z(x_{0i}, y_{0i}), \quad (19)$$

where N_x , N_y , and N_z are components of the unit normal vector, and (x_{0i}, y_{0i}) are the centroid coordinates of each of the specular highlighted areas. To accurately determine the centroids, (x_{0i}, y_{0i}) , a circular Hough transform (CHT) algorithm is used. The Hough Transform can be used to determine the parameters of a circle when a number of points that fall on its perimeter are known.³² A circle with radius R and center (x_0, y_0) can be described with the parametric equations

$$x = x_0 + R \cos(\theta), \quad (20)$$

$$y = y_0 + R \sin(\theta), \quad (21)$$

in which the angle θ sweeps through the full 360 deg range and the points (x, y) trace the perimeter of the circle. The output of

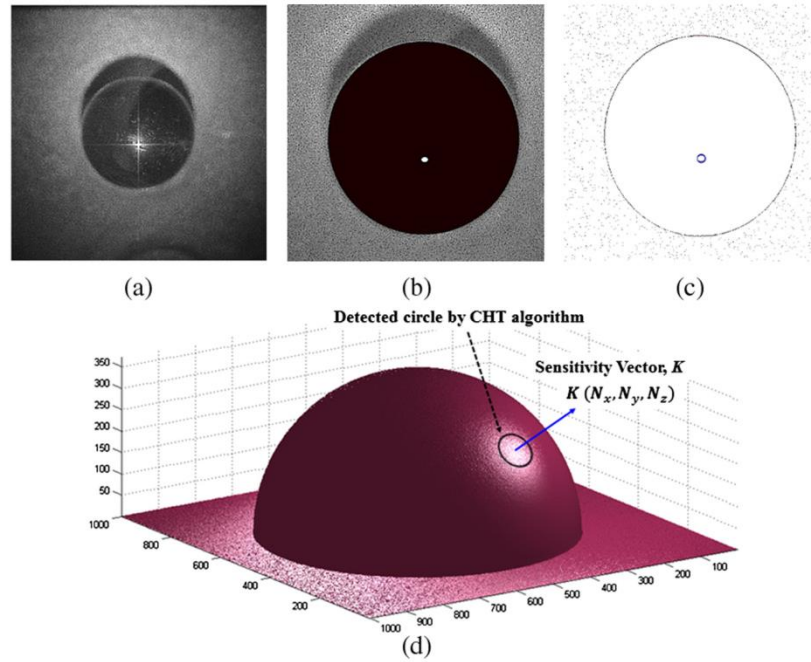


Fig. 7 Automatic determination of a sensitivity vector by use of a specular reflective sphere and circular Hough transformation (CHT): (a) image of a specular reflective sphere illuminated with one of the object beams, (b) cropped, enhanced image of the sphere, (c) CHT algorithm is used to detect the specular highlighted area and its centroid, and (d) the normal vector at the centroid of the detected highlighted area defines the sensitivity vector.

the CHT algorithm is the coordinate of the centroid of the specular highlighted area.

3 Results

3.1 Validation of Measuring Accuracy and Repeatability

Considering the acquisition speed of the 3-D holographic system and the time-dependent mechanical behavior of biological samples like the TM, we characterized the accuracy and repeatability of the measurements of the 3-D holographic system using measurements of artificial samples that have negligible time-varying behaviors. Based on the particular concave shape of the TM, a semispherical membrane with a geometry similar to the TMs is used. For 3-D displacement measurements of

non-flat membranes, the large illumination angles necessary for a well-conditioned 3-D holographic system create shadows on the surface of the membrane. Therefore, the maximum angles of illumination are limited by geometrical constraints induced by the membrane, leaving the holographic system with condition numbers greater than one, as described in Sec. 2.4.1. To calibrate the measuring system and to verify the accuracy of the measurements obtained with such non-ideal 3-D holographic configuration, 3-D displacement components are measured using both of the methods described in Sec. 2.4, in order to ensure that the obtained displacement components are accurate and independent of the measuring approach. Once the accuracy of the measurements is verified, repeatability of the stroboscopic measurements is tested and verified with sound-induced displacement measurements of a latex membrane.

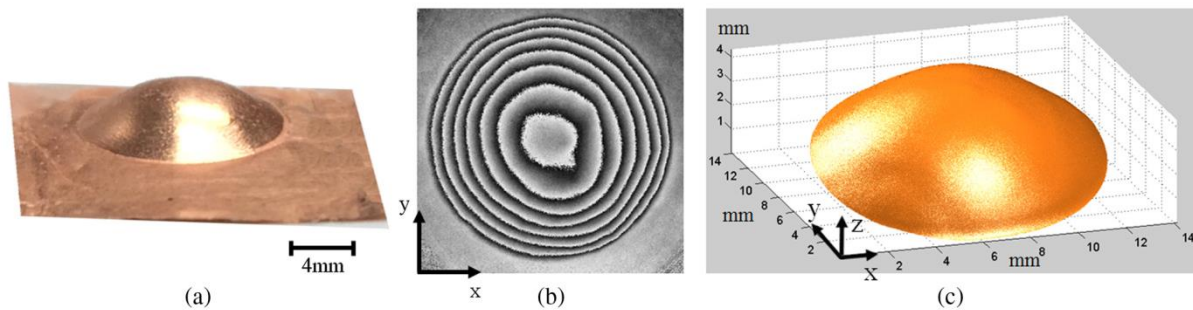


Fig. 8 Measurements of the shape of an artificial membrane using dual-wavelength holographic contouring: (a) semi-spherical membrane with a thickness of $25 \mu\text{m}$ and a radius of 6 mm , (b) wrapped optical phase corresponding to the shape of the membrane, and (c) 3-D scaled shape of the membrane.

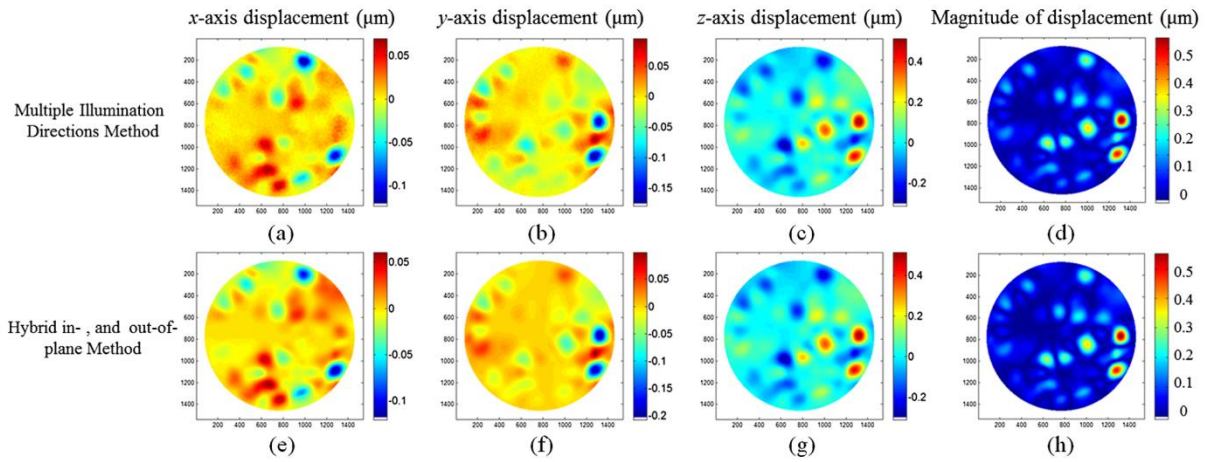


Fig. 9 3-D displacement components of a semi-spherical membrane excited mechanically with a piezoelectric shaker at a frequency of 25,418 Hz. Displacement components measured with the method of multiple illumination directions along (a) x-axis, (b) y-axis, (c) z-axis, (d) magnitude of displacement, and displacement components measured with the hybrid method along (e) x-axis, (f) y-axis, (g) z-axis, (h) magnitude of displacement. The correlation coefficient, \mathbb{R} , of the displacements component obtained with the two methods are 0.95, 0.96, 0.99, and 0.99 for displacement components along x-, y-, z-axes, and magnitude of displacement, respectively. All the displacements are in micrometers.

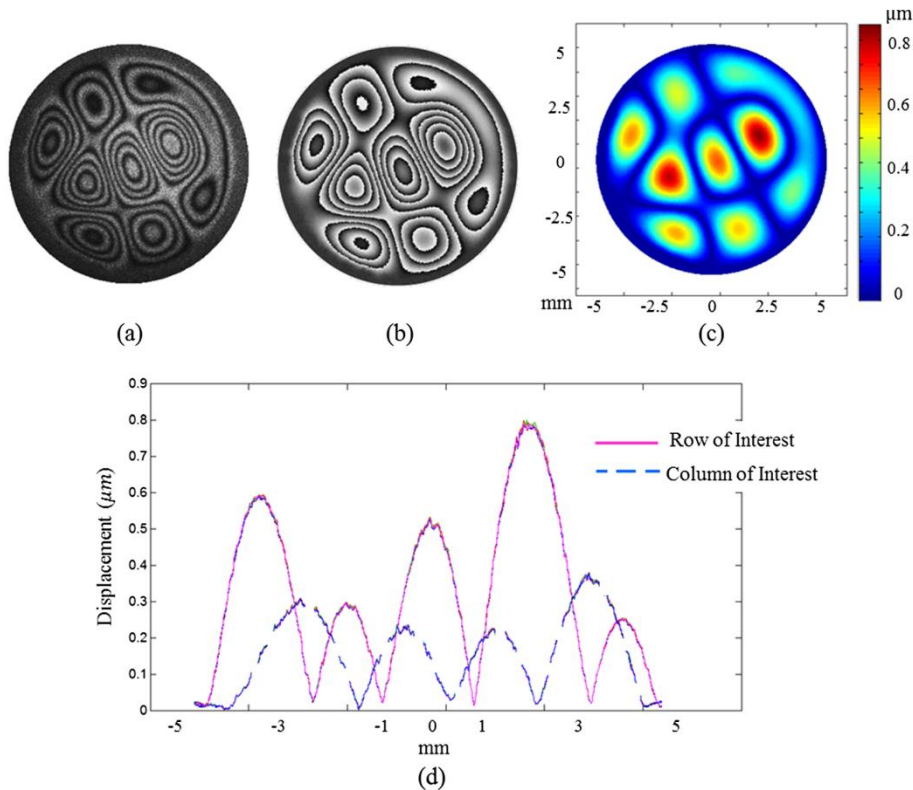


Fig. 10 Repeatability of the holographically obtained displacement measurements of a circular latex membrane acoustically excited with a tone of 2917 Hz at 91 dB SPL along one sensitivity vector. Representative DE (a) modulation, (b) wrapped optical phase, (c) map of the magnitudes of displacements averaged over six consecutive measurements, and (d) cross-sections of six displacement maps along specific horizontal (solid) and vertical lines (dashed), illustrating the repeatability of the measurements.

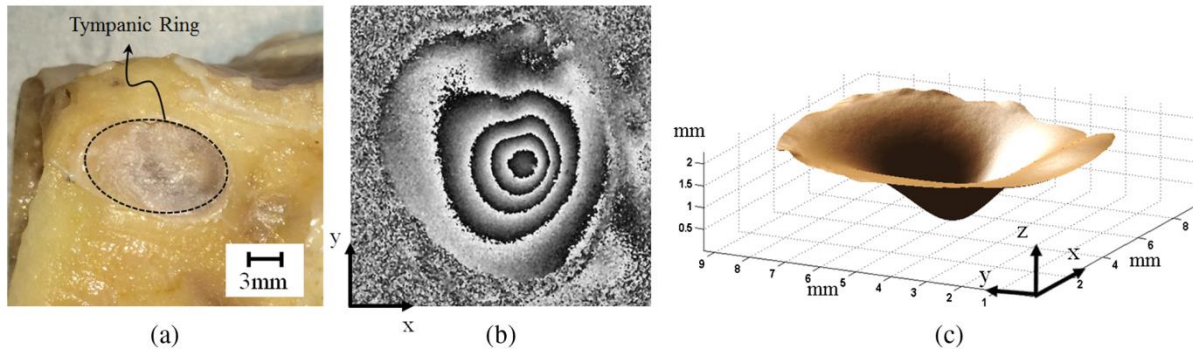


Fig. 11 Measuring the shape of a human tympanic membrane (TM) using dual-wavelength holographic contouring: (a) human temporal bone highlighting the tympanic ring, (b) wrapped optical phase corresponding to the shape of the TM, and (c) 3-D shape of the TM. The shape is measured with wavelengths of 780.2 and 780.6 nm.

3.1.1 Accuracy of 3-D displacement measurements

The shape and 3-D displacements of a thin semispherical membrane, shown in Fig. 8, with a radius of 6 mm and a thickness of 25 μm are measured with the developed holographic system. The shape of the membrane is measured with a dual-wavelength contouring method with wavelengths of 779.8 and 780.6 nm.

Figure 8(b) shows the wrapped optical phase, which is unwrapped and scaled to obtain the corresponding 3-D shape, as shown in Fig. 8(c).

The semispherical membrane is mounted on a piezoelectric shaker (JODON EV-100) that can operate at frequencies as high as 150 kHz. By sweeping the excitation frequency and

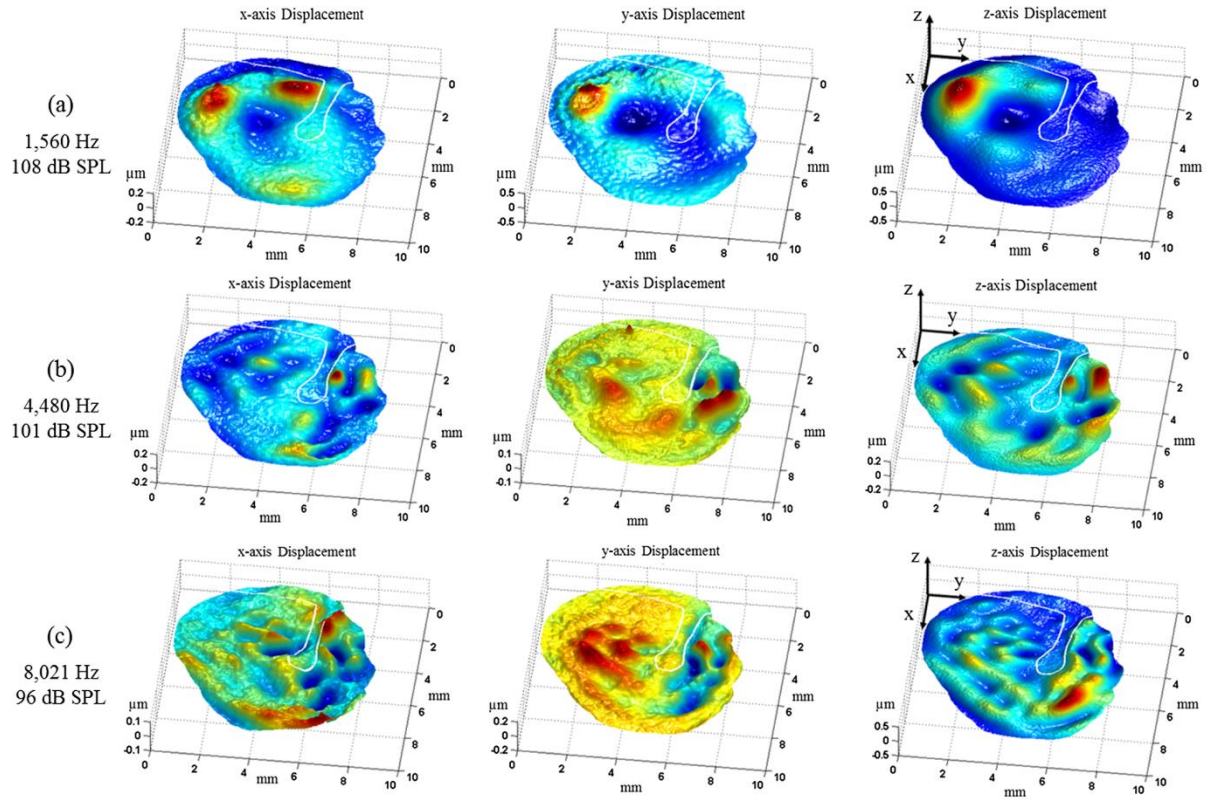


Fig. 12 Measured 3-D sound-induced displacement of a human TM along the x-, y-, and z-axes at three different tonal excitations. Magnitudes of displacements along x-, y-, and z-axes are (a) ± 220 , ± 250 , and ± 520 nm for tonal frequency of 1560 Hz at 108 dB SPL, (b) ± 200 , ± 120 , and ± 220 nm for tonal frequency of 4480 Hz at 101 dB SPL, and (c) ± 110 , ± 210 , and ± 510 nm for tonal frequency of 8021 Hz at 96 dB SPL. The diameter of the TM is 8 mm and the outline shows the handle of malleus (manubrium).

monitoring the membrane's time-averaged motions,^{10,16,33} an appropriate mode of vibration is chosen. Representative results are shown in Fig. 9, in which the membrane is excited with a frequency of 25,418 Hz and amplitude of 0.4 V. Comparisons of the displacement components along the x -, y -, z -axes, and the magnitudes of displacements obtained with both methods show correlation coefficients $>95\%$, illustrating that the measurements are accurate, repeatable, and independent of the measuring method.

3.1.2 Repeatability of stroboscopic measurements

Repeatability of the results obtained with the 3-D holographic system is tested and verified by a series of consecutive stroboscopic measurements of a 10 mm diameter latex membrane excited with a tone of 2917 Hz at 91 dB sound pressure level (SPL), as shown in Fig. 10. Figures 10(a)–10(c) show representative examples of the obtained modulation, wrapped optical phase, and magnitude of displacements, respectively. Furthermore, repeatability of the measurements is shown in Fig. 10(d), where vertical (shown with dashed lines) and horizontal (shown with solid lines) cross-sections of six consecutive displacement measurements lie on top of each other.

3.2 Shape and 3-D Sound-Induced Displacements of Human TM

The TM sample was part of a human right ear temporal bone from a 49-year-old male donor. The sample was prepared in accordance with previously established procedures.^{9,12} In order to have the least amount of shadow on the surface of the TM, all the bony structures around the TM were removed. In preparing the specimen, it was necessary to also open the middle ear cavity, however, those openings were filled by silicone impression materials (Westone Inc.) prior to these measurements in order to avoid and minimize the air flow through the middle ear cavity. Also, to enhance light reflection from the sample and to reduce the required camera exposure time in order to have a better signal to noise ratio, the lateral surface of the TM was coated with a solution of zinc oxide. The effect of this coating on the vibrational patterns of the TM has been shown to be negligible.^{9–11} The shape of the sample was measured with dual-wavelength holographic contouring, as shown in Fig. 11, with two wavelengths of 780.2 and 780.6 nm. Figure 11(b) shows the wrapped optical phase, which is unwrapped and scaled to obtain corresponding 3-D shape, as shown in Fig. 11(c).

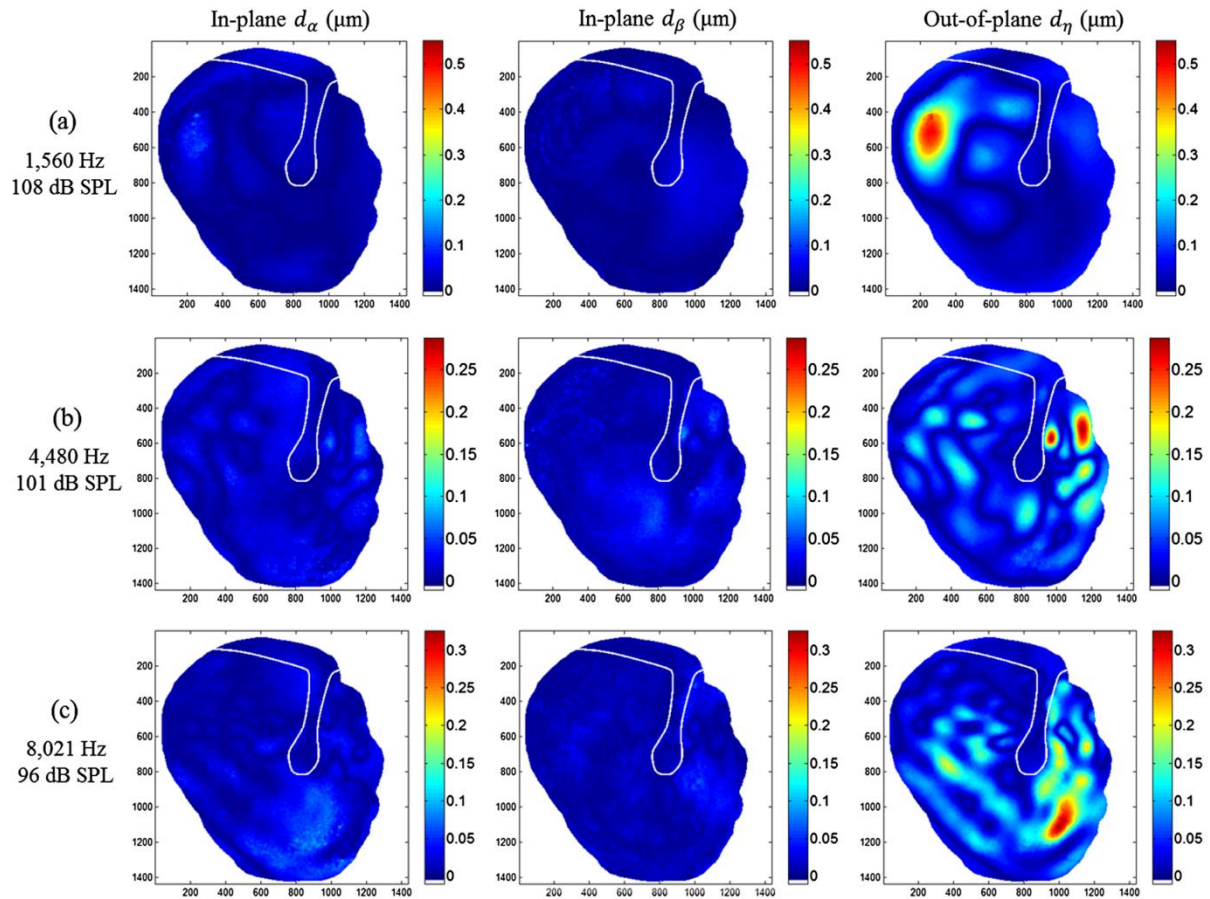


Fig. 13 In-plane and out-of-plane sound-induced motions of a human TM excited with frequency of (a) 1560 Hz at 108 dB SPL, (b) 4480 Hz at 101 dB SPL, and (c) 8021 Hz at 96 dB SPL. It can be clearly seen that tangential (in-plane) components are negligible and the motions are mainly normal (out-of-plane) to the TM surface. Displacements are in the unit of micrometers.

Tones with different frequencies were used to stimulate the membrane and 3-D sound-induced displacement components of the surface of the TM were acquired. Figure 12 shows 3-D displacement components of the TM along the x -, y -, and z -axes produced by tones of 1560 Hz at 108 dB SPL, 4480 Hz at 101 dB SPL, and 8021 Hz at 96 dB SPL. The levels were selected to generate measurable sound-induced TM displacements. As shown in Fig. 12, as sound excitation frequency increases, the number of local maxima in the displacement patterns also increases and sound-induced motion patterns of the TM become more complex.

Combining data obtained from the shape of the membrane, shown in Fig. 11, with measured 3-D sound-induced displacement components, shown in Fig. 12, displacement components tangent (in-plane) and normal (out-of-plane) to the TM surface are obtained. A numerical rotation matrix is used³⁴ to rotate the original Euclidean coordinate system of the measuring system (x, y, z), so that the new coordinate system (α, β, η) has unit vectors tangent and normal to the TM surface. Figure 13 shows the results of the rotation of the coordinate system, where rotated displacements have components tangent (in-plane components d_α and d_β), and normal to the TM surface (out-of-plane component d_η). As shown in this figure, in-plane components are much smaller than out-of-plane components (<20%), so that the displacement vectors can be considered to be mainly normal to the surface of the TM.

These data support hypotheses based on considering the motions of the TM similar to those of thin-shells, in which the tangential motions' components are negligible and the motion vectors are hypothesized to be mainly along the normal vector of the surface of the membrane.^{8,9}

4 Conclusions

While there are many hypotheses of how the TM couples sound to the rest of the ear, there is little data to support them.^{2,3,8}

Knowledge about the shape and 3-D sound-induced displacement of the TM are necessary sets of data in order to better understand the acousto-mechanical transformer behavior of the mammalian TMs. In this direction, we are developing optoelectronic holographic systems capable of measuring shape with sub-millimeter resolution, and 3-D sound-induced displacement of the TM with sub-micrometer resolution. Combining the measured shape and 3-D sound-induced displacements of the TM at each point on its surface enables characterization of the motion's components tangent and normal to the TM surface. Results show that the tangential motions' components are much smaller (<20%) than the out-of-plane motions' components. These results are consistent with the modeling of mammalian TM as thin-shells in which the tangential motions' components are negligible.

Appendix: Rotation Matrix used to Obtain In-Plane and Out-of-Plane Displacements

The original Euclidean coordinate system x, y, z is mathematically rotated in order to obtain the local in-plane and out-of-plane displacement components. In the holographic system and based on the definition of the sensitivity vectors, the observation vector \mathbf{Z} , i.e., a vector perpendicular to the CCD sensor, has unit vector components $Z_x, Z_y,$ and Z_z equal to $[0, 0, 1]$. Also, by having the 3D shape of the membrane, the unit normal vector, \mathbf{N} , at every point on the surface of the TM is quantified. Since, both \mathbf{N} and \mathbf{Z} are unit vectors, the angle between them is calculated with dot product of the two vectors; and the cross product of these two vectors provide a vector, \mathbf{U} , normal to both of them that, in this case, is tangent to the local plane of the membrane and is considered as the axis of rotation.

The rotation matrix R , is used to rotate the original displacement vector $\mathbf{d}(d_x, d_y, d_z)$, based on the rotation angle θ and the unit vector of the axis of rotation \mathbf{U} with

$$R = \begin{bmatrix} \cos \theta + U_1^2(1 - \cos \theta) & U_1 U_2(1 - \cos \theta) - U_3 \sin \theta & U_1 U_3(1 - \cos \theta) + U_2 \sin \theta \\ U_2 U_1(1 - \cos \theta) + U_3 \sin \theta & \cos \theta + U_2^2(1 - \cos \theta) & U_2 U_3(1 - \cos \theta) - U_1 \sin \theta \\ U_3 U_1(1 - \cos \theta) - U_2 \sin \theta & U_3 U_2(1 - \cos \theta) + U_1 \sin \theta & \cos \theta + U_3^2(1 - \cos \theta) \end{bmatrix} \quad (22)$$

where $\mathbf{U} = (U_1, U_2, U_3)$ is the unit vector of the axis of rotation of the observation direction (z -axis in the original measuring coordinate system), and θ is the angle of rotation. Therefore, as shown in Fig. 14, at each point m, n , the rotated displacement vector \mathbf{d}_{rot} has components tangent (\mathbf{d}_α and \mathbf{d}_β)

and normal (\mathbf{d}_η) to the local TM plane and is calculated with the matrix multiplication of the rotation matrix, R , with the original displacement vector \mathbf{d} with

$$\mathbf{d}_{rot}(m, n) = R \times \mathbf{d}(m, n). \quad (23)$$

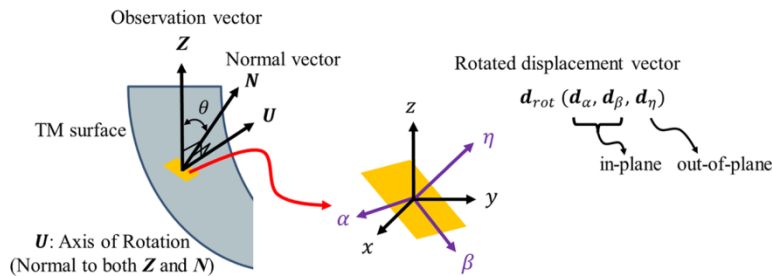


Fig. 14 Transformation of the global measuring coordinate system x, y, z to the local coordinate system α, β, η , of the TM. The observation vector \mathbf{Z} is rotated θ degrees along the axis of rotation \mathbf{U} .

Acknowledgments

This work was supported by the National Institute on Deafness and other Communication Disorders (NIDCD), the National Institutes of Health (NIH), Massachusetts Eye and Ear Infirmary (MEEI), and Mechanical Engineering Department at Worcester Polytechnic Institute. We also acknowledge the support of all of the members of the CHSLT labs at WPI and Eaton-Peabody labs at MEEI, in particular Ellery Harrington and Ivo Dobrev.

References

1. C. D. Geisler, *From Sound to Synapse: Physiology of the Mammalian Ear*, Oxford University Press, New York (1998).
2. S. Puria and C. Steele, "Tympanic-membrane and malleus-incus-complex co-adaptations for high-frequency hearing in mammals," *Hear. Res.* **263**(1), 183–190 (2010).
3. R. Z. Gan et al., "Finite element modeling of sound transmission with perforations of tympanic membrane," *J. Acoust. Soc. Am.* **126**(1), 243–253 (2009).
4. O. Rochefoucauld and E. S. Olson, "A sum of simple and complex motions on the eardrum and manubrium in gerbil," *Hear. Res.* **263**(1), 9–15 (2010).
5. J. P. Fay, S. Puria, and C. R. Steele, "The discordant eardrum," *Proc. Natl Acad. Sci.* **103**(52), 19743–19748 (2006).
6. X. Zhang et al., "Experimental and modeling study of human tympanic membrane motion in the presence of middle ear liquid," *J. Assoc. Res. Otolaryngol.* **15**(6), 867–881 (2014).
7. J. Tonndorf and S. M. Khanna, "Tympanic-membrane vibrations in human cadaver ears studied by time-averaged holography," *J. Acoust. Soc. Am.* **57**(4B), 1221–1233 (1972).
8. W. F. Decraemer and W. R. J. Funnell, "Anatomical and mechanical properties of the tympanic membrane," in *Chronic Otitis Media. Pathogenesis-Oriented Therapeutic Management*, B. Ars, Eds., pp. 51–84, Kugler Publications, Amsterdam, The Netherlands (2008).
9. J. J. Rosowski et al., "Measurements of three-dimensional shape and sound-induced motion of the chinchilla tympanic membrane," *Hear. Res.* **301**, 44–52 (2013).
10. J. J. Rosowski et al., "Computer-assisted time-averaged holography of the motion of the surface of the tympanic membrane with sound stimuli of 0.4 to 25 kHz," *Hear. Res.* **253**(1–2), 83–96 (2009).
11. J. M. Flores-Moreno et al., "Holographic otoscope for nanodisplacement measurements of surfaces under dynamic excitation," *Scanning* **33**(5), 342–352 (2011).
12. J. T. Cheng et al., "Motion of the surface of the human tympanic membrane measured with stroboscopic holography," *Hear. Res.* **263**, 66–77 (2010).
13. U. Schnars et al., *Digital Holography and Wavefront Sensing*, pp. 39–68, Springer, Berlin, Heidelberg (2015).
14. I. Yamaguchi and T. Zhang, "Phase-shifting digital holography," *Opt. Lett.* **22**(16), 1268–1270 (1997).
15. C. M. Vest, *Holographic Interferometry*, John Wiley and Sons, Inc., New York (1979).
16. R. J. Pryputniewicz, "Time average holography in vibration analysis," *Opt. Eng.* **24**(5), 245843 (1985).
17. D. De Greef et al., "Viscoelastic properties of the human tympanic membrane studied with stroboscopic holography and finite element modeling," *Hear. Res.* **312**, 69–80 (2014).
18. M. Khaleghi et al., "Digital holographic measurements of shape and three-dimensional sound-induced displacements of tympanic membrane," *Opt. Eng.* **52**(10), 101916 (2013).
19. J. Leval et al., "Full-field vibrometry with digital Fresnel holography," *App. Opt.* **44**(27), 5763–5772 (2005).
20. G. Pedrini, W. Osten, and M. E. Gusev, "High-speed digital holographic interferometry for vibration measurement," *App. Opt.* **45**(15), 3456–3462 (2006).
21. M. S. Hernández-Montes et al., "Digital holographic interferometry applied to the study of tympanic membrane displacements," *Opt. Laser Eng.* **49**(6), 698–702 (2011).
22. C. Furlong and R. J. Pryputniewicz, "Absolute shape measurements using high-resolution optoelectronic holography methods," *Opt. Eng.* **39**(1), 216–223 (2000).
23. P. Bergström et al., "Shape verification using dual-wavelength holographic interferometry," *Opt. Eng.* **50**(10), 101503 (2011).
24. T. Kreis, *Handbook of Holographic Interferometry*, Wiley-VCH Verlag GmbH & Co. KGaA, Weinheim, Germany (2005).
25. W. F. Decraemer et al., "Three-dimensional vibration of the malleus and incus in the living gerbil," *J. Assoc. Res. Otolaryngol.* **15**, 483–510 (2014).
26. A. Alamdari et al., "Kinetostatic optimization for an adjustable four-bar based articulated leg-wheel subsystem," in *IEEE International Conference on Intelligent Robots and Systems (IROS 2014)*, pp. 2860–2866, IEEE, Piscataway, New Jersey (2014).
27. G. H. Golub and C. F. Van Loan, *Matrix Computations*, JHU Press, Baltimore, Maryland (2012).
28. W. Osten, "Some considerations on the statistical error analysis in holographic interferometry with application to an optimized interferometer," *J. Mod. Opt.* **32**(7), 827–838 (1985).
29. F. Mendoza Santoyo, M. C. Shellabear, and J. R. Tyrer, "Whole field in-plane vibration analysis using pulsed phase-stepped ESPI," *Appl. Opt.* **30**(7), 717–721 (1991).
30. E. Harrington et al., "Automatic acquisition and processing of large sets of holographic measurements in medical research," *Opt. Meas. Model. Metrol.* **5**, 219–228 (2011).
31. G. Earl et al., "Reflectance transformation imaging systems for ancient documentary artefacts," in *Electronic Visualization and the Arts BCS BCS*, London (2011).
32. T. J. Atherton and D. J. Kerbyson, "Size invariant circle detection," *Image Vis. Comput.* **17**(11), 795–803 (1999).
33. A. Asundi and V. R. Singh, "Amplitude and phase analysis in digital dynamic holography," *Opt. Lett.* **31**(16), 2420–2422 (2006).
34. C. J. Taylor and D. J. Kriegman, "Minimization on the Lie group SO(3) and related manifolds," Yale University, New Haven, Connecticut (1994).

Morteza Khaleghi is a PhD candidate in mechanical engineering at Worcester Polytechnic Institute, Worcester, Massachusetts. His research interests include biomedical imaging and developments of optical and nondestructive metrology systems.

Cosme Furlong is an associate professor of mechanical engineering at Worcester Polytechnic Institute, Worcester, Massachusetts, working in mechanics, optical metrology, and nanoengineering science and technology.

Mike Ravicz is an associate scientist and biomechanical engineer at Massachusetts Eye and Ear Infirmary, Boston, Massachusetts, exploring the mechanics and acoustics of the external, middle, and inner ear as well as working in signal processing and noise and vibration control.

Jeffrey Tao Cheng is an instructor in otology and laryngology at Massachusetts Eye and Ear Infirmary, Boston, Massachusetts, working on middle-ear mechanics and ear tissue biomechanics through measurements and modeling.

John J. Rosowski is a professor of otology and laryngology, and also of health sciences and technology, working in acoustics and mechanics of the external, middle, and inner ear, with an interest in comparative middle and external ear structure and function.

10. Paper D: 4D Measurements of the in-Plane and out-of-plane motion of the human tympanic membrane

Overview

In this paper, being prepared for submission to the Journal of the Acoustical Society of America, the developed 3D holographic methodologies are used to study multiple human TM samples in order to better understand the general behavior of sound-induced motions of the human TMs. The main focus of this Chapter is on the study of relative sizes of in-plane motions (components tangent to the local plane of the TM) with respect to the out-of-plane motions (components normal to the local plane of the TM). Shape and sound-induced motions of three human TM samples are measured with our 3D holographic system. Four-dimensional sound-induced motions of the TM (i.e., motions along x , y , z , at each temporal phase θ) are quantified, which in turn, using FFT algorithms enable both magnitudes and phases of three-dimensional sound-induced motion of human TMs along all three axes. A numerical algorithm is developed and implemented to rotate the original global Euclidean coordinates of the measuring system (x , y , z), so that new local coordinate systems (α , β , η) have unit vectors that are tangent (in-plane) and normal (out-of-plane) to the TM surface. The general conclusion is that the in-plane components are generally 10 to 20 dB smaller than the out-of-plane components, which is consistent with the TM acting as a Kirchhoff-Love's thin-shell dominated by out-of-plane motion with little in-plane motion. These results argue against the presence of large in-plane motion components over much of the auditory range, and reduce the probability of the involvement of such motions in acousto-mechanical energy transformation.

Four dimensional (Space + Time) Measurements of the In-Plane and Out-of-Plane Motion of the Human Tympanic Membrane

Morteza Khaleghi ^a, Jeffrey Tao Cheng ^{b,c}, Cosme Furlong ^{a,b,c}, and John J. Rosowski ^{b,c}

^a Center for Holographic Studies and Laser micro-mechaTronics (CHSLT),
Mechanical Engineering Department, Worcester Polytechnic Institute, Worcester, MA 01609

^b Eaton-Peabody Laboratory, Massachusetts Eye and Ear Infirmary, Boston, MA 02114

^c Department of Otolaryngology, Harvard Medical School, Boston, MA 02114

We develop and describe new computer-controlled digital holographic techniques to measure three-dimensional (3D) shape and sound-induced motion of the surface of the tympanic membrane (TM), and present new stroboscopic holography measurements of 3D nano-scale displacements of the surface of the tympanic membrane (TM) in cadaveric human ears in response to tonal sounds. The displacement measurements are made concurrently with detailed micron-scale measurements of the 3D shape of the lateral surface of the TM using the same holographic recording camera. The combination of these measurements allows us to calculate the out-of-plane (normal to the surface) and in-plane (tangential) motion components at over 1,000,000 points on the TM surface with a high-degree of accuracy and sensitivity. A general conclusion is that the in-plane motion components are significantly smaller than the out-of-plane motions calculated from our data whenever the sensitivity and signal-to-noise of our displacement measurements allow accurate determination of the different displacement components. These conditions are most often compromised with higher-frequency sound stimuli where the overall displacements are smaller, and the spatial density of holographic fringes is higher, both of which increase the uncertainty in our measurements. Our results are consistent with the TM acting as a Kirchhoff-Love's thin shell dominated by out-of-plane motion with little in-plane motion, at least with stimulus frequencies up to 8 kHz. These results argue against the presence of large in-plane motion components over much of the auditory range, and reduce the probability of the involvement of such motions in acousto-mechanical energy transformation.

Keywords: 4D motion measurements; Digital Holography; Kirchhoff-Love Thin-shell; Tympanic Membrane.

1. Introduction

It is recognized that sound-induced motions of the tympanic membrane (TM) are the first step in the transduction of airborne sound energy to the mechanical energy associated with motion of the sensory organs within the inner ear; however, our knowledge of the workings of the TM is rather superficial. While there are multiple model descriptions of TM structure and function, progressing from simple piston models (Shaw and Stinson, 1983), through curved-membrane catenary-dependent models (Goll and Dalhoff, 2011), to complex 3D finite element models (e.g., Funnell, Decreamer and Khanna, 1987; Willams and Lesser 1990; Blayney, Willimas and Rice 1997; Gan et al. 2002; Koike, Wada and Kobayashi, 2002; Fay et al., 2005), there is no complete description of how the surface of the TM moves in response to sound to test these models. The most complete descriptions of sound-induced TM motion come

from recent stroboscopic holography measurements that quantify the sound-induced displacement at over 500,000 points on the TM surface, but only along a single measurement direction (Cheng et al. 2010, 2013). While some 3D motion measurements describing the displacement of selected regions of the TM exist (Jackson, Cai and Puria 2012), there has not been a report of the 3D motion of the entire TM surface.

An approximation of such motions has been described from a combination of nano-scale TM displacement measurements with micro-scale measurements of the shape of the lateral surface of the TM, both made on the TM surface in a cadaveric chinchilla preparation (Rosowski et al., 2013; Khaleghi et al., 2013). The technique employed the Kirchhoff-Love approximation of thin shell behavior (which suggests that small motions - much smaller than the thickness - in shells of appropriate

thickness and shape occur in the direction ‘normal’ to the local surface of the shell) to estimate the motion normal to the surface at each measurement point. This procedure ‘corrected’ the measure 1D motions measured along the holographic camera axis for significant variations in the direction normal to the curved surface of the TM (Kraus 1967; Saada 2009). The computed motions ‘normal’ to the TM surface showed more spatially uniform patterns in TM motion magnitude, than were observed in the raw 1D measurements (Rosowski et al. 2013; Khaleghi et al. 2013).

In the present paper we expand on our description of TM motion by directly measuring the 3D motion as well as the shape. This methodological advancement is described in the methods section. The combination of 3D motion measurements and shape allow us to not only describe the motions normal to the surface, but now we also quantify motions that are tangential to the local TM surface, the so called in-plane motions. Quantification of these motions allows us to test the applicability of the Kirchhoff-Love thin shell approximation and also investigate suggestions that in-plane motions are involved in the transformation of acoustic energy into the mechanical energy associated with the motion of the malleus and ossicles (Goll and Dalhoff 2011; Jackson, Cai and Puria 2012). Descriptions of our methods and some preliminary results have been published previously (Khaleghi et al., 2015).

2. Material and Methods

2.1 Preparation and the use of human temporal bones

All of the measurements of TM motion we report here are made in three de-identified normal human temporal bones from donors of age 49 (TM1, male), 77 and 46 (TM2 and TM3, female) years. The bones were either fresh or previously frozen at the time of preparation. The preparation of the temporal bones has been described previously (Cheng et al., 2013, in press) and included: (a) removal of the cartilaginous and most of the boney ear canal to expose over 90% of the TM surface, (b) drilling out the mastoid and opening the facial recess to inspect the stapes and round window, and (c) opening the epitympanic space to view the malleus and incus head. After preparation, the bones were lightly fixed in Thiel solution (Thiel 2002) for more than 2 weeks; this degree of fixation has been demonstrated to have only small effects on sound-induced stapes and umbo velocities (Stieger et al. 2012), and has been demonstrated to have little effect on the patterns of TM motion in treated human temporal bones (Cheng and Guignard 2015). The lateral surface of the TM was then painted with a thin coat of zinc oxide (ZnO) suspended in distilled water at a concentration of 60 mg/cc to increase the light reflected

from the surface. Such painting has been demonstrated to have little effect on the measured motion (Rosowski et al. 2009; Cheng et al. 2013).

The temporal bones were then mounted on a 3D positioner placed on a large vibration-isolated table, which also supported the multiple lasers and optical devices needed for the holographic measurements (Hernandez-Montez et al. 2009; Flores-Moreno et al. 2011). The bones were positioned such that the planes of their tympanic rings were parallel to the holographic recording CCD camera, and the TM image was centered in the camera plane. The sound stimulus from a speaker mounted on the table was conducted to the ear via a flexible tube, which terminated several centimeters in front of the lateral surface of the TM. A pre-calibrated probe-tube microphone positioned near the intersection of the TM and its ring was used to record stimulus sound pressure. The stimuli were all continuous tones (Cheng et al., 2010; 2013).

2.2 Digital Holography

2.2.1 Holography determines the change in the optical path length between an object and a reference position

Digital holography uses changes in the accumulated optical phase between an object and a recording camera plane to quantify the shape or motion of the object (Hernandez-Montez et al., 2009; Rosowski et al., 2013, Khaleghi et al., 2015). The differences in optical phase can arise due to motion of the object (Cheng et al., 2010), or a change in the wavelength of the laser illumination of a stationary object (Khaleghi et al., 2013).

2.2.2 Measurements of shape using dual-wavelength holographic contouring

Our technique for measuring the shape of the TM has been described in previous articles (Khaleghi et al., 2013; Rosowski et al., 2013). Briefly, the shape is estimated from correlation fringe pattern produced by combining a holographic image gathered using a laser with wavelength λ_1 , and a second image gathered using a different laser wavelength λ_2 . The result is a two-dimensional pattern with fringes that code differences in the optical phase captured on the plane of the recording camera, $\Delta\phi(x, y)$, produced by the two different wavelengths as they propagate along a fixed *Optical Path Length (OPL)* that includes the distance light travels from the illumination point, to the reflecting surface, and on to the recording camera, i.e.:

$$\Delta\phi(x, y) = \frac{2\pi}{\Lambda} OPL(x, y), \quad (1)$$

where Λ is the synthetic wavelength defined by

$$\Lambda = \frac{\lambda_1 \lambda_2}{|\lambda_1 - \lambda_2|} . \quad (2)$$

In practice both λ_1 and λ_2 where near 780 nm and differed by ≈ 0.5 nm, such that $\Lambda \approx 1.2$ mm. Since our digital holographic techniques are able to distinguish optical phase difference equivalent to $\sim 1/50$ of a wavelength, the functional sensitivity of our shape measurements is $\sim 24\mu\text{m}$.

2.2.3 Measurements of Motion: Stroboscopic holography

Our techniques for determining the sound-induced motion at hundreds of thousands of points on the surface of the TM have been described in detail elsewhere (Hernandez-Montes et al., 2009; Cheng et al., 2013; Khaleghi et al., 2015). As in the shape determinations, displacement measurements use holographic interference patterns to describe changes in the optical phase; however, the phase changes occur due to change in *OPL* that results from a change in the position of the object between two time instants, while the wavelength of illumination λ is fixed.

In order to ‘freeze’ the motion of an object vibrating in response to a 0.1 to 20 kHz acoustic stimulus, we use a high-speed acousto-optic modulator to strobe the illuminating laser such that it is only illuminating the optical path for a brief instant of time during each cycle of acoustic stimulation (Hernández-Montes et al., 2009). In practice the duration of the illumination is 2 to 5% of the period of the acoustic stimulus. The laser ‘strobe’ is triggered at a specific phase of the acoustic stimulus, and for each stimulus frequency, eight holographic recordings are performed each at a regularly-spaced phase of the acoustic stimulus ($0, \pi/4, \pi/2, \dots 7\pi/4$). From these recordings we reconstruct the cyclic motion at each point on the surface of the TM. We then use Fourier transforms to describe the magnitude and phase of the motion relative to the magnitude and phase of the acoustic stimulus.

2.2.4 Definition of Holographic coordinate system and calculation of sensitivity vectors

An important part of this paper is our methods for quantifying motion and shape in three dimensions, and fundamental to that discussion is the definition of the directionality of our measurement system, which is summarized in Figure 1. The nearly planar tympanic ring that supports the outer edge of the TM is positioned in the *Object Plane*, parallel to the imaging *Camera Plane* of the digital camera. Both of these planes are orthogonal to the *z*-axis, while the *x*- and *y*-axes fall within the object and camera planes.

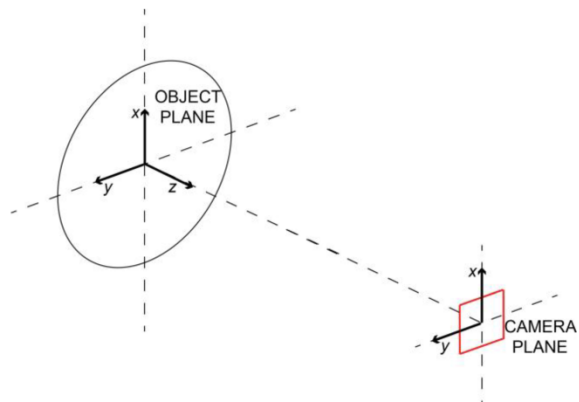


Figure 1. Definition of the camera based Cartesian coordinates with *z* increasing with displacements toward the camera and *x* and *y* defined by the right-hand rule. The camera plane and object plane are parallel.

While Figure 1 describes the physical orientation of the camera and the TM, part of our methods include altering the sensitivity of the holograms recorded by the camera plane to motions of different direction: these alterations occur by varying the direction of the *illumination path* while maintaining a constant *observation path* (Figure 2). To understand the alteration in directional sensitivity of the recorded hologram, we need to define the *unit illumination direction vector*, $\overline{K_I}(x,y)$, and the *unit observation direction vector*, $\overline{K_O}(x,y)$ at each point of the recorded hologram (Figure 2). While $\overline{K_I}$ and $\overline{K_O}$ are dimensionless, the *sensitivity vector*, $\overline{K_S}(x,y)$, is defined by the product of the wave number of the laser light and the vector difference $\frac{2\pi}{\lambda}(\overline{K_O} - \overline{K_I})$, and describes the directional sensitivity of the interference patterns recorded at each point on the hologram. In other words, holographic interferometry measures motions in the direction of the sensitivity vector of the system with sensitivity proportional to the magnitude of $\overline{K_S}(x,y)$, and motion components perpendicular to the sensitivity vector are not captured.



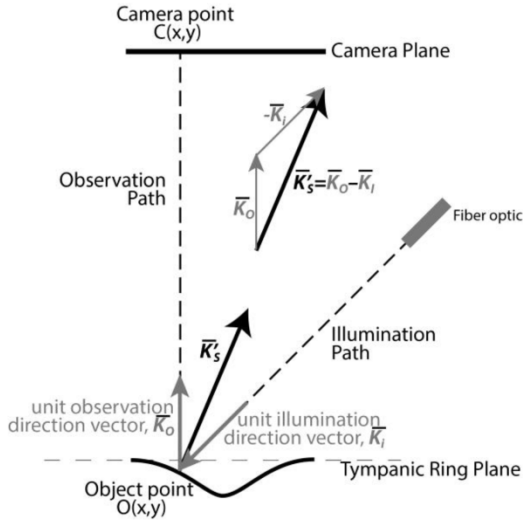


Figure 2. A schematic of the determination of the holographic sensitivity vector \overline{K}_S from the unit illumination vector \overline{K}_I and the unit observation direction vector \overline{K}_O , where $\overline{K}_S = \frac{2\pi}{\lambda} \overline{K}_I = \frac{2\pi}{\lambda} (\overline{K}_O - \overline{K}_I)$. Variations in the direction of \overline{K}_I cause variations in the direction and magnitude of \overline{K}_S .

2.2.5 Description of transformation of three independent measurements to compute motion along three coordinates

In order to determine all three Cartesian components of displacement, at least three independent equations, obtained by varying the sensitivity vector, \overline{K}_S , are needed (Figure 2). To reduce errors, 2D optical phase change maps were obtained from four sensitivity vectors and the 3D displacement vector at each point on the TM surface calculated by the least-squares method (Pryputniewicz and Bowley, 1978). At each x, y point on the TM surface:

$$\{\mathbf{d}\} = [[\mathbf{S}]^T [\mathbf{S}]]^{-1} \{[\mathbf{S}]^T \{\Omega\}\} \quad (3)$$

where $\{\mathbf{d}\}$ is the 3×1 column vector describing the x, y and z components of displacement, and $[\mathbf{S}]$ is the 4×3 sensitivity matrix describing the x, y and z components of the four sensitivity vectors \overline{K}_S , and $\{\Omega\}$ is the 4×1 column vector describing the holographically determined fringe locus functions that describe the motion-induced difference in optical phase in each of the four measurements. The details are provided in Appendix A.

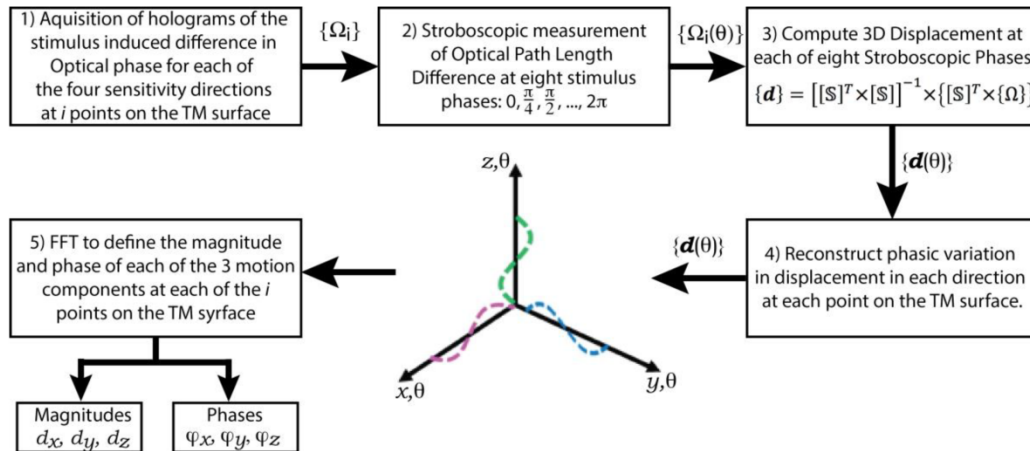


Figure 3. Schematic of the calculation of the magnitude and phase of the Cartesian coordinate representation of the 3D displacements of the TM surface. (1) At all points on the TM surface, (2) we define $\{\Omega\}$ the fringe locus function that describes the optical phase difference due to displacement at 8 stimulus phases for all four sensitivity directions, (3) $\{\Omega\}$ and the sensitivity matrix are used to compute $\{\mathbf{d}\}$ which describes the three Cartesian components of the displacement at each point, and at each phase of the stimulus, (4) The phasic motion of each Cartesian component is reconstructed, and (5) Fourier transformation defines the magnitude and phase of each of the three Cartesian motion components.

The four illumination directions were chosen to produce linearly independent sensitivity vectors. Due to the inverted conical shape of the TM and the TM's position recessed within the remnant of the boney ear canal, most

illumination directions produced noticeable shadows on the TM surface. The illumination paths were chosen to reduce such shadows as much as possible and maintain adequate independence (Khaleghi et al., 2015).

2.3 Quantification of the magnitude and phase of the three dimensional motions

The displacement vector $\{\mathbf{d}\}$ containing the three Cartesian components of 3D motion was calculated at each of the i points on the TM surface for each of the eight stimulus phases. As shown in Figure 3, fringe locus functions, Ω_i , corresponding to the sound-induced difference in optical phase at each point on the TM along every sensitivity direction, are stroboscopically measured at eight different instances of the acoustic waveform (Cheng 2010). Using Eq. 3, 3D sound-induced motions of the TM are calculated at each of the eight stimulus phases, and used to define the variation in the component motion in each of the Cartesian directions as a function of stimulus phase. The Fourier magnitudes (d_x, d_y, d_z) and phase-angles ($\varphi_x, \varphi_y, \varphi_z$) of the phasic displacements of each component were then computed for each point on the TM surface.

2.4 Use of shape to define in- and out-of-plane motions

According to Kirchhoff–Love thin plate theory, in cases where surface displacements are small relative to plate dimensions, the motion of the TM is well approximated by out-of-plane motions along the direction normal to the TM surface, and consequently, in-plane components of displacement tangent to the surface of the TM are negligible (Kraus 1967; Saada 2009). The theory also suggests that knowledge of the unit normal vector η calculated from the shape of the TM at each point on the TM surface (Figure 4), and a measure of motion in one direction, can be used to compute the motion normal to the membrane surface \mathbf{d}_η . Calculations of \mathbf{d}_η based on shape and a 1D measurements and shape and our 3D measurements will be compared.

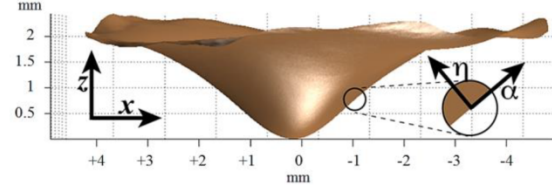


Figure 4. A 2D view of the 3D shape of a human TM. The illustrated x-z plane is orthogonal to the x-y plane of the camera, which is roughly aligned with the plane of the tympanic ring. Increasing x corresponds to superior > inferior. Increasing y is anterior > posterior. Increasing z is medial > lateral. The umbo is the apex of the conical TM. The inset shows the transformation to the local coordinate system at a point on the TM surface, where $\eta(x,y)$ is normal (out-of-plane) to the membrane surface.

Since we also know the shape of the TM we can use the measured x, y and z displacements at each point on the TM to define motions that are normal to the local TM surface, η , (displacements out of the local plane) and motions that are tangential to the local surface (displacements within the local plane, α, β). A numerical rotation matrix $[\mathbb{R}]$ (described in Appendix B) is used to rotate the original Euclidean coordinate system of the measuring system (x, y, z) at each point on the TM surface, to a new coordinate system (α, β, η) with unit vectors tangent and normal to the TM surface, so that at each point on the surface of the TM, the new displacement vector $\{\mathbf{d}_{Rot}\}$ can be obtained

$$\{\mathbf{d}_{Rot}\} = [\mathbb{R}] \times \{\mathbf{d}\}. \quad (4)$$

Comparisons of the magnitude of \mathbf{d}_η with \mathbf{d}_α and \mathbf{d}_β describe the relative magnitude of the out-of-plane and in-plane motions and test the likelihood that sound energy may be carried by in-plane motions of the membrane. It should be noted that the magnitude of the rotated displacement vector $|\mathbf{d}_{rot}|$ is equal to the magnitude of the original displacement vector $|\mathbf{d}|$, i.e.

$$|\mathbf{d}| = \sqrt{d_x^2 + d_y^2 + d_z^2} = |\mathbf{d}_{rot}| = \sqrt{d_\alpha^2 + d_\beta^2 + d_\eta^2}. \quad (5)$$

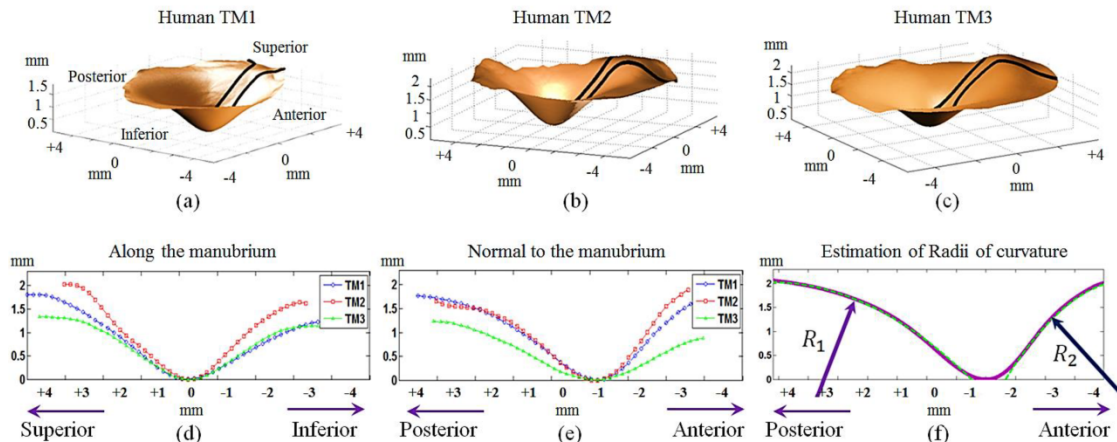


Figure 5. Measured 3D shape of the lateral surfaces of three human TM samples: (a) shape of TM 1; (b) shape of TM 2; shape of TM 3; the black outlines show the borders of the manubrium of the malleus on the medial surface of the TM. (d) Cross sections along the manubrium (bounding the superior part of the membrane) of the shapes of all three TM samples; (e) cross sections of the shapes of the three samples along a line through the umbo, but normal to the manubrium; (f) estimating the individual radius of curvature of the TM by fitting circles to the semi-cross-sections defined by tracing the TM surface between the umbo and the TM rim. In the illustration the posterior semi-cross-section is fit by a circle of radius R_1 , and the posterior section is fit by R_2 .

3. Results

3.1 Measurements of human TM shape

Two dimensional projections of the shape of the three human tympanic membranes are illustrated in the top row of Figure 5. In each illustration the umbo is used to define the x, y, z origin, and the manubrium is positioned along the positive x and y diagonal (toward the far corner in each of the plots). In each specimen the TM appears as a blunted cone, with a depth of about 2 mm and a radius of about 4 mm. The umbo is the most medial point on the TM (z value of 0) and the z -coordinates of all points on the TM surface are ≥ 0 . Figures 5d and e compare the z coordinate of different points along two diameters on the TM surfaces: one diameter that includes the manubrium of the malleus and a second perpendicular to the first that also includes the umbo. To evaluate the radii of curvature, the z -coordinates of the shape along lines normal to the manubrium were considered. The radius of curvature of the toroid section of the TM (as per Fay et al. 2006) was calculated with a least-square fit of a circle equation of the outermost part of the TM. As shown in Figure 5f, circles are fit to the two sides of the TM (left (R_1) and right (R_2)). The computed radii of curvature are listed in Table 1.

Table 1. Estimation of the radii of curvature for three human TM samples.

Radii of Curvature	TM1	TM2	TM3
R_1 (mm)	5.84	4.81	3.78
R_2 (mm)	3.41	4.65	4.94

3.2 Magnitude and phase of motion along different sensitivity vectors

Figure 6 illustrates the measured displacements along 4 sensitivity vectors in one bone at 4.48 kHz. The magnitude and phases at the different points on the TM surface measured along each vector have all been normalized by the motion of the umbo measured with each sensitivity vector. The displacement magnitude and phases are arranged in complex patterns on the TM surface with on the order of 10 local displacement maxima and a similar number of distinct islands of different phase. About half of the membrane moves with a magnitude larger than the umbo displacement. More than half of the membrane moves with a phase that is within ± 0.2 cycles of the umbo, and a large part of the remaining area is nearly moving out of phase with the umbo. Similar patterns have been observed with this frequency of stimulation in other specimens (Rosowski et al. 2009; Cheng et al. 2010, 2013, in press). The magnitudes and phases of the motions of the surface are similar for the four different sensitivity vectors, though there are differences in the relative magnitudes of the peaks and in the phase of motion. The similarity in displacement across the sensitivity vectors is consistent with the relatively small differences in illumination direction that were consistent with minimize shadowing on the TM (See section 2.2.3). Similar results were obtained in the other two bones.

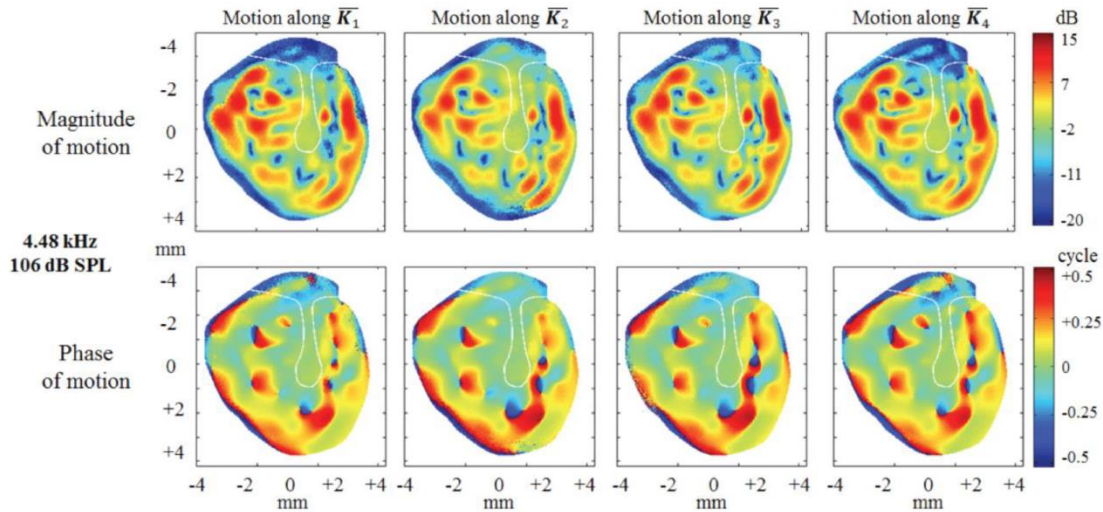


Figure 6. Measurements of the magnitude and phase of the displacements measured along four different sensitivity vectors ($\bar{K}_1, \dots, \bar{K}_4$) in bone TB 1 normalized by the displacement of the umbo measured in each sensitivity vector. The magnitudes scaled as dB re umbo displacement are in the top row. The phase angles relative to the phase of the umbo are in the bottom row. The stimulus was a 4.48 kHz tone of 106 dB SPL.

3.3 4D Motion: Displacement as a function of space (x, y, z) and stimulus phase (θ)

As described in Figure 3, the three dimensional position of the TM at each stroboscopic phase (relative to stimulus phase $\theta=0$) is calculated from the data obtained from all four sensitivity vectors. The three leftmost columns of Figure 7 show the calculated three Cartesian components of surface motion at four representative acoustic stimulus phases ($\theta=45^\circ, 90^\circ, 135^\circ$ and 180°), and display both + and - changes in position with stimulus phase. The rightmost column shows the computed magnitude of the displacement (Eqn. 5) at each stimulus phase and maps only positive values. While parts of the TM surface move in (negative displacements) and others out (positive displacements), the absolute value of all three components and their combined magnitude increase while θ varies from 45° to 135° and change little between 135° and 180° of stimulus phase. The progression of surface displacements with stimulus phase suggest that the $\theta=0$ condition is nearly aligned with a maximum or minimum in the displacement waveforms on much of the TM surface.

3.4 Estimates of TM Motion in the Camera-Based Cartesian Coordinate system

The displacement components at each point on the TM surface gathered from the four illumination directions

(Figure 6) were used with Eqn. 3 to calculate 3D motions at each stroboscopic phases (Figure 7) and then, Fourier transforms were computed of the phasic displacement along each of the three Cartesian axes to compute the magnitudes and phases of motion in the 3-dimensional camera-based coordinate system (Figure 8), where d_x and d_y describe displacements in the measurement plane and d_z describes motions toward and away from the camera. A general result from this calculation is that the x and y components of motion at many locations on the TM surface are 10 dB smaller in magnitude than the z component, though there are regions and frequencies where d_x and d_y are within 5 dB of the magnitude of d_z .

Comparisons of the phase angles of the 3 components are complicated by the small magnitude of d_x and d_y at many locations on the TM surface. These small displacements approach the noise floor of our measurement system and lead to inaccuracies in the phase estimates that cause the speckling visible in the phase maps in regions of low displacement magnitude. Regardless of the noise-associated speckling, it is clear the phase of motion in the x and y directions can differ from the phase in the z direction. For example: ϕ_x the phase angle of d_x , is generally about 0.5 period out of phase with ϕ_z

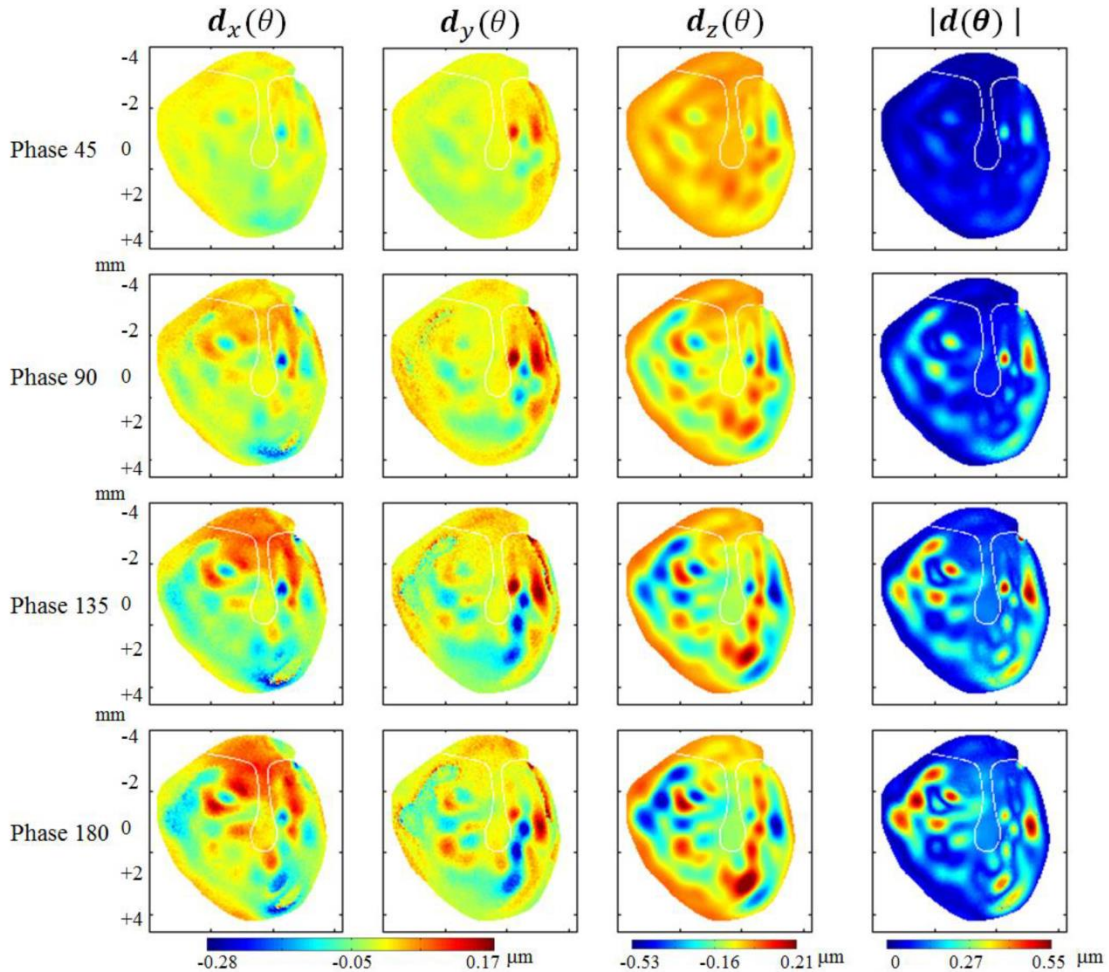


Figure 7. Four-Dimensional (x , y , z and θ) sound-induced motion measurements in one bone at one single frequency of 4.48 kHz at 106 dB SPL at four values of θ (the stimulus phase). The three left hand columns are maps of the relative displacement between the stimulus phase and phase zero, and can contain + or - displacement values (with 0 values coded as pale yellow-green). The right hand column shows the magnitude of the displacement (Eqn. 5) at each location on the TM at the different phases and only displays positive values (with zero values coded as deep blue).

3.5 Estimates of TM Motion in the Camera-Based Cartesian Coordinate system

The displacement components at each point on the TM surface gathered from the four illumination directions (Figure 6) were used with Eqn. 3 to calculate 3D motions at each stroboscopic phases (Figure 7) and then, Fourier transforms were computed of the phasic displacement along each of the three Cartesian axes to compute the magnitudes and phases of motion in the 3-dimensional camera-based coordinate system (Figure 8), where \mathbf{d}_x and \mathbf{d}_y describe displacements in the measurement plane and \mathbf{d}_z describes motions toward and away from the camera. A general result from this calculation is that the x and y components of motion at many locations on the TM

surface are 10 dB smaller in magnitude than the z component, though there are regions and frequencies where \mathbf{d}_x and \mathbf{d}_y are within 5 dB of the magnitude of \mathbf{d}_z .

3.6 Computed Normal and in-TM plane motions

Our methods provide measurements of TM 3D shape and 3D motion that we combine (using Eqns. 3 and 4) to compute the displacement components that are normal to the TM surface \mathbf{d}_η (out-of-TM plane) and the two displacement components describing the motion in the plane orthogonal to the local normal vector \mathbf{d}_α and \mathbf{d}_β (the two components in the local plane of the TM). Figure 9 illustrates maps of the magnitude and phase of these three components for TM 1. Note that in regions

where the magnitude of the motion normal to the TM surface is clearly measurable (≥ 0 dB), the magnitudes of the in-plane motion components $|d_x|$ and $|d_y|$ are generally 10 to 20 dB smaller than the magnitude of the motions normal to the TM surface $|d_z|$. This point will be re-addressed after we look at the computations of d_η for all three of the temporal bones measured in our series. Figure 10 illustrates maps of the magnitude of the computed d_η for all three bones measured at similar frequencies. There are many similarities and differences in the set of three results. Similarities include: (a) The progression from a few displacement maxima with stimulation near 1 kHz to many local maxima with stimulation near 8 kHz; (b) the arrangement of the multiple maxima around the umbo and manubrium

observed with 4-9 kHz stimulation, and (c) the observation that the magnitude of motion of the umbo and manubrium in the direction normal to the local TM surface is at least 10 dB smaller than the maxima displacements on the TM surface. All of these features have been observed in our previous reports of measurements of z-component motion (Cheng et al. 2010, 2013, in press).

Figure 10 also points out differences in how the TMs of individual temporal bones respond to sound. Where we see differences in the shape and location of maxima as well as differences in the rate in which the patterns increase in complexity with frequency (Rosowski et al. 2009).

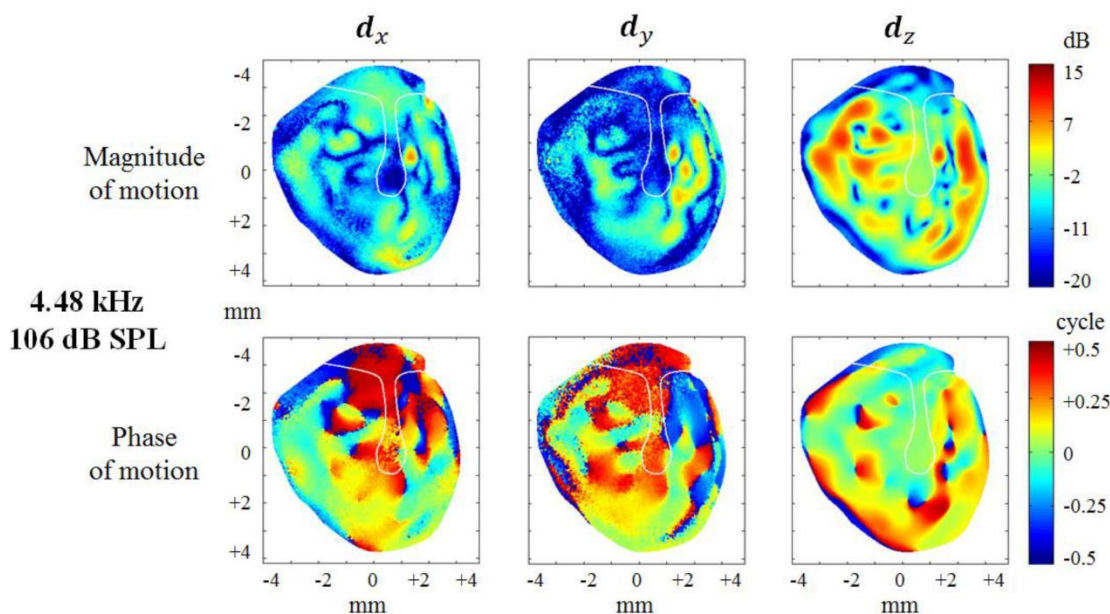


Figure 8. The magnitude and phase of the three camera-based components of the TM displacement in x , y and z (d_x , d_y , d_z) magnitude (in dB) and phase in one ear. The magnitudes are scaled in dB relative to the displacement of the umbo in the z direction. The phases are scaled in periods relative to the phase of umbo motion in the z direction.

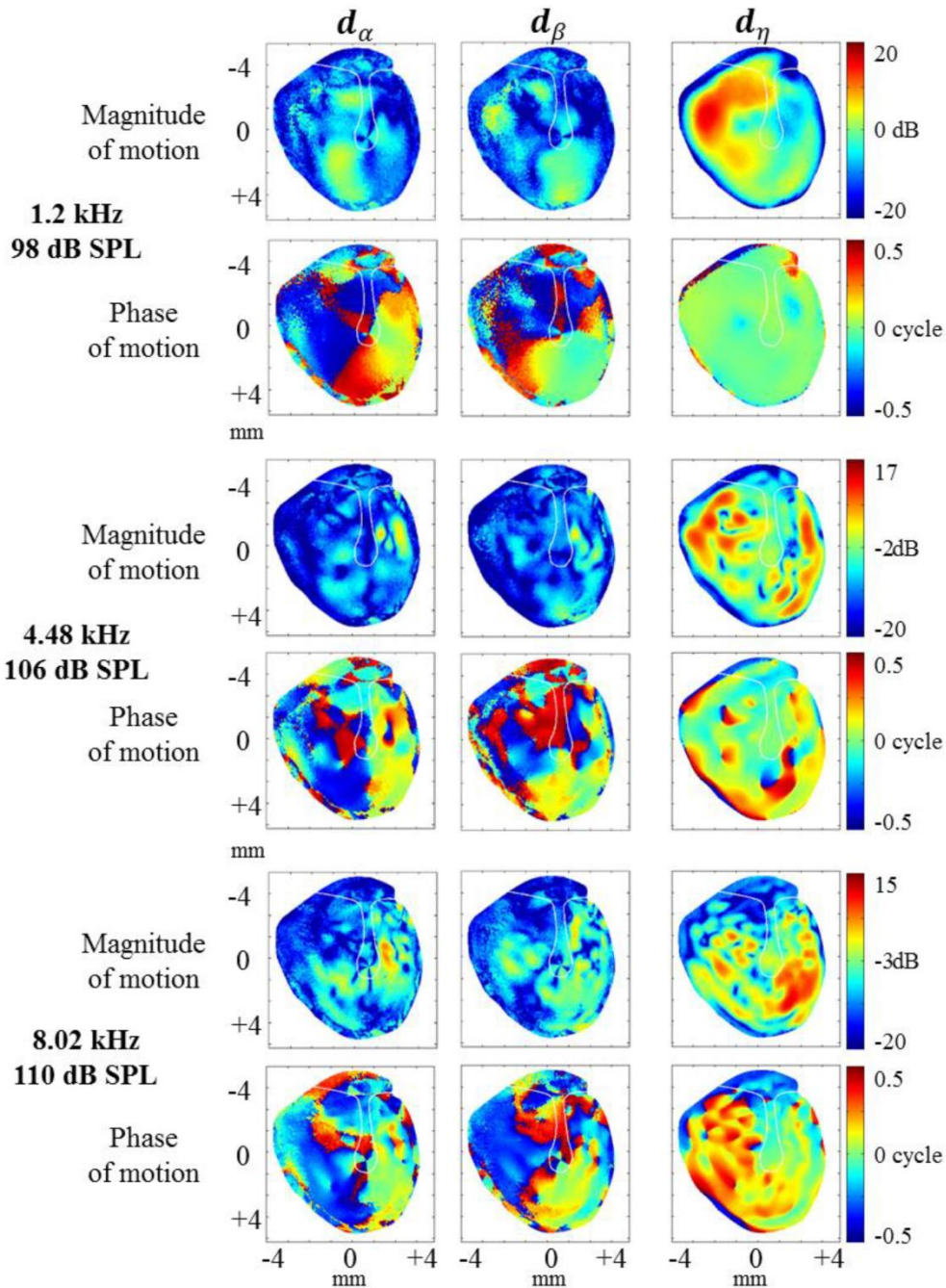


Figure 9. The in- (d_α and d_β) and out-of-plane (d_η) motion components of TM1 normalized by the out-of-plane motion of the Umbo at each frequency. The colorbars are in logarithmic magnitude scale, and phases are in cycles.

We next address the relative magnitudes of the normal, d_η , and in-plane displacements, d_α and d_β , in the three bones. Figure 11 illustrates the point-by-point ratio of the in-plane and normal displacement magnitudes, where the

in-plane magnitude is defined by the mean of the magnitudes of d_α and d_β . These ratio maps indicate that over much of the TM surface with stimulus frequencies less than 2 kHz, the in-plane motion is much smaller in

magnitude (<0.25 or < -12 dB) than the motion normal to the surface (most of the surfaces of the TM are coded from dark blue to green corresponding to -30 to -12 dB). The comparison is more complicated at higher frequencies where the regions colored in orange and red increase in prominence as frequency increases. Careful comparisons of Figures 10 and 11, point out that regions in Figure 11, where the displacement ratio is coded red (i.e. in-plane displacement magnitudes $>$ out-of-plane) correspond to regions in Figure 10, where the motion normal to the surface is of low-magnitude. Indeed, many of the regions in Figure 11 where the ratio is near or greater than 0 dB are attributable to regions where $|\mathbf{d}_\eta|$ is near the measurement noise floor. Therefore, we specified a threshold of 10 nm for the $|\mathbf{d}_\eta|$, and the value of every single pixel with magnitude of <10 nm are removed from

this analysis and their color set to white. Furthermore, since our techniques reconstruct the phasic motion in each of the component direction, we can test for the stimulus driven sinusoidal response of each component at each pixel, by correlating the measured phasic motion with the sinusoidal motion predicted by the fundamental component of the FFT fit to the motion at each pixel (Cheng et al., 2010). Pixels of poor correlation (with squared correlation coefficients values less than 0.5) are also shown as white in these displays. The numbers under each plot panel in Figure 11 note the average of the dB values in each panel. The consistent reading near -10 dB say that on average, the in-plane motion components are about 30% of the magnitude of the out-of-plane motion component.

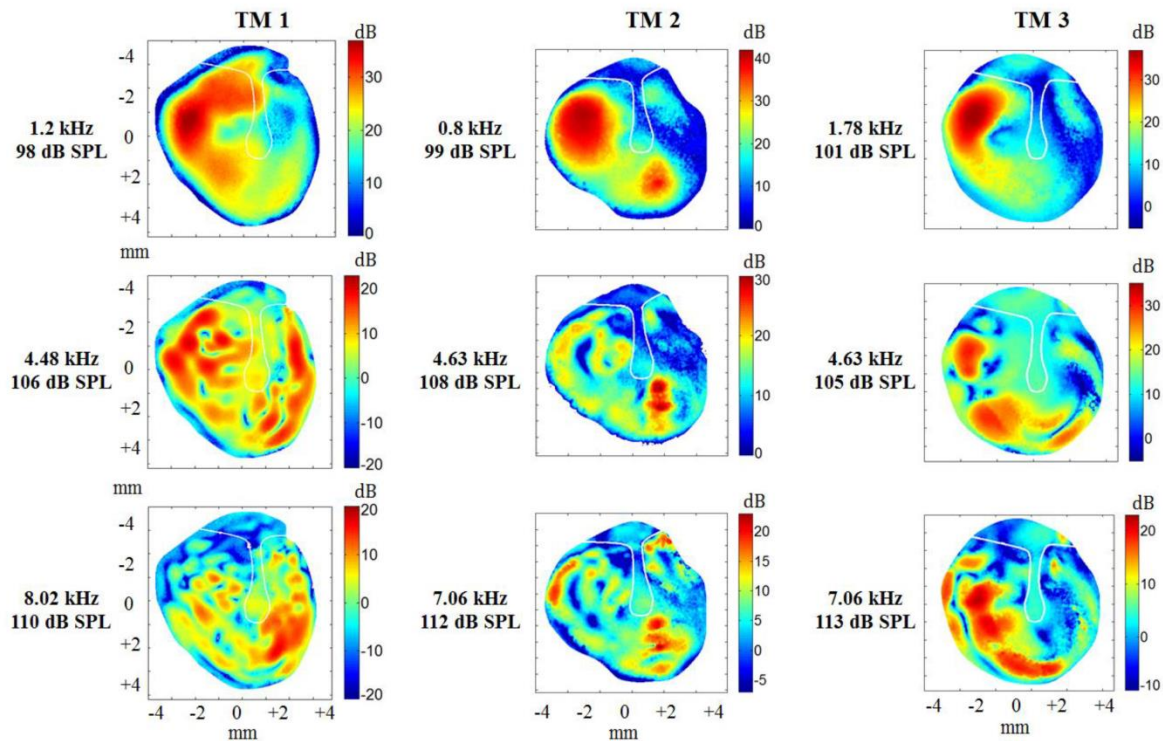


Figure 10. The magnitude of the motion normal to the TM surface $|\mathbf{d}_\eta|$ normalized by the sound pressure at the TM at three frequencies in the three temporal bones in our study. The displacement magnitudes are scaled in terms of dB re 100 nm of displacement per Pascal of sound pressure stimulus.

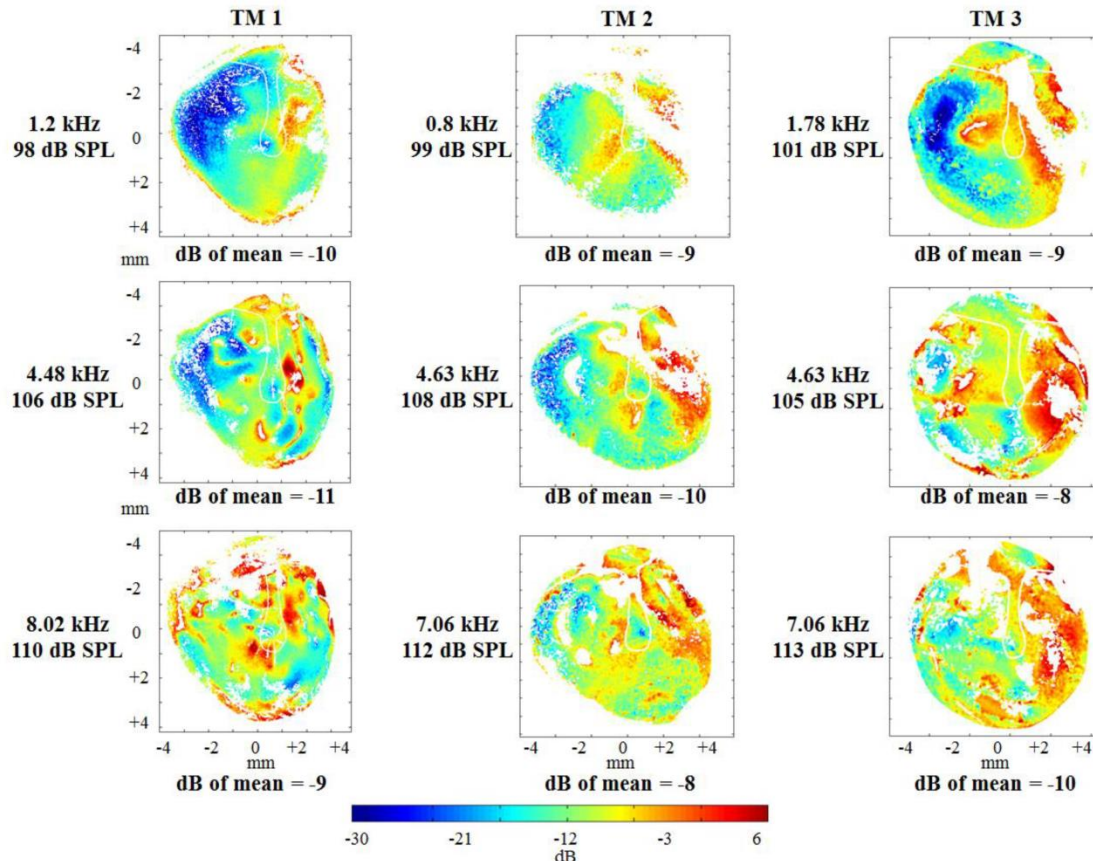


Figure 11. Maps of the ratio of in-plane to out-of-plane where in-plane is defined by (the sum of the magnitudes of the two in-plane motion components)/2.

4. Discussion

New computer-controlled holographic techniques have been used to quantify 3D spatial displacement components at over a million points on the surface of the TM in response to tonal sound stimulation TM, and (nearly simultaneously and using the same observation angle) determine the 3D shape of the lateral surface of the TM. This combination of measurements allows us to quantify the out-of-plane displacements (the displacement component normal to the local surface), and the in-plane displacements (the displacement components tangential to the local surface) associated with sound-induced TM motion.

4.1 Description of the multiple directional components of TM surface motion

Our methods use four independent measurements of the sound-induced motion of the TM, with each measurement associated with a different illumination direction and holographic sensitivity vector \overline{K}_S (Figure 2). Because the variation in sensitivity vector was limited by the geometry

of the TM and its supporting bone, measurements made with the four illumination directions were similar (but not identical) in magnitude and phase (Figure 6). The known sensitivity vectors and the four measurements were used in a least-squares calculation (Equation 3, Appendix 1) to define the motion of over 1,000,000 points on the TM surface in terms of the Cartesian coordinates (\mathbf{d}_x , \mathbf{d}_y and \mathbf{d}_z) imposed by the camera plane, with the z-direction orthogonal to the plane. Because of the flattened cone shape of the TM, the measurement geometry with the TM ring paralleling the camera plane, and the limited variations in the directions of the four sensitivity vectors, the computed \mathbf{d}_z is generally similar in magnitude and phase to the displacements measured with the different illumination directions (Figure 6 and 8).

4.2 Comparison of out-of-plane motion and motion orthogonal to the tympanic ring

Our new measurements allow us to assess the out-of-plane (normal to the local surface) component \mathbf{d}_η of TM motions and compare it to the more usual measurements of motion orthogonal to the tympanic ring (Cheng et al. 2010, 2013, in press) that generally correspond to our \mathbf{d}_z

measurements. Direct comparison of measurements in TBI at 4.48 kHz, show great similarity between d_z (Figure 8, right hand column) and the computed d_η (Figure 9, right hand column, center rows), though there are differences, particularly in areas midway between the center of the TM and its rim. The location of these differences corresponds to regions where the curvature of the TM is largest, while the regions of similarity are explainable in terms of the near orthogonal orientation of the TM ring (and the center of the TM) with the z axis of the camera defined coordinate system employed in our methods.

Further comparisons of the d_η magnitude maps of Figure 10 with similar maps in the literature show great similarities between the measured normal component of motion and the previously published one-dimensional measurements made along the z axis in our previous reports (Cheng et al. 2010, 2013, in press). The d_η data from this study illustrated in Figures 9 and 10 all show the relatively low-magnitude of motion of the umbo at all stimulus frequencies, and the frequency dependent evolution of displacement patterns that we have previously described in our one-dimensional measurements of TM motion. These include: (1) The presence of one or two displacement maxima and generally in phase motion of the entire TM surface near 1 kHz and at lower frequencies, (2) the increase in the number of local displacement maxima with frequency coupled to the introduction of phase variations on the TM surface with stimulus frequencies between 1 and 5 kHz, and (3) the ring-like organization of maxima and iso-phase islands that are circularly arranged around the umbo in the center of the TM at frequencies above 6 kHz.

4.3 Comparison of in-plane displacements (d_α and d_β) with d_x and d_y

Our methods also provide a measurement of the x and y components of displacement d_x and d_y , as well as the two components of in-plane displacements (d_α and d_β) on the TM (those tangent to the local surface). While d_α and d_β components were measurable, they were generally small, and our estimates of their magnitude and angle were often limited by our ability to resolve these components (Figure 9). The motion magnitudes in the x and y , were generally larger in magnitude than the in-plane components (e.g. Figure 8). This is consistent with the cone shape of the TM and a motion that is dominated by displacements normal to the cone's surface. Because of the orientation of the TM cone relative to the $x - y$ plane define by the tympanic ring, motions normal to the surface can have significant x and y motion components, even when the in-plane motions are zero in magnitude. The importance of the TM shape in relating d_α and d_β to d_x and d_y suggests that measurements of the latter two, without knowing shape, are not useful estimates of in-plane TM motions.

4.4 What is the relative magnitude of in-plane and out-of-plane motions

Because of the large variations we observed in the magnitude of d_α and d_β , we performed more direct comparisons of d_α and d_β , and d_η . These are illustrated in Figure 11 as maps of point-by-point computations of the mean magnitude of d_α and d_β divided by d_η magnitude, where this ratio is scaled in dB. In Figure 11, 0 dB (coded in red-orange) is assigned to those regions where the in-plane and out-of-plane displacement magnitudes are equal, red codes where the in-plane motions are larger than the out-of-plane, and orange to blue codes regions where the out-of-plane motions are larger in magnitude. The gestalt from these plots is that out-of-plane motions are generally larger than the in-plane motions. More quantitatively, the ratio of in-plane to out-of-plane motion varies over the surface of the TM between 6 and -30 dB with an average value of near -10 dB. As noted in the results section, this comparison is complicated when the motion of the out-of-plane component is small and near the magnitude of the measurement noise floor, and many, but not all, of the locations where the computed ratio is 0 dB or better surround locations where the measured displacements are small and our displacement estimates are known to be noisy.

Our estimates of the magnitudes of in-plane motion components were not always small, especially in isolated spatial regions in response to stimuli of frequencies above a few kHz. For example, in Figure 9, the d_α and d_β data with the 4.48 kHz stimulus show several small punctate regions (shaded in yellow) just to the right of the manubrium where these 'in-plane' motions are larger than the out-of-plane $|d_\eta|$ motions of the umbo. Small, localized regions near these same locations also show d_α and d_β magnitudes larger than the out-of-plane motion of the umbo with 8 kHz stimulation. The highly localized nature of these regions argues against any functional significance of these puncta where the in-plane motions are large in magnitude.

4.5 Does the TM act as a thin shell?

The Kirchoff-Love theory of thin shells describes a system dominated by out-of-plane displacements (displacements normal to the plate surface; Kraus 1967; Saada 2009). Our measurements of 3D sound-induced motions of the cadaveric human TM and its 3D shape suggest that out-of-plane motions generally dominate the sound-induced motion of the TM; however, our data do suggest the presence of in-plane motions and, in isolated regions of the TM, the in-plane motions can be larger than the out-of-plane.

Thin-shell theory generally applies to shells made of homogenous material, in which the resultant displacements are small compared to the thickness of the shell, and the thickness of the shell is less than 0.05 of the radius of curvature of the curved plate. Our data and TM

preparations are consistent with both of the numerical constraints: The thickness of the human TM varies between 50 and 140 μm (Van der Jeught et al. 2013), and the largest displacements we observe are less than 10 μm , which leads to a displacement to thickness ratio of less than 0.2. Also, the radius of curvature in the three TMs we measured varies between 3.4 and 5.8 mm (Table 1) yielding a ratio of max thickness to this radius of < 0.045 . However, the TM is not homogenous.

The normal TM is tri-laminar structure in which the central layer contains several populations of fibers with different orientations (Decraemer and Funnell 2008), a structure that is not consistent with homogeneity. Furthermore, as ears age, the TM is subject to multiple subclinical alterations in structure, e.g. tympanosclerosis (Merchant et al. 2010). The events can cause scars or mineral deposits in the TM that further impact the heterogeneity of its structure. While each of the three ears used in our study had no overt signs of middle ear disease, none had the clear pristine TM generally observed in children and young adults. Furthermore, non-uniformities in the painting of the TM surface with the ZnO solution are also possible; the TM surface is somewhat hydrophobic and the water-based solution does not always cover the surface equally. Whether paint-induced or natural structural in-homogeneities were associated with the punctate regions of clearly large in-plane displacements is a point of further study.

5. Summary and Conclusion

We have described new holographic methods that can measure the 3D-shape and 3D-motion of the surface of the TM nearly simultaneously using a fixed geometry of TM specimen and digital camera back plane (Khaleghi et al. 2013, 2015). The combination of shape and 3D motion was used to produce the first accurate measurements that separate the out-of-plane (normal to the surface) and in-plane (tangential to the surface) displacement components. While the later were shown to be generally small, consistent with thin plate theory, they were difficult to quantify when the membrane motion was small. There were also small regions of the membrane surface with in-plane motions that were larger in magnitude than the measured out-of-plane.

Acknowledgments

This work was supported by the National Institute on Deafness and other Communication Disorders (NIDCD), Massachusetts Eye and Ear Infirmary (MEEI), and Mechanical Engineering Department at Worcester Polytechnic Institute. We also acknowledge the support of all of the members of the CHSLT labs at WPI and Eaton-Peabody labs at MEEI, in particular Ellery Harrington, Ivo Dobrev, and Jérémie Guignard.

Appendix A: 3D motion measurements with the method of multiple sensitivity vectors

As mentioned in Section 2.2.3, 3D motion components of the TMs are measured with the method of multiple sensitivity vectors in holographic interferometry. The difference in optical phase Ω produced by a displacement \mathbf{d} measured with sensitivity vector $\overline{\mathbf{K}}_S$ is the dot product of the sensitivity vector with the object's displacement vector

$$\Omega = \overline{\mathbf{K}}_S \cdot \overline{\mathbf{d}}, \quad (\text{A1})$$

where the sensitivity vector is the product of the light wave number and the vector difference between the unit observation vector and the unit illumination vector (Figure 2). In the case of a three dimensional motion and a sensitivity vector described in three dimensions, Eq. A1 can be expanded to

$$\begin{aligned} \Omega &= (K_{Sx}, K_{Sy}, K_{Sz}) \cdot (d_x, d_y, d_z) \\ &= K_{Sx}d_x + K_{Sy}d_y + K_{Sz}d_z. \end{aligned} \quad (\text{A2})$$

If we know Ω and $\overline{\mathbf{K}}_S$, we have one equation and three unknowns, d_x , d_y , and d_z . In order to solve (A2), we require at least three different three-dimensional sensitivity vectors: $\overline{\mathbf{K}}_1, \overline{\mathbf{K}}_2$ and $\overline{\mathbf{K}}_3$. In order to minimize experimental errors, we obtain double exposure optical phase maps using four different sensitivity vectors to form an over determined system of equations:

$$\begin{bmatrix} \Omega_1 \\ \Omega_2 \\ \Omega_3 \\ \Omega_4 \end{bmatrix} = \begin{bmatrix} K_{1x} & K_{1y} & K_{1z} \\ K_{2x} & K_{2y} & K_{2z} \\ K_{3x} & K_{3y} & K_{3z} \\ K_{4x} & K_{4y} & K_{4z} \end{bmatrix} \times \begin{bmatrix} d_x \\ d_y \\ d_z \end{bmatrix}. \quad (\text{A3})$$

and they can be simplified into the following equation

$$\{\Omega\}_{4 \times 1} = [\mathbb{S}]_{4 \times 3} \times \{\mathbf{d}\}_{3 \times 1}. \quad (\text{A4})$$

Equation A4 is solved with the least-squares error minimization method. First, both sides are multiplied by the transpose of the sensitivity matrix \mathbb{S} ,

$$[\mathbb{S}]_{3 \times 4}^T \times \{\Omega\}_{4 \times 1} = [\mathbb{S}]_{3 \times 4}^T \times [\mathbb{S}]_{4 \times 3} \times \{\mathbf{d}\}_{3 \times 1} \quad (\text{A5})$$

Thus, the displacement vector $\{\mathbf{d}\}$ can be obtained by

$$\{\mathbf{d}\}_{3 \times 1} = [[\mathbb{S}]_{3 \times 4}^T \times [\mathbb{S}]_{4 \times 3}]_{3 \times 3}^{-1} \times \{[\mathbb{S}]_{3 \times 4}^T \times \{\Omega\}_{4 \times 1}\}_{3 \times 1} \quad (\text{A6})$$

An important consideration in the method of multiple sensitivity vectors is that all the sensitivity vectors need to be as linearly-independent as possible for the system to provide accurate results. Therefore, the condition number, \mathbb{C} , of the square matrix, $[F] = [\mathbb{S}]^T[\mathbb{S}]$,

characterizing the geometry of a holographic setup is calculated (Vest 1979; Golub and Van Loan 2012)

$$\mathbb{C}(\mathbb{S}) = \sqrt{\frac{\lambda_{\max}(F)}{\lambda_{\min}(F)}}, \quad (\text{A7})$$

where λ_{\max} , and λ_{\min} are the maximum and the minimum eigenvalues of $[F]$. A condition number close to one indicates a well-conditioned matrix, but this represents a holographic setup with large angles of illumination (Vest 1979; Osten 1985). However, because of the particular cone-like geometry of the TM and the presence of the bony structures around it, the maximum possible angles of illumination are limited. Therefore, we arranged our different illumination directions to achieve the largest angles of illumination within the constraints imposed by the geometry of the TM (Khaleghi et al., 2015).

Appendix B: Rotation Matrix used to obtain in- and out-of-plane motions

The original Cartesian coordinate system x, y, z is mathematically rotated in order to obtain the local in-plane and out-of-plane displacement components. In the holographic system and based on the definition of the sensitivity vectors (Figure 4), the observation vector $\bar{\mathbf{Z}}$, i.e., a vector perpendicular to the CCD sensor, has unit vector components $\mathbf{Z}_x, \mathbf{Z}_y,$ and \mathbf{Z}_z with magnitudes equal to $[0, 0, 1]$. From the measured 3D shape of the membrane, we can define the unit normal vector, $\bar{\mathbf{N}}$, at every point on the surface of the TM (Khaleghi et al. 2013). Since, both $\bar{\mathbf{N}}$ and $\bar{\mathbf{Z}}$ are unit vectors, the angle θ between them is calculated as the dot product of the two vectors; and the cross product of these two vectors provide a vector, $\bar{\mathbf{U}}$, normal to both of them that, in this case, is tangent to the local plane of the membrane and is considered as the axis of rotation.

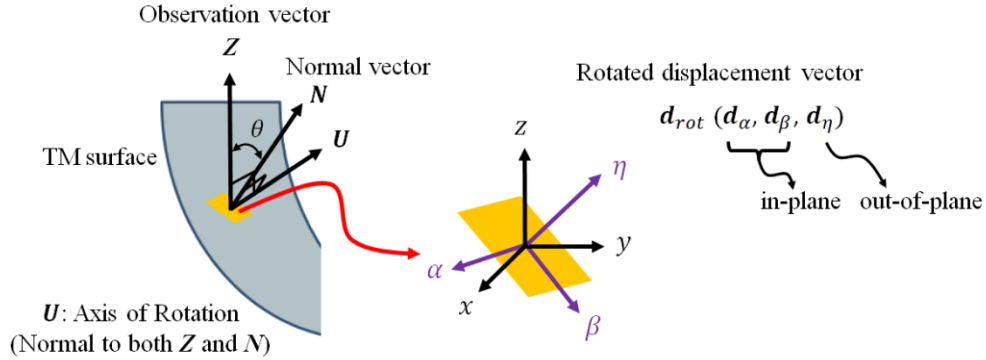


Figure B1. Transformation of the measuring coordinate system to the local coordinate system of the TM by means of a rotation matrix. Left panel: The definition of the normal direction N and U , the axis of rotation between the observation direction Z and N , where U is normal to both N and Z . Middle panel: The transformation between the Cartesian coordinates defined by the camera plane (x, y) and observation direction (z) and the out-of-plane (η normal to the local surface) and in-plane (α and β , tangential to the local surface) motion directions.

The rotation matrix \mathbb{R} , is used to rotate the original displacement vector $\mathbf{d}(\mathbf{d}_x, \mathbf{d}_y, \mathbf{d}_z)$, based on the rotation angle θ and the unit vector of the axis of rotation \mathbf{U} with

$$\mathbb{R} = \begin{bmatrix} \cos \theta + \mathbf{U}_1^2(1 - \cos \theta) & \mathbf{U}_1\mathbf{U}_2(1 - \cos \theta) - \mathbf{U}_3 \sin \theta & \mathbf{U}_1\mathbf{U}_3(1 - \cos \theta) + \mathbf{U}_2 \sin \theta \\ \mathbf{U}_2\mathbf{U}_1(1 - \cos \theta) + \mathbf{U}_3 \sin \theta & \cos \theta + \mathbf{U}_2^2(1 - \cos \theta) & \mathbf{U}_2\mathbf{U}_3(1 - \cos \theta) - \mathbf{U}_1 \sin \theta \\ \mathbf{U}_3\mathbf{U}_1(1 - \cos \theta) - \mathbf{U}_2 \sin \theta & \mathbf{U}_3\mathbf{U}_2(1 - \cos \theta) + \mathbf{U}_1 \sin \theta & \cos \theta + \mathbf{U}_3^2(1 - \cos \theta) \end{bmatrix}, \quad (\text{B1})$$

where $\mathbf{U}(\mathbf{U}_1, \mathbf{U}_2, \mathbf{U}_3)$ is the unit vector of the axis of rotation of the observation direction (z -axis in the original measuring coordinate system), and θ is the angle of rotation. Therefore, as shown in Figure 4, at each point m, n , the rotated displacement vector \mathbf{d}_{rot} has components tangent (\mathbf{d}_α and \mathbf{d}_β) and normal (\mathbf{d}_η) to the local TM plane and is calculated with the matrix multiplication of

the rotation matrix, \mathbb{R} , with the original displacement vector \mathbf{d} with

$$\mathbf{d}_{rot}(m, n) = \mathbb{R} \times \mathbf{d}(m, n). \quad (\text{B2})$$

It should be noted that the magnitude of the rotated displacement vector $|\mathbf{d}_{rot}|$ is equal to the magnitude of the

original displacement vector $|\mathbf{d}|$, and the following condition is always valid

$$\sqrt{d_x^2 + d_y^2 + d_z^2} = \sqrt{d_\alpha^2 + d_\beta^2 + d_\eta^2}, \quad (\text{B3})$$

Appendix C: Procedures for 3D shape measurements

Four phase-stepping holographic contouring technique (Furlong and Pryputniwicz 2000; Khaleghi et al., 2015) is used to quantify the 3D shape of several human TM samples. As shown in Figure C1a, the CCD sensor is illuminated with both reference and object beams at wavelength λ_1 and camera captures four intensity patterns I_1 to I_4 as four consecutive camera frames gathered with accumulating $\pi/2$ phase steps added to the optical path.

Then, the laser is tuned to a new wavelength λ_2 and another set of four intensity patterns at the second wavelength are recorded. The optical phases at each of these two states are calculated as shown in Fig. C1b. Then, the differences between the optical phases of the two states are calculated in order to obtain a fringe pattern corresponding to the shape of the TM. Based on the geometry of the holographic system and mainly sensitivity vectors, carrier fringes are also overlaid on top of the shape-related fringes. Therefore, a numerical plane is subtracted to mathematically remove the carrier fringes. Then, the data are masked and scaled in order to obtain the 3D shape of the object.

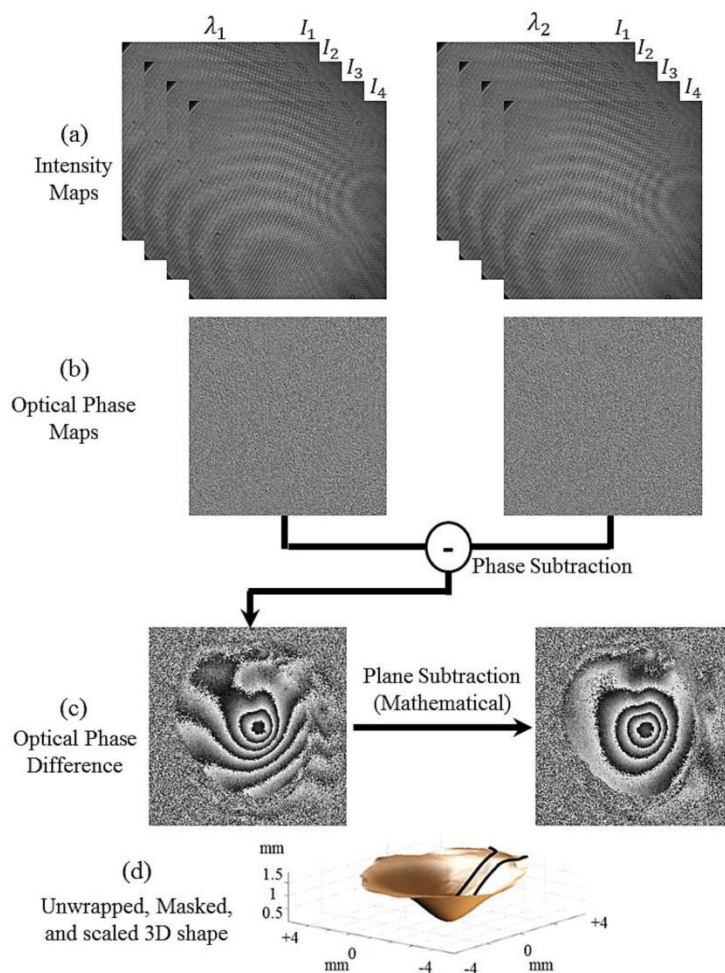


Figure C1. Algorithms used to calculate 3D shape of the objects using dual-wavelength holographic contouring.

References

- Blayney AW, Williams KR, Rice HJ, "A dynamic and harmonic damped finite element analysis model of stapedotomy," *Acta Otolaryngol*, 117, 269-273, 1997.
- Cheng JT, Aarnisalo AA, Harrington E, Hernandez-Montes MdS, Furlong C, Merchant SN, Rosowski JJ. Motion of the surface of the human tympanic membrane measured with stroboscopic holography. *Hear. Res.*, 263:66-77, 2010.
- Cheng, JT, Hamade, M, Harrington, E, Furlong, C, Merchant, SN & Rosowski, JJ, "Wave motion on the surface of the human tympanic membrane: holographic measurement and modeling analysis," *J. Acoust. Soc. Am.*, 133, 918-37, 2013.
- Cheng JT, Ravicz M, Guignard J, Furlong C and Rosowski JJ, "The effect of ear canal orientation on tympanic membrane motion and the sound field near the tympanic membrane," *J Assoc Res Otolaryngol.*, 2015 (in press).
- Decraemer WF, Funnell WRJ, "Anatomical and mechanical properties of the tympanic membrane," In: B Ars (Eds.) *Chronic otitis media. Pathogenesis-oriented therapeutic management.* (pp. 51-84) The Haugue: Kugler, 2008.
- Fay J, Puria S, Decraemer WF, Steele C., "Three approaches for estimating the elastic modulus of the tympanic membrane," *J Biomech*, 38, 1807-1815, 2005.
- Flores-Moreno, JM, Furlong, C, Rosowski, JJ, Harrington, E, Cheng, JT, Scarpino, C and Mendoza, SF, "Holographic otoscope for nano-displacement measurements of surfaces under dynamic excitation," *Scanning*, 33, 342-52, 2011.
- Funnell WR, Decraemer WF, Khanna SM, "On the damped frequency response of a finite-element model of the cat eardrum," *J. Acoust. Soc. Am.*, 81, 1851-1859, 1987.
- Furlong, C, and Pryputniewicz, R J, "Absolute shape measurements using high-resolution optoelectronic holography methods," *Optical Engineering*, 39(1), 216-223, 2000.
- Gan RZ, Sun Q, Dyer RK jr., Chang KH, Dormer KJ, "Three-dimensional modeling of middle-ear biomechanics and its applications," *Otology & Neurotology*, 23, 271-280, 2002.
- Goll E, Dalhoff E, "Modeling the eardrum as a string with distributed force," *J. Acoust. Soc. Am.*, 103, 1452-1462, 2011.
- Hernández-Montes, MdS, Furlong, C, Rosowski, JJ, Hulli, N, Harrington, EJ, Cheng, JT, Ravicz, ME & Santoyo, FM, "Optoelectronic holographic otoscope for measurement of nano-displacements in tympanic membrane," *J. Biomed. Optics*, 14, 034023, 2009.
- Jackson R, Cai H, Puria S, "In search of in-surface modes of sound transmission on the eardrum using three dimensional laser doppler vibrometry," The 6th International Symposium on Middle-Ear Mechanics in Research and Otology, Daegu Korea, Kyungpook National University, 2012.
- Khaleghi, M, Lu, W, Dobrev, I, Harrington, E, Cheng, JT, Furlong, C & Rosowski, JJ, "Digital holographic measurements of shape and 3D sound-induced displacements of Tympanic Membrane," *Optical Engineering* 51, 101916.1-11, 2013.
- Khaleghi M, Furlong C, Ravicz ME, Cheng JT, Rosowski, JJ, "Three-dimensional vibrometry of the human eardrum with stroboscopic lensless digital holography," *J Biomed Opt*, 20(5), 051028, 2015.
- Koike T, Wada H, Kobayashi T, "Modeling of the human middle ear using the finite-element method," *J. Acoust. Soc. Am.*, 111, 1306-1317, 2002.
- Kraus, H, "Thin elastic shells: an introduction to the theoretical foundations and the analysis of their static and dynamic behavior," Wiley, 1967.
- Merchant SN, Nadol JB Jr, "Schuknecht's Pathology of the Ear," Shelton CT, People's Medical Publishing House – USA, 2010.
- Osten, W, "Some considerations on the statistical error analysis in holographic interferometry with application to an optimized interferometer," *Journal of Modern Optics*, 32(7), 827-838, 1985.
- Pryputniewicz, R. J., & Bowley, W. W., "Techniques of holographic displacement measurement: an experimental comparison," *Applied optics*, 17(11), 1748-1756, 1978.
- Rosowski JJ, Cheng JT, Ravicz ME, Hulli N, Harrington EJ, Hernandez-Montes MS, Furlong C. 2009. Computer-assisted time-averaged holography of the motion of the surface of the tympanic membrane with sound stimuli of 0.4 to 25 kHz. *Hear Res*, 253, 83-96.
- Rosowski, JJ, Dobrev, I, Khaleghi, M, Lu, W, Cheng, JT, Harrington, E and Furlong, C, "Measurements of three-dimensional shape and sound-induced motion of the chinchilla tympanic membrane," *Hear Res*, 301, 44-52, 2013.
- Saada, A. S., "Elasticity: theory and applications. J. Ross Pub, 2009.
- Shaw, EG, Stinson, MR. "The human external and middle ear: Models and concepts," In: E. deBoer, M.A. Viergever (Eds.) *Mechanics of Hearing.* (pp. 3-10) Delft University Press, 1983.
- Stieger, C, Candraia, C, Kompis, M, Herrmann, G, Pffiffer, F, Widmer, D & Arnold, A, "Laser Doppler vibrometric assessment of middle motion in Thiel-embalmed heads," *Otol Neurotol*, 33, 311-8, 2012.
- Thiel W., "Ergänzung für die Konservierung ganzer Leichen nach W. Thiel," *Ann Anat.* 184:267-269, 2002.
- Van Der Jeught S, Dirckx JJJ, Aerts JRM, Bradu A, Podoleanu AGH, Buytaert JAN. 2013. Full-field thickness distribution of human tympanic membrane obtained with optical coherence tomography. *J. Assoc. Res. Otolaryngol.*, 14, 483-494.
- Vest, C. M. (1979). Holographic interferometry. New York, John Wiley and Sons, Inc., 1979. 476 p., 1.
- Williams KR, Lesser TH. (1990). A finite element analysis of the natural frequencies of vibration of the human tympanic membrane. Part I. *Br. J. Audiol.*, 24, 319-327.



11. Paper E: Simultaneous full-field three-dimensional vibrometry of the human eardrum using spatial-bandwidth multiplexed holography

Overview

In this paper, published in the Journal of Biomedical Optics in 2015, development of a novel single-frame multiplexed lensless holographic system for truly simultaneous measurements of the motion of samples such as human TM using multiple sensitivity vectors are described. Accepted 3D deformation measurement using holographic techniques require repeating the measurement at least along three different directions, and assume high reproducibility of response (i.e. the observed specimen behaves similarly when stimulated and measured several times). For *in-vivo* measurements reproducibility is affected by a number of factors including changes in shape due to respiration, motion of the subject, and the subject's pulse. A single-frame multiplexed holographic system is developed, which allows for simultaneous holographic measurements along multiple sensitivity vectors. The holograms of the objects of interest are recorded with three simultaneous incoherently-superimposed pairs of reference and object beams, such that the modulation image corresponding to each illumination direction is reconstructed at a different position of the image. An image registration algorithm based on the shift theorem of the Fourier Transform is implemented to register the images. The time needed for a given 3D motion measurement is decreased at least threefold. We demonstrate that the present method is a valid alternative to repetitive holographic methods and offers promising perspectives towards accurate 3D deformation measurements of biological specimens for *in-vivo* applications.

Simultaneous full-field three-dimensional vibrometry of the human eardrum using spatial-bandwidth multiplexed holography

Morteza Khaleghi,^{a,*} Jérémie Guignard,^{b,c} Cosme Furlong,^{a,b,c} and John J. Rosowski^{b,c}

^aWorcester Polytechnic Institute, Center for Holographic Studies and Laser Micro-mechaTronics (CHSLT), Mechanical Engineering Department, Worcester, Massachusetts 01609, United States

^bMassachusetts Eye and Ear Infirmary, Eaton-Peabody Laboratory, Boston, Massachusetts 02114, United States

^cHarvard Medical School, Department of Otolaryngology, Boston, Massachusetts 02114, United States

Abstract. Holographic interferometric methods typically require the use of three sensitivity vectors in order to obtain three-dimensional (3-D) information. Methods based on multiple directions of illumination have limited applications when studying biological tissues that have temporally varying responses such as the tympanic membrane (TM). Therefore, to measure 3-D displacements in such applications, the measurements along all the sensitivity vectors have to be done simultaneously. We propose a multiple-illumination directions approach to measure 3-D displacements from a single-shot hologram that contains displacement information from three sensitivity vectors. The hologram of an object of interest is simultaneously recorded with three incoherently superimposed pairs of reference and object beams. The incident off-axis angles of the reference beams are adjusted such that the frequency components of the multiplexed hologram are completely separate. Because of the differences in the directions and wavelengths of the reference beams, the positions of each reconstructed image corresponding to each sensitivity vector are different. We implemented a registration algorithm to accurately translate individual components of the hologram into a single global coordinate system to calculate 3-D displacements. The results include magnitudes and phases of 3-D sound-induced motions of a human cadaveric TM at several excitation frequencies showing modal and traveling wave motions on its surface. © 2015 Society of Photo-Optical Instrumentation Engineers (SPIE) [DOI: 10.1117/1.JBO.20.11.XXXXXX]

Keywords: three-dimensional displacement measurements; digital holography; image registration; multiplexed holography; tympanic membrane.

Paper 150009SSR received Jan. 7, 2015; accepted for publication Mar. 19, 2015.

1 Introduction

The eardrum, or tympanic membrane (TM), transforms acoustic energy in the ear canal (at its lateral side) into mechanical motions of the ossicles (at its medial side: the middle ear). The acousto-mechanical-transformer behavior of the TM is determined by its shape, thickness, boundary conditions, and mechanical properties. For a better understanding of hearing mechanisms, full-field-of-view techniques are required to quantify shape and nanometer-scale sound-induced displacement of the TM in three-dimensions (3-D).¹⁻⁴ Common 3-D displacement measurement techniques require repeating the measurement at least along three sensitivity directions, which rely on the assumption of reproducibility (i.e., the observed specimen behaves similarly when stimulated and measured several times). Reproducibility is not applicable in cases where the measured phenomena are of temporally varying nature, which is the case of biological tissues such as the TM. Therefore, ideally, 3-D motions of such membranes should be quantified simultaneously.

For *in vivo* measurements,⁵ reproducibility is affected by a number of factors including changes in static pressure preloading or slight changes in shape due to respiration, motion of the subject, and the subject's pulse. For measurements in cadaveric specimens, although the reproducibility is typically better than in live subjects, the response of the TM over time can also be

affected, e.g., by the drying of the tissue. The motivations to measure the 3-D motion of the TM in response to sound *in vivo* potentially include the use of the results for a more accurate diagnostic of TM and middle ear pathologies or to evaluate middle ear surgeries.

In this paper, the development of a single-frame multiplexed lensless holographic system is described in order to minimize the measurement times to address the time-varying nature of the TM. In this method, the hologram is simultaneously illuminated with three incoherently superimposed pairs of reference and object beams, such that the images corresponding to each illumination direction are reconstructed at a different position on the image plane because of the slightly different spatial carrier frequency introduced by the incident off-axis angles of the reference beams.^{6,7} Due to the differences in the position of the reference beams and the wavelength of each pair of beams, the reconstruction distance and magnification of each numerically reconstructed hologram corresponding to each sensitivity vector are different. We, therefore, developed and implemented a registration algorithm to accurately translate individual views into a single global coordinate system. The registration method uses phase-only correlation (POC)⁸ and a swept cut-off filtering to improve robustness. Three images obtained from three sensitivity vectors in a reconstructed multiplexed hologram are

*Address all correspondence to: Morteza Khaleghi, E-mail: mkm@wpi.edu

registered and, consequently, 3-D displacement components are extracted. To validate the method, the 3-D motion of a synthetic (time-invariant) membrane is measured with the presented method and with a method involving sequential measurements from multiple illumination angles. Once the accuracy of the measuring system is verified, sound-induced 3-D motion of human cadaveric TM samples are measured at different tonal frequencies and the results are presented.

2 Methods

2.1 Off-Axis Digital Holography

In holography, the recorded intensity at the CCD (hologram) plane, $I(k, l)$, is given by

$$\begin{aligned} I(k, l) &= |R(k, l) + O(k, l)|^2 \\ &= |R(k, l)|^2 + |O(k, l)|^2 + R^*(k, l)O(k, l) \\ &\quad + R(k, l)O^*(k, l), \end{aligned} \quad (1)$$

where $R(k, l)$ and $O(k, l)$ are the complex amplitudes of the reference and object waves, respectively, k and l are the coordinates of the pixels in the CCD (hologram) plane, and $*$ stands for the complex conjugate. In an off-axis digital holographic configuration^{9–12} similar to the one shown in Fig. 1(a), the CCD sensor is illuminated with a plane reference wave, $R(k, l) = R \exp[i(2\pi f_0 x)]$, at an angle θ , and an object wave, $O(k, l)$, so that the resulting interference has a fringe pattern with equidistant spacing of^{13,14}

$$P_F = \frac{\lambda}{2 \sin\left(\frac{\theta}{2}\right)}, \quad (2)$$

where P_F is the period of the fringe pattern, λ is the laser wavelength, and θ is the off-axis angle. Therefore, the spatial frequency of the interferogram, i.e., reciprocal of the P_F , can be written as

$$f_0 = \frac{2}{\lambda} \sin\left(\frac{\theta}{2}\right). \quad (3)$$

The four terms of Eq. (1) are superimposed in the hologram (spatial) domain. However, if the hologram is recorded in an

off-axis geometry, these terms can be separated by taking the Fourier transform, \mathcal{F} , of the intensity to obtain

$$\begin{aligned} \mathcal{F}[I(k, l)] &= \mathcal{F}(|R(k, l)|^2) + \mathcal{F}(|O(k, l)|^2) \\ &\quad + \mathcal{F}[R^*(k, l)O(k, l)] + \mathcal{F}[R(k, l)O^*(k, l)]. \end{aligned} \quad (4)$$

The spectrum of such an off-axis hologram is schematically shown in Fig. 1(b). The central parts of the hologram spectrum, $\mathcal{F}(|R(k, l)|^2) + \mathcal{F}(|O(k, l)|^2)$, lack the phase information and contain only intensity values and are called the zero-order diffraction (ZOD) terms. The other two terms, symmetrically located from the origin, encode both intensity and phase and are called the twin images.

Based on Wiener–Khinchin theorem, the Fourier transforms (FTs) of the squared fields $|R(k, l)|^2$ and $|O(k, l)|^2$, termed T1 and T2 in Fig. 1(b), are equal to the autocorrelation of the FT of wave fields $R(k, l)$ and $O(k, l)$ in the Fourier domain, respectively, and the FT of the term $R^*(k, l)O(k, l)$ is the cross-correlation of the FT of R^* and O [and similarly for the $R(k, l)O^*(k, l)$ term]. It should be noted that the correlation integral, similar to the convolution integral, represents the scanning of one function by another. The range of variables over which the integral is nonzero is given by the sum of the widths of the scanning and scanned signals. In the case of autocorrelation, the maximum extent is twice the width of the function being autocorrelated.¹⁵ Therefore, considering an ideal plane reference wave $R(k, l)$ providing a single spatial frequency, the bandwidths of cross-correlation terms $\mathcal{F}(R^*O)$ and $\mathcal{F}(RO^*)$ are half of the bandwidth of the autocorrelation term $\mathcal{F}(|O|^2)$. As shown in Fig. 1(b), assuming that the object wave field has a bandwidth of B , the bandwidth of each of the cross-correlation terms, T3 and T4, corresponds to the bandwidth of the object's wavefront and is equal to B , and the bandwidth of the autocorrelation term T2, $\mathcal{F}(|O|^2)$, is $2B$.

To ensure that the information recorded by the off-axis holography is resolvable and useful, two requirements should be satisfied. First, the cross-correlation terms (conjugated data) should be completely separate from the autocorrelation (ZOD) terms; this requirement can be satisfied using a minimum off-axis angle of the reference wave. Second, the CCD sensor should be able to resolve the interference pattern, which can be

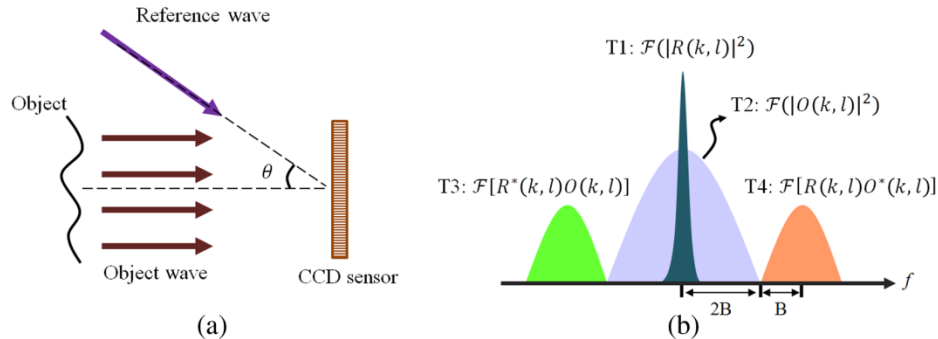


Fig. 1 Principles of the off-axis holographic configuration: (a) spatial carrier frequency is induced by the off-axis angle of the reference wave with respect to the system's optical axis; and (b) four terms in the spectrum of the hologram that consists of two autocorrelation terms T1 and T2 and two cross-correlation terms T3 and T4. The bandwidth of the cross-correlation terms is half the bandwidth of autocorrelation terms.

obtained by limiting the off-axis angle to be less than the Nyquist sampling limit, which requires at least two pixels per fringe period.

2.1.1 Minimum off-axis angle

In order to separate useful data that contain phase information (conjugated data) from the autocorrelation terms, which only include intensity values (ZOD terms), a minimum off-axis angle should be considered for the reference wave. To determine this minimum angle, it is sufficient to determine the minimum carrier frequency f_{\min} for which the autocorrelation and cross-correlation terms are completely separated from each other. As shown in Fig. 1(b), the minimum carrier frequency that produces separated terms occurs when $f_{\min} \geq 3B$, resulting in a highest spatial frequency of at least 4B and a total spatial bandwidth of 8B. Therefore, the optimum bandwidth of the hologram in the case of the Fresnel approximation is adjusted to be 8B.

It was demonstrated that for the case of Fresnel approximation in the scalar diffraction theory, the total bandwidth of the hologram is equal to the sum of the bandwidths of the convolution kernel (quadratic phase-factor) and the bandwidth of the FT of the object field.^{16,17} The spatial bandwidth of the convolution kernel can be determined by taking a partial derivative of the convolution kernel with respect to the two directions and can be calculated with $N\Delta x/\lambda d$ and $N\Delta y/\lambda d$, where N^2 is the number of pixels in the hologram plane, Δx and Δy are the pixel sizes in the x and y directions, and d is the reconstruction distance. On the other hand, it can be geometrically shown that the maximum bandwidth of the object can be calculated from $L_x/\lambda d$ and $L_y/\lambda d$, where L_x and L_y are the dimensions of the object in the horizontal and vertical directions.^{18,19} Assuming $L_x = L_y = L$ and $\Delta x = \Delta y = \Delta p$, the summation of these two bandwidths defines the total bandwidth of the hologram field and can be written as

$$8B = \frac{L + N\Delta p}{\lambda d}. \quad (5)$$

Therefore, the minimum spatial frequency of 3B can be calculated with

$$f_{\min} \geq 3B = \frac{3(L + N\Delta p)}{8\lambda d}, \quad (6)$$

hence, the minimum off-axis angle of the reference wave can be obtained by combining Eqs. (3) and (6) and can be written as

$$\theta_{\min} = 2 \sin^{-1} \left[\frac{3(L + N\Delta p)}{16d} \right]. \quad (7)$$

Therefore, a minimum angle of θ_{\min} should be considered to avoid any overlapping of the twin images and ZOD terms. However, in order for the CCD sensor to be able to resolve the interference patterns, one needs to limit the maximum off-axis angle.

2.1.2 Maximum off-axis angle

The achievable resolution for holographic reconstruction is dictated mainly by the spatial carrier frequency of the reference wave (which influences the fringe spacing) and the sampling resolution of the CCD. Based on the Nyquist theorem, the

maximum spatial frequency of the interferogram that the CCD can resolve is

$$f_{\max} = \frac{1}{2\Delta p}, \quad (8)$$

where Δp is the pixel size of the camera. Combining Eqs. (3) and (8) and considering the small angles for θ , the maximum angle can be obtained using

$$\theta_{\max} = 2 \sin^{-1} \left(\frac{\lambda}{4\Delta p} \right). \quad (9)$$

Therefore, considering the points mentioned in Sec. 2.1 and, in particular, Eqs. (7) and (9), for a CCD sensor with 2048×2048 pixels of size of $\Delta p = 3.45 \mu\text{m}$, an object size of 1 cm, and an object-to-CCD distance of 10 cm, the allowable off-axis angle should be within the range of $3.6 \leq \theta \leq 6.5$ deg. These results are considered in the design of our experimental setup.

2.2 Off-Axis Multiplexed Lensless Digital Holography

For 3-D displacement measurements using off-axis multiplexed holography, three incoherently superimposed pairs of object and reference beams are simultaneously recorded with the CCD sensor. As shown schematically in Fig. 2(a), the object of interest is illuminated concurrently with three object beams from different directions to provide three sensitivity vectors that are required for 3-D displacement measurements.¹⁴ The reference beams provide slightly different spatial carrier frequencies on the CCD to enable single-frame phase extraction.²⁰ The total intensity recorded on the CCD detector, $I(k, l)$, due to incoherent superposition of three pairs of reference-object beams is^{6,7}

$$I(k, l) = \sum_{n=1}^3 I_n(k, l) = \sum_{n=1}^3 |R_n(k, l) + O_n(k, l)|^2, \quad (10)$$

where k and l are the coordinates of the pixels in the CCD (hologram) plane, R_n and O_n are the n 'th reference and object waves, respectively, with $n = 1, 2, 3$. Similar to single sensitivity vector off-axis holography, described in Eqs. (1) and (4), Eq. (10) can be expanded to

$$I(k, l) = \sum_{n=1}^3 a_n(k, l) + c_n(k, l) \exp[2\pi i(f_{n\xi}x + f_{n\eta}y)] + c_n^*(k, l) \exp[-2\pi i(f_{n\xi}x + f_{n\eta}y)], \quad (11)$$

where $a_n(k, l) = R_n^2(k, l) + O_n^2(k, l)$ and $c_n(k, l) = O_n(k, l)R_n(k, l) \exp[i\varphi_n(k, l)]$. The two-dimensional (2-D) FT of Eq. (11) is

$$\text{FT}\{I(k, l)\} = \sum_{n=1}^3 A_n(\xi, \eta) + C_n(\xi - f_{n\xi 0}, \eta - f_{n\eta 0}) + C_n^*(\xi + f_{n\xi 0}, \eta + f_{n\eta 0}), \quad (12)$$

where the uppercase notation denotes the FT components. The terms C_n and C_n^* describe the spatial frequency distribution of the twin images components that are mathematically expressed as complex conjugates of one another, each containing the

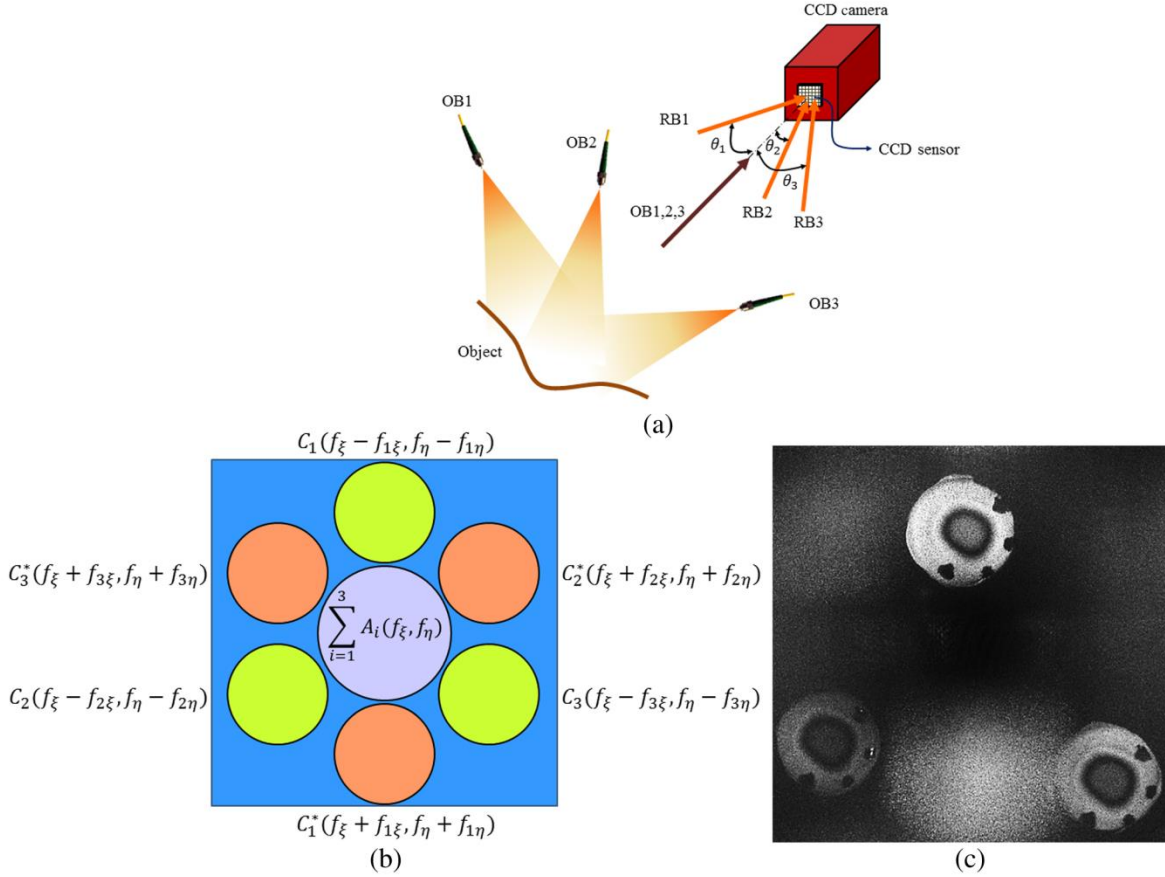


Fig. 2 Multiplexed off-axis holography: (a) schematic of the recording procedure by simultaneous illumination with three pairs of reference and object beams; (b) spectrum of the recorded multiplexed off-axis hologram consisting of three incoherently superimposed interference patterns; and (c) representative numerically reconstructed double-exposure multiplexed hologram that is used for 3-D displacement measurements. The object of interest is a 1-cm diameter latex membrane, acoustically excited by a tone of 1.5 kHz. Sound-induced concentric fringe patterns and four painted marks used to test registration algorithms are visible on each of the reconstructed images.

required phase information. As shown in Fig. 2(b), these terms are shifted in the Fourier domain due to the off-axis angles of the reference waves and can be separated from one another by an appropriate calculation and the setting of carrier frequencies $f_{n\zeta_0}$ and $f_{m\eta_0}$, as described in Sec. 2.1.

Our techniques are based on single-frame lensless digital holography^{21–23} in which reconstructions of the multiplexed holograms are obtained by the Fresnel–Kirchhoff integral that is efficiently computed with the 2-D FFT as

$$\Gamma(m, n) = \text{FFT2}[R(k, l)h(k, l)\psi(k, l)], \quad (13)$$

where $\Gamma(m, n)$ is the complex reconstructed hologram at coordinates m and n in the reconstruction plane, $R(k, l)$ is the complex amplitude of the plane reference wave that is considered to be one in the numerical reconstruction, and $\psi(k, l)$ is the 2-D chirp function defined with

$$\psi(k, l) = \exp\left[\frac{-i\pi}{\lambda d}(k^2 \Delta x^2 + l^2 \Delta y^2)\right], \quad (14)$$

where Δx and Δy are the pixels sizes of the CCD sensor, λ is the laser wavelength, and d is the reconstruction distance. Additionally, the DC component can be mathematically removed from the multiplexed hologram by recognizing that the DC component in the Fourier domain is due to the low-frequency spatial variation in the hologram, and it can thus be isolated by applying a high-pass filter.^{10,11} Therefore, the optical phase of the reconstructed hologram is obtained with

$$\varphi(x, y) = \text{atan} 2 \left\{ \frac{\Im[\Gamma(m, n)]}{\Re[\Gamma(m, n)]} \right\}, \quad (15)$$

where \Im and \Re denote the imaginary and real parts of the complex number $\Gamma(m, n)$. Thus, in one single frame of the camera, optical phase information corresponding to all three sensitivity vectors exists. With the use of double-exposure techniques, i.e., subtracting optical phases of two reconstructed holograms corresponding to deformed and reference states of the object, the 3-D motion components of the objects can be obtained with the method of multiple sensitivity vectors in holographic

interferometry.²⁴ Considering the fact that the fringe-locus function Ω ,²⁵ i.e., the unwrapped optical phase difference between the two states, is the scalar product of the sensitivity vector, $\mathbf{K}(\mathbf{K}_x, \mathbf{K}_y, \mathbf{K}_z)$, with the object's displacement vector, $\mathbf{d}(\mathbf{d}_x, \mathbf{d}_y, \mathbf{d}_z)$, the 3-D displacements components are obtained by

$$\begin{bmatrix} \mathbf{d}_x \\ \mathbf{d}_y \\ \mathbf{d}_z \end{bmatrix} = \frac{\lambda}{2\pi} \begin{bmatrix} \mathbf{K}_x^1 & \mathbf{K}_y^1 & \mathbf{K}_z^1 \\ \mathbf{K}_x^2 & \mathbf{K}_y^2 & \mathbf{K}_z^2 \\ \mathbf{K}_x^3 & \mathbf{K}_y^3 & \mathbf{K}_z^3 \end{bmatrix}^{-1} \times \begin{bmatrix} \Omega_1 \\ \Omega_2 \\ \Omega_3 \end{bmatrix}. \quad (16)$$

However, in the case of off-axis multiplexed holography, the differences in the position of each reference beam and wavelength of each pair of beams cause the position, reconstruction distance, and magnification of each image corresponding to each sensitivity vector to differ. The translation between the images could be computed analytically if the exact relative orientation and position of the reference beams were known. However, such an approach would require additional hardware, and small errors in the measurement of the orientation could lead to large errors in the estimate of the translation. It is thus more efficient to register the resulting images in a postprocessing step. Therefore, for quantification of the 3-D displacement, an image registration algorithm is required to position each image into a common global coordinate system.

2.3 Registration of Multiplexed Holograms

In order to place the images in a common coordinate system, prior to applying Eq. (16), a registration algorithm based on POC has been developed and implemented.^{8,26,27} This algorithm accounts for pure translation of the reconstructed images and an intensity-invariant approach to compensate for slight differences in the overall brightness and intensity of the images.

Considering two translated images $f(n_1, n_2)$ and $g(n_1, n_2) = f(n_1 - \delta_1, n_2 - \delta_2)$, with relative separations of δ_1 and δ_2 in the horizontal and vertical axes, respectively, their corresponding FT images, $F(k_1, k_2)$ and $G(k_1, k_2)$, are related to each other through the shift theorem with

$$G(k_1, k_2) = F(k_1, k_2) \cdot e^{-2\pi j \left[\frac{k_1 \delta_1}{M} + \frac{k_2 \delta_2}{N} \right]}, \quad (17)$$

where M and N are the number of pixels in the image, and k_1 and k_2 are the coordinates in the frequency domain. Therefore, the normalized cross-power spectrum of $F(k_1, k_2)$ and $G(k_1, k_2)$ is

$$R(k_1, k_2) = \frac{F(k_1, k_2)G^*(k_1, k_2)}{|F(k_1, k_2)G^*(k_1, k_2)|} = e^{2\pi j \left[\frac{k_1 \delta_1}{M} + \frac{k_2 \delta_2}{N} \right]}, \quad (18)$$

where $*$ defines the corresponding complex conjugated functions. By applying the inverse 2-D FFT to Eq. (18), the POC function, $r(n_1, n_2)$ is calculated with

$$r(n_1, n_2) = \mathcal{F}^{-1}\{R(k_1, k_2)\} = \delta(x + \delta_1, y + \delta_2), \quad (19)$$

with δ being the Kronecker delta function having a single peak, whose location defines the translation between the two images⁸ and can be computed with

$$[\delta_1, \delta_2] = \text{argmax}\{r(n_1, n_2)\}. \quad (20)$$

The phase correlation, r [Eqs. (19) and (20)] was calculated from a series of subsets of R with regularly decreasing high-frequency limit (equivalent to spatial filtering with regularly

decreasing low-pass cut-off frequencies). The translation between two images is obtained by considering the most frequent peak of the POC functions resulting from the calculation series.

2.4 Multiplexed Holographic System

In our experimental system, incoherent superposition of the beams is implemented by using three different near-infrared external cavity tunable laser sources with wavelengths centered at 779.8, 780.2, and 780.6 nm. As shown in Fig. 3, the acousto-optic modulators (AOMs) contained in each laser delivery subsystem (LD1 to LD3) are used to switch the laser on/off to enable stroboscopic measurement capabilities^{2,28} (Hernández-Montes et al., 2011). A dual-channel function generator is used with one of the channels sets to acoustically stimulate the TM sample with a calibrated speaker, while the second channel is set to pulse mode to simultaneously drive all three AOMs. The duty cycle of the pulse signal sent to the AOMs is typically set to 2% to 5% of the period of the tonal stimulus; however, the multiplexed holographic system (MHS) temporal resolution, i.e., the system's maximum detection bandwidth, is determined by the 200-kHz limit of the AOMs used to strobe the phasic illumination. As shown in Fig. 3, each laser is coupled into single-mode polarization maintaining fibers and then split into reference and object beams. The reference beams illuminate the CCD in an off-axis configuration by a beam splitter and the object beams concomitantly illuminate the sample from three different directions to define the sensitivity vectors for 3-D displacement measurements. In Fig. 3, the optoelectronic components are shown for only one of the laser delivery subsystems; however, all three laser delivery subsystems contain similar components.

The computing platform performs multiple tasks that include synchronizing the stroboscopic illumination of the lasers with different stimulus phases, acquiring multiplexed holograms with a 5 MPix CCD camera having a pixel size of $3.45 \times 3.45 \mu\text{m}^2$, and reconstructing the holograms in real time. A live 2-D FFT is used to ensure that the components of the frequency spectrum of the hologram do not overlap with each other.²⁹

3 Validation of Measuring Capabilities

In order to validate the measuring capabilities of the MHS, the results of an artificial membrane obtained with our MHS are compared with the ones obtained with a documented repetitive holographic interferometric method.²³ The artificial sample is a thin semispherical membrane mounted on a mechanical shaker that can operate over a wide range of frequencies up to 150 kHz. The results of the vibration of this sample at 25-kHz frequency are shown in Fig. 4. Modulation and wrapped optical phase images of both twin components are shown to illustrate how the three pairs of complex conjugated reconstructed holograms are distributed.

To determine the 3-D deformations of the membrane, the POC image registration algorithm described in Sec. 2.3 is used to place the wrapped optical phases in a common coordinate system prior to unwrapping and applying Eq. (16). Figures 5(a)–5(c) show the registered wrapped and corresponding unwrapped optical phases of the artificial sample along three sensitivity vectors \mathbf{K}_1 to \mathbf{K}_3 that are used to quantify 3-D displacements of the membrane. Unwrapping of the optical phases might add a constant phase value (DC) to the unwrapped data, therefore, as shown in Fig. 5(c), a seed point at an area with no deformation is selected and the value of this point is considered

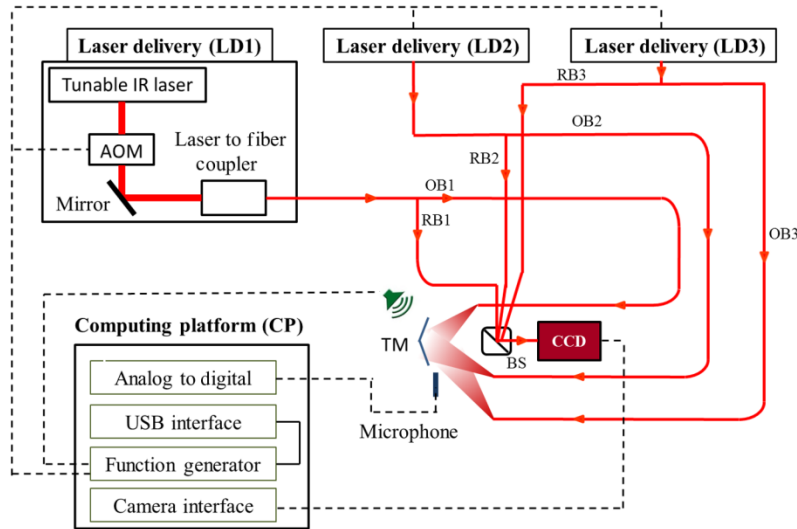


Fig. 3 Experimental system for simultaneous 3-D displacement measurements with multiplexed holography. The solid lines denote the beam paths and the dashed lines the connections between components. AOM is the acousto-optic modulator; RB and OB are the reference and object beams, respectively; BS is the beam splitter; and TM is the tympanic membrane sample. Each of the three laser delivery subsystems contains similar components.

as the DC, so that all the pixels' values in this image are subtracted from this DC. This step is repeated for all three unwrapped phases so that the data are all normalized before quantification of 3-D motion.

The registered, unwrapped, normalized phases are used to quantify 3-D deformation. To test and verify the validity of the measurements obtained with MHS, the results are compared with results obtained with a documented repetitive holographic interferometric method.²³ The results obtained with both methods are shown in Fig. 6. On visual inspection, the results of both methods are almost indistinguishable from each other. A point-by-point correlation measure indicates a Pearson correlation coefficient of 97%, 96%, and 99% along the x -, y -, and z -axes, respectively. It should be noted that since the resolution of the results obtained from the two methods is different (in the MHS the image resolution is 500×500 while in the regular repetitive method the resolution is 1500×1500), the images with higher resolution are first downsampled and then the correlations are evaluated.

4 Representative Measurements of Three-Dimensional Motions of Human Tympanic Membrane

The cadaveric human TM of a female, 46-year-old donor was prepared by removing the bony portion of the ear canal in a lightly fixed temporal bone. The middle-ear space of the sample was widely opened, which enabled assessment of the normality of the TM and ossicles. The temporal bone was immersed in Thiel embalming solution for several weeks before the experiments to stop decay and eliminate potential pathogens.³⁰ Due to semitransparency of the mammalian TMs, the sample was coated with a thin layer of zinc oxide to increase the laser light reflection, as shown in Fig. 7(a). The effect of coating on shape and deformation patterns has been studied by several researchers and found to be negligible.^{31,32} The

temporal bone was held with an adjustable clamp and mounted on a post in front of the holographic system. Figure 7(b) schematically shows the simultaneous recording of a multiplexed hologram of the cadaveric human TM. As shown in this figure, the x -axis is along the superior-inferior direction and the y -axis is along posterior-anterior direction, while the z -axis is perpendicular to the tympanic ring plane and along the lateral side of the TM. Figure 7(c) shows a representative example of wrapped optical phase of sound-induced motion of the TM acquired with a double-exposure multiplexed hologram of the TM surface. The three fringe patterns show the similarities and differences in their spatial arrangement and their optical phase magnitudes.

Prior to stroboscopic measurements, the time-averaged response of the TM at different tonal stimuli was monitored³² and the excitation frequencies were chosen at the maximum motion of the TM. At each stroboscopic phase, sound-induced motions of the TM along three orthogonal axes x , y , and z are calculated from the unwrapped optical phases, as described in Sec. 2.2. Then, FFT algorithms are used to reconstruct magnitudes and phases of motions along all three axes² and the results are shown in Fig. 8. The displacement patterns are simpler at lower frequencies, and as the excitation frequency increases, the complexity of the displacement maps also increases. At 0.8 kHz, one or two regions of large displacement are visible with a relatively homogenous phase along all three axes. As excitation frequency increases nodal lines appear, characterized by lines of minimum magnitude corresponding to separations between regions where the phase is different by 0.5 cycles, suggesting that the number of areas on the surface of the TM that are moving out-of-phase also increases. Such a phenomenon can be clearly seen in TM's motion patterns obtained with excitation frequencies of 4.68 and 13.2 kHz, as shown in Fig. 8. An interesting observation is that in low excitation frequencies, the magnitude of motion along the x -axis is slightly greater than along

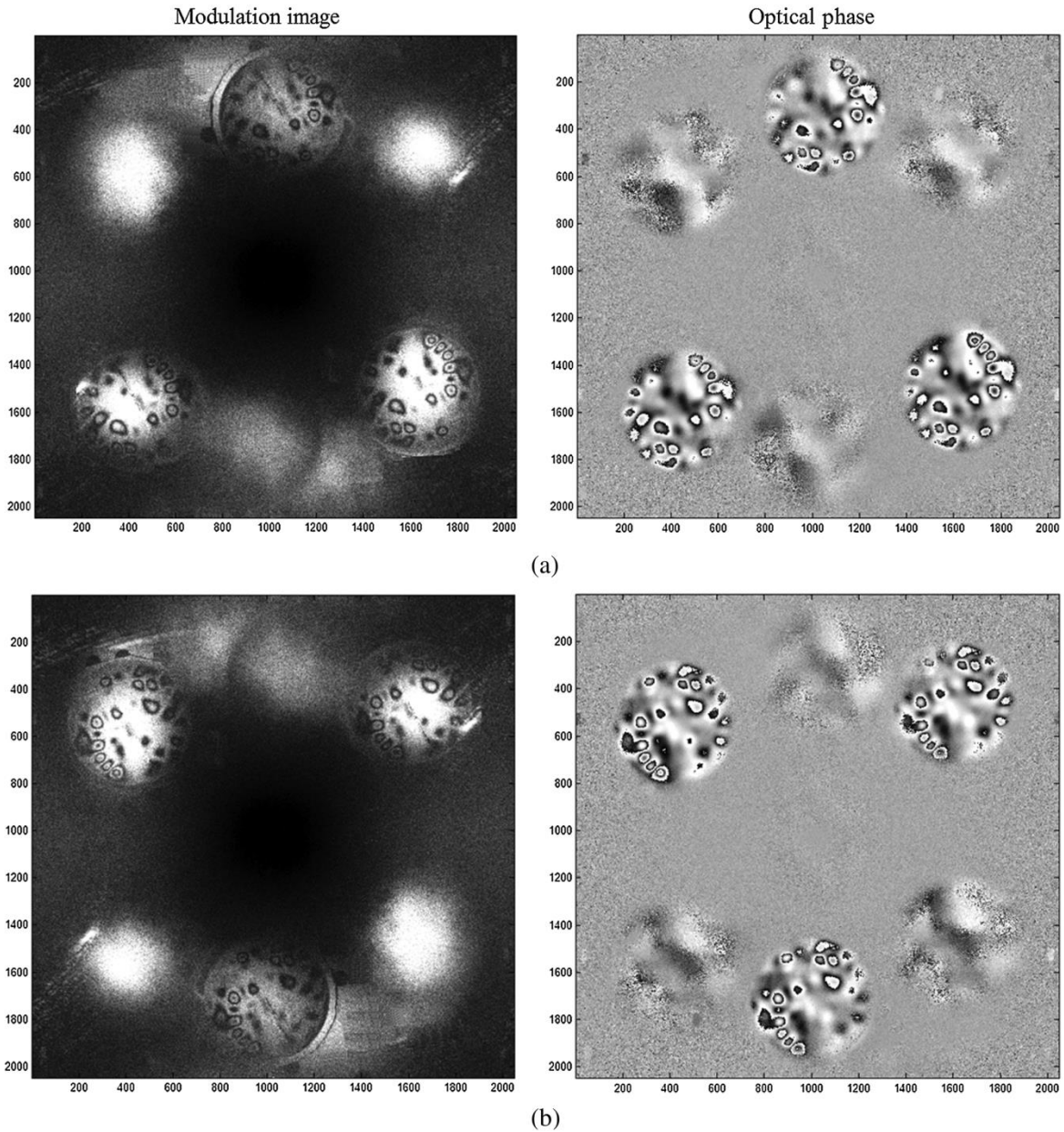


Fig. 4 Stroboscopic measurements of a vibrating thin semispherical membrane clamped around its perimeter: (a) and (b) are the modulation and wrapped optical phase of the real and conjugated reconstructed multiplexed holograms. The excitation frequency is 25 kHz and the membrane is concomitantly illuminated from three different directions to define the sensitivity vectors for 3-D measurements, which in this case correspond to the difference in the motion of the membrane between two stimuli phases of 0 deg and 90 deg. The images for each of the three sensitivity vectors and their corresponding conjugates (fuzzy images) are symmetrically arranged around the center of each figure panel.

the y -axis. Since the manubrium is located along the x -axis of the measuring system [Fig. 7(b)], a possible interpretation is that the TM, in response to sound, deforms more in the direction parallel to the manubrium than in the direction perpendicular to it.

The presence of delay in the sound transfer of the middle ear triggered the idea of the existence of traveling waves on

the surface of the TM and it was suggested by several researchers.^{33,34} Although our data show that the majority of the TM motions are modal, there are indications of a combination of modal and traveling wave like motions on the surface of the TM. Figure 9 shows the sound-induced motions of the TM excited with a tone of 6.884 kHz at several instances of the

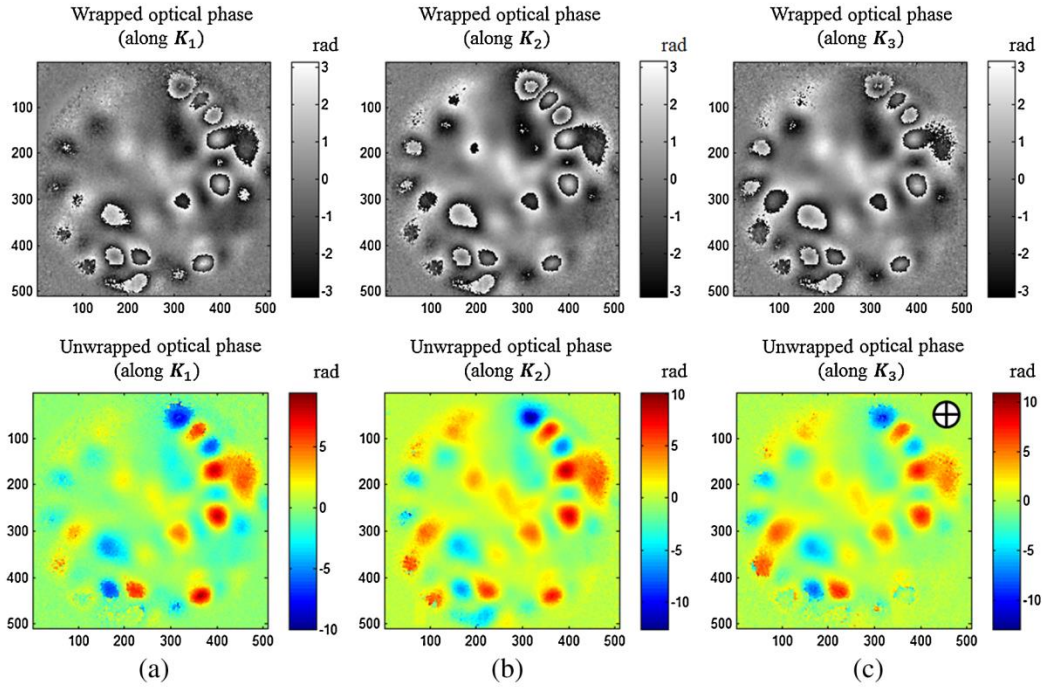


Fig. 5 Registered optical phases corresponding to sound-induced displacement of an artificial membrane: (a)–(c) wrapped and unwrapped optical phases corresponding to sensitivity vectors K_1 to K_3 , respectively. “+” in the unwrapped optical phase along K_3 denotes the location of the seed point to identify the DC of the unwrapped data. The color and grayscale coded wrapped and unwrapped phases are in radians.

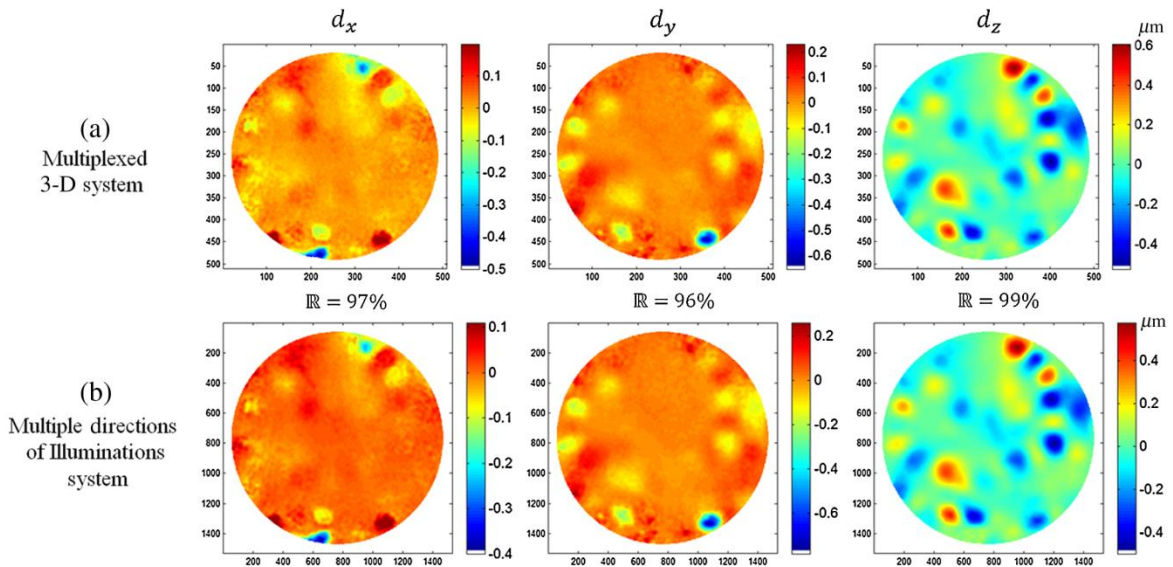


Fig. 6 Validation of the results of three-dimensional (3-D) displacement measurements versus a documented method:²³ (a) displacement components along x , y , and z obtained using MHS; and (b) displacement components along x , y , and z obtained with the method of repetitive holographic interferometry. R is the Pearson correlation coefficient between the results obtained with the two methods.

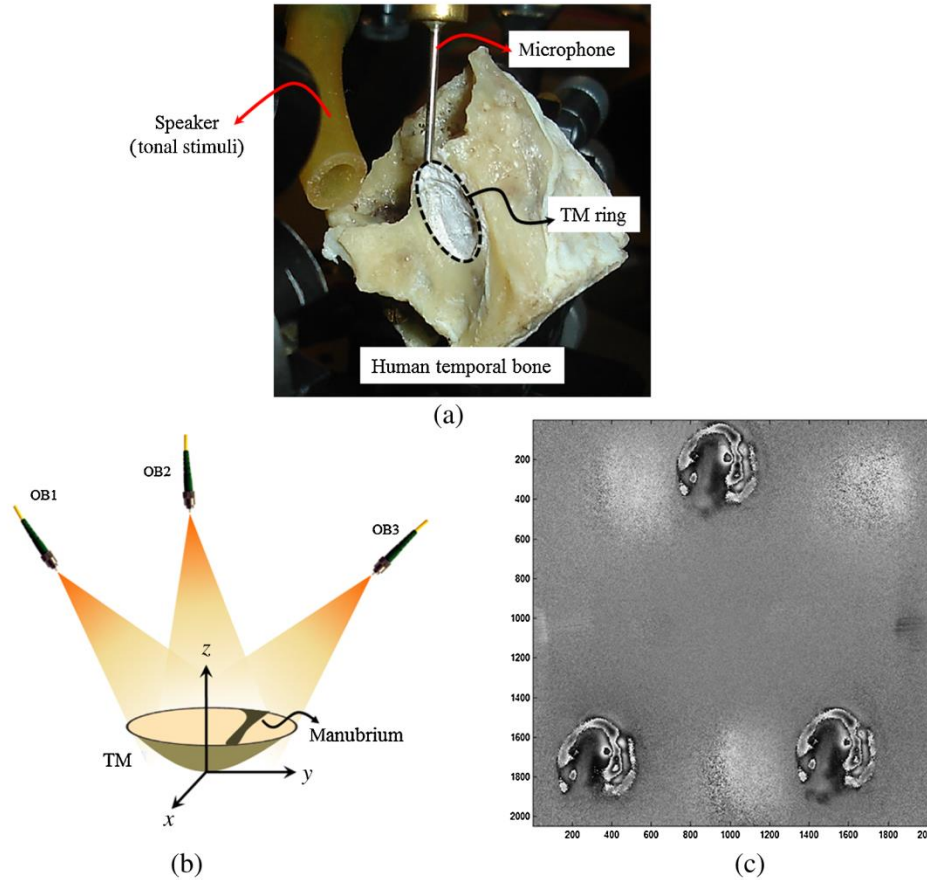


Fig. 7 Simultaneous recording of a multiplexed hologram of a cadaveric human TM in order to acquire 3-D sound-induced displacements: (a) the human temporal bone including the TM under investigations with the location of speaker and microphone; (b) schematic of the recording of the multiplexed hologram illustrating simultaneous illumination of the three light sources on the TM samples from different sensitivity vectors; and (c) acoustically induced wrapped optical phase corresponding to the stroboscopic measurement of a human TM motion at a stimulus frequency of 6.884 kHz. The optical phases correspond to the difference in the motion of the TM at two acoustic phases of 0 deg and 90 deg. Bright blurry regions facing each of them on the opposite of the image's center are the corresponding complex conjugates.

full-cycle vibration obtained from stroboscopic illumination at different phases of the excitation signal. Two arrows shown in Fig. 9 illustrate the main traveling waves' paths. As shown in this figure, the motion of the first traveling wave is initiated from the posterior-inferior quadrant and travels in a semicircular way toward the posterior-superior quadrants. The second one circulates in the posterior-inferior quadrant. Considering the excitation frequency and the travel distance, a wave speed of 21 m/s can be calculated.

5 Discussion

In this paper, we have shown the results of simultaneous 3-D vibrometry of the human eardrum using MHS. The results show great similarities with state-of-the-art multiple sensitivity vectors holographic methods, while the recording time is drastically reduced (decrease in the acquisition time by a factor of 3 in the case of a single frame and a factor of 12 in the case of four phase-stepping techniques). The developed method has promising applications in the experimental measurement of the

motion of biological membranes such as the TM. Simultaneous 3-D motion measurement is a crucial step toward holographic measurements of live biological specimens.

5.1 Choice of the Registration Technique

The success of the registration depends on the similarities in spatial patterns. In theory, if the motion of the measured object is very different along the multiple sensitivity vectors, the registration might be less accurate. However, since the sensitivity vectors are not orthogonal, the motions along all sensitivity vectors are correlated. Moreover, the pattern made by nodes (regions with no membrane motion) is likely to be similar along several vectors since the displacement is equally zero along the multiple directions. The choice of an FFT-based method over a moving correlation method is motivated by its lower computational load. Also, the FFT needs to be calculated only once for spatial filtering and registration. An alternative to use *a posteriori* registration would be the analytic computation

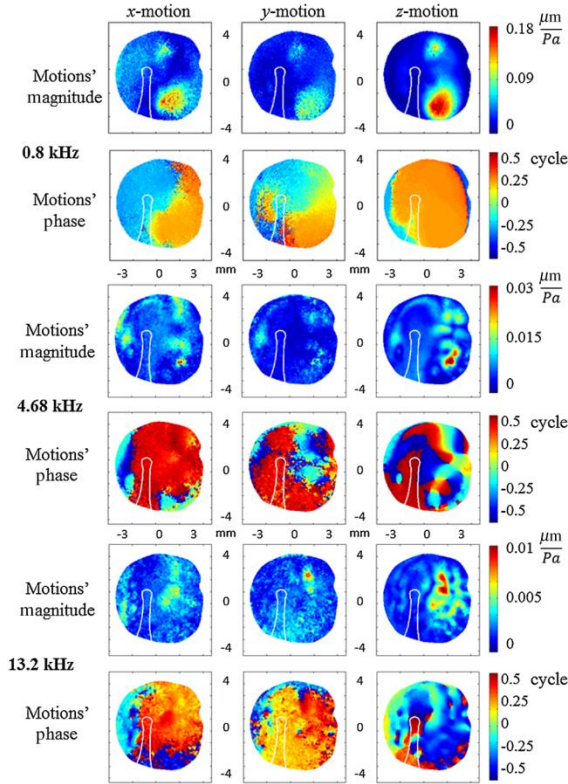


Fig. 8 Magnitudes and phases of 3-D sound-induced displacements of the human TM excited at three different frequencies obtained with FFT-reconstruction algorithm along three orthogonal axes x , y , and z . The displacements are normalized based on the sound pressure level obtained from the microphone. The outline of the manubrium is shown in white in all the figures.

of the translation between the reconstructed images. In this case, a very accurate measure of the position and orientation of all elements of the optical system would be required. Such an approach would not only be cumbersome, but small errors could lead to large errors in the translation calculation. For these reasons, the developed method is preferred.

5.2 Dynamics of Human Tympanic Membranes

Our previous studies have shown that the sound-induced motions of the mammalian TMs follow several patterns (simple, complex, ordered) at different stimulus frequency ranges.^{21,32} It was shown that at low excitation frequencies (up to 1 kHz), most of the points (>90%) on the surface of the TM are moving in-phase and the surface displacements are well described by low-order modal motions without any nodal points.^{2,35} As the excitation frequency increases, the displacement patterns can be described with a combination of higher-order modal displacements (with multiple nodes) and traveling waves. The 3-D results shown in this paper show similar types of dynamics along all three axes, which are in the plane of the tympanic ring (along the x - and y -axes) and normal to such a plane (along the z -axis). The motion pattern is simple at 0.8 kHz (top 2 rows of Fig. 8), complex at 4.68 kHz (middle 2 rows of Fig. 8), and ordered at 13.2 kHz (bottom 2 rows of Fig. 8) stimuli.

6 Conclusions

Due to the time-varying nature of biological tissues like the TM, a unique method for 3-D displacement measurements based on multiplexed holography is developed that allows for simultaneous holographic measurements along multiple sensitivity vectors. The developed methodology is a critical step toward *in vivo* measurements of 3-D TM motions. In our approach, the hologram of an object of interest is recorded with three simultaneous incoherently superimposed pairs of reference and object beams, such that the modulation image corresponding to each illumination direction is reconstructed at a different position of

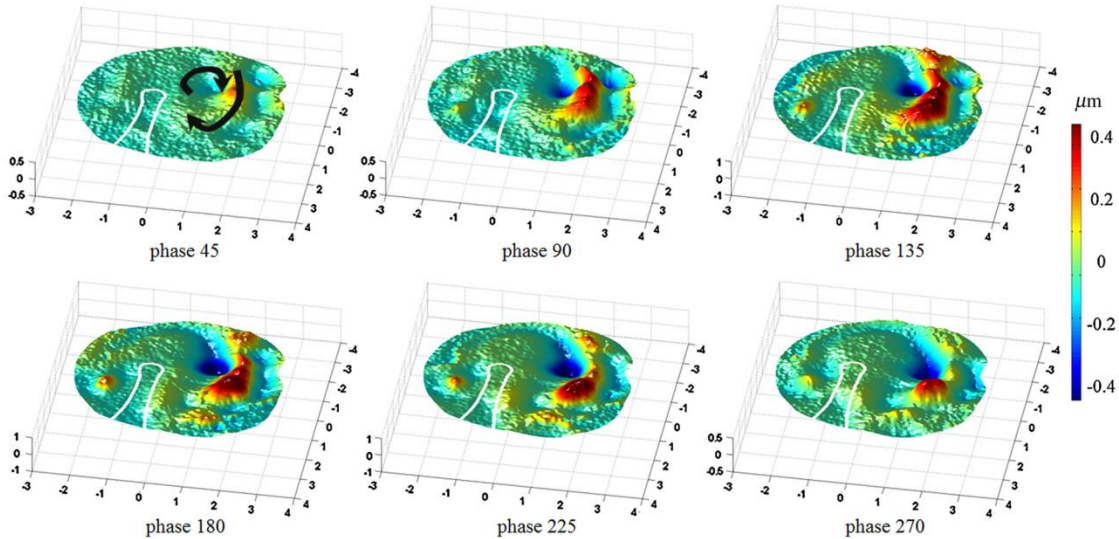


Fig. 9 Responses of the human TM excited with a tone of 6.884 kHz at different acoustic phases suggesting the presence of a combination of modal and traveling wave patterns. Black arrows shown in the pattern of phase 45 deg indicate the main paths of the traveling waves.

the image. An image registration algorithm based on the shift theorem of the FT is implemented to register the images. The displacement measurements are in good agreement (greater than 96%) with other documented methods, while simultaneous acquisition of all three measurements reduces the effects of temporal variations of the specimens. The time needed for a given 3-D displacement measurement is decreased at least threefold. We demonstrate that the present method is a valid alternative to repetitive holographic methods and offers promising perspectives toward faster accurate displacement measurements of biological specimens.

Acknowledgments

This work was supported by the National Institute on Deafness and other Communication Disorders (NIDCD), Massachusetts Eye and Ear Infirmary (MEEI), the Swiss National Science Foundation (SNSF), and the Mechanical Engineering Department at Worcester Polytechnic Institute. We also acknowledge the support of all the members of the CHSLT labs at WPI and Eaton-Peabody labs at MEEI, in particular Ellery Harrington and Jeffrey Tao Cheng.

References

- W. F. Decraemer, S. M. Khanna, and W. R. J. Funnell, "A method for determining three-dimensional vibration in the ear," *Hear. Res.* **77**, 19–37 (1994).
- J. J. Rosowski et al., "Measurements of three-dimensional shape and sound-induced motion of the chinchilla tympanic membrane," *Hear. Res.* **301**, 44–52 (2013).
- H. Motallebzadeh, M. Charlebois, and W. R. J. Funnell, "A non-linear viscoelastic model for the tympanic membrane," *J. Acoust. Soc. Am.* **134**(6), 4427–4434 (2013).
- D. De Greef et al., "Viscoelastic properties of the human tympanic membrane studied with stroboscopic holography and finite element modeling," *Hear. Res.* **312**, 69–80 (2014).
- O. J. Løkberg, K. Hagmoen, and T. Gundersen, "Vibration measurement of the human tympanic membrane *in vivo*," *Acta Oto-Laryngol.* **89**(1–2), 37–42 (1980).
- S. Schedin et al., "Simultaneous three-dimensional dynamic deformation measurements with pulsed digital holography," *Appl. Opt.* **38**(34), 7056–7062 (1999).
- P. Picart, E. Moisson, and D. Mounier, "Twin-sensitivity measurement by spatial multiplexing of digitally recorded holograms," *Appl. Opt.* **42**(11), 1947–1957 (2003).
- K. Takita et al., "High-accuracy subpixel image registration based on phase-only correlation," *IEICE Trans. Fundam. Electron. Commun. Comput. Sci.* **86**(8), 1925–1934 (2003).
- E. N. Leith and J. Upatnieks, "Reconstructed wavefronts and communication theory," *J. Opt. Soc. Am.* **52**(10), 1123–1128 (1962).
- E. Cuhe, P. Marquet, and C. Depeursinge, "Spatial filtering for zero-order and twin-image elimination in digital off-axis holography," *Appl. Opt.* **39**(23), 4070–4075 (2000).
- N. Pavillon et al., "Suppression of the zero-order term in off-axis digital holography through nonlinear filtering," *Appl. Opt.* **48**(34), H186–H195 (2009).
- S. De Nicola et al., "Infrared holography for wavefront reconstruction and interferometric metrology," in *Advanced Holography—Metrology and Imaging*, pp. 157–180, Intech (2011).
- T. M. Kreis, M. Adams, and W. P. O. Jüptner, "Methods of digital holography: a comparison," *Proc. SPIE* **3098**, 224 (1997).
- U. Schnars et al., *Digital Holography and Wavefront Sensing*, Springer, Berlin, Heidelberg (2015).
- R. J. Collier, C. B. Burckhardt, and L. H. Lin, *Optical Holography*, Academic Press, New York (1971).
- J. Goodman, Eds., *Introduction to Fourier Optics*, 2nd ed., McGraw-Hill Series in Electrical and Computer Engineering (2008).
- P. Picart et al., "Spatial bandwidth extended reconstruction for digital color Fresnel holograms," *Opt. Express* **17**(11), 9145–9156 (2009).
- F. Gori, "Fresnel transform and sampling theorem," *Opt. Commun.* **39**(5), 293–297 (1981).
- A. Stern and B. Javidi, "Improved-resolution digital holography using the generalized sampling theorem for locally band-limited fields," *J. Opt. Soc. Am. A* **23**(5), 1227–1235 (2006).
- M. Takeda, H. Ina, and S. Kobayashi, "Fourier-transform method of fringe-pattern analysis for computer-based topography and interferometry," *J. Opt. Soc. Am.* **72**, 156–160 (1982).
- M. Hernández-Montes et al., "Optoelectronic holographic otoscope for measurement of nano-displacements in tympanic membranes," *J. Biomed. Opt.* **14**(3), 034023 (2009).
- J. M. Flores-Moreno et al., "Holographic otoscope for nanodisplacement measurements of surfaces under dynamic excitation," *Scanning* **33**(5), 342–352 (2011).
- M. Khaleghi et al., "Three-dimensional vibrometry of the human eardrum with stroboscopic lensless digital holography," *J. Biomed Opt.* **20**(5), 051028 (2015).
- C. M. Vest, *Holographic Interferometry*, John Wiley and Sons, Inc., New York (1979).
- R. Pryputniewicz and K. A. Stetson, "Holographic strain analysis: extension of fringe-vector method to include perspective," *Appl. Opt.* **15**(3), 725–728 (1976).
- H. Foroosh, J. B. Zerubia, and M. Berthod, "Extension of phase correlation to subpixel registration," *IEEE Trans. Image Process.* **11**(3), 188–200 (2002).
- J. Guignard, "POCShift," <http://www.mathworks.com/matlabcentral/fileexchange/46978-pocshift-m>, (20 February 2014).
- J. Leval et al., "Full-field vibrometry with digital Fresnel holography," *Appl. Opt.* **44**(27), 5763–5772 (2005).
- E. Harrington et al., "Development of an optoelectronic holographic platform for otolaryngology applications," *Proc. SPIE* **7791**, 77910J (2010).
- J. Guignard et al., "Bone conduction in Thiel-embalmed cadaver heads," *Hear. Res.* **306**, 115–122 (2013).
- J. J. Dirckx and W. F. Decraemer, "Coating techniques in optical interferometric metrology," *Appl. Opt.* **36**(13), 2776–2782 (1997).
- J. J. Rosowski et al., "Computer-assisted time-averaged holograms of the motion of the surface of the mammalian tympanic membrane with sound stimuli of 0.4–25 kHz," *Hear. Res.* **253**(1), 83–96 (2009).
- E. S. Olson, "Observing middle and inner ear mechanics with novel intracochlear pressure sensors," *J. Acoust. Soc. Am.* **103**(6), 3445–3463 (1998).
- S. Puria and J. B. Allen, "Measurements and model of the cat middle ear: evidence of tympanic membrane acoustic delay," *J. Acoust. Soc. Am.* **104**(6), 3463–3481 (1998).
- J. T. Cheng, "Wave motion on the surface of the human tympanic membrane: holographic measurement and modeling analysis," *J. Acoust. Soc. Am.* **133**(2), 918–937 (2013).

Morteza Khaleghi is a PhD candidate in mechanical engineering at Worcester Polytechnic Institute, Worcester, Massachusetts. His research interests include biomedical imaging and developments of optical and nondestructive metrology systems.

Jérémie Guignard received his MSc degree from the Swiss Federal Institute of Technology (EPFL), in 2009 and completed his PhD at the University of Bern, Switzerland, in 2013. He subsequently received a fellowship from the Swiss National Science Foundation (SNSF) to work on eardrum holography at the Massachusetts Eye and Ear Infirmary. His research interests include middle-ear physiology and prosthetics and biomedical image processing.

Cosme Furlong is an associate professor of mechanical engineering, working in mechanics, optical metrology, nanoengineering, science, and technology.

John J. Rosowski is a professor of otology and laryngology, and also of health sciences and technology, working in acoustics and mechanics of the external, middle, and inner ear, with an interest in comparative middle and external ear structure and function.

12. Paper F: Characterization of acoustically-induced forces of the human eardrum

Overview

In this paper, accepted for publication in a proceedings volume of the Society for Experimental Mechanics, acoustically-induced forces of the human TM are characterized to further expand the knowledge on the dynamics of sound-induced energy transfer through the middle ear. Force-sensing techniques are usually contact-based approaches and due to the viscoelastic properties of the TM, any interaction between the probe and the TM may result in modification of its dynamic properties by, potentially, squeezing the membrane, and in turn, inducing localized stresses in the vicinity of the contact area. Furthermore, a biologic tissue like the TM exhibits relaxation and creep behavior, such that the contact force may decrease over time (even to the point of loss of contact between the probe and the TM). In this paper, efforts toward measurements of sound-induced forces of the TM using minimally-invasive sensing methodologies are described. The methodologies consist of integrating MEMS-based force sensors with the developed holographic systems for simultaneous characterizations of kinematics and dynamics of the TM. The MEMS-based force sensor consists of an actuator suspended by four folded springs attached to an outer frame. Compressive or tensile forces applied to the probe in its axial-direction result in a relative motion of the actuator and a set of capacitive electrodes, transducing motion into capacity changes, which are read out by an analog integrated circuit. Sensors have sub-micro-Newton resolution and are capable of measurements along a single axis on a localized area of $50 \times 50 \mu\text{m}^2$ on the TM surface. A computer-controlled 3D nanopositioner, with a resolution of 35 nm and adjustable positioning rate, automatically places and scans the force sensor at several locations on the TM that are critical for the transfer of energy from the outer ear to the inner ear.

12.1. Capacitive force sensing approach

The MEMS-based (MicroElectroMechanical system) capacitive force sensors are suitable for a range of biological studies with forces from picoNewton (10^{-12} N) to milliNewton (10^{-3} N). Commercially-available MEMS-based capacitive sub-micro-Newton force probes FemtoTools FT-S1000 are used to quantify the sound-induced forces of the TM. Capacitance is a measure of the electrical charge between two conductors separated by an air gap. A load applied to the sensor causes a deflection. As the conductors are moved closer to or farther from one another, the air gap changes, and so does the capacitance (Sun and Nelson 2007; Beyeler et al., 2012). An electronic circuit converts the capacitance variations into DC-voltage variations. Figure 12.1 shows the details of the probe used to measure sound-induced forces of the TM.

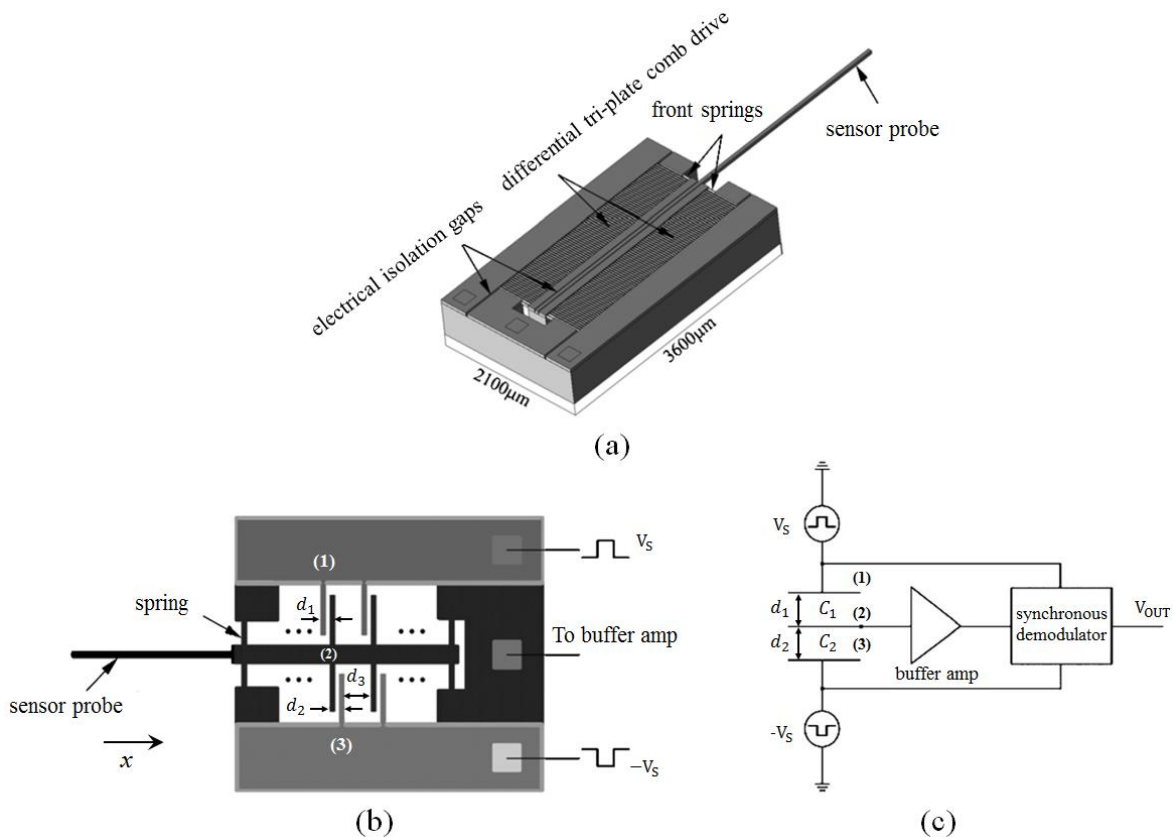


Figure 12.1. MEMS force sensor: (a) a solid model of the sensor; (b) schematic of the internal structure of the sensor; and (c) block diagram of the sensor and its readout circuit (adapted from Sun and Nelson 2007).

As shown in Figure 12.1a, the sensor probe transmits forces axially, which in turn, causes deflection of the unidirectional compliant front springs. As shown in Figure 12.1b, this deflection displaces the inner movable capacitor plates (2), so that with a force applied along the positive x -axis, plates (2) move away from plates (1) and closer to plates (3). An AC signal is applied to the outer capacitors (plates (1) and (3)), and a voltage divider is formed, as shown in Figure 12.1c. The resulting output signal can be obtained by

$$V_{\text{OUT}} = V_S \left(\frac{C_1}{C_1 + C_2} \right) - V_S \left(\frac{C_2}{C_1 + C_2} \right), \quad (12-1)$$

where C_1 and C_2 are the capacitances of the two capacitors and can be calculated with

$$C_1 = \kappa \epsilon_0 \frac{A_1}{d_1}, \quad (12-2)$$

$$C_2 = \kappa \epsilon_0 \frac{A_2}{d_2}, \quad (12-3)$$

where κ is the relative permittivity of the dielectric material between the plates (i.e., equal to one for air), and ϵ_0 is the vacuum permittivity and equal to $\epsilon_0 = 8.8541 \times 10^{-12} \text{ F/m}$.

Considering the nominal plate spacing $d_0 = \frac{d_1 + d_2}{2}$, and the spacing between the plates $d_1 = d_0 + \Delta d$ and $d_2 = d_0 - \Delta d$, the output voltage that is linearly proportional to the displacement can be obtained with

$$V_{\text{OUT}} = V_S \frac{\Delta d}{d_0}, \quad (12-4)$$

By considering the two front springs as one spring constrained on both ends with a point load applied in the middle, the force-deflection relation of this single spring can be obtained with

$$\Delta d = \frac{Fl^3}{4Ew^3t}, \quad (12-5)$$

where F is the applied force, $E=100 \text{ GPa}$ is the Young's modulus of P-type $\langle 100 \rangle$ silicon, l , w , and t are the spring length, width and thickness, respectively (Sun and Nelson 2007).

12.2. Compensation for the stress relaxation of TM

One of the challenging issues in the measurements of sound-induced forces at a point involves viscoelastic stress relaxation phenomena produced by a constant strain load induced by the MEMS probe. As illustrated in Figure 12.2a, there is a gradual stress reduction in time when a constant strain is applied. Thus, during experimental measurements, the preloading force has to be monitored and maintained at a constant level. Therefore, the MEMS-based force sensor shown in Figure 12.1, is mounted on a computer-controlled 3D nanopositioner having a resolution of 35 nm and operating in closed-loop control to maintain a constant DC force level on the order of 250 μN during the time window of acoustic excitations.

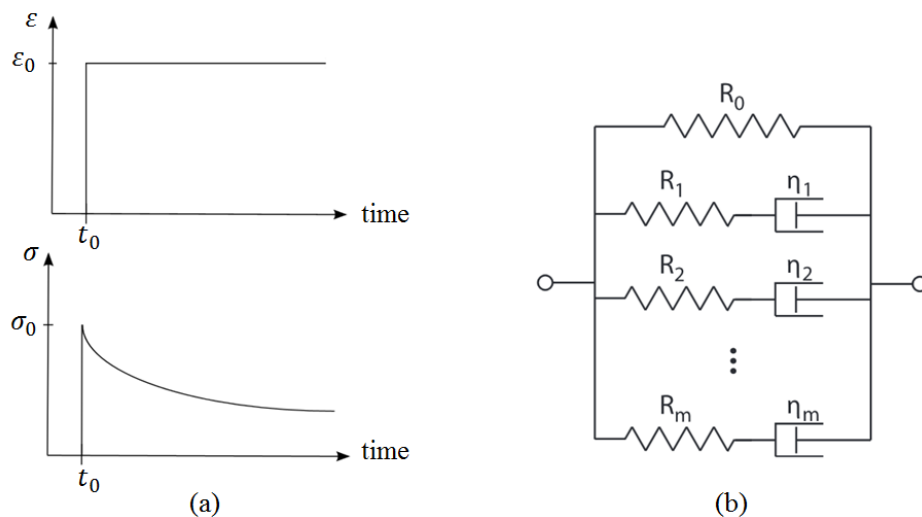


Figure 12.2. Viscoelastic properties of the TM exhibiting stress relaxation: (a) stress relaxation as a function of time under constant strain; and (b) Generalized Maxwell Model (adapted from Zhang et al., 2007).

In order to determine appropriate constant DC force level, analyses similar to those provided by the Generalized Maxwell Model need to be carried out. Such model, shown in Figure 12.2b, can be used to predict viscoelastic properties as well as the time constant needed in the closed loop control of the 3D nanopositioner. Additional models have also been obtained by other researchers (Hoffman and Grigg 2002; Duenwald et al., 2009; Aernouts et al., 2012).

In this Chapter, the frequency-domain transfer function of the sound-induced forces at several points on the surface of the TM are experimentally obtained with frequency sweep of tonal stimuli (harmonic stresses). However, to minimize the acquisition time, the measurements can also be done in transient mode, where the forces are measured by applying either an impulse or a Pseudorandom Gaussian white Noise (PGN) stress input to the specimen, and measuring the resulting strain (Hoffman and Grigg 2002).

Characterization of Acoustically-induced Forces of the Human Eardrum

Morteza Khaleghi¹, Cosme Furlong^{1,2,3}, Jeffrey Tao Cheng^{2,3}, and John J. Rosowski^{2,3}

¹ Center for Holographic Studies and Laser micro-mechaTronics (CHSLT),
Mechanical Engineering Department, Worcester Polytechnic Institute, Worcester, MA 01609

² Eaton-Peabody Laboratory, Massachusetts Eye and Ear Infirmary, Boston, MA 02114

³ Department of Otology and Laryngology, Harvard Medical School, Boston, MA 02114

ABSTRACT

Human eardrum or Tympanic Membrane (TM) is a thin structure located at the boundary between outer and middle ears. Shape, deformations, and thickness of the mammalian TMs have been studied by several groups; however, sound-induced forces of the TM, and the question of “how large the forces produced by acoustic waves are along the manubrium at the input to the middle-ear ossicular system?” have not been fully answered. In this paper, sound-induced forces in the human TM are measured at different tonal frequencies and at several points on its surface. A calibrated force sensor with a resolution of 0.5 μN is used with a 3D nano-positioner, enabling accurate placing of the sensor at points of interests on the TM surface. A closed-loop control system is designed and implemented in order to realize constant preload of the sensor at all the measuring points. Concomitant to the force measurements, time-averaged and three-dimensional stroboscopic holographic interferometry are used to compare the modal shape of the sound-induced motion of the TM before and after the presence of the force sensor. The preliminary results show that the maximum sound-induced forces at the umbo occurs at frequencies between 1.5 to 2.3 kHz, whereas the maximum forces for locations on the surface of the TM occurs at around 5 to 6 kHz.

Keywords: Digital holographic interferometry; Human eardrum; Micro-scale force measurements; Sound-induced motions.

1. Introduction

Mammalian eardrums or Tympanic Membranes (TM) are thin structures (with thickness varying from 20 to 120 μm [1]) located at the boundary between outer and middle ears. Shape, deformations, and thickness of the terrestrial vertebrate TMs have been studied by several groups including our group [2-4]; however, characterization of sound-induced forces in the middle ear have been always challenging and, to the best of our knowledge, there are little or no reports or publications in this field. Some of the challenging issues relating to such force measurements include the dimensions and location of the TM and its viscoelastic properties with relaxation and creep behavior during loading [4]. We have developed a micro-force measuring system to quantify sound-induced forces in the human TM at different tonal frequencies and at several points on its surface. The measuring system uses a MEMS force sensor integrated with a 3D nanopositioner to perform automatic force compensation to account for the TM's relaxation by a closed-loop control. Concomitant to the force measurements, time-averaged and three-dimensional stroboscopic holographic

interferometry [2] are used to compare the modal vibrational patterns of the sound-induced motion of the TM before and after the presence of the force sensor to monitor how the force sensor is changing the kinematics of the TM motions, and more importantly, to relate the sound-induced displacements data to the measured force data in order to develop constitutive equations. One important outcome of this work is a test of the suggestion that prosthetic replacement eardrums can be improved if they maintain the normal curvature and the material properties of a healthy TM.

2. Methods

The experiments include the use of continuous tonal sound stimuli with measurements of the shape and 3D sound-induced motion before and after the use of the force sensor at various locations on the TM surface. The combinations of these force and motion measurements under the different stimulus conditions with measurements of shape and thickness will define: (a) How sound energy is transferred to different locations on the

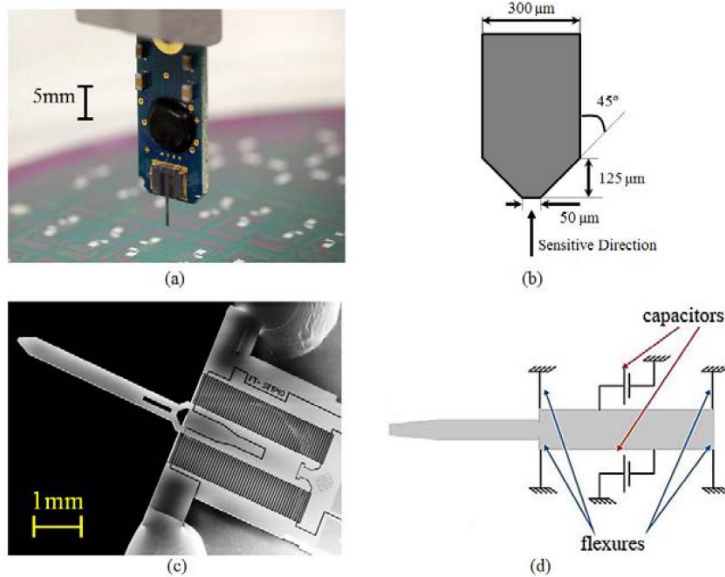


Fig. 1. FEMTOOLS FT-S1000 force sensor used to characterize sound-induced forces in the human TM: (a) an image of the force sensor showing characteristic dimension; (b) the geometry of the tip of the sensor showing its sensitive direction; (c) a microscopic image of the tip of the sensor and its comb structure. The maximum allowable axial deflection of the sensor is 1.5 μm ; and (d) the internal structure of the sensor. Forces are measured based on capacitive changes induced by motion of the tip [7].

TM [5]; (b) What is the timing relation (possible phase lags) of force and motion in the TM surface; (c) Whether the tent-like shape of the TM acts as a lever which concentrates force at the TM rim and ossicular connections while allowing large motions of the region between the TM rim and its center; and (d) How the thickness and stiffness and viscous moduli of the TM vary over its surface.

2.1 Force Measurements

A commercially-available single-axis MEMS-based force sensor (FEMTOOLS FT-S1000 [6]), shown in Fig. 1, with a measuring range of $\pm 1000 \mu\text{N}$ and a resolution of 0.5 μN is used. The sensor is selected based on both its measuring range and dynamic response that has a flat frequency response from DC up to 10 kHz. Both compressive and tensile forces are measured using a differential capacitive readout mechanism that results in

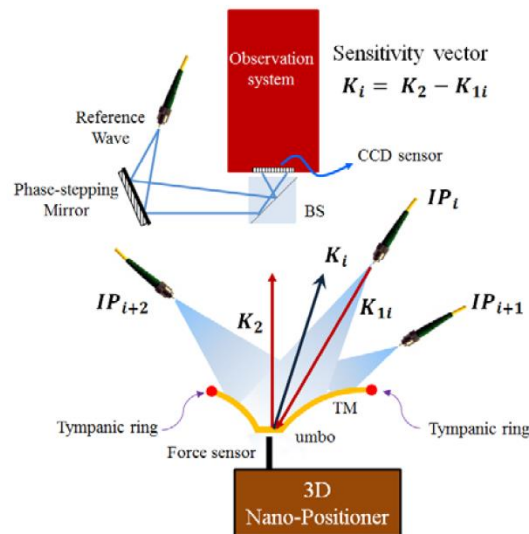


Fig. 2. Schematic of the developed holographic system for shape, sound-induced 3D displacement and forces of the human TM. The force sensor is mounted on a 3D nano-positioner with a resolution of 35 nm. The Holographic system is used to both show the position of the force sensor on the membrane and also to gather shape and 3D displacements data before and after the presence of the force sensor.

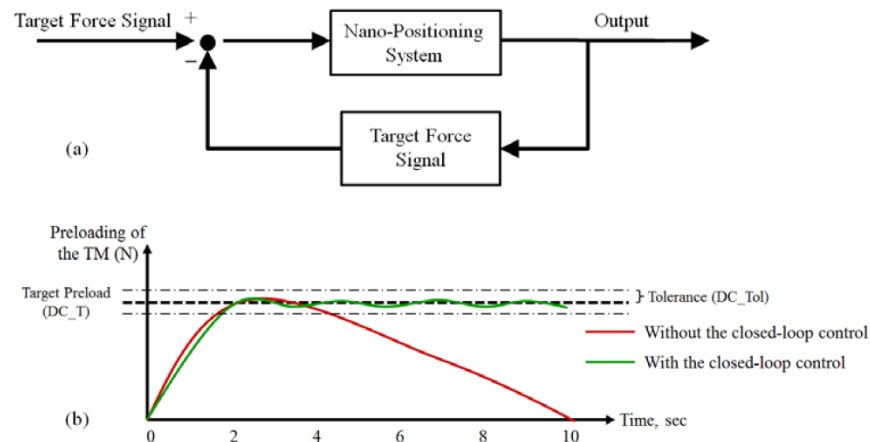


Fig. 3. Closed-loop control scheme to compensate for relaxation of the TM during the measurements: (a) schematic of the closed-loop control; and (b) representative comparisons showing the ability of the developed closed-loop control to maintain constant preloading.

low sensitivity to changes in the environmental conditions. The sensor consists of an actuator suspended by four folded springs attached to an outer frame. A force applied to the probe in its axial-direction results in a relative motion of the actuator and a set of capacitive electrodes to transduce motion into capacity changes, which are read out by an analog integrated circuit [7]. Capacitance is a measure of the electrical charge between two conductors separated by an air gap. A load applied to the sensor causes a deflection and as the conductors are moved closer to or farther from one another, the air gap changes, and so does the capacitance. The change in capacitance is converted into an output voltage by the readout electronics. Due to the single-crystalline silicon structure of the sensor, the results are highly repeatable and the sensors are less likely to degrade over time.

2.2 Development of the Experimental System

Full-field-of-view, 3D, sound-induced displacements of the TM are measured with the method of multiple illumination directions in holographic interferometry, which have been described in detail in [2]. In order to measure the three components of the displacement vector, \mathbf{d} , at least three independent measurements with different sensitivity vectors are required. In our approach, and to minimize experimental errors, optical phase maps are obtained with four sensitivity vectors to form an over determined system of equations that is solved with the least-squares error minimization method with

$$\{\mathbf{d}\} = [[\mathbf{S}]^T [\mathbf{S}]]^{-1} \times \{[\mathbf{S}]^T \{\Omega\}\}, \quad (1)$$

where $[\mathbf{S}]$ is the sensitivity matrix containing all the sensitivity vectors \mathbf{K}_i , and $\{\Omega\}$ is the fringe-locus function vector.

The sensor has a 3 mm long silicone probe that is positioned on the umbo and other points on the medial and lateral surfaces of the TM preparation. This device is mounted on a 3D positioner that can be remotely controlled along three axes with a resolution of 35 nm and integrated with the holographic system, as shown in Fig. 2. Due to the delicate structure of the TM, the approaching and positioning of the force sensor on the TM and the force measurements should be automated in order to avoid any potential damage to the membrane. Furthermore, due to the viscoelastic properties and relaxation of the TM, the preloading of the force sensor has to be such that it remains constant during the measurements while also preventing separation from the TM during acoustic loading. Therefore, a closed-loop control is designed and implemented to realize first, automatic approach, and second, constant preloading throughout entire force measurements cycles. As shown in Fig. 3, the target preloading, DC_T , and its tolerance, DC_{tol} , are specified by the user in a developed LabView-based program. The nanopositioner automatically moves the force sensor to maintain a preloading within $DC_T \pm DC_{tol}$ during force-displacements measurements.

3. Results

3.1 Artificial membrane

Before application of this force measuring system on real biological samples such as human TM, the sound-induced forces of an artificial sample are measured. The sample is a circular latex membrane with a radius of 5 mm and clamped around its perimeter. While the force sensor is approaching to the membrane, the object is monitored with holographic system in Double-Exposure mode, i.e.,

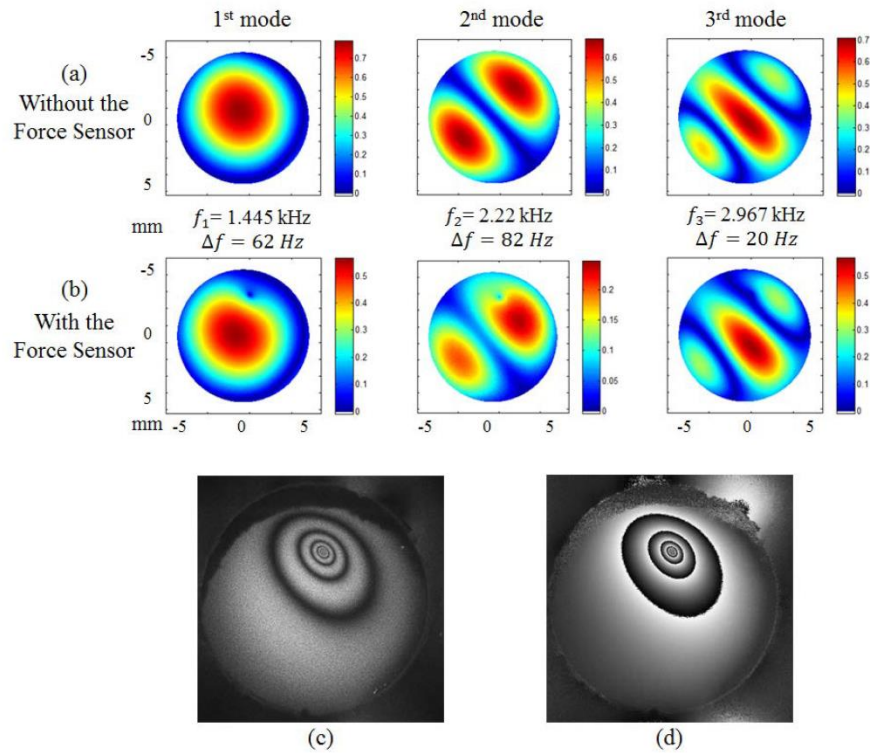


Fig. 4. Sound-induced displacement measurements of a circular latex membrane having a diameter of 10 mm and approximate thickness of 20 μm with and without the presence of the force sensor: (a) and (b) first, second, and third modes of vibration of the membrane before (top) and after (bottom) the presence of the force sensor, respectively. In (b) the location of the sensor is distinguishable. The effects of the force sensor include an increase of the modal frequencies by 1 to 4% and a reduction in the amplitude of displacements by approximately 15% for an applied preload of 250 μN ; (c) and (d) modulation and wrapped optical phase of a reconstructed double exposure hologram corresponding to deformations of the membrane produced by preloading. The applied preload of the membrane is 250 μN producing a displacement of 1.6 μm .

the subtraction of the reconstructed hologram from a reference reconstructed hologram. As shown in Fig. 4, once the tip of the force sensor reaches to the latex membrane, the holographic fringes are produced, indicating the contact of the sensor with the membrane. Then, sound-induced forces and full-field motion of the membrane are measured and the results are compared for both cases of with and without the presence of the force sensor. As shown in Fig. 4b the presence of the force sensor increases the apparent stiffness of the membrane, which causes an increase (1-4%) of its modal frequencies.

3.2 Human Tympanic Membrane

A cadaveric human TM of a male, 53 year-old donor was prepared by removing the bony portion of the ear canal. As shown in Fig. 5, the incus and stapes of the middle ear ossicular chain have been also removed in order to enable positioning of the force sensor on different points on the medial side of the TM. Due to semi-transparency of the mammalian TMs, the sample was coated with a thin layer

of zinc oxide to increase the laser light reflection. The effect of coating on shape and deformation patterns have been studied by several researchers and found to be negligible [8-10]. The temporal bone was held with an adjustable clamp and mounted on a post in front of the holographic system. As was described in Section 2, the force sensor is mounted on the 3D nano-positioner, which is remotely controlled with a computer to place the sensor at different points of interest on the TM.

Prior to stroboscopic measurements, time-averaged response of the TM at different tonal stimuli was monitored [3, 11] and the excitation frequencies were chosen at the maximum motion of the TM. At each stroboscopic phase, sound-induced motions of the TM along three orthogonal axes x , y and z are calculated from the unwrapped optical phases. Then, a numerical rotation matrix is used to calculate the motion components tangent and normal to the local plane of the TM [2, 12]. Definitions of in-plane and out-of-plane motion

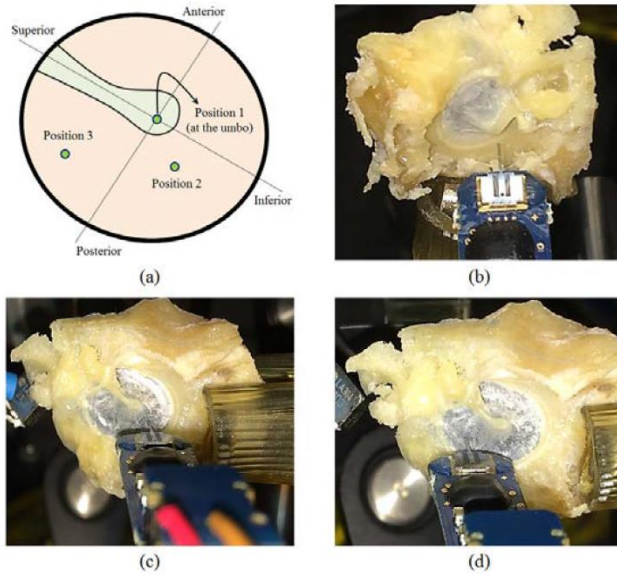


Fig. 5. The force sensor is located at different locations of the TM: (a) schematic of TM showing the locations of all three target points; (b) to (d) shows, respectively, the images corresponding to automatic positioning of the force sensor on position 1 (at the umbo), position 2 (in the inferior-posterior) and position 3 (in the posterior-superior).

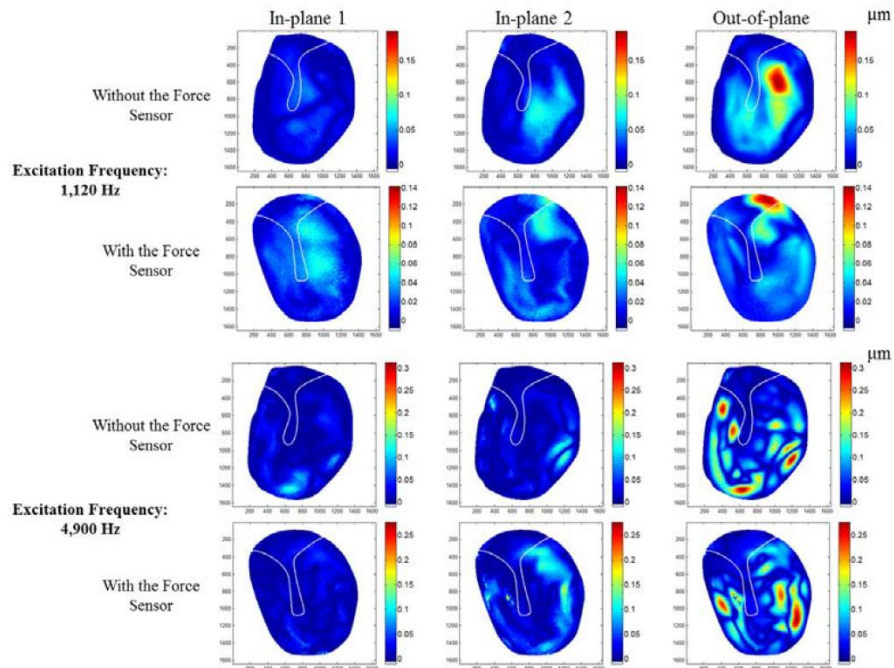


Fig. 6. Sound-induced in-plane and out-of-plane motions of a human TM for two different frequencies before and after the presence of the force sensor as measured with stroboscopic holographic interferometry. In-plane 1 and 2 are displacement components tangent, and out-of-plane, perpendicular to the plane of the TM. The presence of the force sensor at the umbo reduces the amplitude of vibration by less than 10% and changes in the deformation patterns. Magnitudes of displacements are less than 300 nm produced by a sound pressure of 105 dB SPL

components have been described in detail in [2]. In-plane components are the ones tangent to the local plane of the TM, whereas the out-of-plane components are normal to

the local plane of the TM (i.e., along the local normal vector to the shape of the TM). As shown in Fig. 6, the presence of the force sensor reduces the maximum

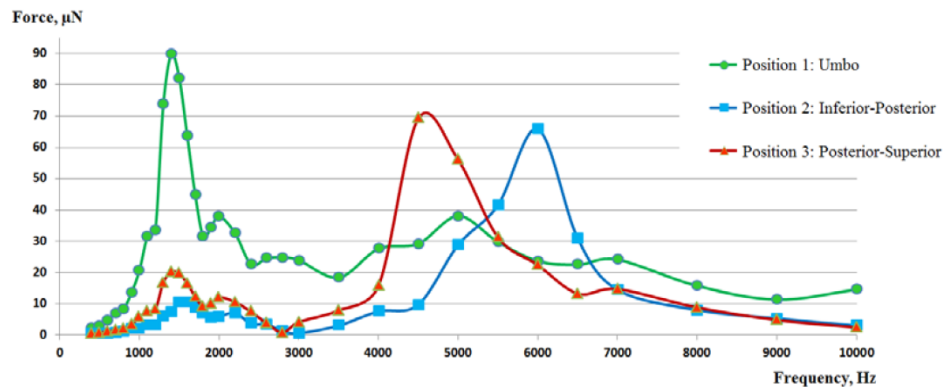


Fig. 7. Normalized sound-induced forces at three different locations on a human TM at different excitation frequencies. The maximum force value for the umbo is at excitation frequency of 1800 Hz, whereas forces at locations on the TM surface have peaks at higher frequencies. Measuring repeatability is within $\pm 3\%$.

amplitude of vibration of the TM by less than 10%. This phenomenon can be explained by the fact that the presence of the force sensor increases the overall stiffness of the system, which in turn, decreases the amplitude of vibration.

Figure 7 shows measured sound-induced forces generated at three different locations on a human TM surface at different tonal frequencies from 300 Hz to 10 kHz. As shown in Fig. 7, the frequency-dependent measured forces are also spatially-dependent. For instance, the sound-induced forces at the umbo (position 1 - shown with circular markers) have a maximum value at around 1.8 kHz, whereas sound-induced forces at points on the surface of the eardrum (position 2 and 3) have their maximum values at higher frequency ranges, i.e., 6.2 and 4.7 kHz for positions 2 and 3, respectively.

Conclusions

We have developed a micro-force measuring system capable of characterizing sound-induced forces in the human TM at different tonal frequencies and at several points on its surface. A close-loop control system is developed to compensate the relaxation and creep behavior of the TM and in order to realize a constant amount of preload in all the measuring points. The force measuring capabilities are combined with digital holographic measurements of shape and true 3D displacements to help expand our knowledge of the hearing processes. The results show that frequency-dependent forces in the middle ear, and in particular the TM, are also spatially dependent. The effects of the force sensor on the dynamic response of the TM will be further investigated as part of our future work. To the best of our knowledge, our force measurements are one of the first attempts to experimentally characterize the sound-induced

forces on the human TM toward understanding their coupling into the ossicular chain.

Acknowledgments

This work was supported by the National Institute on Deafness and other Communication Disorders (NIDCD), Massachusetts Eye and Ear Infirmary (MEEI), and the Mechanical Engineering Department at Worcester Polytechnic Institute. We also acknowledge the support of all of the members of the CHSLT labs at WPI and Eaton-Peabody labs at MEEI.

REFERENCES

- [1] Van der Jeught, S., Dirckx, J. J., Aerts, J. R., Bradu, A., Podoleanu, A. G., and Buytaert, J. A., "Full-field thickness distribution of human tympanic membrane obtained with optical coherence tomography," *JARO*, 14(4):483-494, 2013.
- [2] Khaleghi, M., Furlong, C., Ravicz, M., Cheng, J. T., and Rosowski, J. J., "Three-dimensional vibrometry of the human eardrum with stroboscopic lensless digital holography," *J. Biomed. Opt.*, 20(5):051028-051028, 2015.
- [3] Rosowski, J. J., Dobrev, I., Khaleghi, M., Lu, W., Cheng, J. T., Harrington, E., and Furlong, C., "Measurements of three-dimensional shape and sound-induced motion of the chinchilla tympanic membrane," *Hear. Res.*, 301:44-52, 2013.
- [4] Aernouts, J., Aerts, J. R., & Dirckx, J. J., "Mechanical properties of human tympanic membrane in the quasi-static regime from in situ point indentation measurements," *Hear. Res.*, 290(1), 45-54, 2012.

- [5] Khaleghi, M., Dobrev, I., Harrington, E., Furlong, C., and Rosowski, J. J., "Study of the transient response of Tympanic Membranes under acoustic excitation," In *Mechanics of Biological Systems and Materials*, 4:1-9, 2014.
- [6] FemtoTools Website, <http://www.femtotools.com/products/accessories/ft-s-microforce-sensing-probe>, last accessed on March, 10, 2015.
- [7] Beyeler, F., Muntwyler, S., and Dietze, W., *Sub-Millinewton Capacitive MEMS Force Sensor for Mechanical Testing on a Microscope*, U.S. Patent Application 14/347,421, 2012.
- [8] Dirckx, J. J. J., and Decraemer, W. F., "Coating techniques in optical interferometric metrology," *App. Opt.*, 36(13), 2776-2782, 1997.
- [9] Cheng, J. T., Hamade, M., Merchant, S. N., Rosowski, J. J., Harrington, E., and Furlong, C., "Wave motion on the surface of the human tympanic membrane: holographic measurement and modeling analysis," *JASA*, 133(2), 918-937, 2013.
- [10] Khaleghi, M., Lu, W., Dobrev, I., Cheng, J. T., Furlong, C., and Rosowski, J. J. "Digital holographic measurements of shape and three-dimensional sound-induced displacements of tympanic membrane," *Opt. Eng.*, 52(10), 101916-101916.
- [11] Khaleghi, M., Guignard, J., Furlong, C., and Rosowski, J. J., "Simultaneous Full-field 3D Vibrometry of the Human Eardrum using Spatial-Bandwidth Multiplexed Holography," *J. Biomed. Opt.*, 2015 (in press).
- [12] Alamdari, A., and Krovi, V., "Active Reconfiguration for Performance Enhancement in Articulated Wheeled Vehicles," *Proc. ASME 2014, Dynamic Systems and Control Conference*, V002T27A004-V002T27A004, 2014.

13. Conclusions and Future Work

We have developed laser holographic interferometric systems to quantify shape and sound-induced motions of the mammalian TMs at a new level of detail needed for more accurate investigations of middle ear mechanics. 3D Shape and 4D (space and time) sound-induced motion of TM samples of several species have been characterized using these new holographic systems with spatial resolution of more than one million points on the surface of the TM and a temporal resolution of >100 kHz for tonal stimuli. Sound-induced motion measurements are combined with shape measurements to enable characterization of tangential and normal sound-induced motion components. The motion measurements can be done either in repetitive scheme, where sound-induced motions are quantified by a series of consecutive measurements along different sensitivity vectors; or using an optical multiplexed approach, where the motions are quantified simultaneously in one single frame of the camera. Furthermore, sound-induced forces at the umbo and other well-defined positions on the surface of the human TM have been measured by a closed-loop control force measuring system capable of compensating for the relaxation of the TM.

A general conclusion is that the tangential (in-plane) motion components are 8 to 20 dB smaller than the normal motion components, and hence, the probabilities of the involvement of such in-plane motions in acousto-mechanical energy transformation of the TM are low. Preliminary force measurements data show that frequency-dependent forces in the middle ear, and in particular the TM, are also spatially dependent. For instance, the maximum sound-induced forces at the umbo occur at frequencies between

1.6 to 2.3 kHz, whereas the maximum forces for locations on the surface of the TM occurs at around 4.8 to 6.5 kHz.

These developments will lead to new discoveries in the mysteries of hearing, and encourage and inspire industrial sectors in optics, lasers, and imaging systems to develop new instruments and package such imaging modalities for clinical applications. The following points should be considered as future work and road map to further improve the applicability of this system.

- ***Comprehensive constitutive equations by combining different datasets:*** One of the most important things that should be considered is how to combine these three datasets (shape, 3D sound-induced motion, and force) with currently-existing models in order to come up with comprehensive constitutive equations and mechanical models that fully characterize the mechanics of the middle ear, and in particular the TM. Such a combination should elucidate the factors that influence the coupling of sound from the ear canal to the inner ear, which in turn, should lead to insights on how to improve the surgical outcomes observed after more complex middle ear reconstructions. On the other hand, these measurements are great tools to test, verify, and improve the accuracy and applicability of currently-existing Finite Element Models.
- ***Optical Coherence Tomography:*** In terms of the experimental setup, currently the system can measure shape, 3D sound-induced motions, and forces of the TM; however the system can be modified to have another great capability (i.e., full-field thickness measuring measurements). For doing so, optical coherence tomography capability can be achieved by coupling a low-coherence light source

to the fibers and mounting the reference mirror on a micro-positioner, enabling scanning of the reference beam. The system should be miniaturized and packaged to enhance the maneuverability and become portable in order to enable its application in the clinics.

- ***Full-field 3D Force measurements:*** In terms of the measurements, the force measurements should be expanded significantly, so that instead of having the measurements at a few points, a 2D grid of points on the surface of the TM should be specified and the force sensor should scan all those points in order to provide the full-field sound-induced force of the TM. Furthermore, currently the system can measure only 1D sound-induced forces (i.e., along the single sensitivity axis of the force sensor), however, the same force sensor can be positioned differently (at least along three different orientations) in order to provide the capabilities of 3D force measurements, which in turn, will enable a more comprehensive understanding of the stress-strain state of the TM.

References

- Abramson, N., "Light-in-flight recording: high-speed holographic motion pictures of ultrafast phenomena," *App. Opt.*, 22(2), 215-232, 1983.
- Aernouts, J., and Dirckx, J.J., "Elastic characterization of the gerbil pars flaccida from in situ inflation experiments," *Biomech. Model Mechanobiol.*, 10(5), 727-741, 2011.
- Aernouts, J., Aerts, J.R., and Dirckx, J.J., "Mechanical properties of human tympanic membrane in the quasi-static regime from in situ point indentation measurements," *Hear. Res.*, 290(1), 45-54, 2012.
- Aibara, R., Welsh, J.T., Puria, S., and Goode, R.L., "Human middle-ear sound transfer function and cochlear input impedance," *Hear. Res.*, 152(1), 100-109, 2001.
- Atherton T.J., and Kerbyson, D.J., "Size invariant circle detection," *Imag. Vis. Comp.*, 17(11), 795-803, 1999.
- Beyeler, F, Muntwyler, S., and Dietze, W., "Sub-Millinewton Capacitive Mems Force Sensor for Mechanical Testing on a Microscope," U.S. Patent Application 14/347,421, 2012.
- Chen, F., Brown, G.M., and Song, M., "Overview of three-dimensional shape measurement using optical methods," *Opt. Eng.*, 39(1), 10-22, 2000.
- Cheng, T., Dai, C., Gan, R.Z., "Viscoelastic Properties of Human Tympanic Membrane," *Ann. Biomed. Eng.*, 35(2), 304-314, 2007.
- Cheng J.T., Aarnisalo, A.A., Harrington, E.J., Hernández-Montes, M.dS., Furlong, C., Merchant, S.N., and Rosowski, J.J., "Motion of the surface of the human tympanic membrane measured with stroboscopic holography," *Hear. Res.*, 263, 66-77, 2010.
- Cheng, J.T., Hamade, M., Merchant, S.N., Rosowski, J.J., Harrington, E., and Furlong, C., "Wave motion on the surface of the human tympanic membrane: holographic measurement and modeling analysis," *JASA*, 133(2), 918-937, 2013.
- Chittka, L., Brockmann, A., "Perception Space-The Final Frontier," *PLoS Biol*, 3(4), e137, 2005.
- Collier R.J., Burckhardt, C.B., and Lin, L.H., *Optical Holography*, Academic Press, New York, 1971.

- Cuche E., Marquet, P, and Depeursinge, C., "Spatial filtering for zero-order and twin-image elimination in digital off-axis holography," *App. Opt.*, 39(23), 4070-4075, 2000.
- Cui, Y., Schuon, S., Chan, D., Thrun, S., and Theobalt, C., "3D shape scanning with a time-of-flight camera," *Proc. IEEE 2010, Computer Vision and Pattern Recognition (CVPR)*, 1173-1180, 2010.
- De Greef, D., Aernouts, J., Aerts, J., Cheng, J.T., Horwitz, R., Rosowski, J.J., and Dirckx, J.J.J., "Viscoelastic properties of the human tympanic membrane studied with stroboscopic holography and finite element modeling," *Hear. Res.*, 312, 69-80, 2014.
- De Nicola, S., Geltrude, A., Locatelli, M., Al-Naimee, K., Meucci, R., and Arecchi, F.T., "Infrared Holography for Wavefront Reconstruction and Interferometric Metrology," *Advanced Holography - Metrology and Imaging*, 57, 180, 2011.
- De La Rochefoucauld, O., and Olson, E.S., "A sum of simple and complex motions on the eardrum and manubrium in gerbil," *Hear. Res.*, 263(1), 9-15, 2010.
- Decraemer, W.F., Dirckx, J.J., and Funnell, W.R.J., "Shape and derived geometrical parameters of the adult, human tympanic membrane measured with a phase-shift moiré interferometer," *Hear. Res.*, 51(1), 107-121, 1991.
- Decraemer, W.F., Khanna, S.M., and Funnell, W.R.J., "A method for determining three-dimensional vibration in the ear," *Hear. Res.*, 77(1), 19-37, 1994.
- Decraemer W.F., and Funnell, W.R.J., "Anatomical and mechanical properties of the tympanic membrane," *B. Ars (Eds.), Chronic Otitis Media. Pathogenesis-Oriented Therapeutic Management*, 51-84, 2008.
- Decraemer, W.F., Rochefoucauld, O.L., Funnell, W.R.J, and Olson, E.S., "Three-Dimensional Vibration of the Malleus and Incus in the Living Gerbil," *JARO*, 15, 483-510, 2014.
- Dirckx, J.J., and Decraemer, W.F., "Optoelectronic moiré projector for real-time shape and deformation studies of the tympanic membrane," *J. Biomed. Opt.*, 2(2), 176-185, 1997.
- Dirckx, J.J.J., and Decraemer W.F., "Coating techniques in optical interferometric metrology," *App. Opt.*, 36(13), 2776-2782, 1997.
- Dobrev, I., Harrington, E.J., Cheng, T., Furlong, C., and Rosowski, J.J., "Digital holographic otoscope for measurements of the human tympanic membrane *in-vivo*," *Proc. SEM 2013, Imaging Methods for Novel Materials and Challenging Applications*, 3, 39-45, 2013.

- Dobrev, I., Furlong, C., Cheng, J.T., and Rosowski, J.J., "Optimization of a Lensless Digital Holographic Oscope System for Transient Measurements of the Human Tympanic Membrane," *Exp. Mech.*, 1-12, 2014.
- Dobrev, I., Furlong, C., Cheng, J.T., and Rosowski, J.J., "Full-field transient vibrometry of the human tympanic membrane by local phase correlation and high-speed holography," *J. Biomed. Opt.*, 19(9), 096001-096001, 2014.
- Dobrev, I. T., "Full-field vibrometry by high-speed digital holography for middle-ear mechanics," PhD Dissertation, Worcester Polytechnic Institute, Worcester, MA, USA, 2014.
- Duenwald, S.E., Vanderby, R., and Lakes, R.S., "Viscoelastic relaxation and recovery of tendon," *Annals of biomedical engineering*, 37(6), 1131-1140, 2009.
- Earl G., Basford, P.J, Bischoff, A.S., Bowman, A, Crowther, C., Dahl, J., Hodgson, M. et al., "Reflectance transformation imaging systems for ancient documentary artefacts," *EVA 2011*, Electronic Visualization and the Arts BCS, 2011.
- Egolf, D. P., Kennedy, W.A., and Larson, V.D., "Occluded-ear simulator with variable acoustic properties," *JASA*, 91(5), 2813-2823, 1992.
- Emanuel, D.C., and Letowski, T., *Hearing science*, Wolters Kluwer Health/Lippincott Williams and Wilkins, 2009.
- Esser, M.H., "The mechanism of the middle ear: I. The two piston problem," *Bulletin Math. Biophysics*, 9(1), 29-40, 1947.
- Fay J.P., Puria, S., and Steele, C.R., "The discordant eardrum," *PNAS*, 103(52), 19743-19748, 2006.
- Feng, B., Gan, R.Z., "Lumped parametric model of the human ear for sound transmission," *Biomech. and Model. Mechanobio.*, 3(1), 33-47, 2004.
- Ferrazzini, M., "Virtual middle ear: a dynamic mathematical model based on [the] finite element method," Doctoral Dissertation, Technische Wissenschaften ETH Zürich, Nr. 15294, 2003.
- Flores Moreno J.M., Furlong, C., Rosowski, J.J., Harrington, E., Cheng, J.T., Scarpino, C., and Mendoza Santoyo, F., "Holographic otoscope for nanodisplacement measurements of surfaces under dynamic excitation," *Scanning*, 33(5), 342-352, 2011.
- Foroosh H., Zerubia, J.B., Berthod, M., "Extension of phase correlation to subpixel registration," *IEEE Trans. Imag. Proc.*, 1(3), 188-200, 2002.

- Foth, H. J., Huthoff, C., Brenner, M., Färber, S., Stasche, N., Baker-Schreyer, A., and Hörmann, K., "Measuring the motions in the human middle ear by Laser Doppler Vibrometry," *Opt. Las Eng.*, 25(4), 289-301, 1996.
- Furlong, C., "Hybrid, experimental and computational, approach for the efficient study and optimization of mechanical and electro-mechanical components," PhD Dissertation, Worcester Polytechnic Institute, Worcester, MA, 1999.
- Furlong C., and R.J. Pryputniewicz, "Absolute shape measurements using high-resolution optoelectronic holography methods," *Opt. Eng.*, 39(1), 216-223, 2000.
- Furlong, C., Kolenovic, E., and Ferguson, C. F., "Quantitative optical metrology with CMOS cameras," *Proc. SPIE 2004*, 49th Annual Meeting In Optical Science and Technology, 1-15, 2004.
- Furlong, C., Rosowski, J.J., Hulli, N., and Ravicz, M.E., "Preliminary analyses of tympanic membrane motion from holographic measurements," *Strain*, 45(3), 301-309, 2009.
- Furlong, C., Dobrev, I., Harrington, E., Hefti, P., and Khaleghi, M., "Miniaturization as a key factor to the development and application of advanced metrology systems," *Proc. SPECKLE 2012*, V International Conference on Speckle Metrology, 84130T-84130T, 2012.
- Furlong, C., Dobrev, I., Tao Cheng, J., Khaleghi, M., and Rosowski, J.J., "High-speed Digital Holography in Middle-ear Mechanics: From Laboratory to Clinical Use," *Digital Holography and Three-Dimensional Imaging*, Optical Society of America, DW3B-1, 2014.
- Funnell, W.R.J., and Laszlo, C.A., "Modeling of the cat eardrum as a thin shell using the finite-element method," *JASA*, 63(5), 1461-1467, 1978.
- Funnell, W.R. and C.A. Laszlo, "A critical review of experimental observations on eardrum structure and function," *ORL J. Otorhinolaryngol. Relat. Spec.*, 44(4), 181-205, 1982.
- Gan, R.Z., Feng, B., and Sun, Q., "Three-dimensional finite element modeling of human ear for sound transmission," *Annals Biomed. Eng.*, 32(6), 847-859, 2004.
- Gan R.Z., Cheng, J.T., Dai, C., and Yang, F., "Finite element modeling of sound transmission with perforations of tympanic membrane," *JASA*, 126(1), 243-253, 2009.

- Geisler C.D., *From sound to synapse: physiology of the mammalian ear*, Oxford University Press, 1998.
- Gelfand, S.A., *Hearing, an Introduction to Psychological and Physiological Acoustics*, New York, M. Dekker, 85-102, 1981.
- Goll, E., and Dalhoff, E., “Modeling the eardrum as a string with distributed force,” *JASA*, 130(3), 1452-1462, 2011.
- Golub G.H., and Van Loan, C.F., *Matrix computations*, JHU Press, 2012.
- Goodman J., *Introduction to Fourier optics*, 2nd Ed., McGraw-Hill Series in Electrical and Computer Engineering, 2008.
- Gori F., “Fresnel transform and sampling theorem,” *Opt. Comm.*, 39(5), 293-297, 1981.
- Guignard J., Stieger, C., Kompis, M., Caversaccio, M., and Arnold, A., “Bone conduction in Thiel-embalmed cadaver heads,” *Hear. Res.*, 306, 115-122, 2013.
- Harrington E., Dobrev, I., Bapat, N., Mauricio Flores, J., Furlong, C., Rosowski, J.J., Cheng, J.T., Scarpino, C., and Ravicz, M., “Development of an optoelectronic holographic platform for otolaryngology applications,” *SPIE Optical Engineering+ Applications*, 77910J-77910, 2010.
- Harrington E., Furlong, C., Rosowski, J.J., and Cheng, J.T., “Automatic acquisition and processing of large sets of holographic measurements in medical research,” *Proc. SEM 2011*, Optical Measurements, Modeling, and Metrology, 5, 219-228, 2011.
- Hecht, E., *Optics*, 4th edition, Addison Wesley Longman Inc, 1998.
- Helmholtz, H., “The mechanism of the ossicles of the ear and the tympanic membrane,” *Pflugers. Arch. Physiol.*, 1, 1-60, 1868.
- Helmholtz, H., “Originally Published in Pfluger Archiv fur Physiologie,” *The Mechanism of the Ossicles of the Ear and Membrana Tympani*, vol. 1. Bonn, Germany. Translated by Albert H. Buck and Normand Smith (1873), 1868.
- Hernández-Montes M., Furlong, C., Rosowski, J.J., Hulli, N., Cheng, J.T., Mendoza Santoyo, F., Ravicz, M.E., and Harrington, E., “Optoelectronic holographic otoscope for measurement of nano-displacements in tympanic membranes,” *J. of Biomed. Opt.*, 14(3), 034023-03402, 2009.
- Hernández-Montes M.S., Mendoza Santoyo, F., Pérez López, C., Muñoz Solís, S., and Esquivel, J., “Digital holographic interferometry applied to the study of tympanic membrane displacements,” *Opt. Las. Eng.*, 49(6), 698-702, 2011.

- Herráez, M.A., Burton, D.R., Lalor, M.J., and Gdeisat, M.A., “Fast two-dimensional phase-unwrapping algorithm based on sorting by reliability following a noncontinuous path,” *App. Opt.*, 41(35), 7437-7444, 2002.
- Hoffman, A. H., and Grigg, P., “Using uniaxial pseudorandom stress stimuli to develop soft tissue constitutive equations,” *Annals of biomedical engineering*, 30(1), 44-53, 2002.
- Hung, Y.Y., Turner, J.L., Tafraian, M., Hovanesian, J.D., and Taylor, C.E., “Optical method for measuring contour slopes of an object,” *App. Opt.*, 17(1), 128-131, 1978.
- Joenathan, C., Pfister, B., and Tiziani, H.J., “Contouring by electronic speckle pattern interferometry employing dual beam illumination,” *App. Opt.*, 29(13), 1905-1911, 1990.
- Kawabata, I., Ishii, H., “Fiber arrangement in the Tympanic Membrane,” *Acta Otolaryng*, 72, 243-254, 1971.
- Khanna, S.M., and Tonndorf, J., “Tympanic Membrane Vibrations in Cats Studied by Time-Averaged Holography,” *JASA*, 51(6B), 1904-1920, 1972.
- Khaleghi M., Lu, W., Dobrev, I., Cheng, J.T., Furlong, C., and Rosowski, J.J., “Digital holographic measurements of shape and three-dimensional sound-induced displacements of tympanic membrane,” *Opt. Eng.*, 52(10): 101916-101916, 2013.
- Khaleghi, M., Furlong, C., Cheng, J.T., and Rosowski, J.J., “Shape and 3D acoustically induced vibrations of the human eardrum characterized by digital holography,” *Proc. SPIE 2014*, Optical Engineering+ Applications, 920404-920404, 2014.
- Khaleghi, M., Dobrev, I., Harrington, E., Furlong, C., and Rosowski, J.J., “Study of the transient response of Tympanic Membranes under acoustic excitation,” *Proc. SEM 2013*, In Mechanics of Biological Systems and Materials, 4, 1-9, 2014.
- Khaleghi, M., Furlong, C., Cheng, J.T., and Rosowski, J.J., “3-Dimensional quantification of surface shape and acoustically-induced vibrations of TM by digital holography,” *Proc. Fringe 2013*, 599-602, 2014.
- Khaleghi, M., Furlong, C., Guignard, J., Dobrev, I., Cheng, J.T., and Rosowski, J.J., “Multiplexed Holography for Single-Shot Three-Dimensional Shape and Displacement Measurements,” *Proc. SEM 2014*, In Advancement of Optical Methods in Experimental Mechanics, 3, 103-108, 2015.

- Khaleghi, M., Furlong, C., Cheng, J.T., and Rosowski, J.J., "Thin-Shell Behavior of Mammalian Tympanic Membrane Studied by Digital Holography," *Proc. SEM 2014*, In Mechanics of Biological Systems and Materials, 7, 19-25, 2015.
- Khaleghi, M., Furlong, C., Ravicz, M., Cheng, J.T., and Rosowski, J.J., "Three-dimensional vibrometry of the human eardrum with stroboscopic lensless digital holography," *J. Biomed. Opt.*, 20(5), 051028-051028, 2015.
- Khaleghi, M., Guignard, J., Furlong, C., and Rosowski, J.J., "Simultaneous full-field three-dimensional vibrometry of the human eardrum using spatial-bandwidth multiplexed holography," *J. Biomed. Opt.*, 2015.
- Khaleghi, M., Furlong, C., Cheng, J.T., and Rosowski, J.J., "Characterization of Acoustically-induced Forces of the Human Eardrum," *Proc. SEM 2015*, 2016.
- Khaleghi, M., Furlong, C., Cheng, J.T., and Rosowski, J.J., "Extended field-of-view imaging achieved by multiplexed digital holography," *Proc. SEM 2015*, 2016.
- Khaleghi, M., Guignard, J., Furlong, C., and Rosowski, J.J., "Full-field Three-Dimensional Characterization of Non-repetitive Motions by Single-shot Multiplexed Digital Holography," *Proc. SEM 2015*, 2016.
- Khanna S.M., and Tonndorf, J., "Tympanic Membrane Vibrations in Cats Studied by Time-Averaged Holography," *JASA*, 51(6B), 1904-1920, 1972.
- Khanna S.M., and Tonndorf, J., "Tympanic membrane shape determined by moiré topography," *JASA*, 57(72), 1975.
- Karasev, P.A., Campbell, D.P., and Richards, M.A., "Obtaining a 35x speedup in 2d phase unwrapping using commodity graphics processors," *IEEE Radar Conference*, 574-578, 2007.
- Kolenovic, E., Furlong, C., and Jüptner, W., "Inspection of micro-optical components by novel digital holographic techniques," *Proc. SEM*, 470-475, 2004.
- Kreis T.M., Adams, M., Jüptner, W.P.O., "Methods of digital holography: a comparison," *Proc. SPIE 3098*, Optical Inspection and Micromasurements II, 224, 1997.
- Kreis T., *Handbook of Holographic Interferometry*, Wiley-VCH Verlag GmbH & Co. KGaA, 2005.
- Lee, C.F., Chen, P.R., Lee, W.J., Chen, J.H., and Liu, T.C., "Three-Dimensional Reconstruction and Modeling of Middle Ear Biomechanics by High-Resolution

- Computed Tomography and Finite Element Analysis,” *The Laryngoscope*, 116 (5), 711-716, 2006.
- Leval J., Picart, P., Boileau, J.P., and Pascal, J.C., “Full-field vibrometry with digital Fresnel holography,” *App. Opt.*, 44(27), 5763-5772, 2005.
- Leith E.N., and Upatnieks, J., “Reconstructed wavefronts and communication theory,” *JOSA*, 52(10), 1123-1128, 1962.
- Li, Y., “Digital holography and optical contouring,” PhD Dissertation, Liverpool John Moores University, 2009.
- Lim, D. J., “Human tympanic membrane: an ultrastructural observation,” *Acta Otolaryngol*, 70(3), 176-186, 1970.
- Løkberg O.J., Hagmoen, K., and Gundersen, T., “Vibration measurement of the human tympanic membrane in vivo,” *Acta oto-laryngologica*, 89(1-2), 37-42, 1980.
- Maftoon, N., Funnell, W.R.J., Daniel, S.J., and Decraemer, W.F., “Experimental study of vibrations of gerbil tympanic membrane with closed middle ear cavity,” *JARO*, 14(4), 467-481, 2013.
- Makynen, A. J., Kostamovaara, J.T., and Myllyla, R.A., “Tracking laser radar for 3-D shape measurements of large industrial objects based on time-of-flight laser rangefinding and position-sensitive detection techniques,” *IEEE Trans. Instrument. Meas.*, 43(1), 40-49, 1994.
- Møller, A.R., “An experimental study of the acoustic impedance of the middle ear and its transmission properties,” *Acta oto-laryngologica*, 60(1-6), 129-149, 1965.
- Møller, A.R. *Function of the middle ear, Auditory System*, Springer Berlin Heidelberg, 491-517, 1974.
- Mendoza Santoyo F., Shellabear, M.C., and Tyrer, J.R., “Whole field in-plane vibration analysis using pulsed phase-stepped ESPI,” *App. Opt.*, 30(7), 717-721, 1991.
- Merchant, S.N., Ravicz, M.E., Rosowski, J.J., “Acoustic input impedance of the stapes and cochlea in human temporal bones,” *Hear. Res.*, 97(1), 30-45, 1996.
- Nilsson, B., and Carlsson, T. E., “Direct three-dimensional shape measurement by digital light-in-flight holography,” *App. Opt.*, 37(34), 7954-7959, 1998.
- Nilsson, B., and Carlsson, T.E., “Simultaneous measurement of shape and deformation using digital light-in-flight recording by holography,” *Opt. Eng.*, 39(1), 244-253, 2000.

- Ogura, Y., Masuda, Y., Miki, M., Takeda, T., Watanabe, S., Ogawara, T., et al., "Vibration analysis of the human skull and auditory ossicles by holographic interferometry," *Holography in Medicine and Biology*, 218-222, 1979.
- Ogura, Y., Masuda, Y., Takeda, T., Kawakami, S. I., Ishihara, M., Tsujiuchi, J., "Three-dimensional holographic display of images of otological specimens," *Auris Nasus Larynx*, 10(2), 71-77, 1983.
- Olson E.S., "Observing middle and inner ear mechanics with novel intracochlear pressure sensors," *JASA*, 103(6), 3445-3463, 1998.
- Onchi, Y., "Mechanism of the middle ear," *JASA*, 33(6), 794-805, 1961.
- Osten W., Some considerations on the statistical error analysis in holographic interferometry with application to an optimized interferometer," *J. Mod. Opt.*, 32, 827-838, 1985.
- Pavillon N., C.S. Seelamantula, J. Kühn, M. Unser, and C. Depeursinge, "Suppression of the zero-order term in off-axis digital holography through nonlinear filtering," *App. Opt.*, 48(34), H186-H195, 2009.
- Peake, W. T., Rosowski, J.J., and Lynch, T.J., "Middle-ear transmission: acoustic versus ossicular coupling in cat and human," *Hear. Res.*, 57(2), 245-268, 1992.
- Pedrini, G., Fröning, P., Tiziani, H.J., and Santoyo, F.M., "Shape measurement of microscopic structures using digital holograms," *Opt. Comm.*, 164(4), 257-268, 1999.
- Pedrini G., Osten, W., and Gusev, M.E., "High-speed digital holographic interferometry for vibration measurement," *App. Opt.*, 45(15), 3456-3462, 2006.
- Pham, H., Ding, H., Sobh, N., Do, M., Patel, S., and Popescu, G., "Off-axis quantitative phase imaging processing using CUDA: toward real-time applications," *Biomed. Opt. Exp.*, 2(7), 1781-1793, 2011.
- Picart P., Moisson, E., and Mounier, D., "Twin-sensitivity measurement by spatial multiplexing of digitally recorded holograms," *App. Opt.*, 42(11), 1947-1957, 2003.
- Picart P., Tankam, P., Mounier, D., Peng, Z., and Li, J., "Spatial bandwidth extended reconstruction for digital color Fresnel holograms," *Opt. Exp.*, 17(11), 9145-9156, 2009.
- Polhemus, C. "Two-wavelength interferometry." *App. Opt.*, 12(9), 2071-2074, 1973.

- Pryputniewicz, R., and Stetson K.A., "Holographic strain analysis: extension of fringe-vector method to include perspective," *App. Opt.*, 15(3), 725-728, 1976.
- Pryputniewicz R.J., "Time average holography in vibration analysis," *Opt. Eng.*, 24(5), 245843-245843, 1985.
- Pryputniewicz, R. J., "Quantitative determination of displacements and strains from holograms," *Holographic Interferometry*, 33-74, 1994.
- Pryputniewicz, R. J., Furlong, C., and Pryputniewicz, E. J., "Optimization of contact dynamics for an RF MEMS switch," *Proc. ASME 2002*, International Mechanical Engineering Congress and Exposition, 233-239, 2002.
- Puria S., Allen, J.B., "Measurements and model of the cat middle ear: Evidence of tympanic membrane acoustic delay," *JASA*, 104(6), 3463-3481, 1998.
- Puria, S., "Measurements of human middle ear forward and reverse acoustics: implications for otoacoustic emissions," *JASA*, 113(5), 2773-2789, 2003.
- Puria, S., and Steele, C.R., *Mechano-acoustical transformations*, Handbook of the senses, Chapter 7, A comprehensive reference 3, 165-202, 2008.
- Puria S., and Steele, C., "Tympanic-membrane and malleus-incus-complex co-adaptations for high-frequency hearing in mammals," *Hear. Res.*, 263(1), 183-190, 2010.
- Rawitscher, G., and Liss, J., "The vibrating inhomogeneous string," *Am. J. Phys.*, 79(4), 417-427, 2011.
- Rochefoucauld O., and Olson, E.S., "A sum of simple and complex motions on the eardrum and manubrium in gerbil," *Hear. Res.*, 263(1), 9-15, 2010.
- Rossing, T.D., *Springer handbook of acoustics*, Springer Science and Business Media, 2007.
- Rosowski, J.J., "The effects of external and middle-ear filtering on auditory threshold and noise-induced hearing loss," *JASA*, 90(1), 124-135, 1991.
- Rosowski, J.J., *Outer and middle ear*, in *Comparative Hearing in Mammals*, edited by A. N. Popper and R. R. Fay, Springer-Verlag, New York, 173-247, 1994.
- Rosowski, J. J., Mehta, R. P., and Merchant, S. N., "Diagnostic utility of laser-Doppler vibrometry in conductive hearing loss with normal tympanic membrane," *Otol. Neurotol.*, 24(2), 165, 2003.

- Rosowski, J. J., Mehta, R.P., and Merchant, S.N., “Diagnostic utility of laser-Doppler vibrometry in conductive hearing loss with normal tympanic membrane,” *Otol. Neurotol.*, 24(2), 165, 2003.
- Rosowski J.J., Cheng, J.T., Ravicz, M.E., Hulli, N., Harrington, E.J., Hernández-Montes, M. dS., and Furlong, C., “Computer-assisted time-averaged holography of the motion of the surface of the tympanic membrane with sound stimuli of 0.4 to 25 kHz,” *Hear. Res.*, 253(1-2), 83-96, 2009.
- Rosowski J.J., Dobrev, I., Khaleghi, M., Lu, W., Cheng, J.T., Harrington, E., and Furlong, C., “Measurements of three-dimensional shape and sound-induced motion of the chinchilla tympanic membrane,” *Hear. Res.*, 301, 44-52, 2013.
- Santoyo F.M., Pedrini, G., Schedin, S., and Tiziani, H.J., “3D displacement measurements of vibrating objects with multi-pulse digital holography,” *Meas. Sci. Tech.*, 10(12), 1305, 1999.
- Schedin S., G. Pedrini, H.J. Tiziani, and F. Mendoza Santoyo, “Simultaneous three-dimensional dynamic deformation measurements with pulsed digital holography,” *App. Opt.*, 38(34), 7056-7062, 1999.
- Schnars, U., and Jüptner, W.P., “Digital recording and numerical reconstruction of holograms,” *Meas. Sci. Tech.*, 13(9), R85, 2002.
- Schnars U., and Jüptner, W., *Digital holography*, Springer Berlin Heidelberg, 2005.
- Schnars U., Falldorf, C., Watson, J., and Jüptner, W., *Digital Holography and Wavefront Sensing*, Springer Berlin Heidelberg, 2015.
- Seebacher, S., Osten, W., and Jueptner, W.P., “Measuring shape and deformation of small objects using digital holography,” *Proc. SPIE 1998*, Optical Science, Engineering, and Instrumentation, 104-115, 1998.
- Shera, C.A., and Zweig, G., “An empirical bound on the compressibility of the cochlea,” *JASA*, 92(3), 1382-1388, 1992.
- Shaw, E.A.G., and Stinson, M.R., “The human external and middle ear: Models and concepts,” *Mech. Hear.*, 3-10, Springer Netherlands, 1983.
- Smith, H.M., *Holographic recording materials*, Berlin, Heidelberg, Springer, 1977.
- Solís S.M., Santoyo, F.M., Hernández-Montes, M., “3D displacement measurements of the tympanic membrane with digital holographic interferometry,” *Opt. Exp.*, 20(5), 5613-5621, 2012.

- Solís, S.M., Hernández-Montes, M.D.S., and Santoyo, F.M., Tympanic membrane contour measurement with two source positions in digital holographic interferometry,” *Biomed. Opt. Exp.*, 3(12), 3203-3210.
- Sun, Q., Gan, R.Z., Chang, K.H., and Dormer, K.J., “Computer-integrated finite element modeling of human middle ear,” *Biomech. Model. Mechanobiol.*, 1(2), 109-122, 2002.
- Sun, Y., and Nelson, B.J., “MEMS capacitive force sensors for cellular and flight biomechanics,” *Biomedical Materials*, 2(1), S16, 2007.
- Stern A., and Javidi, B., “Improved-resolution digital holography using the generalized sampling theorem for locally band-limited fields,” *JOSA A*, 23(5), 1227-1235, 2006.
- Takeda M., Ina, H., Kobayashi, S., “Fourier-transform method of fringe-pattern analysis for computer-based topography and interferometry,” *JOSA*, 72, 156-160, 1982.
- Takeda M., and Kitoh, M., “Spatiotemporal frequency multiplex heterodyne interferometry,” *JOSA A*, 9(9), 1607-1614, 1992.
- Takita K., Y. Sasaki, T. Higuchi, and K. Kobayashi, “High-accuracy subpixel image registration based on phase-only correlation,” *IEICE Trans. Fund. Elect. Comm. Comp. Sci.*, 86(8), 1925-1934, 2003.
- Tankam P., Song, Q., Karray, M., Li, J.C., Dese, J.M., and Picart, P., “Real-time three-sensitivity measurements based on three-color digital Fresnel holographic interferometry,” *Opt. Lett.*, 35(12), 2055-2057, 2010.
- Taylor C.J., and Kriegman, D.J., “Minimization on the Lie group SO (3) and related manifolds,” Yale University, 1994.
- Uyemura, T., Ogura, Y., Yamamoto, Y., and Shibata, S., “Holographic interferometry for study on hearing mechanism and combination with optical fibers,” *Proc. SPIE*, 23rd Annual Technical Symposium, 209-216, 1979.
- Valera J.D.R., Jones, J.D.C., Løkberg, O.J., Buckberry, C.H., and Towers, D.P., “Bi-modal vibration analysis with stroboscopic heterodyned ESPI,” *Meas. Sci. Tech.*, 8(6), 648, 1997.
- Van der Jeught, S., Dirckx, J.J.J., Aerts, J.R.M., Bradu, A., Podoleanu, A.Gh., and Buytaert, J.A.N, “Full-field thickness distribution of human tympanic membrane obtained with optical coherence tomography,” *JARO*, 14(4), 483-494, 2013.
- Volandri, G., Di Puccio, F., Forte, P., and Carmignani, C., “Biomechanics of the tympanic membrane,” *J. Biomech.*, 44(7), 1219-1236.

- Von Bally, G., *Holography in otology*, In *Holography in Medicine and Biology*, 183-197, Springer Berlin Heidelberg, 1979.
- von Bally, G., "Otosopic investigations by holographic interferometry: a fiber endoscopic approach using a pulsed ruby laser system," *Opt. Biomed. Sci.*, 110-114, Springer Berlin Heidelberg, 1982.
- von Bally, G., and Greguss, P., *Optics in Biomedical Sciences*, Springer-Verlag, 1982.
- Von Békésy, G., *Experiments in hearing*, E. G. Wever, McGraw-Hill, New York, 1960.
- Von Unge, M., Buytaert, J. A., and Dirckx, J. J., "Anatomical Boundary of the Tympanic Membrane Pars Flaccida of the Meriones unguiculatus (Mongolian Gerbil)," *Anatom. Rec.*, 294(6), 987-995, 2011.
- Voss, S.E., and Allen, J.B., "Measurement of acoustic impedance and reflectance in the human ear canal," *JASA*, 95(1), 372-384, 1994.
- Vest C.M., *Holographic Interferometry*, New York, John Wiley and Sons, Inc., 1979.
- Wada, H., Ando, M., Takeuchi, M., Sugawara, H., Koike, T., Kobayashi, T., et al., "Vibration measurement of the tympanic membrane of guinea pig temporal bones using time-averaged speckle pattern interferometry," *JASA*, 111(5), 2189-2199, 2002.
- Wagner, C., Osten, W., and Seebacher, S., "Direct shape measurement by digital wavefront reconstruction and multiwavelength contouring," *Opt. Eng.*, 39(1), 79-85, 2000.
- Yamaguchi I., and T. Zhang, "Phase-shifting digital holography," *Opt. Lett.*, 22(16):1268-1270, 1997.
- Yamaguchi, I., Ida, T., and Yokota, M., "Surface shape measurement by phase-shifting digital holography with dual wavelengths," *SPIE Optics+ Photonics*, 62920V-62920V, 2006.
- Zelenka, J.S., Varner, J.R., "Multiple-index holographic contouring," *App. Opt.*, 8(7), 1431-1434, 1969.
- Zhang, W., Chen, H.Y., and Kassab, G.S., "A rate-insensitive linear viscoelastic model for soft tissues," *Biomaterials*, 28(24), 3579-3586, 2007.
- Zhang X., Guan, X., Nakmali, D., Palan, V., Pineda, M., and Gan, R.Z., "Experimental and Modeling Study of Human Tympanic Membrane Motion in the Presence of Middle Ear Liquid," *JARO*, 1-15, 2014.

Zwislocki, J., "Analysis of the Middle-Ear Function. Part I: Input Impedance," *JASA*, 34(9B), 1514-1523, 1962.